

Fully coupled Maxwell-Kohn-Sham systems:

Electromagnetic field propagation in Schrödinger-like form
and
ab initio self-consistent light-matter simulations

vorgelegt von
Diplom-Physiker

René Jestädt

Fulda

von der Fakultät II - Mathematik und Naturwissenschaften
der Technischen Universität Berlin
zur Erlangung des akademischen Grades
Doktor der Naturwissenschaften
Dr. rer. nat.

vorgelegte Dissertation

Promotionsausschuss:

Vorsitzende : Prof. Dr. Ulrike Woggon
Berichter/Gutachter: Prof. Dr. Angel Rubio
Berichter/Gutachter: Prof. Dr. Andreas Knorr
Berichter/Gutachter: Prof. Dr. Walter Pfeiffer

Tag der wissenschaftlichen Aussprache:

Berlin 2018

Abstract

Light-matter interactions have always been an essential aspect of research. They cover the main properties of light and matter in atomic and molecular systems, in condensed phase, in chemical reactions, and in optics. This thesis presents a feasible implementation to simulate three-dimensional, real-time, real-space self-consistently coupled light-matter systems based on the theoretical background of a generalized Pauli-Fierz field theory. Due to the one-to-one correspondence between external fields and internal variables, we use a Kohn-Sham construction to approach the many-body problem in a non-relativistic low energy regime. The formalism leads in mean-field and effective nuclei approximation to coupled Ehrenfest-Maxwell-Pauli-Kohn-Sham equations.

In the first part of the thesis, we use a complex bilinear representation of the classical microscopic and macroscopic Maxwell's equations based on the Riemann-Silberstein vector. Maxwell's equations in Riemann-Silberstein representation have the form of an inhomogeneous Schrödinger equation, which allows to introduce time-evolution operators similar to quantum mechanics and to use existing time-evolution algorithms. In this manner, the Riemann-Silberstein propagation scheme can solve the microscopic Maxwell's equation in vacuum and the macroscopic ones in linear media. Such a Riemann-Silberstein implementation for propagating electromagnetic fields requires proper boundary conditions. Therefore, we introduce incident plane wave boundaries to simulate incoming plane waves, as well as perfectly matched layer boundaries for efficient absorption. We demonstrate our novel Riemann-Silberstein Maxwell propagation implementation for different typical electromagnetic applications, for instance, external current densities, plane wave propagation and field scattering in a linear medium. Our approach provides an alternative method of simulating electromagnetic fields compared to the standard finite-difference time-domain approach.

In the second part of the thesis, we couple the Kohn-Sham current density from our generalized Pauli-Fierz Hamiltonian self-consistently to the Riemann-Silberstein propagator, and in turn the electromagnetic field to the Kohn-Sham Hamiltonian. Including the back reaction of the matter on the electromagnetic field goes beyond what is typically considered in literature. Starting with full minimal coupling, we derive for the Kohn-Sham Hamiltonian a multipole expansion based on the Power-Zienau-Woolley transformation. We introduce a predictor-corrector scheme that provides a practical method to simulate self-consistent light-matter systems. Propagating both, the matter wavefunctions as well as the electromagnetic fields alongside, allows to improve the efficiency by exploiting the different length- and time-scales of light and matter. As consequence of taking the back-reaction of the electromagnetic field into account, we are able to define electromagnetic detectors next to the absorbing boundaries, which allows to analyze directly spectroscopic signals in the outgoing radiation in the far-field of the simulation box.

We present a first application of our novel approach by inducing plasmons in a nanoplasmonic system by an external laser and investigate the corresponding nano-optical effects, in particular the electromagnetic field enhancements in the vicinity of the nanoparticles. It reveals that the self-consistent fully coupled forward-backward simulations lead to significant changes in observables compared to a conventional forward-only coupling. The differences are larger than the ones found between using local density and gradient corrected approximations for the exchange-correlation functionals. Additionally, the directly measured outgoing electromagnetic fields show also harmonic generation only beyond dipole approximation.

Overall, the presented implementation is a comprehensive tool to handle fully coupled light-matter systems, especially for nano-optics, nano-plasmonics, (photo) electrocatalysis, light propagation with orbital angular momentum or light-tailored chemical reactions in optical cavities.

Deutsche Zusammenfassung

Die Wechselwirkung zwischen elektromagnetischen Feldern und Materie bildet die Basis für den Zusammenhalt von Atomen, Molekülen und Festkörpern. Während eine fundamentale Beschreibung der elementaren gekoppelten Größen, geladene Teilchen und Photonen, durch die Mitte des 20. Jahrhunderts entwickelten Quantenelektrodynamik die Wechselwirkung sehr exakt beschreibt, so wird der Einfluss und die Berechnung mit steigender Teilchenzahl immer schwieriger. Aus diesem Grund werden oft vereinfachte Modelle oder Näherungen angewendet, bei denen nicht die volle Wechselwirkung berücksichtigt wird. So wird meist die Rückkopplung der Materie auf das elektromagnetische Feld vernachlässigt. In dieser Arbeit wird auf Basis eines generalisierten Pauli-Fierz Hamiltonians die vollständige Licht-Materie Kopplung betrachtet und mit Hilfe der quantenelektrodynamischen Dichtefunktionaltheorie eine Methode und Implementierung vorgestellt, die realistische, dreidimensionale Licht-Materie Vielteilchensysteme simulieren kann.

Zu Beginn der Arbeit stellen wir eine alternative Beschreibung der inhomogenen Maxwell'schen Gleichungen mit Hilfe des komplexen bilinearen Riemann-Silberstein Vektors vor. In dieser Darstellung wird das mikroskopische elektromagnetische Feld durch zwei linear unabhängige Riemann-Silberstein Vektoren beschrieben, die einmal selbst und deren Riemann-Silberstein Maxwell Gleichungen durch komplexe Konjugation ineinander übergehen. Es kann gezeigt werden, dass mit diesen zwei verschiedenen Vektordarstellungen die Spin-Natur, hier in Form der Helizität, des Photonfeldes dargestellt wird. Im Falle der mikroskopischen Gleichungen, koppeln die beiden unterschiedlichen Helizitätsvektoren nicht, erst bei der Bestimmung der makroskopischen Riemann-Silberstein Maxwell-Gleichungen im linearen Medium findet eine Kopplung statt. In der Riemann-Silberstein Darstellung haben die kombinierten Ampère'schen und Faraday'schen Gleichungen eine zur Schrödinger Gleichung äquivalente Form. Damit lässt sich die zeitliche Entwicklung des elektromagnetischen Feldes durch eine quantenmechanische Propagation darstellen. Basierend auf dieser Riemann-Silberstein Formulierung stellen wir eine Implementierung vor, die die Zetentwicklung elektromagnetischer Felder simuliert. Dazu gehören verschiedene Randbedingungen, wie einfallende Ebene Wellen und absorbierende Box-Ränder, die ausgehende Signale möglichst ohne Reflexionen simuliert. Anhand mehrerer typischer Beispielanwendungen demonstrieren wir, dass unsere Implementierung eine Alternative zu der gängigen Finite-Differenzen-Methode im Zeitbereich für elektromagnetische Felder bietet.

Im weiteren Verlauf der Arbeit wird die klassische Stromdichte der Maxwell Gleichungen durch die quantenmechanischen Betrachtung der Materie bestimmt. Dazu nutzen wir, ausgehend von einem verallgemeinerten Pauli-Fierz Hamiltonian, einen Kohn-Sham Hamiltonian, dessen Stromdichte direkt an das elektromagnetische Feld gekoppelt ist. In umgekehrter Richtung beeinflusst das Elektromagnetische Feld durch die minimale Kopplung die Materie. Ausgehend vom Prinzip der minimalen Kopplung gehen wir mit Hilfe der Power-Zienau-Woolley Transformation in einen Hamiltonian über, dessen Wechselwirkung zwischen elektromagnetischen Feld und Materie durch Multipolterme des elektromagnetischen Feldes dargestellt wird. Damit die beiden Systeme, Materie und elektromagnetisches Feld, selbstkonsistent propagieren, führen wir eine Prädiktor-Korrektor-Verfahren ein. Zusätzlich nutzen wir die unterschiedlichen Längen- und Zeitskalen der Systeme aus, um eine bessere Effizienz der Implementierung vor allem bei groß Systemen zu erhalten.

Im letzten Teil der Arbeit zeigen wir den Einfluss der vollständigen Vorwärts-Rückwärts-

Kopplung am Beispiel eines nanoplasmonischen Dimers. Wir vergleichen konventionelle rein vorwärts gekoppelten Licht-Materie Simulationen mit der hier neu entwickelten vollständigen selbstkonsistenten Licht-Materie Kopplung. Die zum Teil stark abweichenden Ergebnisse werden anschaulich dargestellt und verdeutlichen die Notwendigkeit der Betrachtung einer vollständigen Licht-Materie Kopplung. Diese Einschätzung wird auch durch unsere Berechnungen mit unterschiedlichen Dichtefunktionalen verdeutlicht, bei der die Unterschiede der Ergebnisse zwischen den Funktionalen der lokalen und gradientkorrigierten Dichtenäherung kleiner waren als die Unterschiede zwischen vorwärts- und vollständiger Kopplung.

Insgesamt bietet die Implementierung damit eine praktikable Möglichkeit vollständig gekoppelte Systeme zu simulieren, z.B. für die Nanooptik, Nanoplasmonik oder Elektrokatalyse, um nur einige zu nennen.

Contents

| | |
|---|------------|
| Abstract | I |
| Deutsche Zusammenfassung | III |
| Content | V |
| Introduction | 1 |
| 1 Maxwell's equations in Riemann-Silberstein formalism | 5 |
| 1.1 Riemann-Silberstein microscopic Maxwell's equations | 5 |
| 1.1.1 Definition of the microscopic Riemann-Silberstein vectors | 6 |
| 1.1.2 Microscopic Maxwell's equations | 7 |
| 1.1.3 Curl operation in representation of Spin-1 matrices | 8 |
| 1.1.4 Riemann-Silberstein Maxwell Hamiltonian and eigensystem | 10 |
| 1.1.5 Combined six-component helicity Riemann-Silberstein vector | 11 |
| 1.1.6 Photon - anti-photon relation of the six-component Riemann-Silberstein vector | 13 |
| 1.1.7 Scalar product of the six-component Riemann-Silberstein vector | 15 |
| 1.1.8 Eigenstate expansion of the Riemann-Silberstein six-vector | 16 |
| 1.2 Riemann-Silberstein approach for macroscopic Maxwell's equations | 17 |
| 1.2.1 Riemann-Silberstein Maxwell's equations for linear media | 17 |
| 1.2.2 Definition of the macroscopic Riemann-Silberstein vectors | 18 |
| 1.2.3 Macroscopic Maxwell's equations | 19 |
| 1.2.4 Combined helicity Riemann-Silberstein six-vector in linear medium | 21 |
| 2 Riemann-Silberstein time-evolution of Maxwell fields in Schrödinger-like form | 24 |
| 2.1 Time-evolution of homogeneous microscopic Maxwell's equations | 24 |
| 2.2 Time-evolution of inhomogeneous microscopic Riemann-Silberstein six-vector | 27 |
| 2.3 Time-evolution of macroscopic Maxwell's equations in linear medium | 29 |
| 2.4 Conservation of electric and magnetic Gauß laws in time | 30 |
| 3 Implementation of the Riemann-Silberstein Maxwell propagation in the real-time real-space code Octopus | 33 |
| 3.1 Discretized three-dimensional grid for the Maxwell field | 34 |
| 3.1.1 Riemann-Silberstein Maxwell grid | 34 |
| 3.1.2 Finite difference stencil | 34 |
| 3.1.3 Parallelization strategy in the first principles code octopus | 39 |
| 3.2 Discretized Riemann-Silberstein time-evolution operators | 40 |
| 3.3 Maxwell-propagation with Octopus | 41 |

| | | |
|----------|---|------------|
| 3.3.1 | Comparison of the Octopus Maxwell-propagation with the electromagnetic propagation program MEEP | 42 |
| 3.3.2 | Longitudinal and transverse electromagnetic fields and currents | 46 |
| 3.4 | Maxwell boundaries | 52 |
| 3.4.1 | Absorbing boundaries by mask function | 52 |
| 3.4.2 | Absorbing boundaries by perfectly matched layer | 53 |
| 3.4.3 | Comparison of absorbing mask and perfectly matched layer boundaries | 63 |
| 3.4.4 | Incident plane waves boundaries | 63 |
| 3.4.5 | Numerical dispersion for plane wave propagation | 68 |
| 3.4.6 | Incident waves boundaries plus absorbing boundaries | 70 |
| 3.5 | Riemann-Silberstein Maxwell propagation for linear media | 71 |
| 4 | Theoretical fundamentals of light-matter coupling | 77 |
| 4.1 | Relativistic covariant notation | 77 |
| 4.2 | Relativistic decomposition of spin particles and derivation of Maxwell's equations | 79 |
| 4.3 | Multi-species Hamiltonian | 82 |
| 4.4 | Quantum-electrodynamical density-functional theory for multi species | 84 |
| 4.5 | Coupled Maxwell-Pauli-Kohn-Sham equations | 85 |
| 4.6 | Classical limit for Nuclei | 87 |
| 5 | Maxwell-Pauli-Kohn-Sham propagation on a three-dimensional grid | 90 |
| 5.1 | Riemann-Silberstein Maxwell's equations with Kohn-Sham current density | 91 |
| 5.2 | Riemann-Silberstein Maxwell propagation coupled to the Kohn-Sham current density | 94 |
| 5.3 | Discretized time-evolution and Time-reversal symmetry of the Maxwell system | 96 |
| 5.4 | Discretized time-evolution and Time-reversal symmetry of the matter system | 97 |
| 5.5 | Kohn-Sham interaction Hamiltonian | 99 |
| 5.5.1 | Full minimal coupling | 99 |
| 5.5.2 | Multipole expansion | 100 |
| 5.5.3 | Transverse Riemann-Silberstein vector calculation | 101 |
| 5.6 | Maxwell-Kohn-Sham multi-scale implementation | 102 |
| 5.6.1 | Multi-grid types | 102 |
| 5.6.2 | Multi-scales in time | 104 |
| 5.6.3 | Finite difference operators and parallelization strategy | 105 |
| 5.6.4 | Predictor-corrector method | 106 |
| 5.6.5 | Forward coupling | 106 |
| 5.6.6 | Forward and backward coupling | 107 |
| 5.7 | Simulation of open quantum systems with the Maxwell-Kohn-Sham propagation | 108 |
| 5.8 | Electromagnetic detectors | 108 |
| 5.9 | Broken time reversal symmetry | 109 |
| 6 | Applications | 110 |
| 6.1 | Laser pulse simulation scheme for a plasmonic nanoparticle system and simulation parameters | 110 |
| 6.1.1 | Na ₂₉₇ -dimer geometry and optical spectra | 112 |
| 6.1.2 | Simulation boxes and grid alignment | 113 |
| 6.1.3 | Measurement and detector regions | 113 |
| 6.1.4 | Laser pulse shape | 114 |
| 6.1.5 | Propagators | 115 |

| | | |
|----------|--|------------|
| 6.2 | Results from Ehrenfest-Maxwell-Pauli-Kohn-Sham simulations | 116 |
| 6.2.1 | Electric field enhancement | 116 |
| 6.2.2 | Next order in multipole coupling and energies | 124 |
| 6.2.3 | Electromagnetic detectors and harmonic generation | 126 |
| 6.2.4 | Ion motion | 128 |
| 6.2.5 | Comparison of different density functionals | 130 |
| | Summary, conclusion and outlook | 132 |
| | Appendices | 136 |
| A | Non-relativistic Pauli Hamiltonian in Coulomb gauge | 137 |
| A.1 | Vector potential and Coulomb gauge | 137 |
| A.2 | Pauli-equation as non-relativistic limit of coupled light-matter systems . . . | 138 |
| A.3 | Free matter Hamiltonians | 139 |
| A.4 | Free photon Hamiltonian | 140 |
| A.5 | Interaction Hamiltonians | 144 |
| A.5.1 | Longitudinal (Coulomb) interactions | 144 |
| A.5.2 | Transverse interactions | 145 |
| | List of Figures | 148 |
| | List of Tables | 149 |
| | Bibliography | 150 |
| | Publication | 160 |
| | Acronyms | 161 |
| | Acknowledgements | 162 |
| | Colophon | 163 |

Introduction

The complexity of light-matter interactions for realistic systems is very challenging for a full ab initio theoretical description. In this work, we present a first feasible methodology to simulate fully coupled systems. First, we summarize in the following the state of the art how complex light-matter systems are usually considered. One common way to describe the interaction of electromagnetic fields with matter relies on the reduction of the considered degrees of freedom. The choices for what is considered relevant depends on the aspects of interest. Historically as a consequence of this, the description of light-matter interactions has developed into different subfields. In case of quantum physics, one large area of research considers low-energy quantum physics which is again divided into different topics, i.e., quantum chemistry, quantum optics and solid-state physics. Each of these research areas is focussing on different aspects of low-energy physics and is based on the assumption that the effects that are in the focus of the respective other fields are rather small. The two main different aspects in this case can be summarized as follows. In quantum chemistry and solid state physics, the electromagnetic field is typically treated as a given environment that determines material science and a focus is on a detailed description of matter. On the other hand in quantum optics, certain matter properties are prescribed and a focus is placed on the electromagnetic fields. In this context, it becomes clear, that the theoretical methodology of considering the two topics depends on the corresponding subfield. Hence, some literature describes the matter degrees of freedom more detailed [1, 2, 3, 4], or in turn the electromagnetic fields [5, 6, 7].

While both research directions have reached significant progress in the past decades, mostly relying on the assumption of neglecting one main part, recent experiments go beyond this conventional picture into the regime, where both, light and matter, reveal a strong mutual correlation. Such strongly coupled systems, e.g., polaritons as light-matter hybrid states, can be observed when molecules are placed into nanocavities [8], microcavities [9] or other large nanostructures [10]. The large number of atoms inside nanostructures or molecules causes in most cases strong coupling effects [11], which has also an effect on a larger scale for chemical properties. As a consequence, strong electromagnetic fields can modify chemical reactions [12], changes in commonly used selection rules can be observed [13], or energy transfer can be altered [14]. Similar to chemical reactions, the optical behavior changes significantly in strongly coupled systems. New features in spectroscopy have been found, e.g., the enhancement of Raman processes [15], creation of polariton condensates [16] or retardation effects like energy transfer induced by attosecond laser pulses [17]. Indeed, research in strongly coupled systems has revealed neglected properties and new materials. We emphasize along these lines, e.g., detailed optical responses [18, 19], or a new color (Vantablack) arising for long nanotubes, which absorb almost any visual light [18]. Additionally, photons carrying angular momentum [20, 21, 22] have been proposed for large volume and long distance information transport [23], and even some processes in living bacteria show strong coupling effects [24].

The common underlying basis of all previously listed examples is the triad of particle species of electrons, nuclei, and photons. The ab-initio description of all three kinds of particle species together in one picture is in most cases considered in a reduced form to consider only the important ones [25], since all their corresponding degrees of freedom lead to a non-feasible problem. One way to reduce the degrees of freedom is based on the limit of a one- or two-dimensional spatial description, while keeping the full particle interactions. Here, the full rotational symmetry is missing, and all its corresponding effects. Model systems are another option to simplify the considered degrees of freedom, which still try to catch most relevant features of the real system, but they neglect also per construction some effects. Consequently, the choice of a model system is pre-decision which effects can be observed. In a third way, one particle species and the corresponding degrees of freedom are only considered as an external perturbation of the system. Hence, the back-reaction on this external particle species is neglected, which always breaks in the conservation of energy. The driven matter system gains too much energy when they get excited since they cannot screen the external electromagnetic field due to their induced current. However, in electronic structure theory, for example, photons and nuclei are typically only external variables, which leads to solvable systems [1] with different kinds of methods [26, 27, 28, 29, 30, 31, 32]. Due to the simplification of the full problem, many effects cannot be observed, which are caused by the neglected back-reaction. As a consequence, some techniques add more degrees of freedom, e.g., the electron-nucleus interaction via exact-factorization [33, 34] or trajectory-based solutions [35, 36, 37], but taking all three interactions into account including the photon field, is up to now only considered in a very limited set of approaches. Only very recently some theoretical developments have emerged that attempt to treat matter and electromagnetic radiation on an equal ab-initio footing. Examples include cases where light-matter coupling is treated classically [38, 39, 40, 41, 42, 43, 44, 45, 46] or as a quantized field [47, 48, 49, 50, 51, 52, 53, 54]. Up to now only a few works describe all three particle types on the same level of description [55, 56, 57, 58]. This leads to interesting light-matter behavior, e.g. due to modified Maxwell's equations in vacuum [59], as well as polariton states with new potential-energy surfaces [60] or detailed chemical structures [61]. These researches followed the bottom-up direction to describe the fully coupled picture in terms of quantum electrodynamics. They provide applications to investigate the full particle interactions, but their applications are limited to few particle systems. This is where the present work is framed and follow the opposite top-down direction of handling with a large number of particles with mass. Since it is not possible to consider the full quantum nature of such large systems especially the degrees of freedom of the photons, we introduce a semi-classical method of coupled electromagnetic mean-field and quantum-mechanical matter. This first approximation should give us an impression how strong the electromagnetic back-reaction change the results compared to conventional simulations. Additionally such a mean-field simulation provides a basis which can be expand and modified by new developed QED approaches to catch more quantum effects.

The previously discussed methods to simplify the complete problem, like neglecting nuclear motion or using the dipole approximation of the Maxwell-matter coupling or are not applicable to larger realistic (three-dimensional, non-model) systems. The present work aims at describing electrons, nuclei and photons on an equal ab-initio level. The starting point for our approach is a generalized Pauli-Fierz Hamiltonian for non-relativistic quantum electrodynamics (QED) [62, 25]. Using density functional theory, this formulation in a multi-species and multi-scale ansatz leads to coupled Maxwell-Pauli-Kohn-Sham equations (MPKS) [63]. In a first numerical application for a nanoplasmonic dimer, we demonstrate the difference of considering only the forward coupling of electromagnetic fields to matter

and compare to self-consistent forward and backward coupling between light and matter. Taking this feature and varying different options, e.g., the degrees of freedom of ion motion or the multipole expansion terms for Maxwell to matter coupling, and different density functionals, gives a first overview of new effects and perspectives for self-consistent light-matter coupling. We show that common stating that missing correlations among one type of particles (e.g. electrons) is the cause for a disagreement between theory and experiment can be misleading. Instead, the cause for a discrepancy might also be the conventionally omitted self-consistent light-matter coupling. Our first implementation based on the newly introduced theoretical technique is a comprehensive tool to investigate experimental results, or design and control novel materials. Additionally we emphasize here, that simulating the physically electromagnetic field including the back-reaction of the matter superposed with the external field, has the advance to be directly detected. For instance, we can analyze the outgoing electromagnetic field at the simulation box boundaries. In contrast, conventional simulations obtain the corresponding spectroscopy indirectly by investigating only the matter reaction. Therefore, our implementation can measure the error between such usual "indirect" spectroscopy and the "real" emitted electromagnetic field.

The present PhD focuses on the combination of propagating the quantum mechanical matter, the corresponding internal and external electromagnetic fields, and their mutual coupling. Hence, we provide a mathematical and physically consistent framework to deal with in interactions of classical light with matter at arbitrary strength, length and time scales. We have organized the thesis as follows. Using the Riemann-Silberstein vector of classical electrodynamics, we show in chapter 1 how to rewrite the microscopic Maxwell's equations in Schrödinger like form. Additionally in a similar manner, we obtain the macroscopic Maxwell's equations in linear media which requires a linear combination of the two electromagnetic helicity states of the electromagnetic field, i.e., Riemann-Silberstein vectors, which refer to different spin states. Following the usual construction of quantum-mechanical time-evolution operators, we show in chapter 2 how to construct the Riemann-Silberstein time-evolution operators for homogeneous and inhomogeneous propagations in vacuum or linear media. In this representation, the implemented code provides a method for simulating the propagation of electromagnetic fields which is an alternative to the commonly used finite difference time domain method (FDTD) [64, 65]. Consequently, in chapter 3 we describe the practical details of the Maxwell implementation on a three-dimensional grid including useful boundary conditions as absorbing boundaries, a perfectly matched layer formulation for the Riemann-Silberstein case, incident plane waves and a combination of both. For each of these features, we demonstrate some applications to demonstrate the stand-alone electromagnetic field propagation simulation.

After introducing the novel Riemann-Silberstein electromagnetic field simulation, we summarize and introduce in chapter 4 the fundamentals of quantum electrodynamics to obtain the generalized many-body Pauli-Fierz Hamiltonian, which forms the basis to couple quantized matter variables like current and charge densities to the classical electromagnetic fields. Furthermore, we employ this Pauli-Fierz Hamiltonian to develop a density-functional theory (DFT) [66, 67] for non-relativistic QED for photons, electrons and effective nuclei on the level of a generalized quantum-electrodynamical density-functional theory (QEDFT) [62, 49, 25]. Taking the mean-field approximation of the electromagnetic field and nuclei, we arrive at coupled Ehrenfest-Maxwell-Pauli-Kohn-Sham (EMPKS) equations that build the basis for our coupled light-matter implementation, which is introduced in detail in chapter 5. This chapter also includes a discussion for using multi-scale grids and time steps to properly handle the different features of the systems, as well as full minimal-coupling and the multipole expansion, and a predictor-corrector scheme for self-consistent

forward-backward coupling of light and matter. In chapter 6, the significance of the entire forward-backward coupling is taken into account and compared to the commonly used forward-coupling in a first Maxwell-Kohn-Sham application for a nanoplasmonic system excited by a laser. Applying different simulation options, we investigate the near-field effects of the electromagnetic fields, especially their field enhancements. Furthermore, we decompose the total field into a longitudinal and transverse fields, and investigate the interference of both transverse internal and external fields with corresponding frequency shift. The advantage of propagating the total electromagnetic fields on a numerical grid allows us to define corresponding electromagnetic detectors to analyze the outgoing electromagnetic radiation in the far-field. This provides a novel simulation tool to record commonly employed spectroscopies that are used in experiments. In the [Summary](#) and the Outlook, we recapitulate the complex work that was required to achieve our novel introduced methodology of considering electromagnetic field and matter fully coupled. Further, we emphasize the main aspects and results of our first applications which demonstrate that we provide a proper ab initio implementation which opens a new research area in material science and optics. Stepping forward in a field that was thought of being non-reachable means that a lot of new arising problems can be tackled in the near future. Hence, the insights of this thesis can be seen as a basic ingredient for future theoretical developments, for instance, finding methods to include QEDFT effects [52, 54, 57, 58, 25, 48].

Chapter 1

Maxwell's equations in Riemann-Silberstein formalism

Classical electrodynamics describes the evolution of electric and magnetic fields, determined by the four Maxwell's equations, separately known as Ampère's law, Faraday's law, electric and magnetic Gauss law. All equations are first order differential equations. They can be classified into two groups. The two Gauß laws, which belong to the first group, contain only first order spatial derivatives (second order in time if working with the potential and vector fields, as in standard text books). On the other hand, Ampère's law and Faraday's law, which belong to the second group, include a first order time derivative and determine the time evolution as the underlying equations of motion for Maxwell fields.

In non-relativistic quantum mechanics, the determining time-evolution equation is the Schrödinger equation which has also a first order time derivative but second order spatial derivatives. Historically it was noticed very early that Ampère's law and Faraday's law can be cast in an equivalent Schrödinger-like form [68, 69, 70, 71]. Since electromagnetic fields are given in terms of three-component vectors, the Schrödinger-form of Maxwell's equations contains a matrix-valued Hamiltonian. Taking this into account and the fact that the Maxwell's equations are Lorentz-invariant, the corresponding Maxwell Hamiltonian matrix has similarities to the four-dimensional Dirac Hamiltonian. Indeed, we illustrate in the following that the basic form of the Maxwell-Schrödinger Hamiltonian is based on spin-1 matrices that are analogous to the Dirac gamma matrices. Based on these features, we highlight mathematical similarities of a classical Maxwell field description and quantum mechanics to emphasize the utility of this alternative representation of electrodynamics. The mathematical similarity of both physical systems become increasingly important when we consider quantum electrodynamics (QED) in chapter 4.

1.1 Riemann-Silberstein microscopic Maxwell's equations

The microscopic Maxwell's equations describe both electromagnetic fields and the matter variables i.e. charge and current density in vacuum. In 1907, Ludwik Silberstein defined a six-dimensional bilinear complex vector for the two real three-dimensional electric and magnetic fields [68]. To set up a whole basis set for arbitrary electromagnetic field superpositions, it is necessary to define two different kinds of such complex vectors, which differ only in the sign of the imaginary part. We discuss later, that both vectors can be referred to positive respectively negative helicity of light [72]. Based on the Riemann-Silberstein vector, we transform the Maxwell's equations into two complex equations by combining Faraday's law and Ampère's law and equally the two Gauß laws into one [73]. We combine

the positive and negative helicity Riemann-Silberstein vectors in a six-dimensional vector and describe a formalism similar to quantum mechanics. Therefore, we introduce a curl operation identity using quantum mechanical spin-1 matrices to replace the curl operations in Faraday's and Ampère's law as well as in the Riemann-Silberstein combination. The spin-1 matrix operation is not the only similarity to equations in quantum mechanics. We deduce, that the Riemann-Silberstein combination of Faraday's and Ampère's law is equivalent to a homogeneous time-dependent Schrödinger equation, that becomes inhomogeneous in the presence of current densities. Our formalism is based on the considerations in Ref. [72, 73]. In case of Maxwell's equations in vacuum, it is sufficient to use either the positive helicity Riemann-Silberstein vector and its Maxwell Riemann-Silberstein equations or vice versa the negative version to determine the electromagnetic fields and their propagation in time.

1.1.1 Definition of the microscopic Riemann-Silberstein vectors

The Riemann-Silberstein approach of classical electrodynamics maps both three-dimensional electromagnetic fields into one bilinear complex vector, called Riemann-Silberstein vector and generally expressed by $\vec{F}(\vec{r}, t)$ [68, 73, 74]. Due to unit considerations it is useful to multiply real part and imaginary part of \vec{F} by different factors depending on the permittivity ϵ in the real part and permeability μ in the imaginary part. In general, two complex vectors $\vec{a} + i\vec{b}$ and $\vec{a} - i\vec{b}$ with real \vec{a} , and \vec{b} are linearly independent. Hence, the Riemann-Silberstein vector can be written in two linearly independent versions, where the plus respectively minus sign between real and imaginary part is shown by a superscript sign index. We start with the two variants of Riemann-Silberstein vectors in vacuum, denoted as \vec{F}_+ and \vec{F}_- . In the vacuum case, the electric permittivity and magnetic permeability are equal to the natural constants ϵ_0 , μ_0 , hence the two Riemann-Silberstein vectors in vacuum are defined by

$$\vec{F}_+(\vec{r}, t) = \sqrt{\frac{\epsilon_0}{2}}\vec{E}(\vec{r}, t) + i\sqrt{\frac{1}{2\mu_0}}\vec{B}(\vec{r}, t), \quad (1.1.1)$$

$$\vec{F}_-(\vec{r}, t) = \sqrt{\frac{\epsilon_0}{2}}\vec{E}(\vec{r}, t) - i\sqrt{\frac{1}{2\mu_0}}\vec{B}(\vec{r}, t), \quad (1.1.2)$$

in terms of the electric field $\vec{E}(\vec{r}, t)$ and magnetic field $\vec{B}(\vec{r}, t)$ at position \vec{r} at time t . We note here a general form for the indices notation in this thesis. Italic letters indices denote a component or running index, whereas non-italic letters and symbols names the considered variable. In the following, we denote often \pm , which means $+$ or $-$ and \mp vice versa as two possible options for the sign. The upper sign option is linked to formulas for the positive defined $\vec{F}_+(\vec{r}, t)$, and consequently the lower sign option represents the ones for the negative defined $\vec{F}_-(\vec{r}, t)$. The two vectors $\vec{F}_\pm(\vec{r}, t)$ are directly linked since they are always the complex conjugate $\vec{F}_\pm^*(\vec{r}, t)$ of each other

$$\vec{F}_- = \vec{F}_+^*, \quad \vec{F}_+ = \vec{F}_-^*. \quad (1.1.3)$$

The two prefactors $\sqrt{\epsilon_0/2}$ and $\sqrt{1/2\mu_0}$ are selected such that the square of the absolute value of $\vec{F}_+(\vec{r}, t)$ or $\vec{F}_-(\vec{r}, t)$ results in the classical energy density $u(\vec{r}, t)$ of the Maxwell fields

$$u(\vec{r}, t) = \frac{1}{2} \left(\epsilon_0 \vec{E}^2(\vec{r}, t) + \frac{1}{\mu_0} \vec{B}^2(\vec{r}, t) \right). \quad (1.1.4)$$

Therefore, the energy density $u(\vec{r}, t)$ in Eq. (1.1.4) is equal to the scalar product of two complex Riemann-Silberstein vectors with

$$u(\vec{r}, t) = \vec{F}_+^*(\vec{r}, t) \cdot \vec{F}_+(\vec{r}, t) = \vec{F}_-^*(\vec{r}, t) \cdot \vec{F}_-(\vec{r}, t). \quad (1.1.5)$$

The back transformation to obtain the electromagnetic fields $\vec{E}(\vec{r}, t)$ and $\vec{B}(\vec{r}, t)$ from the Riemann-Silberstein vectors $\vec{F}_\pm(\vec{r}, t)$ can be written as

$$\vec{E}(\vec{r}, t) = \sqrt{\frac{1}{2\epsilon_0}} \left(\vec{F}_+(\vec{r}, t) + \vec{F}_+^*(\vec{r}, t) \right) = \sqrt{\frac{1}{2\epsilon_0}} \left(\vec{F}_+(\vec{r}, t) + \vec{F}_-(\vec{r}, t) \right), \quad (1.1.6)$$

$$\vec{B}(\vec{r}, t) = -i\sqrt{\frac{\mu_0}{2}} \left(\vec{F}_+(\vec{r}, t) - \vec{F}_+^*(\vec{r}, t) \right) = -i\sqrt{\frac{\mu_0}{2}} \left(\vec{F}_+(\vec{r}, t) - \vec{F}_-(\vec{r}, t) \right). \quad (1.1.7)$$

1.1.2 Microscopic Maxwell's equations

Based on the previously defined vectors $\vec{F}_\pm(\vec{r}, t)$, it is possible to describe two equations which are equivalent to the microscopic Maxwell's equations with electric field \vec{E} , magnetic field \vec{B} , charge density $\rho(\vec{r}, t)$ and current density $\vec{j}(\vec{r}, t)$ in vacuum. The well known microscopic Maxwell's equations in SI units are given by [75]

$$\nabla \cdot \vec{E}(\vec{r}, t) = \epsilon_0^{-1} \rho(\vec{r}, t), \quad (1.1.8)$$

$$\nabla \cdot \vec{B}(\vec{r}, t) = 0, \quad (1.1.9)$$

$$\nabla \times \vec{E}(\vec{r}, t) = -\frac{\partial}{\partial t} \vec{B}(\vec{r}, t), \quad (1.1.10)$$

$$\nabla \times \vec{B}(\vec{r}, t) = \mu_0 \left(\vec{j}(\vec{r}, t) + \epsilon_0 \frac{\partial}{\partial t} \vec{E}(\vec{r}, t) \right). \quad (1.1.11)$$

The electric charge density contribution $\vec{\rho}(\vec{r}, t)$ on the right-hand side of the electric Gauß law in Eq. (1.1.8) causes a longitudinal field component. Conversely, the contribution of the charge density can be obtained by the longitudinal field component of the electric field. In contrast, the magnetic field Gauß law in Eq. (1.1.9) shows that the magnetic field is always solenoidal at all times. Taking these Gauß law conditions into account, the two remaining equations, Eq. (1.1.10) and Eq. (1.1.11), determine the time-evolution of the Maxwell field. In Eq. (1.1.10) the curl of the electric field describes the time variation of the magnetic field. In contrast to Faraday's law, the time variation of the electric Field in Ampère's law depends in general on the curl of the magnetic field but also on the displacement current density $\vec{j}(\vec{r}, t)$. In case of mapping the two relevant electromagnetic field vectors into a complex Riemann-Silberstein vector $\vec{F}_\pm(\vec{r}, t)$, it is possible to combine the electric and magnetic Gauß laws as well as the remaining Faraday's and Ampère's law into one equation.

The two divergence conditions in Eq. (1.1.8) and Eq. (1.1.9) represented by the two Riemann-Silberstein vectors $\vec{F}_\pm(\vec{r}, t)$ are given by

$$\nabla \cdot \vec{F}_\pm(\vec{r}, t) = \sqrt{\frac{1}{2\epsilon_0}} \rho(\vec{r}, t). \quad (1.1.12)$$

Although we obtained two equations here, one for $\vec{F}_+(\vec{r}, t)$ and one for $\vec{F}_-(\vec{r}, t)$, both Gauß laws hold in both equations simultaneously. Furthermore, the right-hand side is equal irrespectively of applying the divergence operation to positive $\vec{F}_+(\vec{r}, t)$ or negative $\vec{F}_-(\vec{r}, t)$, and emphasizes the solenoidal magnetic vector field in the imaginary part. The difference

between the positive or negative version of Eq. (1.1.12) consists of the intrinsic positive helicity described by the $\vec{F}_+(\vec{r}, t)$ version or negative helicity for the $\vec{F}_-(\vec{r}, t)$ version which we consider later in this section.

In a similar way, the two time-derivative Maxwell's equations, Faraday's law in Eq. (1.1.10) and Ampère's law in Eq. (1.1.11), can be written in terms of the Riemann-Silberstein vectors defined in Eq. (1.1.1) and Eq. (1.1.2) and the speed of light in vacuum $c_0 = \frac{1}{\sqrt{\epsilon_0 \mu_0}}$. We arrive at the form

$$i \frac{\partial}{\partial t} \vec{F}_\pm(\vec{r}, t) = \pm c_0 \vec{\nabla} \times \vec{F}_\pm(\vec{r}, t) - i \frac{1}{\sqrt{2\epsilon_0}} \vec{j}(\vec{r}, t). \quad (1.1.13)$$

The comparison of the plus and minus version of the combined Faraday's and Ampère's laws in Eq. (1.1.13) shows that the signs of the terms on the right-hand side are not equal for both cases. The \vec{F}_- version of Eq. (1.1.13) requires a change of sign for all terms on the right-hand side compared to the $\vec{F}_+(\vec{r}, t)$ equation. This change in sign is contrary to the previously discussed Gauß laws in Riemann-Silberstein representation in Eq. (1.1.12). However, this becomes more clear later in this section, when we consider the corresponding helicity of $\vec{F}_\pm(\vec{r}, t)$.

1.1.3 Curl operation in representation of Spin-1 matrices

Now, after combining Maxwell's equations with a bilinear vector, we search for a relation of these Riemann-Silberstein equations with the well known ones in quantum mechanics, especially the time-dependent Schrödinger form. The curl operation in Eq. (1.1.13) is equivalent to a spin-1 matrix-vector operation. This operation obeys the following cross product for general vectors \vec{a} and \vec{b} [73]

$$\vec{a} \times \vec{b} = -i(\vec{S} \cdot \vec{a})\vec{b}, \quad (1.1.14)$$

where the vector \vec{S} of spin-1 matrices is defined in Cartesian representation by

$$\vec{S} = \begin{pmatrix} S_1 \\ S_2 \\ S_3 \end{pmatrix}, \quad (1.1.15)$$

with

$$S_1 = \begin{pmatrix} 0 & 0 & 0 \\ 0 & 0 & -i \\ 0 & i & 0 \end{pmatrix}, \quad S_2 = \begin{pmatrix} 0 & 0 & i \\ 0 & 0 & 0 \\ -i & 0 & 0 \end{pmatrix}, \quad S_3 = \begin{pmatrix} 0 & -i & 0 \\ i & 0 & 0 \\ 0 & 0 & 0 \end{pmatrix}. \quad (1.1.16)$$

The corresponding Cartesian basis vectors are denoted as

$$\vec{e}_1 = \begin{pmatrix} 1 \\ 0 \\ 0 \end{pmatrix}, \quad \vec{e}_2 = \begin{pmatrix} 0 \\ 1 \\ 0 \end{pmatrix}, \quad \vec{e}_3 = \begin{pmatrix} 0 \\ 0 \\ 1 \end{pmatrix} \quad (1.1.17)$$

so that the identity of the cross product in Eq. (1.1.14) can readily be seen, and an arbitrary \vec{a} with its components

$$\vec{a} = \begin{pmatrix} a_x \\ a_y \\ a_z \end{pmatrix} \quad (1.1.18)$$

is expressed with Cartesian basis set by

$$\vec{a} = a_x \vec{e}_1 + a_y \vec{e}_2 + a_z \vec{e}_3 . \quad (1.1.19)$$

However, there is a second representation, the spherical representation, which is discussed in greater detail in Ref. [71] and which we briefly introduce here. In quantum mechanics, the spherical representation is the common Spin representation, where one coordinate axis is distinguished. One spin-matrix is chosen such that its eigenvalues are on the diagonal and that the corresponding eigenvector is parallel to this distinguished axis. We denote the spherical representation with a tilde above the letters. It is common to chose the eigenvector axis along the z-axis and therefore $\vec{e}_3 = \vec{e}_3$. Furthermore, the eigenvalues of the spin-1 matrix are 1, 0, -1 , so that the \tilde{S}_3 matrix is

$$\tilde{S}_3 = \begin{pmatrix} 1 & 0 & 0 \\ 0 & 0 & 0 \\ 0 & 0 & -1 \end{pmatrix} . \quad (1.1.20)$$

The two other matrices \tilde{S}_1 , and \tilde{S}_2 are obtained by a proper rotation using the Wigner-D rotation matrices $\mathcal{D}^{(j)}(\alpha, \beta, \beta)$ in Ref. [76] with rotation angles α, β, β and $j = 1$ which corresponds to spin 1. The proper rotations for \tilde{S}_1 , and \tilde{S}_2 are in accord with [71] given by

$$\tilde{S}_1 = \mathcal{D}^{(1)}(0, \pi/2, 0) \tilde{S}_3 \mathcal{D}^{(1)}(0, -\pi/2, 0) = \frac{1}{\sqrt{2}} \begin{pmatrix} 0 & 1 & 0 \\ 1 & 0 & 1 \\ 0 & 1 & 0 \end{pmatrix} , \quad (1.1.21)$$

$$\tilde{S}_2 = \mathcal{D}^{(1)}(0, 0, \pi/2) \tilde{S}_1 \mathcal{D}^{(1)}(0, 0, -\pi/2) = \frac{i}{\sqrt{2}} \begin{pmatrix} 0 & -1 & 0 \\ 1 & 0 & -1 \\ 0 & 1 & 0 \end{pmatrix} , \quad (1.1.22)$$

Consequently, we have to transform the basis vectors in Eq. (1.1.17) to the corresponding spherical basis vectors $\vec{e}_1, \vec{e}_2, \vec{e}_3$

$$\vec{e}_1 = \begin{pmatrix} -\frac{1}{\sqrt{2}} \\ -i\frac{1}{\sqrt{2}} \\ 0 \end{pmatrix} , \quad \vec{e}_2 = \begin{pmatrix} \frac{1}{\sqrt{2}} \\ -i\frac{1}{\sqrt{2}} \\ 0 \end{pmatrix} , \quad \vec{e}_3 = \begin{pmatrix} 0 \\ 0 \\ 1 \end{pmatrix} . \quad (1.1.23)$$

Hence, the arbitrary vector \vec{a} in Eq. (1.1.18) can be transformed into spherical representation \vec{a} using the spherical basis set in Eqs. (1.1.23) with

$$\vec{a} = a_x \vec{e}_1 + a_y \vec{e}_2 + a_z \vec{e}_3 . \quad (1.1.24)$$

Finally, the Riemann-Silberstein vectors $\vec{F}_\pm(\vec{r}, t)$ and their underlying operations can be expressed in both representations, the Cartesian or the spherical. However, it is more convenient to use the Cartesian representation of the cross product with three equivalent coordinates. If we substitute the vector \vec{a} in Eqs. (1.1.14) by a nabla vector $\vec{\nabla}$ and \vec{b} by the Riemann-Silberstein vectors $\vec{F}_\pm(\vec{r}, t)$, we get a curl operation described by spin-1 matrices

$$\vec{\nabla} \times \vec{F}_\pm(\vec{r}, t) = -i \left(\vec{\mathbf{S}} \cdot \vec{\nabla} \right) \vec{F}_\pm(\vec{r}, t) . \quad (1.1.25)$$

Hence, the combined Ampère's and Faraday's law in Eq. (1.1.13) result in

$$i\frac{\partial}{\partial t}\vec{F}_{\pm}(\vec{r}, t) = \mp ic_0 (\vec{S} \cdot \vec{\nabla}) \vec{F}_{\pm}(\vec{r}, t) - i\frac{1}{\sqrt{2\epsilon_0}}\vec{j}(\vec{r}, t), \quad (1.1.26)$$

with the upper sign for positive helicity and lower sign for negative helicity. Without any loss of generality, we can multiply the whole equation in Eq. (1.1.26) by Planck's constant \hbar to get an inhomogeneous Schrödinger like Maxwell equation

$$i\hbar\frac{\partial}{\partial t}\vec{F}_{\pm}(\vec{r}, t) = \mp i\hbar c_0 (\vec{S} \cdot \vec{\nabla}) \vec{F}_{\pm}(\vec{r}, t) - i\frac{\hbar}{\sqrt{2\epsilon_0}}\vec{j}(\vec{r}, t), \quad (1.1.27)$$

one for $\vec{F}_+(\vec{r}, t)$ and another one for $\vec{F}_-(\vec{r}, t)$.

1.1.4 Riemann-Silberstein Maxwell Hamiltonian and eigensystem

Owing to the replacement of the curl operation by spin-1 matrix representation, the quantum mechanical momentum operator \vec{p}

$$\vec{p} = -i\hbar\vec{\nabla} \quad (1.1.28)$$

appears in Eq. (1.1.27). It is also well known that the energy-momentum relation of a photon is

$$E = c_0\vec{p}. \quad (1.1.29)$$

Thus, with all these similarities, we can define a Hamiltonian-like operator H_{Mx}

$$H_{\text{Mx}} = -i\hbar c_0 [\vec{\nabla} \cdot \vec{S}] = \hbar c_0 \begin{bmatrix} 0 & -\frac{\partial}{\partial z} & \frac{\partial}{\partial y} \\ \frac{\partial}{\partial z} & 0 & -\frac{\partial}{\partial x} \\ -\frac{\partial}{\partial y} & \frac{\partial}{\partial x} & 0 \end{bmatrix}. \quad (1.1.30)$$

Expressed in the Riemann-Silberstein formalism, Faraday's and Ampère's law can be written as an inhomogeneous Schrödinger equation

$$i\hbar\frac{\partial}{\partial t}\vec{F}_{\pm}(\vec{r}, t) = \pm H_{\text{Mx}}\vec{F}_{\pm}(\vec{r}, t) \mp i\frac{\hbar}{\sqrt{2\epsilon_0}}\vec{j}(\vec{r}, t). \quad (1.1.31)$$

The bilinear Riemann-Silberstein complex vectors $\vec{F}_{\pm}(\vec{r}, t)$ describe the Maxwell's field vectors, i.e the electric and magnetic field, analogously to wave functions in quantum mechanics. In case of homogeneous Maxwell's equations without any current or charge densities in space, the combined Faraday's and Ampère's equation takes directly the form of a time dependent Schrödinger equation

$$i\hbar\frac{\partial}{\partial t}\vec{F}_{\pm}(\vec{r}, t) = \pm H_{\text{Mx}}\vec{F}_{\pm}(\vec{r}, t). \quad (1.1.32)$$

It combines all Maxwell's equations that contain temporal derivatives into only one equation and reveals another important feature of quantum mechanical equations for the Maxwell's equations. In such a spin-1 matrices representation with first order time derivative multiplied by imaginary unit and Planck constant \hbar acting on the Riemann-Silberstein vector on the left-hand side as well as a Hamiltonian-like operator acting on the same Riemann-Silberstein vector on the right-hand side, it is possible to construct a time-evolution operator for Maxwell's fields. In addition, analogous to the stationary solution of

the Schrödinger equation in quantum mechanics, the stationary solution of the Maxwell's wave equation in Eq. (1.1.32) can be considered as a factor of spatial dependent function and a time-dependent phase factor

$$\vec{F}_{\pm}(\vec{r}, t) = e^{-i\omega t} \vec{F}_{\pm}(\vec{r}, t_0), \quad (1.1.33)$$

with constant eigenmode frequency ω . This separation of $\vec{F}_{\pm}(\vec{r}, t)$ leads to the eigenvalue problem for the Riemann-Silberstein Maxwell's wave equation

$$i\hbar \frac{\partial}{\partial t} \vec{F}_{\pm}(\vec{r}, t) = \pm H_{\text{Mx}} \vec{F}_{\pm}(\vec{r}, t) \quad \Leftrightarrow \quad \omega \hbar \vec{F}_{\pm}(\vec{r}, t) = c_0 (\pm \vec{S} \cdot \vec{p}) \vec{F}_{\pm}(\vec{r}, t), \quad (1.1.34)$$

which is the stationary Riemann-Silberstein wave equation similar to the one in quantum mechanics. Thus, it is equally possible to expand the Riemann-Silberstein fields by a superposition in terms of their eigenfunctions with eigenmodes ω . In case of positive ω in Eq. (1.1.34), the helicity, defined as the projection of the momentum \vec{p} on the spin vector \vec{S} , is positive for $\vec{F}_{+}(\vec{r}, t)$ and negative for $\vec{F}_{-}(\vec{r}, t)$. Consequently $\vec{F}_{+}(\vec{r}, t)$ and its corresponding equation is referred to positive helicity and $\vec{F}_{-}(\vec{r}, t)$ to negative helicity.

1.1.5 Combined six-component helicity Riemann-Silberstein vector

For all previously considered Riemann-Silberstein Maxwell's equations, we always found two equivalent expressions, one equation for $\vec{F}_{+}(\vec{r}, t)$ and one for $\vec{F}_{-}(\vec{r}, t)$. Similar to the works of Ref. [73, 77], we introduce a formalism which combines both vectors. Instead of writing two equations, both variants can be expressed combined into one by building a six-dimensional vector \mathcal{F} and its complex conjugate one \mathcal{F}^{\dagger} which contains both $\vec{F}_{+}(\vec{r}, t)$ and $\vec{F}_{-}(\vec{r}, t)$ and are given by

$$\mathcal{F}(\vec{r}, t) = \begin{pmatrix} \vec{F}_{+}(\vec{r}, t) \\ \vec{F}_{-}(\vec{r}, t) \end{pmatrix}, \quad \mathcal{F}^{\dagger}(\vec{r}, t) = \begin{pmatrix} \vec{F}_{-}^{\dagger}(\vec{r}, t) \\ \vec{F}_{+}^{\dagger}(\vec{r}, t) \end{pmatrix}. \quad (1.1.35)$$

We call $\mathcal{F}(\vec{r}, t)$ the six-component Riemann-Silberstein vector of a system. All Maxwell equations can be written in terms of $\mathcal{F}(\vec{r}, t)$ which always contain the positive and negative helicity equations. The first three components of $\mathcal{F}(\vec{r}, t)$ correspond to the positive helicity equations of $\vec{F}_{+}(\vec{r}, t)$ whereas the last three components represent the negative helicity equations of $\vec{F}_{-}(\vec{r}, t)$.

Next, we want to express the microscopic Maxwell's equations in terms of the newly introduced six-dimensional vector $\mathcal{F}(\vec{r}, t)$ in Eq. (1.1.35). In addition to the introduced $\mathcal{F}(\vec{r}, t)$, other variables have to be adapted in a similar way. Hence, the two-dimensional Riemann-Silberstein charge density $\mathcal{Q}(\vec{r}, t)$ can be written as

$$\mathcal{Q}(\vec{r}, t) = \begin{pmatrix} 1 \\ 1 \end{pmatrix}_{2 \times 1} \otimes \left(\frac{1}{\sqrt{2\epsilon_0}} \rho(\vec{r}, t) \right)_{1 \times 1}. \quad (1.1.36)$$

Furthermore, the 2x6 dimensional Riemann-Silberstein divergence operator, built by a Kronecker product of a 2x2 matrix and the 1x3 transposed nabla operator vector, is

$$\mathcal{D} = \begin{pmatrix} 1 & 0 \\ 0 & 1 \end{pmatrix}_{2 \times 2} \otimes \left(\vec{\nabla} \right)_{1 \times 3}^{\top} = \begin{pmatrix} \frac{\partial}{\partial x} & \frac{\partial}{\partial y} & \frac{\partial}{\partial z} & 0 & 0 & 0 \\ 0 & 0 & 0 & \frac{\partial}{\partial x} & \frac{\partial}{\partial y} & \frac{\partial}{\partial z} \end{pmatrix}. \quad (1.1.37)$$

The two equations in Eq. (1.1.12) which represent the Gauß laws condition are equivalent to

$$\mathcal{D} \cdot \mathcal{F}(\vec{r}, t) = \mathcal{Q}(\vec{r}, t), \quad (1.1.38)$$

where we use a dot product formalism denoted by a bold dot product symbol \cdot . The introduced Riemann-Silberstein dot product acts as a 6x2 matrix \mathcal{V} on the six-dimensional \mathcal{F} with its two three-dimensional vectors \vec{F}_{\pm} . The 6x2 \mathcal{V} contains four arbitrary three-dimensional vectors $\vec{V}_1, \vec{V}_2, \vec{V}_3$, and \vec{V}_4 . We define the dot product with

$$\mathcal{V} \cdot \mathcal{F} = \begin{pmatrix} \vec{V}_1^\top & \vec{V}_2^\top \\ \vec{V}_3^\top & \vec{V}_4^\top \end{pmatrix}_{2 \times 6} \cdot \begin{pmatrix} \vec{F}_+ \\ \vec{F}_- \end{pmatrix}_{6 \times 1} = \begin{pmatrix} \vec{V}_1 \cdot \vec{F}_+ + \vec{V}_2 \cdot \vec{F}_- \\ \vec{V}_3 \cdot \vec{F}_+ + \vec{V}_4 \cdot \vec{F}_- \end{pmatrix}_{2 \times 1}. \quad (1.1.39)$$

The small dot product symbols on the very right-hand side of Eq. (1.1.39) represent common three-dimensional scalar products. Hence, this dot product maps a 6x2 matrix and a six-dimensional vector into in a two-dimensional vector. where the upper component again represents the positive helicity, and the lower component the negative one.

Furthermore, the two Riemann-Silberstein combined Ampère's and Faraday's laws given in Eq. (1.1.31) take the form

$$i\hbar \frac{\partial}{\partial t} \mathcal{F}(\vec{r}, t) = \mathcal{H} \mathcal{F}(\vec{r}, t) - i\hbar \mathcal{J}(\vec{r}, t). \quad (1.1.40)$$

Here, the Hamiltonian-like 6x6 matrix \mathcal{H} is a Kronecker product of a diagonal 2x2 matrix and the 3x3 H_{Mx} matrix of Eq. (1.1.30). It is given by

$$\mathcal{H} = \begin{pmatrix} 1 & 0 \\ 0 & -1 \end{pmatrix}_{2 \times 2} \otimes \left(-i\hbar c_0 \left[\vec{\nabla} \cdot \vec{\mathcal{S}} \right] \right)_{3 \times 3} = \begin{pmatrix} 1 & 0 \\ 0 & -1 \end{pmatrix}_{2 \times 2} \otimes \left(H_{\text{Mx}} \right)_{3 \times 3}, \quad (1.1.41)$$

which yields a six-dimensional vector after acting on $\mathcal{F}(\vec{r}, t)$. The remaining current density inhomogeneity in Eq. (1.1.31) is substituted by $\mathcal{J}(\vec{r}, t)$

$$\mathcal{J}(\vec{r}, t) = \begin{pmatrix} 1 \\ 1 \end{pmatrix}_{2 \times 1} \otimes \left(\frac{1}{\sqrt{2\epsilon_0}} \vec{j} \right)_{3 \times 1} \quad (1.1.42)$$

in equation (1.1.40). In case of $\mathcal{J}(\vec{r}, t)$ equal zero, Eq. (1.1.40) becomes a homogeneous Schrödinger-like form with

$$i\hbar \frac{\partial}{\partial t} \mathcal{F}(\vec{r}, t) = \mathcal{H} \mathcal{F}(\vec{r}, t). \quad (1.1.43)$$

Following the $\mathcal{H} \mathcal{F}(\vec{r}, t)$ operation, we emphasize some properties of general $\mathcal{O}(\vec{r}, t) \mathcal{F}(\vec{r}, t)$ operations defined by a general operator \mathcal{O} , which contains four 3x3 matrices

$$\mathcal{O}(\vec{r}, t) = \begin{pmatrix} O_{1,1}(\vec{r}, t) & O_{1,2}(\vec{r}, t) \\ O_{2,1}(\vec{r}, t) & O_{2,2}(\vec{r}, t) \end{pmatrix}. \quad (1.1.44)$$

Therefore, $\mathcal{O}(\vec{r}, t) \mathcal{F}(\vec{r}, t)$ yields

$$\begin{pmatrix} \vec{F}'_+(\vec{r}, t) \\ \vec{F}'_-(\vec{r}, t) \end{pmatrix} = \begin{pmatrix} O_{1,1}(\vec{r}, t) \vec{F}_+(\vec{r}, t) + O_{1,2}(\vec{r}, t) \vec{F}_-(\vec{r}, t) \\ O_{2,1}(\vec{r}, t) \vec{F}_-(\vec{r}, t) + O_{2,2}(\vec{r}, t) \vec{F}_+(\vec{r}, t) \end{pmatrix}. \quad (1.1.45)$$

Obviously the different helicity vectors $\vec{F}'_+(\vec{r}, t)$ and $\vec{F}'_-(\vec{r}, t)$ couple to each other, if the terms $O_{12}(\vec{r}, t)$ and $O_{21}(\vec{r}, t)$ are non-zero. Without loss of generality we can express the general operator $\mathcal{O}(\vec{r}, t)$ by a Kronecker product of the two matrices m_i and $o_i(\vec{r}, t)$

$$\mathcal{O}(\vec{r}, t) = \sum_i (m_i)_{2 \times 2} \otimes (o_i(\vec{r}, t))_{3 \times 3}. \quad (1.1.46)$$

The prefix 2x2 matrix m_i only consists of elements 1 or -1 , the second $o_i(\vec{r}, t)$ contains all other necessary operations so that Eq. (1.1.46) is satisfied. We already used this formalism in Eq. (1.1.41) to define the Hamiltonian-like \mathcal{H} . Consequently, if the off-diagonal entries of m_i are zero and only the diagonal entries are 1 or -1 , it can readily be seen that $o_i(\vec{r}, t)$ do not couple the two helicity vectors. In the following, we therefore call the first 2x2 matrix in Eq. (1.1.46) "coupling" matrix, as it shows if the two Riemann-Silberstein vectors $\vec{F}_{\pm}(\vec{r}, t)$ couple to each other. The second 3x3 "operation" matrix contains all necessary physical variables and operations to satisfy the underlying Maxwell's equations.

With respect of Eq. (1.1.31), we have in principle two independent equations combined into one in Eq. (1.1.40). Hence, there is per construction no coupling between the two linear independent Riemann-Silberstein vectors $\vec{F}_{+}(\vec{r}, t)$ and $\vec{F}_{-}(\vec{r}, t)$. Note, this is only valid for the common classical microscopic Maxwell's equations shown in Eqs. (1.1.8)-(1.1.11). We show in the next section, that a correct description of Maxwell's equation in a linear medium requires a coupling between the positive and negative Riemann-Silberstein vectors. In summary, Eq. (1.1.40) gives us a general and clear form to describe the Maxwell's equations in vacuum as a Schrödinger-like equation well known for describing quantum mechanical wave functions. However, there is one difference to quantum mechanical systems. The Maxwell fields have to satisfy the two Gauß laws as secondary condition. We focus on this condition and how it is conserved during time propagation in chapter 2.

1.1.6 Photon - anti-photon relation of the six-component Riemann-Silberstein vector

We now have a general form with both helicity Riemann-Silberstein vectors in one equation, but this expression of Maxwell vectors in form of a six-dimensional Riemann-Silberstein vector requires some considerations, which are extensively elaborated in Ref. [73, 72]. The six-component vector $\mathcal{F}(\vec{r}, t)$ without any relation between the upper and the lower three-vector doubles the degrees of freedom. This extra freedom has to be constrained to satisfy the photon particle antiparticle relation. Solutions of relativistic quantum mechanics, especially plane wave solutions can have in general positive frequencies that corresponds to particles with positive energy or negative frequencies that correspond to antiparticles with negative energies. In contrast to the different particle antiparticle pairs for matter wavefunctions, the anti-photons are identical with photons. Hence, this condition reduces the degrees of freedom. First, we take the electric field $\vec{E}_{\text{pw}}^{(+)}(\vec{r}, t)$ and magnetic field $\vec{B}_{\text{pw}}^{(+)}(\vec{r}, t)$ for positive frequencies and $\vec{E}_{\text{pw}}^{(-)}(\vec{r}, t)$, $\vec{B}_{\text{pw}}^{(-)}(\vec{r}, t)$ for negative frequencies of an electromagnetic plane wave [75] with initial electric field $\vec{E}_0(\vec{k})$, initial magnetic field $\vec{B}_0(\vec{k})$, wave vector \vec{k} and ω as the absolute value of the frequency. Hence, the plane waves with positive frequencies take the form

$$\vec{E}_{\text{pw}}^{(+)}(\vec{r}, t) = \vec{E}_0(\vec{k}) \exp \left[i \left(\vec{k} \cdot \vec{r} - \omega t \right) \right], \quad (1.1.47)$$

$$\vec{B}_{\text{pw}}^{(+)}(\vec{r}, t) = \vec{B}_0(\vec{k}) \exp \left[i \left(\vec{k} \cdot \vec{r} - \omega t \right) \right], \quad (1.1.48)$$

whereas the ones with negative frequencies are given by

$$\vec{E}_{\text{pw}}^{(-)}(\vec{r}, t) = \vec{E}_0(\vec{k}) \exp \left[i \left(\vec{k} \cdot \vec{r} + \omega t \right) \right], \quad (1.1.49)$$

$$\vec{B}_{\text{pw}}^{(-)}(\vec{r}, t) = \vec{B}_0(\vec{k}) \exp \left[i \left(\vec{k} \cdot \vec{r} + \omega t \right) \right]. \quad (1.1.50)$$

The electromagnetic plane waves additionally obey the relations [75]

$$\vec{k} \cdot \vec{E}_{\text{pw}}^{(\pm)}(\vec{r}, t) = \vec{k} \cdot \vec{B}_{\text{pw}}^{(\pm)}(\vec{r}, t) = 0 \quad (1.1.51)$$

$$\vec{B}_{\text{pw}}^{(\pm)}(\vec{r}, t) = \frac{1}{c_0} \frac{\vec{k}}{|\vec{k}|} \times \vec{E}_{\text{pw}}^{(\pm)}(\vec{r}, t) . \quad (1.1.52)$$

Using the definitions of the Riemann-Silberstein vectors in Eq. (1.1.1) and Eq. (1.1.2) for building the corresponding initial vectors $\vec{F}_+(\vec{k})$ and $\vec{F}_-(\vec{k})$ for a given wavevector \vec{k} leads to the Riemann-Silberstein plane wave expressions $\vec{F}_{\text{pw}}^{(+)}(\vec{r}, t)$ for positive frequencies

$$\vec{F}_{\text{pw},+}^{(+)}(\vec{r}, t) = \vec{F}_+(\vec{k}) \exp \left[i \left(\vec{k} \cdot \vec{r} - \omega t \right) \right] = \vec{F}_+^*(\vec{k}) \exp \left[i \left(-\vec{k} \cdot \vec{r} - \omega t \right) \right] , \quad (1.1.53)$$

$$\vec{F}_{\text{pw},-}^{(+)}(\vec{r}, t) = \vec{F}_-(\vec{k}) \exp \left[i \left(\vec{k} \cdot \vec{r} - \omega t \right) \right] = \vec{F}_-^*(\vec{k}) \exp \left[i \left(-\vec{k} \cdot \vec{r} - \omega t \right) \right] , \quad (1.1.54)$$

and $\vec{F}_{\text{pw}}^{(-)}(\vec{r}, t)$ for negative frequencies

$$\vec{F}_{\text{pw},+}^{(-)}(\vec{r}, t) = \vec{F}_+(\vec{k}) \exp \left[i \left(\vec{k} \cdot \vec{r} + \omega t \right) \right] = \vec{F}_+^*(\vec{k}) \exp \left[i \left(-\vec{k} \cdot \vec{r} + \omega t \right) \right] , \quad (1.1.55)$$

$$\vec{F}_{\text{pw},-}^{(-)}(\vec{r}, t) = \vec{F}_-(\vec{k}) \exp \left[i \left(\vec{k} \cdot \vec{r} + \omega t \right) \right] = \vec{F}_-^*(\vec{k}) \exp \left[i \left(-\vec{k} \cdot \vec{r} + \omega t \right) \right] . \quad (1.1.56)$$

The last equivalence Eqs. (1.1.53)-(1.1.56) follows from the plane wave conditions in Eq. (1.1.51) and Eq. (1.1.52) for the wave vector \vec{k} and magnetic field $\vec{B}_{\text{pw}}(\vec{r}, t)$. Since every electromagnetic field and therefore every Riemann-Silberstein vector can be expressed by a infinite sum of plane waves, we can find a Riemann-Silberstein vector $\vec{F}_{\pm}^{(+)}(\vec{r}, t)$ which only contains positive frequencies by

$$\vec{F}_{\pm}^{(+)}(\vec{r}, t) = \int_0^{\infty} d^3k \vec{F}_{\pm}(\vec{k}) \exp \left[i \left(-\vec{k} \cdot \vec{r} - \omega_{\vec{k}} t \right) \right] , \quad (1.1.57)$$

and a negative counterpart $\vec{F}_{\pm}^{(-)}(\vec{r}, t)$ by

$$\vec{F}_{\pm}^{(-)}(\vec{r}, t) = \int_0^{\infty} d^3k \vec{F}_{\pm}(\vec{k}) \exp \left[i \left(-\vec{k} \cdot \vec{r} + \omega_{\vec{k}} t \right) \right] , \quad (1.1.58)$$

where $\omega_{\vec{k}}$ depends implicitly on the wave vector \vec{k} with $\omega_{\vec{k}} = c|\vec{k}|$. In principle, with using Eq. 1.1.57 and Eq. 1.1.58, we can build two separate Riemann-Silberstein six-vectors, one for positive frequencies $\mathcal{F}^{(+)}(\vec{r}, t)$

$$\mathcal{F}^{(+)}(\vec{r}, t) = \begin{pmatrix} \vec{F}_+^{(+)}(\vec{r}, t) \\ \vec{F}_-^{(+)}(\vec{r}, t) \end{pmatrix} , \quad (1.1.59)$$

and another $\mathcal{F}^{(-)}(\vec{r}, t)$ for negative frequencies

$$\mathcal{F}^{(-)}(\vec{r}, t) = \begin{pmatrix} \vec{F}_+^{(-)}(\vec{r}, t) \\ \vec{F}_-^{(-)}(\vec{r}, t) \end{pmatrix} . \quad (1.1.60)$$

However, as mentioned before, this degree of freedom is reduced due to the fact that photon and anti-photon are described by the same $\mathcal{F}(\vec{r}, t)$. According to quantum mechanical particle-antiparticle conjugation [78, 77] the anti-photon vector $\mathcal{F}^{\text{a}}(\vec{r}, t)$ has to obey

$$\mathcal{F}^{\text{a}} = \begin{pmatrix} 0 & 1 \\ 1 & 0 \end{pmatrix} \mathcal{F}^* , \quad (1.1.61)$$

and the antiparticles are defined as the particles corresponding to negative energy. In terms of electromagnetic fields, this corresponds to photons with negative frequencies. Therefore, if we substitute $\mathcal{F}(\vec{r}, t)$ on the right-hand side of equation (1.1.61) by positive energy referred $\mathcal{F}^{(+)}(\vec{r}, t)$, we obtain the constraint condition for $\mathcal{F}^{(+)}(\vec{r}, t)$ with

$$\mathcal{F}^{(+)}(\vec{r}, t) = \begin{pmatrix} 0 & 1 \\ 1 & 0 \end{pmatrix} \mathcal{F}^{(-)*}(\vec{r}, t). \quad (1.1.62)$$

As a consequence, $\mathcal{F}^{(+)}(\vec{r}, t)$ can always be constructed from an arbitrary Riemann-Silberstein vector $\vec{F}_{\pm}(\vec{r}, t)$ by splitting $\vec{F}(\vec{r}, t)$ into positive and negative frequency parts and inserting the positive frequency part $\vec{F}_{\pm}^{(+)}(\vec{r}, t)$ and the complex conjugate part $\vec{F}_{\pm}^{(-)}(\vec{r}, t)$ into $\mathcal{F}(\vec{r}, t)$ [73]

$$\mathcal{F}^{(+)}(\vec{r}, t) = \begin{pmatrix} \vec{F}_{\pm}^{(+)}(\vec{r}, t) \\ \vec{F}_{\pm}^{(-)*}(\vec{r}, t) \end{pmatrix}. \quad (1.1.63)$$

Since $\mathcal{F}^{(-)}(\vec{r}, t)$ can be directly obtained from $\mathcal{F}^{(+)}(\vec{r}, t)$, we use in the following only $\mathcal{F}^{(+)}(\vec{r}, t)$ for $\mathcal{F}(\vec{r}, t)$ and drop the index (+).

1.1.7 Scalar product of the six-component Riemann-Silberstein vector

In analogy to quantum mechanics, we introduce a scalar product formalism for the six-component Riemann-Silberstein vector $\mathcal{F}(\vec{r}, t)$ similar to Ref. ([77]). With the previous considerations, we can define the scalar product for an arbitrary 6x6 dimensional operator $\mathcal{O}(\vec{r}, t)$ which contains four three times three matrices

$$\mathcal{O}(\vec{r}, t) = \begin{pmatrix} O_{1,1}(\vec{r}, t) & O_{1,2}(\vec{r}, t) \\ O_{2,1}(\vec{r}, t) & O_{2,2}(\vec{r}, t) \end{pmatrix}. \quad (1.1.64)$$

Hence, the scalar product for $\mathcal{F}(\vec{r}, t)$ based on Eq. (1.1.35) is defined as

$$\begin{aligned} \langle \mathcal{F}(t) | \mathcal{O} | \mathcal{F}(t) \rangle &= \int_{-\infty}^{\infty} d^3r \mathcal{F}^\dagger(\vec{r}, t) \mathcal{H}^{-1} \mathcal{O}(\vec{r}, t) \mathcal{F}(\vec{r}, t) \\ &= \begin{pmatrix} \int_{-\infty}^{\infty} d^3r \vec{F}_-(\vec{r}, t) [\mathcal{H}^{-1}]_{1,1} O_{1,1}(\vec{r}, t) \vec{F}_+(\vec{r}, t) + \vec{F}_-(\vec{r}, t) [\mathcal{H}^{-1}]_{2,1} O_{1,2}(\vec{r}, t) \vec{F}_-(\vec{r}, t) \\ \int_{-\infty}^{\infty} d^3r \vec{F}_+(\vec{r}, t) [\mathcal{H}^{-1}]_{1,2} O_{2,1}(\vec{r}, t) \vec{F}_+(\vec{r}, t) + \vec{F}_+(\vec{r}, t) [\mathcal{H}^{-1}]_{2,2} O_{2,2}(\vec{r}, t) \vec{F}_-(\vec{r}, t) \end{pmatrix}. \end{aligned} \quad (1.1.65)$$

The right-hand side of Eq. (1.1.65) uses the inverse of \mathcal{H} given in Eq. (1.1.41) and in principle can be expressed in terms of four submatrices by

$$\mathcal{H}^{-1} = \begin{pmatrix} [\mathcal{H}^{-1}]_{1,1} & [\mathcal{H}^{-1}]_{1,2} \\ [\mathcal{H}^{-1}]_{2,1} & [\mathcal{H}^{-1}]_{2,2} \end{pmatrix}, \quad (1.1.66)$$

which is also used on the right-hand side in Eq. (1.1.65). Unfortunately, \mathcal{H} is a non-invertible singular matrix. However, we keep the expressions in Eq. (1.1.65) and Eq. (1.1.66) since relevant physical operators for $\mathcal{O}(\vec{r}, t)$ can be expressed or factorized by \mathcal{H} , which means, that it cancels the corresponding inverse \mathcal{H} expression in Eq. (1.1.65) [73]. In contrast to the usual scalar product with only one scalar number as result, our defined scalar product consists of two scalar numbers representing the upper and lower helicity

vectors $\vec{F}_+(\vec{r}, t)$ and $\vec{F}_-(\vec{r}, t)$ of $\mathcal{F}(\vec{r}, t)$. Since $\vec{F}_+^*(\vec{r}, t) = \vec{F}_-(\vec{r}, t)$ and $\vec{F}_-^*(\vec{r}, t) = \vec{F}_+(\vec{r}, t)$, the first integral of the upper component on the right-hand side and the second integral of the lower component on the right-hand side represent the usual integrals to obtain the physical scalar products. However, in our definition, if $O_{1,2}(\vec{r}, t)$ and $O_{2,1}(\vec{r}, t)$ are non-zero, we obtain additional scalars for each component that concerns coupling between the helicity vectors. Another difference to usual scalar products in quantum mechanics is the inverse \mathcal{H} operator in Eq. (1.1.65). The reason for this modification is based on the energy density $u(\vec{r}, t)$ formula in the Riemann-Silberstein formalism. From Eq. (1.1.67) we already explained the prefactors for the real and imaginary part of the Riemann-Silberstein vector and it is equivalent to

$$\begin{pmatrix} u(\vec{r}, t) \\ u(\vec{r}, t) \end{pmatrix} = \begin{pmatrix} \vec{F}_-(\vec{r}, t) \cdot \vec{F}_+(\vec{r}, t) \\ \vec{F}_+(\vec{r}, t) \cdot \vec{F}_-(\vec{r}, t) \end{pmatrix}. \quad (1.1.67)$$

Hence, the electric energy of a system is given by

$$\begin{pmatrix} E(t) \\ E(t) \end{pmatrix} = \begin{pmatrix} \int d^3r \vec{F}_-(\vec{r}, t) \cdot \vec{F}_+(\vec{r}, t) \\ \int d^3r \vec{F}_+(\vec{r}, t) \cdot \vec{F}_-(\vec{r}, t) \end{pmatrix}, \quad (1.1.68)$$

which could equivalently be expressed similar to a quantum mechanical expectation value with

$$\langle E(t) \rangle = \langle \mathcal{F}(t) | \mathcal{H} | \mathcal{F}(t) \rangle, \quad (1.1.69)$$

if the scalar product of the six-dimensional Riemann-Silberstein formalism is defined like in Eq. (1.1.65). Therefore, the introduced Riemann-Silberstein scalar product can be used for other operators similar to the one in quantum mechanics. Most physical operators can be expressed in terms of \mathcal{H} with additional operators, so that it eliminates the inverse of \mathcal{H} in Eq. (1.1.65). If \mathcal{O} in Eq. (1.1.64) is a physical operator, the upper and lower value on the left-hand side of Eq. (1.1.65) are always equal since the photon-anti-photon relation in Eq. (1.1.63) holds. An overview of some physical operators for the photon field, which has similarities to the corresponding quantum operators is given in [73].

In quantum mechanics, the expectation value describes the mean expectation value for a large number of measurements, whereas the Riemann-Silberstein scalar product calculates the integrated mean field value. We note here, that the mean field value of the Maxwell fields at a certain point in space can be seen as the quantum mechanical expectation value of the field, which is obtained by a very large photon number. In this picture, it is sufficient to approximate the Maxwell field by a mean field vector and neglect photon fluctuations [79].

1.1.8 Eigenstate expansion of the Riemann-Silberstein six-vector

We already considered stationary solutions for the Riemann-Silberstein vectors $\vec{F}_\pm(\vec{r}, t)$, which are given in Eq. (1.1.33) and satisfy the corresponding eigenvalue problem in Eq. (1.1.34). Consequently, the corresponding stationary solution ansatz of the six-component Riemann-Silberstein vector takes the form

$$\mathcal{F}(\vec{r}, t) = e^{-i\omega t} \mathcal{F}(\vec{r}, t_0), \quad (1.1.70)$$

This solves the updated eigenvalue problem of Eq. (1.1.34) for six-component Riemann-Silberstein vectors with operator \mathcal{H} in Eq. (1.1.41)

$$\mathcal{H}\mathcal{F}(\vec{r}, t) = \hbar\omega\mathcal{F}(\vec{r}, t). \quad (1.1.71)$$

Following the usual quantum mechanical wave function expansion, we can use an eigenvalue and eigenstate expansion of the Riemann-Silberstein six-vector by

$$\mathcal{F}(\vec{r}, t) = \sum_j e^{-i\omega_j t} \mathcal{F}_j(\vec{r}) \quad (1.1.72)$$

to expand the six-component Riemann-Silberstein vector in terms of its eigenvalues ω_j and eigenstates $\mathcal{F}_j(\vec{r})$. The corresponding eigensystem can be numerically calculated using an adequate basis set and the scalar product in Eq. (1.1.65) with $\mathcal{O} = \mathcal{H}$ to get a Hamiltonian matrix, which can be diagonalized to obtain the requested eigenvalues ω_j and eigenstates $\mathcal{F}_j(\vec{r})$.

1.2 Riemann-Silberstein approach for macroscopic Maxwell's equations

The previously considered microscopic Maxwell's equations describe the Maxwell fields, charge, and current density in vacuum. In large matter systems with a huge amount of atoms, the correct Maxwell fields can be obtained in principle by solving Maxwell's equations in vacuum. Finding a solution or a proper approximation is barely reachable due to the large particle number with corresponding charge densities and current densities that have to be taken into account. However, quite a lot of atoms are bound by cores and additionally the atomic cores are often bound in a structure, whereas some electrons are able to move freely inside the matter. Thus, the current density inside the matter can be split into two parts. One part describes the bound charge density $\rho_{\text{bound}}(\vec{r}, t)$, whose distribution and motion in terms of a bound current density $\vec{j}_{\text{bound}}(\vec{r}, t)$ is only visible on atomic scale and ensures the stability of the bound system. The remaining free charge density $\rho_{\text{free}}(\vec{r}, t)$ can move through the whole matter and causes a free current density $\vec{j}_{\text{free}}(\vec{r}, t)$, which both are macroscopically measurable in contrast to the bound variables. The effects of the bound charges and currents are summarized in additional vector fields, the electric displacement field $\vec{D}(\vec{r}, t)$ and the H-field $\vec{H}(\vec{r}, t)$. Both fields and the electromagnetic fields, $\vec{E}(\vec{r}, t)$, $\vec{B}(\vec{r}, t)$, determine the macroscopic Maxwell's equations. In contrast to the microscopic Maxwell's equations, we show that the macroscopic description in a linear medium in terms of Riemann-Silberstein vectors requires a linear combination of both helicity vectors \vec{F}_{\pm} [73, 74]. Now, the macroscopic Riemann-Silberstein six-vector \mathcal{F}_{lm} becomes more important since the corresponding 6x6 matrices couple the upper $\vec{F}_{+, \text{lm}}$ and the lower $\vec{F}_{-, \text{lm}}$ vectors of \mathcal{F}_{lm} . In this section we follow the previously considered steps of the microscopic Riemann-Silberstein Maxwell's equations in Sec. (1.1) to find the correspond macroscopic ones. To get a more general form, we assume a time-dependent linear medium and add electric and magnetic loss.

1.2.1 Riemann-Silberstein Maxwell's equations for linear media

In a linear medium, the total charge density $\rho(\vec{r}, t)$ and current density $\vec{j}(\vec{r}, t)$ are split into two components, one microscopically bound and one free component. The sum of both components corresponds of course still to the total values of the system, so that the total $\rho(\vec{r}, t)$ and $\vec{j}(\vec{r}, t)$ of the system are given by

$$\rho(\vec{r}, t) = \rho_{\text{bound}}(\vec{r}, t) + \rho_{\text{free}}(\vec{r}, t), \quad (1.2.1)$$

$$\vec{j}(\vec{r}, t) = \vec{j}_{\text{bound}}(\vec{r}, t) + \vec{j}_{\text{free}}(\vec{r}, t). \quad (1.2.2)$$

If the requested Maxwell fields are more of interest on a macroscopic scale, where the detailed behavior of the Maxwell fields inside the matter system is negligible, it is sufficient not to take into account all bound charges and currents and to use a macroscopic mean value for the fields instead. It is shown in common textbooks like Ref. [75, 80], that the influence of the bound charge density $\rho_{\text{bound}}(\vec{r}, t)$ and current density $\vec{j}_{\text{bound}}(\vec{r}, t)$ on the total electric and magnetic field can be expressed by two additional vector fields, the polarisation $\vec{P}(\vec{r}, t)$ and the magnetization $\vec{M}(\vec{r}, t)$. Hence, the relevant mean fields, the displacement field $\vec{D}(\vec{r}, t)$ and magnetic $\vec{H}(\vec{r}, t)$ field, are a superposition of the electric and magnetic field $\vec{E}(\vec{r}, t)$, $\vec{B}(\vec{r}, t)$ in vacuum with $\vec{P}(\vec{r}, t)$ or $\vec{M}(\vec{r}, t)$, and take the form [80]

$$\vec{D}(\vec{r}, t) = \epsilon_0 \vec{E}(\vec{r}, t) + \vec{P}(\vec{r}, t) , \quad (1.2.3)$$

$$\vec{H}(\vec{r}, t) = \frac{1}{\mu_0} \vec{B}(\vec{r}, t) - \vec{M}(\vec{r}, t) . \quad (1.2.4)$$

In general, the briefly introduced vectors \vec{P} , and \vec{M} are given by a series expansion with matter specific tensors [75]. In the following, we consider only linear isotropic media, where $\vec{P}(\vec{r}, t)$ and $\vec{M}(\vec{r}, t)$ are always parallel to $\vec{E}(\vec{r}, t)$ and $\vec{B}(\vec{r}, t)$. Hence, \vec{D} and \vec{B} depend linearly on $\vec{E}(\vec{r}, t)$ and $\vec{B}(\vec{r}, t)$, which turns Eq. (1.2.3) and Eq. (1.2.4) into

$$\vec{D}(\vec{r}, t) = \epsilon_0 (1 + \chi_{\text{el}}(\vec{r}, t)) \vec{E}(\vec{r}, t) , \quad (1.2.5)$$

$$\vec{B}(\vec{r}, t) = \mu_0 (1 + \chi_{\text{mag}}(\vec{r}, t)) \vec{H}(\vec{r}, t) , \quad (1.2.6)$$

with the electric susceptibility $\chi_{\text{el}}(\vec{r}, t)$ and magnetic susceptibility $\chi_{\text{mag}}(\vec{r}, t)$ which are matter specific and in general depend on space and time [80]. All scalar prefactors in front of $\vec{E}(\vec{r}, t)$ and $\vec{H}(\vec{r}, t)$ can be summarized in a corresponding linear coefficient, namely the electric permittivity $\epsilon(\vec{r}, t)$ and magnetic permeability $\mu(\vec{r}, t)$. Using the equations Eq. (1.2.3-1.2.6) the variables $\epsilon(\vec{r}, t)$, $\mu(\vec{r}, t)$, $\vec{P}(\vec{r}, t)$, and $\vec{M}(\vec{r}, t)$ for a linear medium are given by

$$\epsilon(\vec{r}, t) = \epsilon_0 (1 + \chi_{\text{el}}(\vec{r}, t)) , \quad (1.2.7)$$

$$\mu(\vec{r}, t) = \mu_0 (1 + \chi_{\text{mag}}(\vec{r}, t)) , \quad (1.2.8)$$

$$\vec{P}(\vec{r}, t) = \epsilon_0 \chi_{\text{el}}(\vec{r}, t) \vec{E}(\vec{r}, t) , \quad (1.2.9)$$

$$\vec{M}(\vec{r}, t) = \mu_0 \chi_{\text{mag}}(\vec{r}, t) \vec{H}(\vec{r}, t) . \quad (1.2.10)$$

1.2.2 Definition of the macroscopic Riemann-Silberstein vectors

The macroscopic Riemann-Silberstein vectors in a linear isotropic medium have a similar form like the previously introduced microscopic ones in Eqs. (1.1.1-1.1.2). Since the electric permittivity $\epsilon(\vec{r}, t)$ and the magnetic permeability $\mu(\vec{r}, t)$ now depend on space and time, the electric constant ϵ_0 as well as the magnetic constant μ_0 in the definitions are replaced by their time and space dependent corresponding variables from Eqs. (1.2.7)-(1.2.8). Therefore, the Riemann-Silberstein vectors $\vec{F}_{\pm, \text{lm}}$ in a linear medium are defined as [73]

$$\vec{F}_{+, \text{lm}}(\vec{r}, t) = \sqrt{\frac{\epsilon(\vec{r}, t)}{2}} \vec{E}(\vec{r}, t) + i \sqrt{\frac{1}{2\mu(\vec{r}, t)}} \vec{B}(\vec{r}, t) \quad (1.2.11)$$

for the positive helicity vector $\vec{F}_{+, \text{lm}}(\vec{r}, t)$, and

$$\vec{F}_{-, \text{lm}}(\vec{r}, t) = \sqrt{\frac{\epsilon(\vec{r}, t)}{2}} \vec{E}(\vec{r}, t) - i \sqrt{\frac{1}{2\mu(\vec{r}, t)}} \vec{B}(\vec{r}, t) \quad (1.2.12)$$

for the negative helicity vector $\vec{F}_{-,lm}(\vec{r}, t)$ where the subindex "lm" stands for "linear medium". Similar to the microscopic electromagnetic energy density u in Eq. (1.1.67) in terms of the microscopic Riemann-Silberstein vector, the macroscopic electromagnetic energy density $u_{lm}(\vec{r}, t)$ in a linear medium is given by [75]

$$u_{lm}(\vec{r}, t) = \frac{1}{2} \left(\vec{E}(\vec{r}, t) \cdot \vec{D}(\vec{r}, t) + \vec{B}(\vec{r}, t) \cdot \vec{H}(\vec{r}, t) \right). \quad (1.2.13)$$

Using the Eqs. (1.2.5)-(1.2.8) and Eq. (1.2.11 - 1.2.12) leads directly to the equivalent form of the electromagnetic energy density $u_{lm}(\vec{r}, t)$ in terms of the macroscopic Riemann-Silberstein vectors

$$\begin{aligned} u_{lm}(\vec{r}, t) &= \vec{F}_{\pm,lm}^*(\vec{r}, t) \cdot \vec{F}_{\pm,lm}(\vec{r}, t) \\ &= \vec{F}_{\mp,lm}(\vec{r}, t) \cdot \vec{F}_{\pm,lm}(\vec{r}, t). \end{aligned} \quad (1.2.14)$$

Again, with Eqs. (1.2.5)-(1.2.8) we obtain the four underlying macroscopic Maxwell fields $\vec{E}(\vec{r}, t)$, $\vec{D}(\vec{r}, t)$, $\vec{B}(\vec{r}, t)$, and $\vec{H}(\vec{r}, t)$

$$\vec{E}(\vec{r}, t) = \sqrt{\frac{1}{2\epsilon(\vec{r}, t)}} \left(\vec{F}_{+,lm}^*(\vec{r}, t) + \vec{F}_{+,lm}(\vec{r}, t) \right) = \sqrt{\frac{1}{2\epsilon(\vec{r}, t)}} \left(\vec{F}_{-,lm}(\vec{r}, t) + \vec{F}_{+,lm}(\vec{r}, t) \right), \quad (1.2.15)$$

$$\vec{D}(\vec{r}, t) = \sqrt{\frac{\epsilon(\vec{r}, t)}{2}} \left(\vec{F}_{+,lm}^*(\vec{r}, t) + \vec{F}_{+,lm}(\vec{r}, t) \right) = \sqrt{\frac{\epsilon(\vec{r}, t)}{2}} \left(\vec{F}_{-,lm}(\vec{r}, t) + \vec{F}_{+,lm}(\vec{r}, t) \right), \quad (1.2.16)$$

$$\vec{B}(\vec{r}, t) = i\sqrt{\frac{\mu(\vec{r}, t)}{2}} \left(\vec{F}_{+,lm}^*(\vec{r}, t) - \vec{F}_{+,lm}(\vec{r}, t) \right) = i\sqrt{\frac{\mu(\vec{r}, t)}{2}} \left(\vec{F}_{-,lm}(\vec{r}, t) - \vec{F}_{+,lm}(\vec{r}, t) \right), \quad (1.2.17)$$

$$\vec{H}(\vec{r}, t) = i\sqrt{\frac{1}{2\mu(\vec{r}, t)}} \left(\vec{F}_{+,lm}^*(\vec{r}, t) - \vec{F}_{+,lm}(\vec{r}, t) \right) = i\sqrt{\frac{1}{2\mu(\vec{r}, t)}} \left(\vec{F}_{-,lm}(\vec{r}, t) - \vec{F}_{+,lm}(\vec{r}, t) \right). \quad (1.2.18)$$

1.2.3 Macroscopic Maxwell's equations

Based on the microscopic Maxwell's equations in Eq. (1.1.8-1.1.11), and by applying a macroscopic field averaging for the Maxwell fields inside a medium, we arrive at the macroscopic Maxwell's equations [75, 80]

$$\vec{\nabla} \cdot \vec{D}(\vec{r}, t) = \rho_{\text{free}}(\vec{r}, t), \quad (1.2.19)$$

$$\vec{\nabla} \cdot \vec{B}(\vec{r}, t) = 0, \quad (1.2.20)$$

$$\vec{\nabla} \times \vec{E}(\vec{r}, t) = -\frac{\partial}{\partial t} \vec{B}(\vec{r}, t), \quad (1.2.21)$$

$$\vec{\nabla} \times \vec{H}(\vec{r}, t) = \frac{\partial}{\partial t} \vec{D}(\vec{r}, t) + \vec{j}_{\text{free}}(\vec{r}, t). \quad (1.2.22)$$

Similar to the Riemann-Silberstein Maxwell's equation in section Sec. 1.1.2 we want now to combine the four Maxwell's equation in a linear medium (1.2.19) - (1.2.22) to arrive at Riemann-Silberstein equations. Only the unbounded free part of the charge density and current density determine the electromagnetic field on a macroscopic scale. Based on those four Maxwell's equations in a medium there is an equivalent description in terms of bilinear Riemann-Silberstein vectors and spin-1 matrices, which can be obtained similar to the vacuum considerations.

We start with a complex addition of the two Gauß laws in Eqs (1.2.19)-(1.2.20)

$$\vec{\nabla} \cdot \vec{D}(\vec{r}, t) \pm i\vec{\nabla} \cdot \vec{B}(\vec{r}, t) = \rho_{\text{free}}(\vec{r}, t). \quad (1.2.23)$$

This equation can be expressed in terms of the Riemann-Silberstein vectors $\vec{F}_{\pm, \text{lm}}(\vec{r}, t)$ and is equivalent to

$$\vec{\nabla} \cdot \vec{F}_{\pm, \text{lm}}(\vec{r}, t) + \vec{K}_{\mp}(\vec{r}, t) \cdot \vec{F}_{+, \text{lm}}(\vec{r}, t) + \vec{K}_{\pm}(\vec{r}, t) \cdot \vec{F}_{-, \text{lm}}(\vec{r}, t) = \frac{1}{\sqrt{2\epsilon(\vec{r}, t)}} \rho_{\text{free}}(\vec{r}, t), \quad (1.2.24)$$

with

$$\vec{K}_{\pm}(\vec{r}, t) = \frac{(\vec{\nabla}\epsilon(\vec{r}, t))}{4\epsilon(\vec{r}, t)} \pm \frac{(\vec{\nabla}\mu(\vec{r}, t))}{4\mu(\vec{r}, t)}, \quad \vec{K}_{\mp}(\vec{r}, t) = \frac{(\vec{\nabla}\epsilon(\vec{r}, t))}{4\epsilon(\vec{r}, t)} \mp \frac{(\vec{\nabla}\mu(\vec{r}, t))}{4\mu(\vec{r}, t)}. \quad (1.2.25)$$

Note, that the macroscopic Gauß laws conditions in Eq. (1.2.24) can only be obeyed by a linear combination of both, $\vec{F}_{+, \text{lm}}(\vec{r}, t)$ and $\vec{F}_{-, \text{lm}}(\vec{r}, t)$, which is in contrast to the microscopic equation Eq. (1.2.24), where already only one of the different helicity vectors $\vec{F}_{\pm, \text{lm}}(\vec{r}, t)$ satisfies the Gauß conditions. Hence, the correct macroscopic Maxwell's equations require a coupling of the two helicity Riemann-Silberstein vectors. The same situation arises, when we consider the transformation of the macroscopic Faraday's and Ampère's laws in Eqs. (1.2.21)-(1.2.22) for the corresponding Riemann-Silberstein equation. Later in chapter 3, we need a more general form of Faraday's and Ampère's law. Therefore, we expand both equations in Eq. (1.2.21-1.2.22) by an additional term to describe a damping of the electromagnetic field, e.g. in a lossy medium region. The damping terms are assumed to be proportional to the electromagnetic field. The underlying constants of proportionality are the electric conductivity $\sigma_e(\vec{r}, t)$ and the magnetic conductivity $\sigma_m(\vec{r}, t)$. Therefore, Faraday's law and Ampère's law in Eq. (1.2.21-1.2.22) with lossy electric and magnetic layer are given by

$$\vec{\nabla} \times \vec{E}(\vec{r}, t) = -\left(\frac{\partial}{\partial t} + \sigma_m(\vec{r}, t)\right)\vec{B}(\vec{r}, t), \quad (1.2.26)$$

$$\vec{\nabla} \times \vec{H}(\vec{r}, t) = \left(\frac{\partial}{\partial t} + \sigma_e(\vec{r}, t)\right)\vec{D}(\vec{r}, t) + \vec{j}_{\text{free}}(\vec{r}, t). \quad (1.2.27)$$

By separating the temporal derivative terms on the right-hand side and adding Eq. (1.2.26) as imaginary part to Eq. (1.2.27) and multiplying the whole equation by the imaginary unit leads to

$$i\frac{\partial}{\partial t}\left(\epsilon(\vec{r}, t)\vec{E}(\vec{r}, t) \pm i\vec{B}(\vec{r}, t)\right) = \pm\vec{\nabla} \times \vec{E}(\vec{r}, t) + i\vec{\nabla} \times \frac{1}{\mu(\vec{r}, t)}\vec{B}(\vec{r}, t) \pm \sigma_m(\vec{r}, t)\vec{B}(\vec{r}, t) - i\sigma_e(\vec{r}, t)\vec{D}(\vec{r}, t) - i\vec{j}_{\text{free}}(\vec{r}, t). \quad (1.2.28)$$

As before in the Gauß Riemann-Silberstein equation in a medium, it is not possible to describe the Faraday's and Ampère's law only with one of the Riemann-Silberstein vectors, either $\vec{F}_{+, \text{lm}}(\vec{r}, t)$ or $\vec{F}_{-, \text{lm}}(\vec{r}, t)$. Therefore, after substituting the Maxwell fields with the corresponding Riemann-Silberstein vector expressions, multiplying Eq. (1.2.28) and using the curl operator in spin-1 matrix representation in Eq. (1.1.25) with the Planck constant

\hbar , the final form of Faraday's and Ampère's law as Riemann-Silberstein equation is

$$\begin{aligned}
i\hbar \frac{\partial}{\partial t} \vec{F}_{\pm, \text{lm}}(\vec{r}, t) &= \pm \hbar c(\vec{r}, t) \vec{\nabla} \times \vec{F}_{\pm, \text{lm}}(\vec{r}, t) - i\hbar \frac{1}{\sqrt{2\epsilon(\vec{r}, t)}} \vec{j}_{\text{free}}(\vec{r}, t) \\
&\mp \hbar c(\vec{r}, t) \vec{K}_{\pm}(\vec{r}, t) \times \vec{F}_{+, \text{lm}}(\vec{r}, t) \mp \hbar(\vec{r}, t) c(\vec{r}, t) \vec{K}_{\mp}(\vec{r}, t) \times \vec{F}_{-, \text{lm}}(\vec{r}, t) \\
&- i\hbar \sigma_{e, m, \pm}(\vec{r}, t) \vec{F}_{+, \text{lm}}(\vec{r}, t) - i\hbar \sigma_{e, m, \mp}(\vec{r}, t) \vec{F}_{-, \text{lm}}(\vec{r}, t) \\
&- i\hbar \beta_{\epsilon, \mu, \pm}(\vec{r}, t) \vec{F}_{+, \text{lm}}(\vec{r}, t) - i\hbar \beta_{\epsilon, \mu, \mp}(\vec{r}, t) \vec{F}_{-, \text{lm}}(\vec{r}, t).
\end{aligned} \tag{1.2.29}$$

Here \vec{K}_{\pm} , \vec{K}_{\mp} are defined by Eq. (1.2.25) and $\sigma_{e, m, \pm}(\vec{r}, t)$, $\sigma_{e, m, \mp}(\vec{r}, t)$, $\beta_{\epsilon, \mu, \pm}(\vec{r}, t)$, $\beta_{\epsilon, \mu, \mp}(\vec{r}, t)$ are defined by

$$\sigma_{e, m, \pm}(\vec{r}, t) = \frac{1}{2} [\sigma_e(\vec{r}, t) \pm \sigma_m(\vec{r}, t)] , \quad \sigma_{e, m, \mp}(\vec{r}, t) = \frac{1}{2} [\sigma_e(\vec{r}, t) \mp \sigma_m(\vec{r}, t)] \tag{1.2.30}$$

$$\beta_{\epsilon, \mu, \pm}(\vec{r}, t) = \frac{\dot{\epsilon}(\vec{r}, t)}{4\epsilon(\vec{r}, t)} \pm \frac{\dot{\mu}(\vec{r}, t)}{4\mu(\vec{r}, t)} , \quad \beta_{\epsilon, \mu, \mp}(\vec{r}, t) = \frac{\dot{\epsilon}(\vec{r}, t)}{4\epsilon(\vec{r}, t)} \mp \frac{\dot{\mu}(\vec{r}, t)}{4\mu(\vec{r}, t)} . \tag{1.2.31}$$

All terms in Eq. (1.2.29) agree with the result of Ref. [74] for the macroscopic Riemann-Silberstein equations in a linear medium, except the lossy layer terms in the third line of this equation, which contain the layer property functions $\sigma_{e, m, \pm}(\vec{r}, t)$ and $\sigma_{e, m, \mp}(\vec{r}, t)$. These terms will become relevant later when we introduce a perfectly matched layer to absorb outgoing electromagnetic radiation.

To summarize, in contrast to the previous microscopic considerations, the additional spatial dependency due to the media properties requires an important modification in both Riemann-Silberstein Maxwell's equations, in the combined two Gauß laws as well as in the combined Faraday's and Ampère's laws. In both cases, it is not possible anymore to find a form obeying Maxwell's equations depending on only one of the $\vec{F}_{+, \text{lm}}(\vec{r}, t)$ or $\vec{F}_{-, \text{lm}}(\vec{r}, t)$ terms. As a consequence, Riemann-Silberstein Maxwell's equations in a medium have to be formulated as a six-dimensional problem which we consider in the next section.

1.2.4 Combined helicity Riemann-Silberstein six-vector in linear medium

The fact that macroscopic Riemann-Silberstein vectors $\vec{F}_{\pm, \text{lm}}(\vec{r}, t)$ couple to each other in the macroscopic Riemann-Silberstein equations in Eq. (1.2.24) and Eq. (1.2.29) demonstrates clearly the necessity of the six-dimensional representation of the Riemann-Silberstein Maxwell's vector, like previously considered in section Sec. 1.1.5. Referring to the microscopic definition of $\mathcal{F}(\vec{r}, t)$ in Eq. (1.1.35), the corresponding macroscopic six-component Riemann-Silberstein vector $\mathcal{F}_{\text{lm}}(\vec{r}, t)$ is defined as

$$\mathcal{F}_{\text{lm}}(\vec{r}, t) = \begin{pmatrix} \vec{F}_{+, \text{lm}}(\vec{r}, t) \\ \vec{F}_{-, \text{lm}}(\vec{r}, t) \end{pmatrix} . \tag{1.2.32}$$

Therefore, the corresponding total combined Maxwell Riemann-Silberstein Gauß law takes with the scalar product definition of Eq. (1.1.39) the form [73]

$$\mathcal{D}_{\text{lm}}(\vec{r}, t) \cdot \mathcal{F}(\vec{r}, t) = \mathcal{Q}_{\text{lm}}(\vec{r}, t) \tag{1.2.33}$$

with the six-dimensional Riemann-Silberstein free charge density $\mathcal{Q}_{\text{lm}}(\vec{r}, t)$

$$\mathcal{Q}_{\text{lm}}(\vec{r}, t) = \begin{pmatrix} 1 \\ 1 \end{pmatrix}_{2 \times 1} \otimes \left(\frac{1}{\sqrt{2\epsilon_0(\vec{r}, t)}} \rho_{\text{free}}(\vec{r}, t) \right)_{1 \times 1} \tag{1.2.34}$$

and a six-dimensional operator $\mathcal{D}_{\text{lm}}(\vec{r}, t)$

$$\begin{aligned} \mathcal{D}_{\text{lm}}(\vec{r}, t) &= \begin{pmatrix} 1 & 0 \\ 0 & 1 \end{pmatrix}_{2 \times 2} \otimes \left(\vec{\nabla} \right)_{1 \times 3}^{\top} \\ &+ \begin{pmatrix} 1 & 1 \\ 1 & 1 \end{pmatrix}_{2 \times 2} \otimes \left(\frac{(\vec{\nabla} \epsilon(\vec{r}, t))}{4\epsilon(\vec{r}, t)} \right)_{1 \times 3}^{\top} \\ &+ \begin{pmatrix} -1 & 1 \\ 1 & -1 \end{pmatrix}_{2 \times 2} \otimes \left(\frac{(\vec{\nabla} \mu(\vec{r}, t))}{4\mu(\vec{r}, t)} \right)_{1 \times 3}^{\top} \end{aligned} \quad (1.2.35)$$

that corresponds to the divergence operator in the common Gauß laws. The Gauß laws in the Riemann-Silberstein representation does not only depend on the electric permittivity $\epsilon(\vec{r}, t)$ and magnetic permeability $\mu(\vec{r}, t)$, but also on their spatial derivatives $\vec{\nabla} \epsilon(\vec{r}, t)$ and $\vec{\nabla} \mu(\vec{r}, t)$.

Next, we convert the remaining Riemann-Silberstein equation in Eq. (1.2.29) into a six-dimensional representation. First, we define similar to the six-dimensional Riemann-Silberstein charge density $\mathcal{Q}(\vec{r}, t)$ in Eq. (1.2.34) an adequate six-dimensional Riemann-Silberstein current density $\mathcal{J}(\vec{r}, t)$ with

$$\mathcal{J}_{\text{lm}}(\vec{r}, t) = \begin{pmatrix} 1 \\ 1 \end{pmatrix}_{2 \times 1} \otimes \left(\frac{1}{\sqrt{2\epsilon(\vec{r}, t)}} \vec{J}_{\text{free}}(\vec{r}, t) \right)_{3 \times 1}. \quad (1.2.36)$$

Let us define $H_{\text{Mx,lm}}(\vec{r}, t)$

$$H_{\text{Mx,lm}}(\vec{r}, t) = -i\hbar c(\vec{r}, t) \vec{\nabla} \cdot \vec{\mathbf{S}}, \quad (1.2.37)$$

which depends explicitly on time and spatial coordinates due to the speed of light $c(\vec{r}, t)$ inside the linear medium. The combined coupled equations in Eq. (1.2.29) can be expressed in a similar inhomogeneous Schrödinger like form as in Eq. (1.1.40) with

$$i\hbar \frac{\partial}{\partial t} \mathcal{F}(\vec{r}, t) = \mathcal{H}_{\text{lm}}(\vec{r}, t) \mathcal{F}(\vec{r}, t) - i\hbar \mathcal{J}_{\text{free}}(\vec{r}, t), \quad (1.2.38)$$

where $\mathcal{H}_{\text{lm}}(\vec{r}, t)$ consists of

$$\mathcal{H}_{\text{lm}}(\vec{r}, t) = \mathcal{H}_{\text{lm,(0)}}(\vec{r}, t) + \mathcal{K}_{\text{lm}}(\vec{r}, t). \quad (1.2.39)$$

The operator $\mathcal{H}_{\text{lm,(0)}}(\vec{r}, t)$ only contains the uncoupled part with the spin-curl operation representing the first term on the right-hand side of Eq. (1.2.29), and could also be expressed as a Kronecker product of $H_{\text{Mx,lm}}(\vec{r}, t)$

$$\mathcal{H}_{\text{lm,(0)}}(\vec{r}, t) = \begin{pmatrix} 1 & 0 \\ 0 & -1 \end{pmatrix}_{2 \times 2} \otimes \left(H_{\text{Mx,lm}}(\vec{r}, t) \right)_{3 \times 3}. \quad (1.2.40)$$

Note, that the macroscopic $\mathcal{H}_{\text{lm}}(\vec{r}, t)$ only locally depends on space and time. We see in chapter 5, that this fact changes if we consider the Maxwell-matter coupling in the fundamental microscopic regime and some non-localized terms arise. Finally, all remaining terms except the first one on the right-hand side of Eq. (1.2.29) are represented by $\mathcal{K}_{\text{lm}}(\vec{r}, t)$ and it includes all coupling terms which determine mainly the properties of the linear

medium and is explicitly given by

$$\begin{aligned}
\mathcal{K}_{\text{lm}}(\vec{r}, t) = & \begin{pmatrix} -1 & -1 \\ 1 & 1 \end{pmatrix}_{2 \times 2} \otimes \left(-i\hbar \frac{c(\vec{r}, t)}{4\epsilon(\vec{r}, t)} \left[\vec{\mathcal{S}} \cdot \left(\vec{\nabla} \epsilon(\vec{r}, t) \right) \right] \right)_{3 \times 3} \\
& + \begin{pmatrix} -1 & 1 \\ -1 & 1 \end{pmatrix}_{2 \times 2} \otimes \left(-i\hbar \frac{c(\vec{r}, t)}{4\mu(\vec{r}, t)} \left[\vec{\mathcal{S}} \cdot \left(\vec{\nabla} \mu(\vec{r}, t) \right) \right] \right)_{3 \times 3} \\
& + \begin{pmatrix} -1 & -1 \\ -1 & -1 \end{pmatrix}_{2 \times 2} \otimes \left(i\hbar \frac{\dot{\epsilon}(\vec{r}, t)}{4\epsilon(\vec{r}, t)} \mathbb{1}_3 \right)_{3 \times 3} + \begin{pmatrix} -1 & 1 \\ 1 & -1 \end{pmatrix}_{2 \times 2} \otimes \left(i\hbar \frac{\dot{\mu}(\vec{r}, t)}{4\mu(\vec{r}, t)} \mathbb{1}_3 \right)_{3 \times 3} \\
& + \begin{pmatrix} -1 & -1 \\ -1 & -1 \end{pmatrix}_{2 \times 2} \otimes \left(i\hbar \frac{\sigma_e}{2} \mathbb{1}_3 \right)_{3 \times 3} + \begin{pmatrix} -1 & 1 \\ 1 & -1 \end{pmatrix}_{2 \times 2} \otimes \left(i\hbar \frac{\sigma_m}{2} \mathbb{1}_3 \right)_{3 \times 3}.
\end{aligned} \tag{1.2.41}$$

We replaced again all occurring cross products and curl operations by the corresponding spin-1 representation in Eq. (1.1.14) and Eq. (1.1.25). In a medium without any electromagnetic loss, both conductivities $\sigma_e(\vec{r}, t)$ and $\sigma_m(\vec{r}, t)$ are equal to zero and the remaining equation is equal to the common Maxwell Faraday's and Ampère's law shown in (1.2.21) and (1.2.22) which agrees with the corresponding equations in Ref. [73].

In principle, the common expression of the macroscopic Maxwell's equations in Eqs. (1.2.19)-(1.2.22) and the Riemann-Silberstein correspondence representation in Eqs. (1.2.33) and (1.2.38) are exactly equal for an isotropic linear medium, but in case of border surfaces with sharp edges, e.g. between two different homogeneous media, the spatial derivatives of $\vec{\nabla} \epsilon(\vec{r}, t)$ and $\vec{\nabla} \mu(\vec{r}, t)$ are not continuous. Hence, the spatial derivatives at the border surface are not defined. This fact has to be taken into account in case of numerical calculations of the spatial derivatives. However, in a homogeneous medium with constant $\epsilon(\vec{r}, t)$ and $\mu(\vec{r}, t)$, the extra terms are equal to zero due to the fact that $\vec{\nabla} \epsilon(\vec{r}, t) = 0$ and $\vec{\nabla} \mu(\vec{r}, t) = 0$.

In section Sec. 1.1.7 and Sec. 1.1.8, we introduced the Riemann-Silberstein scalar product and the eigenstate expansion of the Riemann-Silberstein six-vectors. Note, that both can also be applied for the macroscopic Riemann-Silberstein six-vector $\mathcal{F}_{\text{lm}}(\vec{r}, t)$ in isotropic linear media, if $\mathcal{F}(\vec{r}, t)$ is replaced by $\mathcal{F}_{\text{lm}}(\vec{r}, t)$ and the operator \mathcal{H} by $\mathcal{H}_{\text{lm}}(\vec{r}, t)$ from Sec. 1.1.7 and Sec. 1.1.8.

So far, our considerations have shown that if the Maxwell fields are defined as a complex bilinear Riemann-Silberstein vector, the microscopic and macroscopic Maxwell's equations can be expressed in Schrödinger form. The main difference to matter wavefunctions is the additional constraint that the Riemann-Silberstein vector has to obey the Gauß law. We show in chapter 4 that this constraint automatically arises for the homogeneous Maxwell's equations, if we consider the Maxwell fields as quantum mechanical relativistic spin-1 fields. In this picture, the Riemann-Silberstein vector fulfills the relativistic energy-momentum relation only if the Gauß laws hold.

Chapter 2

Riemann-Silberstein time-evolution of Maxwell fields in Schrödinger-like form

The underlying fundamental equations, which determine the electromagnetic field in time are Faraday's and Ampère's law, since they describe the temporal changes of the corresponding field. Both equations are directly coupled to each other so that both equations have to be consistent. This circumstance makes it difficult to find an analytic solution for the time-evolution of the electromagnetic field. We introduce in this chapter a consistent and efficient propagation scheme to solve these coupled equations numerically.

Based on the transformed Maxwell's equations in Schrödinger-like form that we introduced in the previous chapter, we develop here a Schrödinger-like time-evolution of the electromagnetic fields for three different cases. The first one describes simple homogeneous microscopic Maxwell's equations without any charge or current densities, the second one adds microscopic charge and current densities to an inhomogeneous Schrödinger-like time evolution operator. Finally, both of these two derivations for a Maxwell time-evolution operator can be combined to find the corresponding one for Maxwell's equations in a linear medium including lossy layers.

2.1 Time-evolution of homogeneous microscopic Maxwell's equations

In chapter 1, we have used the Riemann-Silberstein vector to transform the common microscopic Maxwell's equations into two combined equations, one for the Gauß laws and one for Ampère's and Faraday's laws. Whereas the Gauß laws constitute a side condition which has to be valid for all times, the combined Ampère's and Faraday's laws which contains first order time derivative determine the propagation of the field.

First, we use the six-dimensional microscopic Riemann-Silberstein six-vector $\mathcal{F}(\vec{r}, t)$ defined in Eq. (1.1.35) and start with the simplest case without charge and current densities. Hence, all Eqs. (1.1.8)-(1.1.11) reduce to homogeneous differential equations. The microscopic Riemann-Silberstein Gauß law in Eq. (1.1.38) with $\mathcal{Q}(\vec{r}, t)$ equal to zero becomes

$$\mathcal{D} \cdot \mathcal{F}(\vec{r}, t) = 0 . \tag{2.1.1}$$

We request this condition for an initial Riemann-Silberstein six-vector $\mathcal{F}(\vec{r}, t_0)$ with initial time t_0 and show in section Sec. 2.4 that the time-evolution in Eq. (1.1.40) preserves this

constraint, if it is given for an initial time. For the homogeneous case without any current density $\mathcal{J}(\vec{r}, t)$ as inhomogeneity, Eq. (1.1.40) can be rewritten as

$$\frac{\partial}{\partial t} \mathcal{F}(\vec{r}, t) = -\frac{i}{\hbar} \mathcal{H} \mathcal{F}(\vec{r}, t) . \quad (2.1.2)$$

Obviously, this equation is formally equivalent to the general quantum mechanical time-dependent Schrödinger equation [81, 82]

$$i\hbar \frac{\partial}{\partial t} \psi(\vec{r}, t) = \hat{H}_{\text{qm}} \psi(\vec{r}, t) \quad (2.1.3)$$

with a scalar quantum mechanical wavefunction $\psi(\vec{r}, t)$ and a quantum mechanical Hamiltonian \hat{H}_{qm} . For a given wavefunction $\psi(\vec{r}, t_0)$ at time t_0 and a general given time-independent Hamiltonian \hat{H}_{qm} , that describes the system, the future wavefunction for $t > t_0$ is determined by the well known time-evolution operator $\hat{U}_{\text{qm}}(t, t_0)$ [82]

$$\hat{U}_{\text{qm}}(t, t_0) = \exp \left[\frac{-i(t - t_0) \hat{H}_{\text{qm}}}{\hbar} \right] , \quad (2.1.4)$$

such that the wave function at time t can be obtained by

$$\psi(\vec{r}, t) = \hat{U}_{\text{qm}}(t, t_0) \psi(\vec{r}, t_0) . \quad (2.1.5)$$

Our purpose here is to derive the corresponding time evolution operator $\mathcal{U}(t, t_0)$ for the Riemann-Silberstein six-vector $\mathcal{F}(\vec{r}, t)$ to get the time evolved \mathcal{F} from starting time t_0 to time t with

$$\mathcal{F}(\vec{r}, t) = \mathcal{U}(t, t_0) \mathcal{F}(\vec{r}, t_0) . \quad (2.1.6)$$

Similar to the derivation of the quantum mechanical time-evolution operator \hat{U}_{qm} , we start with the properties of the evolution operator to ensure the correct form of $\mathcal{U}(t, t_0)$. All following requested time-evolution properties are equivalent to those in quantum mechanics, which are listed in Ref. [83]. First, for time t equal to t_0 the operator $\mathcal{U}(t_0, t_0)$ has to obey

$$\mathcal{U}(t_0, t_0) = \mathbb{1}_6 , \quad (2.1.7)$$

with $\mathbb{1}_6$ being the six-dimensional unity matrix so that the initial $\mathcal{F}(\vec{r}, t_0)$ remains identical. In quantum mechanics, all wavefunctions have to be normalized at all times. Consequently the quantum mechanical time-evolution operator is unitary. In case of Maxwell fields, we do not have exactly the normalization condition, but the total field energy $E = \langle \mathcal{F} | \mathcal{F} \rangle$ has to be constant in time if there is no coupling to matter or any loss. Using Eq. (1.1.69) and Eq. (2.1.6) to get the energy of the field yields the condition

$$\begin{aligned} \langle \mathcal{F}(t_0) | E | \mathcal{F}(t_0) \rangle &\equiv \langle \mathcal{F}(t) | \mathcal{H} | \mathcal{F}(t) \rangle \\ \langle \mathcal{F}(t_0) | E | \mathcal{F}(t_0) \rangle &\equiv \langle \mathcal{U}(t, t_0) \mathcal{F}(t_0) | \mathcal{H} | \mathcal{U}(t, t_0) \mathcal{F}(t_0) \rangle \\ \int_{-\infty}^{\infty} d^3r \mathcal{F}^\dagger(\vec{r}, t_0) \mathcal{F}(\vec{r}, t_0) &\equiv \int_{-\infty}^{\infty} d^3r (\mathcal{U}(t, t_0) \mathcal{F}(\vec{r}, t_0))^\dagger \mathcal{U}(t, t_0) \mathcal{F}(\vec{r}, t_0) \\ \int_{-\infty}^{\infty} d^3r \mathcal{F}^\dagger(\vec{r}, t_0) \mathcal{F}(\vec{r}, t_0) &\equiv \int_{-\infty}^{\infty} d^3r \mathcal{F}^\dagger(\vec{r}, t_0) \mathcal{U}^\dagger(t, t_0) \mathcal{U}(t, t_0) \mathcal{F}(\vec{r}, t_0) , \end{aligned} \quad (2.1.8)$$

where we used the definition of the Riemann-Silberstein scalar product in Eq. (1.1.65). Therefore, to satisfy the equation in Eq. (2.1.8) the Riemann-Silberstein time-evolution operator has to obey the unitary condition

$$\mathcal{U}^\dagger(t, t_0)\mathcal{U}(t, t_0) = \mathbb{1}_6 . \quad (2.1.9)$$

Furthermore, the time evolution operator has the composition property. Two intermediate operators propagating a vector first from time t_0 to t' and afterwards from t' to the final time t , are equal to

$$\mathcal{U}(t, t_0) = \mathcal{U}(t, t')\mathcal{U}(t', t_0) . \quad (2.1.10)$$

We request the same properties for the time-evolution operator like in quantum mechanics, and chose the same infinitesimal ansatz for the Riemann-Silberstein vector $\mathcal{F}(\vec{r}, t)$. Consequently, the Maxwell time-evolution operator $\mathcal{U}(t, t_0)$ is a operator-valued 6 times 6 matrix. Starting with an infinitesimal small time propagation $t + dt$, we assume that the difference between the identity matrix $\mathbb{1}_6$ and $\mathcal{U}(t_0 + dt, t_0)$ is linear and first order of dt . Similar as in quantum mechanics, we chose the first order of an exponential series with the exponent $-\frac{i}{\hbar}$

$$\mathcal{U}(t_0 + dt, t_0) = \mathbb{1}_6 - \frac{i}{\hbar}\mathcal{H}dt . \quad (2.1.11)$$

with the Maxwell Hamiltonian operator \mathcal{H} in Eq. (1.1.41) as an linear approximated ansatz. Eq. (2.1.11) is clearly the unity operator for $dt \rightarrow 0$. Due to the Hermitian operator \mathcal{H} the unitary condition yields

$$\mathcal{U}^\dagger\mathcal{U} = \left(\mathbb{1}_6 + \frac{i}{\hbar}\mathcal{H}dt\right) \left(\mathbb{1}_6 - \frac{i}{\hbar}\mathcal{H}dt\right) = \mathbb{1}_6 + \frac{1}{\hbar^2}\mathcal{H}^2(dt)^2 , \quad (2.1.12)$$

which is equal to $\mathbb{1}_6$ after truncating all non-linear higher order terms in dt for infinitesimal considerations. The composition $\mathcal{U}(t_0 + dt + dt, t_0)$ applied to the ansatz in Eq. (2.1.11) gives

$$\begin{aligned} \mathcal{U}(t_0 + dt + dt, t_0) &= \mathcal{U}(t_0 + dt + dt, t_0 + dt)\mathcal{U}(t_0 + dt, t_0) \\ &= \left(\mathbb{1}_6 - \frac{i}{\hbar}\mathcal{H}dt\right) \left(\mathbb{1}_6 - \frac{i}{\hbar}\mathcal{H}dt\right) \\ &= \mathbb{1} - 2\frac{i}{\hbar}\mathcal{H}dt - \frac{1}{\hbar^2}\mathcal{H}(dt)^2 . \end{aligned} \quad (2.1.13)$$

The required composition condition holds if we take only first order terms in dt into account. Hence, $\mathcal{U}(t_0 + dt + dt, t_0)$ differs only by a linear term in dt from the identity operator. Next, each time interval t_0 to t can be separated in N time steps with $\Delta t_N = (t - t_0)/N$. In the limit $N \rightarrow \infty$, Δt reaches the infinitesimal time step dt . Obviously, if we apply Eq. (2.1.11) N times to the latest updated Riemann-Silberstein six-vector, the total time-evolution operator from t_0 to t in one operation is obtained by

$$\lim_{N \rightarrow \infty} \left(\mathbb{1}_6 - \frac{i}{\hbar}\mathcal{H}\left(\frac{t - t_0}{N}\right)\right)^N = \exp\left[-\frac{i}{\hbar}(t - t_0)\mathcal{H}\right] . \quad (2.1.14)$$

This provides us with the Riemann-Silberstein time-evolution operator \mathcal{U}

$$\mathcal{U}(t, t_0) = \exp\left[-\frac{i}{\hbar}(t - t_0)\mathcal{H}\right] . \quad (2.1.15)$$

2.2 Time-evolution of inhomogeneous microscopic Riemann-Silberstein six-vector

Any charge or current density in vacuum makes Maxwell's equations inhomogeneous and the inhomogeneous contributions have a main influence on the Maxwell field propagation. In the presence of charge and current densities, the underlying Riemann-Silberstein equations in the six-dimensional representation in Eq. (1.1.38) and Eq. (1.1.40) have also charge and current density terms, which make them inhomogeneous as well. The Riemann-Silberstein divergence condition is now equal to Eq. (1.1.38), given by

$$\mathcal{D} \cdot \mathcal{F}(\vec{r}, t) = \mathcal{Q}(\vec{r}, t), \quad (2.2.1)$$

with operator \mathcal{D} from Eq. (1.1.37) and the six-component Riemann-Silberstein current density $\mathcal{Q}(\vec{r}, t)$ in Eq. (1.1.36). According to the previous section Sec. 2.1, we consider Eq. (2.2.1) is given for the initial $\mathcal{F}(\vec{r}, t_0)$ at the initial time t_0 and this constraint is conserved after applying the time-evolution operator and obtaining $\mathcal{F}(\vec{r}, t)$. We show the proof for this assumption later in section Sec. 2.4.

As before in section Sec. 2.1, the main time-evolution equations are Faraday's and Ampère's equations in Eq. (1.1.40). Including the inhomogeneous contributions, the equation of motion then reads

$$\frac{\partial}{\partial t} \mathcal{F}(\vec{r}, t) = -\frac{i}{\hbar} \mathcal{H} \mathcal{F}(\vec{r}, t) - \mathcal{J}(\vec{r}, t). \quad (2.2.2)$$

Again, also here a mathematical analogy to quantum mechanics can be drawn. As shown in Ref. [84, 85], one can construct time-evolution schemes for inhomogeneous Schrödinger equations. In the following, we apply these considerations for our propagation of Maxwell's fields in the Riemann-Silberstein form. Let us start with the substitution of the inhomogeneity term $\mathcal{J}(\vec{r}, t)$ in Eq. (2.3.7) with

$$\mathcal{J}(\vec{r}, t) = \mathcal{A}(\vec{r}, t) \mathcal{F}(\vec{r}, t_0), \quad (2.2.3)$$

with the initial $\mathcal{F}(\vec{r}, t_0)$ and a six-times-six-dimensional matrix \mathcal{A} given by

$$\begin{aligned} \mathcal{A}(\vec{r}, t) = & \begin{pmatrix} 1 & 0 \\ 0 & 0 \end{pmatrix}_{2 \times 2} \otimes \frac{1}{\sqrt{2\epsilon_0}} \begin{pmatrix} \frac{j_x(\vec{r}, t) F_{+,x}^*(\vec{r}, t_0)}{|F_{+,x}|} & 0 & 0 \\ 0 & \frac{j_y(\vec{r}, t) F_{+,y}^*(\vec{r}, t_0)}{|F_{+,y}|} & 0 \\ 0 & 0 & \frac{j_z(\vec{r}, t) F_{+,z}^*(\vec{r}, t_0)}{|F_{+,z}|} \end{pmatrix}_{3 \times 3} \\ & + \begin{pmatrix} 0 & 0 \\ 0 & 1 \end{pmatrix}_{2 \times 2} \otimes \frac{1}{\sqrt{2\epsilon_0}} \begin{pmatrix} \frac{j_x(\vec{r}, t) F_{-,x}^*(\vec{r}, t_0)}{|F_{-,x}|} & 0 & 0 \\ 0 & \frac{j_y(\vec{r}, t) F_{-,y}^*(\vec{r}, t_0)}{|F_{-,y}|} & 0 \\ 0 & 0 & \frac{j_z(\vec{r}, t) F_{-,z}^*(\vec{r}, t_0)}{|F_{-,z}|} \end{pmatrix}_{3 \times 3}, \end{aligned} \quad (2.2.4)$$

where we assume that the initial Riemann-Silberstein vector $\mathcal{F}(\vec{r}, t_0)$ is non-zero for all \vec{r} . In analogy to the homogeneous time evolution ansatz in Eq. (2.1.6), we assume that $\mathcal{F}(\vec{r}, t)$ can be obtained by the inhomogeneous time-evolution operator $\mathcal{W}(t, t_0)$ and the initial $\mathcal{F}(\vec{r}, t_0)$ by

$$\mathcal{F}(\vec{r}, t) = \mathcal{W}(t, t_0) \mathcal{F}(\vec{r}, t_0) \quad (2.2.5)$$

Using Eq. (2.2.5) and Eq. (2.2.3) in Eq. (2.3.7) leads to

$$\frac{\partial}{\partial t} \mathcal{W}(t, t_0) \mathcal{F}(\vec{r}, t_0) = -\frac{i}{\hbar} \mathcal{H} \mathcal{W}(t, t_0) \mathcal{F}(\vec{r}, t_0) - \mathcal{A}(\vec{r}, t) \mathcal{F}(\vec{r}, t_0). \quad (2.2.6)$$

Hence, the corresponding equation for the inhomogeneous time-evolution operator without the initial Riemann-Silberstein six-vector $\mathcal{F}(\vec{r}, t_0)$ is

$$\frac{\partial}{\partial t} \mathcal{W}(t, t_0) = -\frac{i}{\hbar} \mathcal{H} \mathcal{W}(t, t_0) - \mathcal{A}(\vec{r}, t). \quad (2.2.7)$$

The ansatz for the inhomogeneous time-evolution operator is to factorize $\mathcal{W}(t, t_0)$ into the homogeneous time-evolution operator $\mathcal{U}(t, t_0)$ Eq. (2.1.15) and a second operator $\mathcal{Z}(t)$ so that

$$\mathcal{W}(t, t_0) = \mathcal{U}(t, t_0) \mathcal{Z}(t). \quad (2.2.8)$$

The time evolution operator depends on times t and t_0 , whereas the additional factor $\mathcal{Z}(t)$ depends only on time t . If we directly take the time derivative of $\mathcal{W}(t, t_0)$ and compare the result with Eq. (2.2.7), we arrive at the differential equation

$$\mathcal{A}(\vec{r}, t) = \mathcal{U}(t, t_0) \frac{\partial}{\partial t} \mathcal{Z}(t) \quad (2.2.9)$$

which leads us, after integrating, to the solution for $\mathcal{Z}(t)$

$$\mathcal{Z}(t) = \mathcal{Z}(t_0) + \int_{t_0}^t d\tau \mathcal{U}^{-1}(\tau, t_0) \mathcal{A}(\tau) = \mathbb{1}_6 + \int_{t_0}^t d\tau \mathcal{U}(t_0, \tau) \mathcal{A}(\tau). \quad (2.2.10)$$

The initial value $\mathcal{Z}(t_0)$ is equal to the identity operator $\mathbb{1}_6$ if we take into account, that $\mathcal{W}(t_0, t_0)$ also has to be the identity operator $\mathbb{1}_6$ in this case since \mathcal{W} has to hold the time-evolution property in Eq. (2.1.7). Finally, the appropriate solution for the inhomogeneous time-evolution operator $\mathcal{W}(t, t_0)$ is given by [84, 85]

$$\mathcal{W}(t, t_0) = \mathcal{U}(t, t_0) - \int_{t_0}^t d\tau \mathcal{U}(t, \tau) \mathcal{A}(\vec{r}, \tau) \quad (2.2.11)$$

including the homogeneous Riemann-Silberstein time-evolution operator $\mathcal{U}(t, \tau)$ of Eq. (2.1.15). Note, although the solution in Eq. (2.2.11) of the inhomogeneous time-propagation in Eq. (2.3.7) obeys the initial condition $\mathcal{W}(t_0, t_0) = \mathbb{1}_6$, $\mathcal{W}(t, t_0)$ breaks in general the composition criterion in Eq. (2.1.10) of a valid time-evolution operator which means that

$$\mathcal{W}(t, t_0) \neq \mathcal{W}(t, t') \mathcal{W}(t', t_0). \quad (2.2.12)$$

Nevertheless, we can use Eq. (2.2.5) and Eq. (2.2.11) to obtain a formal solution of the Riemann-Silberstein six-vector \mathcal{F} with

$$\mathcal{F}(\vec{r}, t) = \mathcal{U}(t, t_0) \mathcal{F}(\vec{r}, t_0) - \int_{t_0}^t \mathcal{U}(t, \tau) \mathcal{A}(\tau) \mathcal{F}(\vec{r}, t_0). \quad (2.2.13)$$

Using again the auxiliary term for expressing the current density in Eq. (2.2.3) and reverting the substitution means that the condition in Eq. (2.2.4) which implies that $\mathcal{F}(\vec{r}, t_0)$ has to be non-zero for all \vec{r} is no restriction any more. The following final explicit expression

$$\mathcal{F}(\vec{r}, t) = \mathcal{U}(t, t_0) \mathcal{F}(\vec{r}, t_0) - \int_{t_0}^t d\tau \mathcal{U}(t, \tau) \mathcal{J}(\vec{r}, \tau) \quad (2.2.14)$$

describes the time propagation of $\mathcal{F}(\vec{r}, t)$ in vacuum with a current density contribution. It can be seen that for a vanishing current density with \mathcal{J} equal to zero, the remaining part in Eq. (2.2.14) is consistent with the homogeneous time evolution described by Eq. (2.1.6).

If we analyze the structure of $\mathcal{U}(t, t_0)$ in Eq. (2.1.15) in more detail, we find that the time evolution operator $\mathcal{U}(t, t_0)$ does not couple the different Riemann-Silberstein vectors \vec{F}_+ and \vec{F}_- . The reason for this is based on the structure of \mathcal{H} in Eq. (1.1.41). Its off-diagonal blocks are zero. This block structure with zero off diagonal blocks holds for the exponential series expansion in Eq. (2.1.15). This means, in case of the microscopic Maxwell propagation it is sufficient to consider only one Riemann-Silberstein vector and its corresponding diagonal block of $\mathcal{U}(t, t_0)$ for the full propagation. This reduction is very useful to reduce significantly computational cost in an actual implementation of the approach.

2.3 Time-evolution of macroscopic Maxwell's equations in linear medium

The time-evolution equations derived previously in Sec. 2.1 and Sec. 2.2 can also be used for the macroscopic time evolution of the Riemann-Silberstein six-vector \mathcal{F}_{lm} in isotropic linear media. The homogeneous Schrödinger-like time-evolution equation for the macroscopic \mathcal{F}_{lm} is with Eq. (1.2.38) given by

$$\frac{\partial}{\partial t} \mathcal{F}_{\text{lm}}(\vec{r}, t) = -\frac{i}{\hbar} \mathcal{H}_{\text{lm}}(\vec{r}, t) \mathcal{F}_{\text{lm}}(\vec{r}, t). \quad (2.3.1)$$

In contrast to the previously considered microscopic equation in Eq. (2.1.2), the present Eq. (2.3.1) includes the time-dependent operator $\mathcal{H}_{\text{lm}}(\vec{r}, t)$ given in Eq. (1.2.39), which leads in general to a modified time-evolution operator compared to Eq. (2.1.15). Using the same steps and properties as in Sec. 2.1 results in the homogeneous macroscopic time evolution operator ansatz $\mathcal{U}_{\text{lm}}(t_0 + dt, t_0)$

$$\mathcal{U}_{\text{lm}}(t_0 + dt, t_0) = \mathbb{1}_6 - \frac{i}{\hbar} \mathcal{H}_{\text{lm}}(\vec{r}, t_0) dt \quad (2.3.2)$$

for an infinitesimal time step. The first order linear approximation for the time evolution operator

$\mathcal{U}_{\text{lm}}(t_0 + \Delta t, t_0)$ with a time step $\Delta t = t - t_0$ is

$$\mathcal{U}_{\text{lm}}(t_0 + \Delta t, t_0) \approx -\frac{i}{\hbar} \int_{t_0}^{t_0 + \Delta t} \mathcal{H}_{\text{lm}}(\vec{r}, \tau) d\tau. \quad (2.3.3)$$

Again, we split a time interval t_0 to t in N small intervals with $\Delta t_N = (t - t_0)/N$, which gives us for the limit $N \rightarrow \infty$ for $\mathcal{U}_{\text{lm}}(t, t_0)$ the following Dyson series

$$\mathcal{U}_{\text{lm}}(t, t_0) = N \rightarrow \infty \left[\mathbb{1}_6 + \sum_{k=1}^N \left(-\frac{i}{\hbar} \right)^k \prod_{m=1}^k \int_{t_0}^{m\Delta t_N} d\tau_m \mathcal{H}_{\text{lm}}(\vec{r}, \tau_m) \right]. \quad (2.3.4)$$

The Dyson series in Eq. (2.3.4) can be simplified by symmetric considerations of the integrals and their limits so that we can use for each time integral the lower limit with t_0 and the upper one with t . However, we have to add a factor to correct double counting. This rearrangement of the Dyson series is derived in Ref. [83]. In general, the medium Hamiltonian $\mathcal{H}_{\text{lm}}(t)$ has the property of $[\mathcal{H}_{\text{lm}}(t_1), \mathcal{H}_{\text{lm}}(t_1)] \neq 0$, which means that the ordering of

$\mathcal{H}_{\text{lm}}(\tau_m)$ is relevant and the times have to be time ordered. Therefore, we use in the final expression for $\mathcal{U}_{\text{lm}}(t, t_0)$ the time ordering operator which is defined also in Ref. [83]

$$\begin{aligned} \mathcal{U}_{\text{lm}}(t, t_0) &= N \rightarrow \infty \left[\mathbb{1}_6 + \sum_{k=1}^N \frac{1}{k!} \left(-\frac{i}{\hbar} \right)^k \mathcal{T} \prod_{m=1}^k \int_{t_0}^t d\tau_m \mathcal{H}_{\text{lm}}(\tau_m) \right] \\ &= \mathcal{T} \exp \left[- \int_{t_0}^t d\tau \frac{i}{\hbar} \mathcal{H}_{\text{lm}}(\vec{r}, \tau) \right]. \end{aligned} \quad (2.3.5)$$

In case of a time independent static isotropic linear medium, the Hamiltonian operator in Eq. (1.2.39) is constant in time and therefore the integral in Eq. (2.3.5) can be directly calculated and the time-evolution operator results in the same simple form as in the microscopic case in Eq.(2.1.15)

$$\mathcal{U}_{\text{lm}}(t, t_0) = \exp \left[-\frac{i}{\hbar} (t - t_0) \mathcal{H}_{\text{lm}}(\vec{r}) \right]. \quad (2.3.6)$$

Until now, we have only considered the time-evolution of the homogeneous Maxwell's equations in linear media, which is a very restricted assumption since free charges and free current densities are not allowed in this case. In general, the free charge density in Eq. (1.2.34) and free current density in Eq. (1.1.42) lead to the underlying divergence condition in Eq. (1.2.33) and the inhomogeneous Schrödinger-like equation of Eq. (1.2.38), which is equal to

$$\frac{\partial}{\partial t} \mathcal{F}_{\text{lm}}(\vec{r}, t) = -\frac{i}{\hbar} \mathcal{H}_{\text{lm}} \mathcal{F}_{\text{lm}}(\vec{r}, t) - \mathcal{J}_{\text{free}}(\vec{r}, t). \quad (2.3.7)$$

All steps for the derivation in section Sec. 2.2 are also valid here. Hence, replacing the microscopic Hamiltonian \mathcal{H} and current density term \mathcal{J} in the general microscopic time evolution equation in Eq. (2.2.14) by the macroscopic Hamiltonian \mathcal{H}_{lm} in Eq. (1.2.39) and current density \mathcal{J}_{lm} of Eq. (1.1.42) leads directly to the time-evolution equation in isotropic linear media

$$\mathcal{F}_{\text{lm}}(\vec{r}, t) = \mathcal{U}_{\text{lm}}(t, t_0) \mathcal{F}_{\text{lm}}(\vec{r}, t_0) - \int_{t_0}^t d\tau \mathcal{U}_{\text{lm}}(t, \tau) \mathcal{J}_{\text{lm}}(\vec{r}, \tau). \quad (2.3.8)$$

The included homogeneous time evolution operator $\mathcal{U}_{\text{lm}}(t, t_0)$ is given by either Eq. (2.3.5) or Eq. (2.3.7), depending on the time-dependent properties of the medium.

Note, in this section we do not consider the Maxwell Gauß laws side conditions, As before in the previous considered cases, if the condition Eq. (1.2.33) holds for $\mathcal{F}(\vec{r}, t_0)$, the divergence side condition is satisfied during the time propagation. We prove this important property for the Maxwell time propagation in the following section.

2.4 Conservation of electric and magnetic Gauß laws in time

In the previous three sections Sec. 2.1-2.3, we have always assumed that the corresponding divergence constraints hold if they are given for an initial Maxwell Riemann-Silberstein six-vector $\mathcal{F}(\vec{r}, t_0)$. Finally, in this section we prove our assumption for all previously considered cases.

Since the homogeneous divergence condition in Eq. (2.1.1) is a special case of the inhomogeneous divergence condition, we start with the more general microscopic inhomogeneous divergence condition in Eq. (2.2.1)

$$\mathcal{D} \cdot \mathcal{F}(\vec{r}, t_0) = \mathcal{Q}(\vec{r}, t_0), \quad (2.4.1)$$

which we request to hold for a given Maxwell Riemann-Silberstein vector $\mathcal{F}(\vec{r}, t_0)$ at t_0 . Now, we have to show that the same condition is holds at later times t with

$$\mathcal{D} \cdot \mathcal{F}(\vec{r}, t) = \mathcal{Q}(\vec{r}, t), \quad (2.4.2)$$

if we use the inhomogeneous Maxwell time-evolution operator in Eq. (2.2.14) to reach $\mathcal{F}(\vec{r}, t)$ from the starting vector $\mathcal{F}(\vec{r}, t_0)$. Therefore, inserting Eq. (2.2.14) into Eq. (2.4.2) yields

$$\mathcal{D} \cdot \mathcal{F}(\vec{r}, t) = \mathcal{D} \cdot \left[\mathcal{U}(t, t_0) \mathcal{F}(\vec{r}, t_0) \right] - \mathcal{D} \cdot \left[\int_{t_0}^t d\tau \mathcal{U}(t, \tau) \mathcal{J}(\vec{r}, \tau) \right]. \quad (2.4.3)$$

In the following, we use that the Riemann-Silberstein dot product in Eq. 1.1.39 with the divergence operator \mathcal{D} acting on $\mathcal{H}\mathcal{F}(\vec{r}, t)$ is equal to zero

$$\mathcal{D} \cdot \left(\mathcal{H}\mathcal{F}(\vec{r}, t) \right) = \begin{pmatrix} 0 \\ 0 \end{pmatrix} \quad (2.4.4)$$

for all times and for all $\mathcal{F}(\vec{r}, t)$. Using this property and expanding $\mathcal{U}(t, \tau)$ in Eq. (2.1.15) in terms of the defining exponential series, we see that only the first term of the series, the identity operator returns a non-zero value. All other terms are obtained by a Riemann-Silberstein dot product after the Hamiltonian \mathcal{H} was applied on a certain updated $\mathcal{F}(\vec{r}, t)$ vector. Thus, the first term in Eq. (2.4.3) results exactly in the initial condition

$$\mathcal{D} \cdot \left[\mathcal{U}(t, t_0) \mathcal{F}(\vec{r}, t_0) \right] = \mathcal{D} \cdot \mathcal{F}(\vec{r}, t_0) = \mathcal{Q}(\vec{r}, t_0). \quad (2.4.5)$$

Here, we can already see that the special case of homogeneous divergence conditions in Eq. (2.1.1) holds with Eq. (2.4.5). For the general inhomogeneous divergence condition, we have to consider the inhomogeneity term in Eq. (2.4.3). This term has to contribute to the charge density and to $\mathcal{Q}(\vec{r}, t_0)$ in such way, that it updates the charge density, in time considering always the divergence constraint of Eq. (2.4.2). The inhomogeneity term includes the current density which is directly connected to the charge density by the continuity equation [75]

$$\partial_t \rho(\vec{r}, t) + \vec{\nabla} \cdot \vec{j}(\vec{r}, t) = 0. \quad (2.4.6)$$

In terms of the Riemann-Silberstein charge and current density $\mathcal{J}(\vec{r}, t)$ and $\mathcal{Q}(\vec{r}, t)$ of Eq. (1.1.36) and Eq. (1.1.42), it takes the form

$$\frac{\partial}{\partial t} \mathcal{Q}(\vec{r}, t) + \mathcal{D} \cdot \mathcal{J}(\vec{r}, t) = 0. \quad (2.4.7)$$

Finally, we move the divergence operator inside the integral in Eq. (2.4.3) and use the series expression of $\mathcal{U}(t, \tau)$ to conclude, that only the identity operator term of the series leads to a contribution. Hence, Eq. (2.4.3) takes the form

$$\mathcal{D} \cdot \mathcal{F}(\vec{r}, t) = \mathcal{Q}(\vec{r}, t_0) - \int_{t_0}^t d\tau \mathcal{D} \cdot \mathcal{J}(\vec{r}, \tau). \quad (2.4.8)$$

In a last step, using the continuity equation in Eq. (2.4.7), we substitute $(\mathcal{D} \cdot \mathcal{J}(\vec{r}, \tau))$ by the time, derivative of the Riemann-Silberstein charge density $\mathcal{Q}(\vec{r}, t)$ and obtain

$$\mathcal{D} \cdot \mathcal{F}(\vec{r}, t) = \mathcal{Q}(\vec{r}, t_0) + \int_{t_0}^t \frac{\partial}{\partial \tau} \mathcal{Q}(\vec{r}, \tau) d\tau = \mathcal{Q}(\vec{r}, t). \quad (2.4.9)$$

This result is directly the equation in Eq. (2.4.2) and proves our assumption, that the divergence side conditions in Eq. (2.1.1) and Eq. (2.2.1) hold during evolution of time, if the initial vector obeys this condition.

All previous steps can be repeated by using the corresponding macroscopic variables $\mathcal{F}_{\text{lm}}(\vec{r}, t)$, $\mathcal{D}_{\text{lm}}(\vec{r}, t)$, $\mathcal{H}_{\text{lm}}(\vec{r}, t)$, $\mathcal{J}_{\text{lm}}(\vec{r}, t)$, and $\mathcal{U}_{\text{lm}}(\vec{r}, t)$ from Sec. (1.2.4) and Sec. (2.3) to prove that also the divergence condition for a linear medium in Eq. (1.2.33) holds for a time propagation with Eq. (2.3.8).

Chapter 3

Implementation of the Riemann-Silberstein Maxwell propagation in the real-time real-space code Octopus

The time-evolution of classical electromagnetic fields has been discussed extensively in literature during the last decades. In general, solving the Maxwell's equations in three-dimensional space takes some effort.

In only very few special cases, e.g. electromagnetic plane waves, or Gaussian beams in the paraxial limit, it is possible to find a closed-form analytical expression that describes exactly the electromagnetic fields in time. But there are several techniques to evolve the fields in time approximately. A commonly used method in classical electrodynamics is the so called Yee-algorithm [64] or finite-difference-time-domain (FDTD) method. This method splits the electric field and magnetic field into two separated grids. Both grids have the same spacing but they are shifted by half of the spacing in each direction so that no point of the two different grids lies on the top of each other. In a similar way, one full propagation step in time is split in two steps, each propagates half of the time interval. For each half time step, the Yee-algorithm provides an update of either Faraday's or Ampère's law.

In contrast, our considered Riemann-Silberstein propagation scheme is based on only one grid for the complex Riemann-Silberstein six-vector and both, Faraday's and Ampère's law, are evolved simultaneously in one step. In case of considering only the electromagnetic fields, the Yee algorithm is one of the most popular and efficient Maxwell-propagation methods. On the other hand, time evolution in quantum mechanics is very well described and implemented in quantum mechanical simulations in terms of time-evolution operators. In chapters 1 and 2, we have shown how to transform the Maxwell's equation into a Schrödinger-like form and how to evolve them with time-evolution schemes similar to quantum mechanics. We exploit here this mathematical similarity to implement the electromagnetic field propagation in Octopus, an open-source code that simulates quantum mechanical many-body problems using time-dependent density functional theory (DFT) [66]. Since Octopus provides efficient algorithms to evolve quantum mechanical wavefunctions, i.e. Kohn-Sham (KS) orbitals [86], in time, we treat each dimension of the six-component Riemann-Silberstein vector as one KS orbital. Additionally, we adapt and expand the quantum mechanical time-evolution algorithms in Octopus to solve Maxwell's equations in Riemann-Silberstein form.

In this chapter, we introduce our implementation of a Maxwell propagation scheme in Octopus. Furthermore, we show two different methods for absorbing boundaries. The first one is equivalent to mask absorption in quantum mechanics and easier to implement than the second one, the perfectly matched layer absorption. Based on the Bérenger method in Ref. [87] for a perfectly matched layer in FDTD, we adapt this scheme for the Riemann-Silberstein time evolution.

After introducing these features, we compare our implementation with the MIT Electromagnetic Equation Propagation (MEEP) [88], a program to simulate classical electromagnetic problems.

3.1 Discretized three-dimensional grid for the Maxwell field

In this section, we discuss the three-dimensional grid and spatial derivative operations for the six-component Riemann-Silberstein vector $\mathcal{F}(\vec{r}, t)$. After introducing the basic setup of the grid and operations, we describe the parallelization strategy to divide the computational tasks into separate partitions to speed up the calculation.

3.1.1 Riemann-Silberstein Maxwell grid

We describe the electromagnetic field as complex Riemann-Silberstein vector field, discretized on a three-dimensional Cartesian grid. Hence, in contrast to FDTD, the grid points of both fields are not shifted and lie on top of each other. The whole simulation box is divided into inner and boundary regions. In the inner box region, the real physical equations are applied to simulate "free" Riemann-Silberstein propagation. The boundary region is adjusted to fulfill the corresponding simulation condition, for example absorbing boundaries or incident plane waves. A two-dimensional slice of the simulation box and the boundary region is shown in Figure 3.1, where the grid points with light-grey background illustrate the inner region of the simulation box. The outer grid points are marked by the dark-grey background. The outer box limits are determined by L_u for direction $u \in (x, y, z)$ and the boundary region is limited by b_u . We note, that L_u and b_u are always positive and the box center is always located at the Cartesian origin. The total box dimension in each direction is $-L_u$ to $+L_u$, and the inner borders of the free propagation region are $-b_u$ and $+b_u$, whereas the area between $b_u < |u| < L_u$ describes the boundary regions. In general, the points are always equidistant in the same dimension but the spacing in each direction can be chosen independently. All mathematical spatial operators, for example spatial derivatives are determined by the grid points.

3.1.2 Finite difference stencil

As shown in chapter 2, the Riemann-Silberstein time-evolution depends on first order spatial derivatives. Such derivatives for each grid point can be obtained by the finite-difference method which is explained in detail in Ref. [89, 90, 91] and briefly summarized in the next steps. For a given function $f(x)$, it is assumed that the function value $f(x_0 + \Delta x)$ at point $x_0 + \Delta x$ with small Δx and the known function value $f(x_0)$ at x_0 correspond to a Taylor expansion of n^{th} order

$$f(x_0 + \Delta x) = f(x_0) + \sum_{n=1}^{\infty} \frac{1}{n!} \frac{d^n f(x)}{dx^n} (\Delta x)^n . \quad (3.1.1)$$

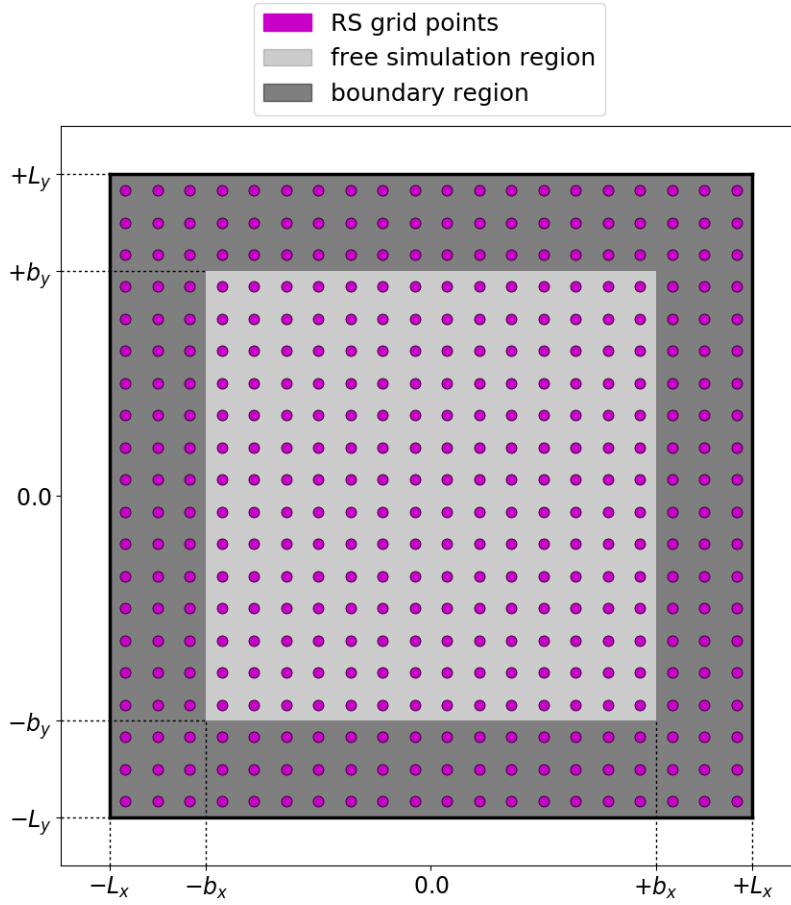


Figure 3.1: The figure shows a two-dimensional slice of the three-dimensional simulation box with different simulation regions. The inner light-grey region shows all grid points where Maxwell's equations are propagated. The dark-grey region contains the grid points to simulate the correct boundary conditions. The underlying equations in this case are artificial modified Maxwell's equations to satisfy the boundary conditions. The inner free Maxwell propagation area is limited by the boundary box limits b_x and b_y of the boundary region and the whole box is limited by the outer limits L_x and L_y .

The $n!$ factor denotes the factorial of n . Without loss of generality the function $f(x)$ can also be expanded at point $x_0 - \Delta x$, which modifies equation (3.1.1) to

$$f(x_0 - \Delta x) = f(x_0) + \sum_{n=1}^{\infty} (-1)^n \frac{1}{n!} \frac{d^n f(x)}{dx^n} (\Delta x)^n. \quad (3.1.2)$$

In both cases, solving for the first derivative $f'(x)$ leads to

$$f'(x) = \frac{f(x + \Delta x) - f(x)}{\Delta x} - \sum_{n=2}^{\infty} \frac{1}{n!} \frac{d^n f(x)}{dx^n} (\Delta x)^{n-1} = \frac{f(x + \Delta x) - f(x)}{\Delta x} + \mathcal{O}(\Delta x), \quad (3.1.3)$$

and

$$f'(x) = \frac{f(x) - f(x - \Delta x)}{\Delta x} - \sum_{n=2}^{\infty} (-1)^n \frac{1}{n!} \frac{d^n f(x)}{dx^n} (\Delta x)^{n-1} = \frac{f(x) - f(x - \Delta x)}{\Delta x} + \mathcal{O}(\Delta x), \quad (3.1.4)$$

where the remaining term $\mathcal{O}(\Delta x)$ represents the difference between the exact value $f'(x)$ and the finite difference term in Eq. (3.1.4). For an equidistant regular grid, the small Δx is equal to the spacing between two grid points, i.g. x_i and x_{i+1} or x_i and x_{i-1}

$$\Delta x = x_{i+1} - x_i = x_i - x_{i-1}. \quad (3.1.5)$$

Therefore, by using the function values $f(x_i)$ at the grid points x_{i-1}, x_i, x_{i+1} , the Taylor series in Eq. (3.1.3) can be expressed as

$$f'(x_i) = \frac{f(x_{i+1}) - f(x_i)}{\Delta x} + \mathcal{O}(\Delta x), \quad (3.1.6)$$

which is called forward expansion. Consequently the backward expansion of Eq. (3.1.4) takes the form

$$f'(x_i) = \frac{f(x_i) - f(x_{i-1})}{\Delta x} + \mathcal{O}(\Delta x), \quad (3.1.7)$$

A third formula, called center difference formula, is given by subtracting Eq. (3.1.6) from Eq. (3.1.7) and solving for $f'(x_i)$

$$f'(x_i) = \frac{f(x_{i+1}) - f(x_{i-1}))}{2\Delta x} + \mathcal{O}(\Delta x^3). \quad (3.1.8)$$

In contrast to the forward and backward difference formula, the even terms of $\Delta x^2, \Delta x^4, \dots$ in the center difference formula vanish. Therefore, the remaining term in equation (3.1.8) has the order of Δx^3 , which means that the center difference formula is more accurate. The accuracy can also be increased by using additional grid points. Assuming the spatial derivative $f'(x_i)$ at point x_i can be expressed as a linear combination of the grid point function values of $f(x_i)$ and the next nearest ones, the ansatz for the formula in center difference calculation with accuracy of order n is given by

$$f'(x_i) = a_{i-n}f(x_{i-n}) + \dots + a_{i-1}f(x_{i-1}) + a_i f(x_i) + a_{i+1}f(x_{i+1}) + \dots + a_{i+n}f(x_{i+n}). \quad (3.1.9)$$

Therefore the required number of grid points is $2n + 1$. The coefficients $a_{i-n} \dots a_{i+n}$ have to be determined by $2n$ equations, n forward and n backward Taylor series of order n of the functions $f(x_{i-n}), \dots, f(x_{i-1}), f(x_{i+1}), \dots, f(x_{i+n})$. For a given order n the Taylor series

takes the form

$$\begin{aligned}
f(x_{i+n}) &= f(x_i + n\Delta x) = f(x_i) + \frac{n}{1!}f'(x_i)\Delta x + \dots + \frac{n^n}{n!}f^{(n)}(x_i)\Delta x^n + \mathcal{O}(\Delta x^{n+1}) \\
&\quad \vdots \\
f(x_{i+2}) &= f(x_i + 2\Delta x) = f(x_i) + 2f'(x_i)\Delta x + \dots + \frac{2^n}{n!}f^{(n)}(x_i)\Delta x^n + \mathcal{O}(\Delta x^{n+1}) \\
f(x_{i+1}) &= f(x_i + \Delta x) = f(x_i) + f'(x_i)\Delta x + \dots + \frac{1^n}{n!}f^{(n)}(x_i)\Delta x^n + \mathcal{O}(\Delta x^{n+1}) \\
f(x_i) &= f(x_i) \\
f(x_{i-1}) &= f(x_i - \Delta x) = f(x_i) - f'(x_i)\Delta x + \dots - \frac{1^n}{n!}f^{(n)}(x_i)\Delta x^n + \mathcal{O}(\Delta x^{n+1}) \\
f(x_{i-2}) &= f(x_i - 2\Delta x) = f(x_i) - 2f'(x_i)\Delta x + \dots - \frac{2^n}{n!}f^{(n)}(x_i)\Delta x^n + \mathcal{O}(\Delta x^{n+1}) \\
&\quad \vdots \\
f(x_{i-n}) &= f(x_i - n\Delta x) = f(x_i) - \frac{n}{1!}f'(x_i)\Delta x + \dots + \frac{(-n)^n}{n!}f^{(n)}(x_i)\Delta x^n + \mathcal{O}(\Delta x^{n+1}) .
\end{aligned} \tag{3.1.10}$$

The functions $f(x_{i-n}), \dots, f(x_{i-1}), f(x_{i+1}), \dots, f(x_{i+n})$ on the right-hand side of equation (3.1.9) can be substituted by the equations in (3.1.10). Hence, the first derivative $f'(x_i)$ is given by

$$f'(x_i) = b_0 f(x_i) + b_1 f'(x_i) + b_2 f''(x_i) + \dots + f^{(n)}(x_i) \tag{3.1.11}$$

with

$$\begin{aligned}
b_0 &= a_{i-n} + \dots + a_{i-1} + a_i + a_{i+1} + \dots + a_{i+n} \\
b_1 &= (na_{i-n} + \dots + 2a_{i-2} + a_{i-1} + a_{i+1} + 2a_{i+2} + \dots + na_{i+n}) \Delta x \\
b_2 &= \frac{1}{2} (n^2 a_{i-n} + \dots + 4a_{i-2} + a_{i-1} + a_{i+1} + 4a_{i+2} + \dots + n^2 a_{i+n}) \Delta x^2 \\
&\quad \vdots \\
b_n &= \frac{1}{n!} (n^n a_{i-n} + \dots + 2^n a_{i-2} + a_{i-1} + a_{i+1} + 2^n a_{i+2} + \dots + n^n a_{i+n}) \Delta x^n .
\end{aligned} \tag{3.1.12}$$

Equating left-hand and right-hand side in equation (3.1.11) leads to the condition, that only b_1 in Eq.(3.1.13) is equal to one. Whereas all other remaining coefficients b_i are equal to zero. Consequently, the coefficients a_i in equation (3.1.9) can be obtained by a system of linear equations

$$\begin{aligned}
0 &= a_{i-n} + \dots + a_{i-1} + a_i + a_{i+1} + \dots + a_{i+n} , \\
1 &= (na_{i-n} + \dots + 2a_{i-2} + a_{i-1} + a_{i+1} + 2a_{i+2} + \dots + na_{i+n}) \Delta x , \\
0 &= \frac{1}{2} (n^2 a_{i-n} + \dots + 4a_{i-2} + a_{i-1} + a_{i+1} + 4a_{i+2} + \dots + n^2 a_{i+n}) \Delta x^2 , \\
&\quad \vdots \\
0 &= \frac{1}{n!} (n^n a_{i-n} + \dots + 2^n a_{i-2} + a_{i-1} + a_{i+1} + 2^n a_{i+2} + \dots + n^n a_{i+n}) \Delta x^n .
\end{aligned} \tag{3.1.13}$$

Of course, the whole system of linear equations can be expressed equivalently as a matrix vector product

$$\begin{pmatrix} 1 & \dots & 1 & 1 & 1 & \dots & 1 \\ -n\Delta x & \dots & -2\Delta x & 0 & 2\Delta x & \dots & n\Delta x \\ -\frac{1}{2}n^2\Delta x^2 & \dots & -4\Delta x^2 & 0 & 4\Delta x^2 & \dots & \frac{1}{2}n^2\Delta x^2 \\ \vdots & & \vdots & 0 & \vdots & & \vdots \\ -\frac{1}{n!}n^n\Delta x^n & \dots & 2^n\Delta x^n & 0 & 2^n\Delta x^n & \dots & \frac{1}{n!}n^n\Delta x^n \end{pmatrix} \begin{pmatrix} a_{i-n} \\ \vdots \\ a_{i-1} \\ a_i \\ a_{i+1} \\ \vdots \\ a_{i+n} \end{pmatrix} = \begin{pmatrix} 0 \\ 1 \\ 0 \\ \vdots \\ 0 \end{pmatrix}. \quad (3.1.14)$$

There are several techniques shown in Ref. [92] to solve Eq. (3.1.14). The resulting coefficients a_{i-n}, \dots, a_{i+n} define a one-dimensional stencil which is here a $(2n + 1)$ -dimensional vector. Multiplying this vector with the function values that correspond to the stencil coefficient yields with Eq. (3.1.9)

$$f'(x_i) \approx \begin{pmatrix} a_{i-n} & \dots & a_i & \dots & a_{i+n} \end{pmatrix} \cdot \begin{pmatrix} f(x_{i-n}) \\ \vdots \\ f(x_i) \\ \vdots \\ f(x_{i+n}) \end{pmatrix}. \quad (3.1.15)$$

In the previous steps, we briefly introduced the finite difference method to derive the approximated first derivative of a function on a discrete grid in one dimension. Since we consider the Maxwell field propagation in three dimensions, we have to extend the one-dimensional stencil to a three-dimensional one. While the one-dimensional stencil is a chain, the two- and three-dimensional stencils form a two-dimensional respectively three-dimensional cross stencil. Figure 3.2 illustrates such a cross stencil in the xy-plane. For a given three-dimensional function $f(x_i, y_j, z_k)$ at the grid points x_i, y_j, z_j , the corresponding finite difference coefficients are $a_{x,i-n} \dots a_{x,i+n}$ for the partial derivative in x, and $a_{y,j-n} \dots a_{y,j+n}$, respectively $a_{z,k-n} \dots a_{z,k+n}$ for the remaining two partial derivatives. Similar to Eq. (3.1.15), the approximation for the spatial partial derivatives take the form

$$\frac{\partial}{\partial x} f(x, y, z) \approx \begin{pmatrix} a_{x,i-n} & \dots & a_{x,i+n} & 0 & \dots & 0 & 0 & \dots & 0 \end{pmatrix} \cdot \begin{pmatrix} f(x_{i-n}) \\ \vdots \\ f(x_{i+n}) \\ f(y_{j-n}) \\ \vdots \\ f(y_{j+n}) \\ f(z_{k-n}) \\ \vdots \\ f(z_{k+n}) \end{pmatrix}, \quad (3.1.16)$$

$$\frac{\partial}{\partial y} f(x, y, z) \approx \begin{pmatrix} 0 & \dots & 0 & a_{y,j-n} & \dots & a_{y,j+n} & 0 & \dots & 0 \end{pmatrix} \cdot \begin{pmatrix} f(x_{i-n}) \\ \vdots \\ f(x_{i+n}) \\ f(y_{j-n}) \\ \vdots \\ f(y_{j+n}) \\ f(z_{k-n}) \\ \vdots \\ f(z_{k+n}) \end{pmatrix}, \quad (3.1.17)$$

$$\frac{\partial}{\partial z} f(x, y, z) \approx \begin{pmatrix} 0 & \cdots & 0 & 0 & \cdots & 0 & a_{z,k-n} & \cdots & a_{z,k+n} \end{pmatrix} \cdot \begin{pmatrix} f(x_{i-n}) \\ \vdots \\ f(x_{i+n}) \\ f(y_{j-n}) \\ \vdots \\ f(y_{j+n}) \\ f(z_{k-n}) \\ \vdots \\ f(z_{k+n}) \end{pmatrix}. \quad (3.1.18)$$

The stencil and grid point vectors in Eqs. (3.1.16)-(3.1.18) have the size $6n + 1$. All operations are independent in each dimension, since we do not consider mixed derivatives for the Maxwell time propagation.

3.1.3 Parallelization strategy in the first principles code octopus

Large grids increase the computational cost. To speed up the calculations, it is useful to divide the computational task into several partitions and use parallel processors. Taking the grid setup from Sec. (3.1.1), we employ a domain parallelization. A schematic plot of a divided grid into four domains is shown in Figure 3.3. Each of the four partitions covers only a part of the whole grid. The partial grids have to take the boundary region of the total grid into account. Furthermore, to achieve a correct calculation which is equivalent to the serial case, the derivative operation has to be equivalent. In the boundary region, the operation stencils contain several stencil points which are located on another domain. The cross stencil in Figure 3.3 illustrates this case, where two stencil points lie in partition 1 and one point in partition 2. To obtain a correct parallelization, the processors send

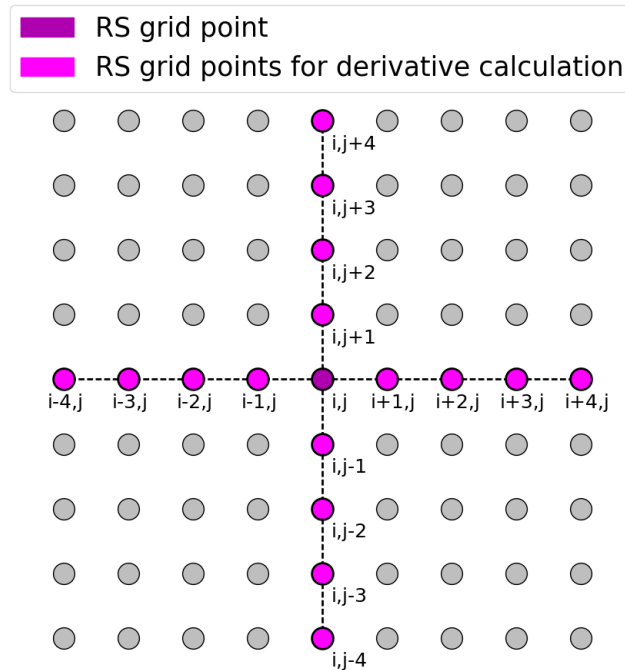


Figure 3.2: Two-dimensional stencil. All grid points which determine the first derivative of $f_{i,j}$ at point $x_{i,j}$ build a cross of $2n + 1$ grid points in each dimension, where n denotes the accuracy order of the derivative. The figure shows an example for such a two-dimensional stencil for $n = 4$.

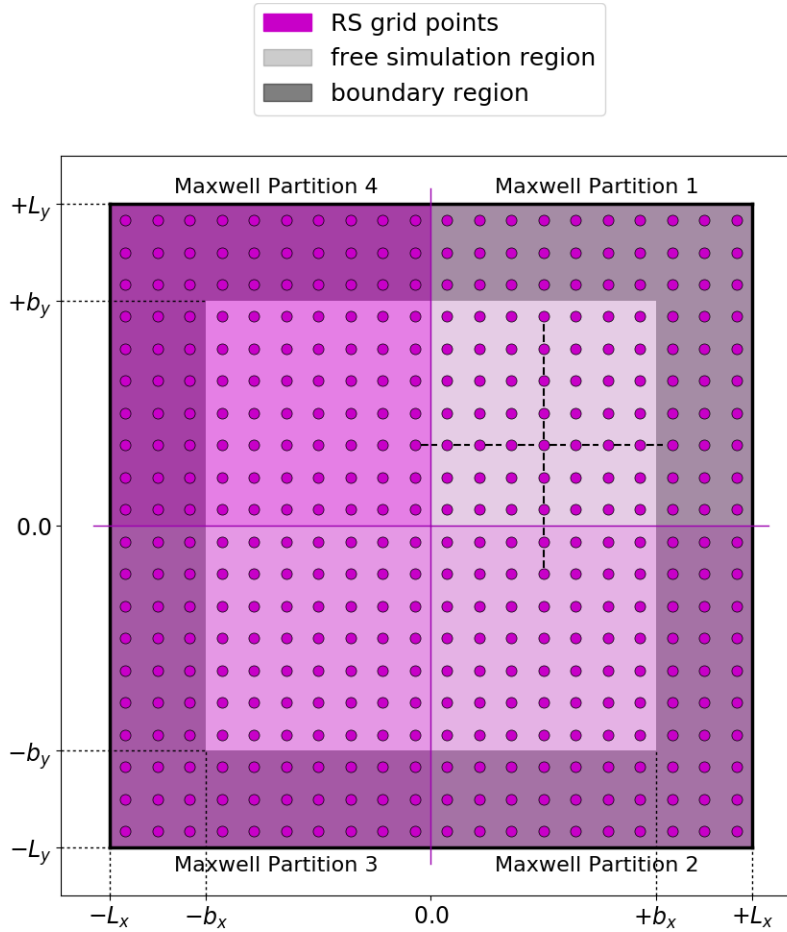


Figure 3.3: Parallelization scheme for dividing the Maxwell grid into four partitions. The cross in partition 1 illustrates a two-dimensional stencil of order $n = 4$. Some stencil points are located in different partitions, which has to be taken into account. For each propagation step, the necessary variables at the grid boundaries are sent and received by the neighbouring partitions.

and receive the necessary data for each time step. Octopus uses domain parallelization [93] for the Kohn-Sham orbitals. Therefore, we adapt this scheme for the six-component Riemann-Silberstein vector and treat each vector component as a Kohn-Sham orbital.

3.2 Discretized Riemann-Silberstein time-evolution operators

In section 2.2, we derived the time-evolution equation in (2.2.14) to evolve the six-component Riemann-Silberstein vector $\mathcal{F}(\vec{r}, t)$, which has the explicit form

$$\mathcal{F}(\vec{r}, t) = \mathcal{U}(t, t_0)\mathcal{F}(\vec{r}, t_0) - \int_{t_0}^t d\tau \mathcal{U}(t, \tau)\mathcal{J}(\vec{r}, \tau). \quad (3.2.1)$$

In general, the solution of the Riemann-Silberstein time-evolution is not analytical. However, a recursive time-evolution of the Riemann-Silberstein vector with a rather small time step Δt yields a numerical solution. The size of Δt is chosen such that the propagation

stays stable. Therefore, the recursive form to obtain the next Riemann-Silberstein vector $\mathcal{F}(\vec{r}, (m+1)\Delta t)$ from a given $\mathcal{F}(\vec{r}, m\Delta t)$ at the discrete time $m\Delta t$ leads from Eq.(3.2.1) to

$$\mathcal{F}(\vec{r}, (m+1)\Delta t) = \mathcal{U}((m+1)\Delta t, m\Delta t)\mathcal{F}(\vec{r}, m\Delta t) - \int_{m\Delta t}^{(m+1)\Delta t} d\tau \mathcal{U}(\tau, m\Delta t)\mathcal{J}(\vec{r}, \tau). \quad (3.2.2)$$

The integral on the right-hand side is approximated by the trapezoidal rule. This leads to the discrete time evolution equation

$$\begin{aligned} \mathcal{F}(\vec{r}, (m+1)\Delta t) \approx & \hat{\mathcal{U}}((m+1)\Delta t, m\Delta t)\mathcal{F}(\vec{r}, m\Delta t) - \frac{\Delta t}{2}\hat{\mathcal{U}}((m+1)\Delta t, m\Delta t)\mathcal{J}(\vec{r}, m\Delta t) \\ & - \frac{\Delta t}{2}\mathcal{J}(\vec{r}, (m+1)\Delta t), \end{aligned} \quad (3.2.3)$$

We put the Riemann-Silberstein vector and the Riemann-Silberstein current density $\mathcal{J}(\vec{r}, t)$ on a three-dimensional Cartesian grid as it is introduced in Sec. (3.1.1). Hence, both variables at the grid position $\vec{r}_{i,j,k}$ are denoted by $\mathcal{F}(x_i, y_j, z_k)$ and $\mathcal{J}(x_i, y_j, z_k)$. The time-evolution operator \mathcal{U} that is required in Eq. (3.2.1), has been introduced in Eq. (2.1.15). This operator is a matrix exponential that acts on the Riemann-Silberstein vector. For our electromagnetic time-evolution simulation, we truncate the series expansion. Some stability tests versus efficiency have shown, that the fourth order of the exponential series leads in most cases to stable and efficient runs. Furthermore, the spatial partial derivative is calculated with the three-dimensional derivative stencil, which we discussed in Sec. (3.1.2). To speed up large system calculations, we use the parallelization in domain strategy from Sec. (3.1.3)

The location of the grid points is determined by the dimensions of the simulation box and by the grid spacing $\Delta x, \Delta y, \Delta z$, which can be selected independently. On the other hand, the time step parameter Δt has to be chosen such that the propagation remains stable and accurate. A very well-known criterion for Δt that always leads to stable runs is described by the Courant-Friedrichs-Lewy (CFL) condition [94, 95]

$$\Delta t_{\text{Mx,CFL}} \leq \frac{S_{\text{CFL,max}}}{c_0 \sqrt{\frac{1}{\Delta x^2} + \frac{1}{\Delta y^2} + \frac{1}{\Delta z^2}}}, \quad (3.2.4)$$

and depends basically on the grid point spacing $\Delta x, \Delta y, \Delta z$, and the Courant number $S_{\text{CFL,max}}$. The $S_{\text{CFL,max}}$ number changes for different propagation methods. In case of FDTD in three dimensions, $S_{\text{CFL,max}}$ is equal to one [94, 95] which we used for all of our simulations. We have performed convergence tests for our implemented Riemann-Silberstein Maxwell time-evolution and have found that also Courant numbers a little larger than one leads to stable and accurate simulations. However, we could not find a fixed value for $S_{\text{CFL}} > S_{\text{CFL,max}}$ which is valid universally. The actual maximal value varies and depends on the grid spacing.

3.3 Maxwell-propagation with Octopus

After introducing the Maxwell-Riemann-Silberstein propagation scheme on a three-dimensional grid, we show in this section the first electromagnetic field simulations performed with our new implementation. We consider as example a case where a given external current density is prescribed for the solution of Maxwell's equations. The current density

has a Gaussian shape and is located in the center of the simulation box. The box size is chosen large enough such that the electromagnetic fields do not reach the box boundaries within the simulation time. For a validation of our implementation, we compare our results with the electromagnetic evolution program MEEP. We also show for this example that the Gauß laws are obeyed in time.

3.3.1 Comparison of the Octopus Maxwell-propagation with the electromagnetic propagation program MEEP

The program MIT Electromagnetic Equation Propagation (MEEP) [88] is a common simulation package for electromagnetic field propagations. The implemented Maxwell field propagation in MEEP is based on the Finite Difference Time Domain method (FDTD) and the Yee-algorithm [64]. The underlying electromagnetic simulation grid is split into two grids shifted by half of the grid spacing of the corresponding direction. As a consequence, the required spatial and time derivative points for the propagation equation are in the middle of two sample grid points. Therefore, the center finite difference method leads to the first derivative equation, here for simplicity discussed in one dimension

$$f'(x_0) = \frac{f(x_0 + \frac{\Delta x}{2}) - f(x_0 - \frac{\Delta x}{2})}{\Delta x} - \frac{1}{3!} f'''(x_0) \left(\frac{\Delta x}{2}\right)^2 + \dots . \quad (3.3.1)$$

In case of the Yee grid, there are no grid points at the derivative point x_0 but next to it at $x_0 - \Delta x/2$ and $x_0 + \Delta x/2$. We also use the center finite difference discretization in Octopus, but the derivative points lie always on top of a sample grid point. Thus, the derivative equation takes the form

$$f'(x_0) = \frac{f(x_0 + \Delta x) - f(x_0 - \Delta x)}{2\Delta x} - \frac{1}{3!} f'''(x_0) (\Delta x)^2 + \dots , \quad (3.3.2)$$

which means that the error of $f'(x_0)$ is smaller for the Yee-algorithm if we consider the same order terms of the finite difference method. However, the MEEP finite difference stencil operation is always of order two whereas the Octopus stencil order can be set to higher orders to obtain better accuracy for the derivative operators. The MEEP internal unit for the speed of light is equal one. Consequently, the electric permittivity in vacuum ϵ_0 and the magnetic permeability in vacuum μ_0 are also equal to one. To compare our electromagnetic field propagation with MEEP, we set our internal constants in Octopus equal to the MEEP internal units, which means that $\epsilon_0 = \mu_0 = c_0 = 1$ with finite difference order of two for the runs in this section. Additionally, the exponential series expansion order is four.

As test scenarios, we simulate four different spatial and temporal shaped external current densities inside a box and plot several relevant physical variables. For all runs, we use the same spatial current density distribution $\vec{j}_0(\vec{r})$

$$\vec{j}_0(\vec{r}) = \vec{e}_z \exp\left(\frac{-x^2 - y^2 - z^2}{2}\right) . \quad (3.3.3)$$

The external current flows along the z-axis and has a three-dimensional Gaussian shape. Figure 3.4 visualizes the spatial current amplitude in the xy-plane. We chose the following

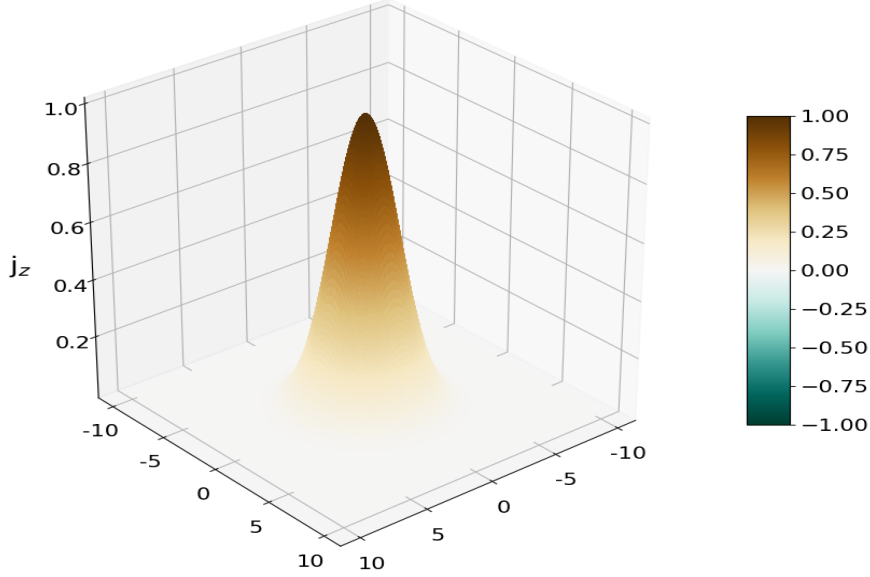


Figure 3.4: The spatial external current density distribution for the comparison calculation with MEEP is a three-dimensional Gaussian function represented in equation (3.3.3). The only contribution is along the z-axis. The figure shows a two-dimensional cut through the xy-plane.

four spatial and time dependent current densities $\vec{j}_i(\vec{r}, t)$, with $i = \{1, 2, 3, 4\}$

$$\vec{j}_1(\vec{r}, t) = \vec{j}_0(\vec{r}) \exp\left(-\frac{(t-10.0)^2}{8}\right), \quad (3.3.4)$$

$$\vec{j}_2(\vec{r}, t) = \vec{j}_0(\vec{r}) \left[\exp\left(-\frac{(t-10.0)^2}{8}\right) - \exp\left(-\frac{(t-12.0)^2}{8}\right) \right], \quad (3.3.5)$$

$$\vec{j}_3(\vec{r}, t) = \vec{j}_0(\vec{r}) \exp\left(-\frac{(t-10.0)^2}{8}\right) \sin(2.0(t - 10.0)), \quad (3.3.6)$$

$$\vec{j}_4(\vec{r}, t) = \vec{j}_0(\vec{r}) \exp\left(-\frac{(t-10.0)^2}{8}\right) \cos(2.0(t - 10.0)). \quad (3.3.7)$$

We select a cubic simulation box of length 80.0, i.e., the box length parameter referring to the simulation box scheme in Figure 3.1 are given by $L_x = L_y = L_z = 40.0$. We use a zero boundary condition, which means that the field variables are set to zero at the simulation box limits. We select a sufficiently large box that the boundary effects cannot influence the simulation during the simulation time. For all four test currents in Eqs. (3.3.4)-(3.4.51), we evaluate the electric field, the magnetic field, the electromagnetic energy density at the box point (5, 0, 0), as well as the integrated electromagnetic energy inside the simulation box. The grid spacing in each dimension is $\Delta x = \Delta y = \Delta z = 0.2$, which leads to a mutual time step in MEEP and Octopus of $\Delta t = 0.1$. An overview of all relevant parameters for both simulations is shown in Table 3.1.

Figure 3.5 shows the comparison of our Maxwell propagation implementation in Octopus and MEEP for the different current densities in Eqs (3.3.4)-(3.4.51). All results are evaluated at point (5, 0, 0).

In the first panels 1 - a) to 4 - a), we plot the initial current density $\vec{j}(\vec{r}, t)$ in z-direction. Due to the spatial shape of the current density, the maximum value of $\vec{j}(\vec{r}, t)$ is damped by the factor $e^{-5^2/2}$. The next panels 1 - b) to 4 - b) and 1 - c) to 4 - c) show the electric field in z-direction and the magnetic field in y-direction also both at coordinate (5, 0, 0).

| variable | MEEP units |
|--------------------------------|------------|
| L_x | 40.0 |
| L_y | 40.0 |
| L_z | 40.0 |
| $\Delta x, \Delta y, \Delta z$ | 0.2 |
| finite difference order | 2 |
| exponential order | 4 |
| Δt | 0.1 |
| ϵ_0 | 1 |
| μ_0 | 1 |
| c_0 | 1 |

Table 3.1: Simulation parameters for the Octopus and MEEP comparison run.

The Maxwell energy densities at this point calculated by Octopus and MEEP also match, and are plotted in the panels 1 - c) to 4 - c). The last panels 1 - d) to 4 - d) illustrate the total Maxwell energy inside the box of size $-40.0 \leq x \leq 40.0$, $-40.0 \leq y \leq 40.0$, and $-40.0 \leq z \leq 40.0$.

As a first summary, we can confirm, that our implementation of a Maxwell propagation yields the same results as MEEP. Each curve of the electric and magnetic fields in Figure 3.5 in panels b) respectively c), and the Maxwell energy density in d), calculated by Octopus, is covered by the corresponding MEEP curve. Additionally, all four total energies inside the two simulation boxes match and confirm that our implementation leads to similar results like MEEP.

Next, we consider some field reactions in more detail. According to Eqs. (3.3.4)-(3.4.51), the spatial center is at the origin of the box and the temporal center of the current densities is at time $t = 10.0$. Therefore, the electromagnetic field reaction is shifted by $\Delta t = 5.0$ time in MEEP units to reach the evaluation point at (5,0,0).

In contrast to all other electric fields, which return to zero later in time, the electric field in Figure 3.5 1 - b) takes a constant value around $t = 25.0$. At this point, we refer to Sec. 2.4, where we show that the Maxwell side condition, the electric and magnetic Gauß laws, hold during our Maxwell propagation. The reason for this feature is based on the continuity equation which we discuss in the next section.

Looking at the Gaussian pulse with sine carrier wave in 3 - a), we notice that it is very similar shaped to the electric field reaction of the Gaussian pulse with cosine carrier wave in 4 - b). In the same way, the magnetic field reaction in 3 - c) is similar to the current density in 4 - a). This similarity can be explained by taking Faraday's and Ampère's laws with Eq.(2.3.7), rearranged to

$$i\hbar \frac{\partial}{\partial t} \mathcal{F}(\vec{r}, t) + i\hbar \mathcal{J}(\vec{r}, t) = \mathcal{H}\mathcal{F}(\vec{r}, t). \quad (3.3.8)$$

In principle, the current density term can be expressed by

$$\mathcal{J}(\vec{r}, t) = \frac{\partial}{\partial t} \mathcal{F}_{\mathcal{J}}(\vec{r}, t), \quad \Rightarrow \mathcal{F}_{\mathcal{J}}(\vec{r}, t) = \int_{t_0}^t d\tau \mathcal{J}(\vec{r}, \tau), \quad (3.3.9)$$

where $\mathcal{F}_{\mathcal{J}}(\vec{r}, t)$ denotes the integral of $\mathcal{J}(\vec{r}, \tau)$. Consequently, Eq. (3.3.8) becomes

$$i\hbar \frac{\partial}{\partial t} (\mathcal{F}(\vec{r}, t) + \mathcal{F}_{\mathcal{J}}(\vec{r}, t)) = \mathcal{H}\mathcal{F}(\vec{r}, t). \quad (3.3.10)$$

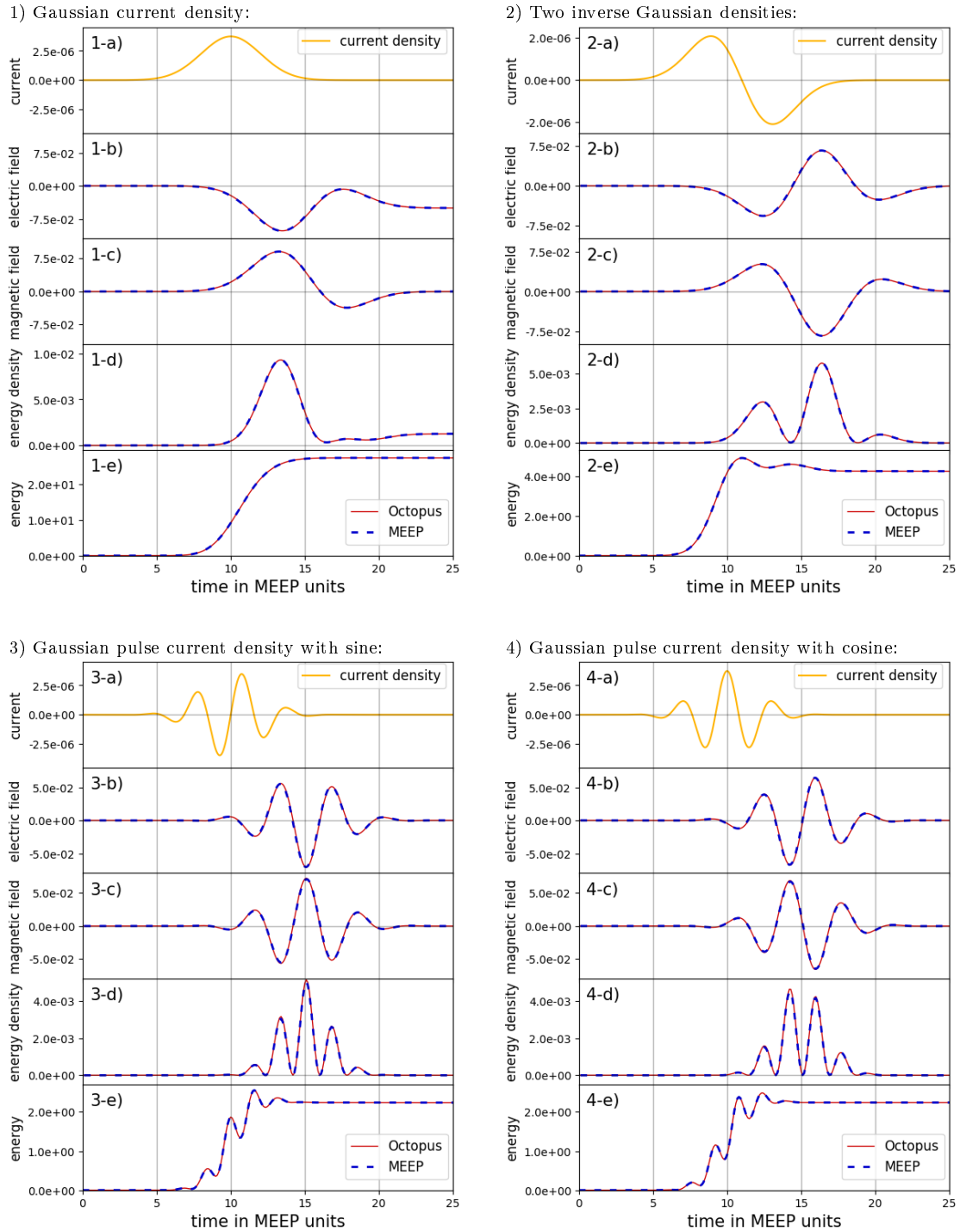


Figure 3.5: Electromagnetic variables at grid point $(5,0,0)$ for a Gaussian external current signal, calculated by the Octopus and MEEP simulations. The external current density, shown in a), causes an electromagnetic field reaction, which is plotted as electric field in b), magnetic field in c), and energy density in d). The last curves in e) show the total electromagnetic energy inside the simulation box. Both simulation results, Octopus and MEEP agree, and differences are of negligible magnitude.

Since the integral of the Gaussian shaped pulse with sine carrier wave is given by a Gaussian shaped pulse with cosine carrier wave and vice versa, the previously described similarity

of the corresponding signals become clear. The fact, that both shapes are only similar and not equal can be understood with the first Riemann-Silberstein field variable $\mathcal{F}(\vec{r}, t)$ in Eq. (3.3.10) which influences slightly the resulting field.

3.3.2 Longitudinal and transverse electromagnetic fields and currents

To demonstrate the properties of longitudinal and transverse current densities, we take a further look at the four calculations in Sec. 3.3.1. Using Eq. (3.3.23) for the current densities $\vec{j}_1(\vec{r}, t) - \vec{j}_2(\vec{r}, t)$ from Eqs. (3.3.4)-(3.4.51) gives the corresponding motion of charge densities $\rho_1(\vec{r}, t) - \rho_2(\vec{r}, t)$, which we express approximately since they contain more error functions with constant arguments, i.e.,

$$\rho_1(\vec{r}, t) \approx \sqrt{2\pi} z |\vec{j}_0(\vec{r})| \left[\text{Erf} \left(\frac{t - 10.0}{2\sqrt{2}} \right) + 1 \right], \quad (3.3.11)$$

$$\rho_2(\vec{r}, t) \approx \sqrt{2\pi} z |\vec{j}_0(\vec{r})| \left[\text{Erf} \left(\frac{t - 10.0}{2\sqrt{2}} \right) - \text{Erf} \left(\frac{t - 12.0}{2\sqrt{2}} \right) \right], \quad (3.3.12)$$

$$\rho_3(\vec{r}, t) \approx \sqrt{\frac{\pi}{2}} z |\vec{j}_0(\vec{r})| e^{-8} \left[\text{Erf} \left(\frac{t - (10.0 + 8.0i)}{2\sqrt{2}} \right) - \text{Erf} \left(\frac{t - (10.0 - 8.0i)}{2\sqrt{2}} \right) + 2.677e^{-3} \right], \quad (3.3.13)$$

$$\rho_4(\vec{r}, t) \approx \sqrt{\frac{\pi}{2}} z |\vec{j}_0(\vec{r})| e^{-8} \left[\text{Erf} \left(\frac{t - (10.0 + 8.0i)}{2\sqrt{2}} \right) - \text{Erf} \left(\frac{t - (10.0 - 8.0i)}{2\sqrt{2}} \right) + 2.0 \right]. \quad (3.3.14)$$

with the error function $\text{Erf}(t)$. For large time $t \rightarrow \infty$, Eqs. (3.3.11)-(3.3.14) yield approximately

$$\rho_1(\vec{r}, t \rightarrow \infty) \approx 2\sqrt{2\pi} z |\vec{j}_0(\vec{r})|, \quad (3.3.15)$$

$$\rho_2(\vec{r}, t \rightarrow \infty) \approx 0, \quad (3.3.16)$$

$$\rho_3(\vec{r}, t \rightarrow \infty) \approx 0, \quad (3.3.17)$$

$$\rho_4(\vec{r}, t \rightarrow \infty) \approx 0. \quad (3.3.18)$$

Consequently, the current density $\vec{j}_1(\vec{r}, t)$ moves charges just along one direction, which leads to a permanent positive charge density distribution $\rho_1(\vec{r}, t)$ inside the simulation box, whereas the remaining current densities $\vec{j}_2(\vec{r}, t) - \vec{j}_4(\vec{r}, t)$ also move charges, but in both directions so that they in total approximately cancel out and leave an almost zero charge density. The charge density $\rho_1(\vec{r}, t)$ causes an static electric field for $t \rightarrow \infty$, whereas the remaining three charge densities are very close to zero. Therefore, the electric field in Figure 3.5 1-b) reaches approximately a constant electric field at time $t = 25.0$, and the three other electric fields in Figures 3.5 2-b) to 4-b) decrease to zero. Figure 3.6 illustrates some snapshots of the electric field propagation polarized in z-direction for selected time steps. All four snapshots of the panels a) are taken at time $t = 16.0$. They all show a spherical outgoing wave of different shapes. The number of oscillations depend on the corresponding number of temporal oscillations of the current pulses given in Eqs. (3.3.4)-(3.4.51). The spherical waves propagates to the outside, which can be seen in the four panels 1-4 a), until they left the box in panels 1-4 b) at time $t = 25.0$, and 1-4 c) at time $t = 30.0$. Again, according to Eqs. (3.3.15)-(3.3.16) the current density $\vec{j}_1(\vec{r}, t)$ causes a permanent charge density. Consequently, besides the outgoing wave in Figure 3.6 1-a) to 1-c), a permanent electric field with Gaussian shape arises which is centered at the origin.

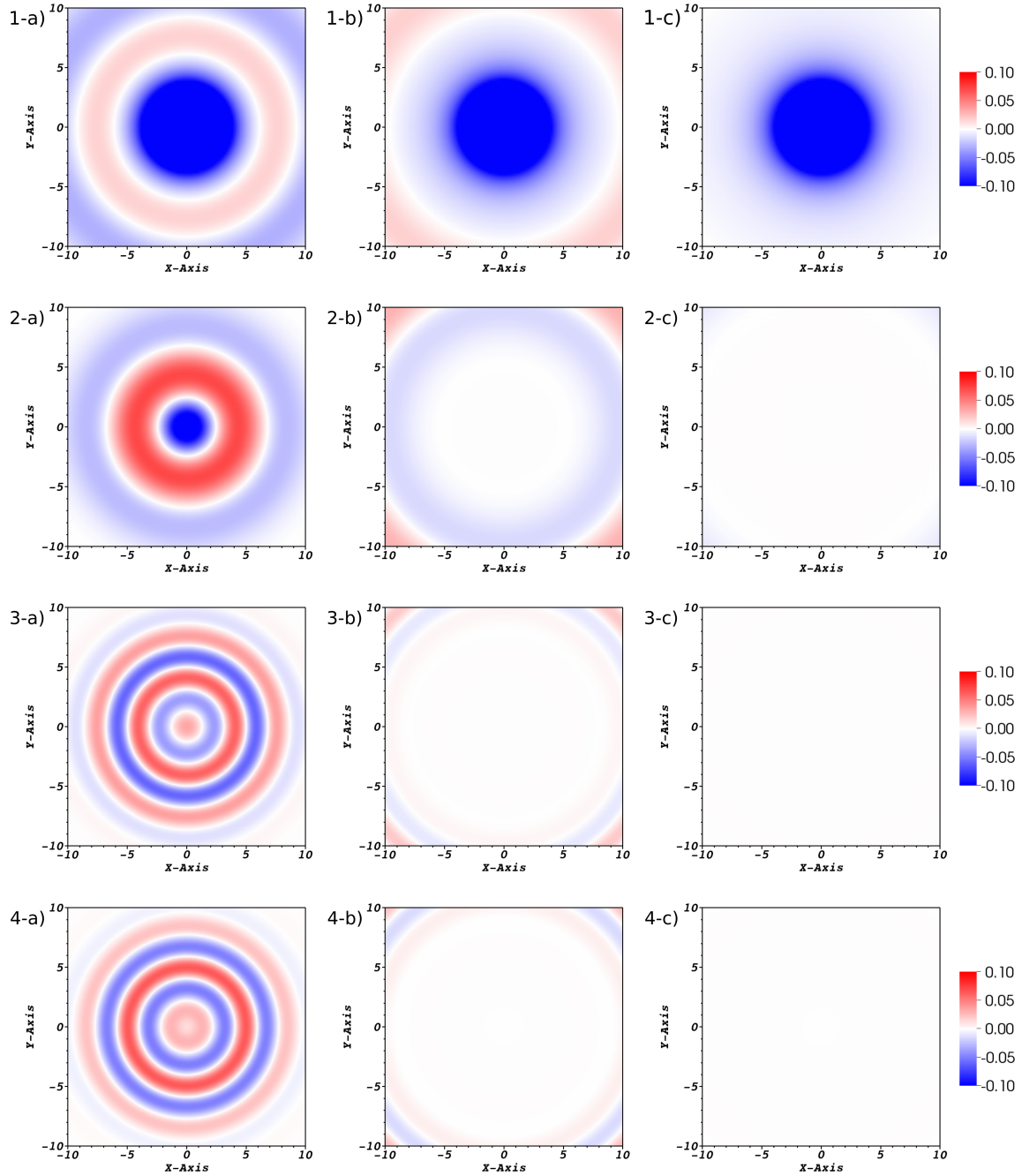


Figure 3.6: Contour snapshots along the xy -plane of the electric field in z -direction for the electromagnetic field propagation using the four external currents of Eqs. (3.3.4)-(3.4.51). The first panels 1-4 a) show the electric field at time $t = 16.0$. The arising spherical waves move radially to the outside, which is illustrated in panels 1-4 b) at $t = 25.0$. The last snapshots in panels 1-4 c) taken at $t = 30.0$ visualize that the electric fields return to zero after the current pulse. An exception is the first one, where the permanent charge density causes a corresponding static electric field.

In the above examples the question arises, what kind of field, i.e., longitudinal or transverse, leads to the outgoing waves or localized field inside the simulation box. Therefore

in the following, we decompose the Maxwell's equations in Riemann-Silberstein representation into a longitudinal and transverse set of equations.

Due to the continuity equation, a given external current density leads to an implicit motion of charge, which also ensures that the Maxwell constraint, i.e., the two Gauß laws hold. The continuity equation relates the current density and charge density by [75]

$$\vec{\nabla} \cdot \vec{j}(\vec{r}, t) = -\frac{\partial}{\partial t} \rho(\vec{r}, t). \quad (3.3.19)$$

Without loss of generality, the current density can be split via the Helmholtz decomposition into a longitudinal component $\vec{j}_{\parallel}(\vec{r}, t)$ and a transverse one $\vec{j}_{\perp}(\vec{r}, t)$ [75]

$$\vec{j}(\vec{r}, t) = \vec{j}_{\parallel}(\vec{r}, t) + \vec{j}_{\perp}(\vec{r}, t). \quad (3.3.20)$$

Using the Helmholtz decomposition leads to

$$\vec{\nabla} \cdot \vec{j}_{\perp}(\vec{r}, t) = 0, \quad \vec{\nabla} \cdot \vec{j}_{\parallel}(\vec{r}, t) = -\frac{\partial}{\partial t} \rho(\vec{r}, t). \quad (3.3.21)$$

As a consequence, we split the Riemann-Silberstein current density $\mathcal{J}(\vec{r}, t)$ into the longitudinal Riemann-Silberstein part $\mathcal{J}_{\parallel}(\vec{r}, t)$, build by $\vec{j}_{\parallel}(\vec{r}, t)$, and the transverse one $\mathcal{J}_{\perp}(\vec{r}, t)$ using $\vec{j}_{\perp}(\vec{r}, t)$. Taking the Riemann-Silberstein current density $\mathcal{Q}(\vec{r}, t)$, Eq. (3.3.19) is equivalent to

$$\mathcal{D} \cdot \mathcal{J}(\vec{r}, t) = \mathcal{D} \cdot \mathcal{J}_{\parallel}(\vec{r}, t) = -\frac{\partial}{\partial t} \mathcal{Q}(\vec{r}, t). \quad (3.3.22)$$

Using Eq. (2.4.9) leads to

$$\mathcal{Q}(\vec{r}, t) = \mathcal{Q}(\vec{r}, t_0) - \int_{t_0}^t d\tau \mathcal{D} \cdot \mathcal{J}_{\parallel}(\vec{r}, \tau) = \mathcal{Q}(\vec{r}, t_0) + \int_{t_0}^t d\tau \frac{\partial}{\partial t} \mathcal{Q}(\vec{r}, \tau). \quad (3.3.23)$$

Since the Riemann-Silberstein Maxwell's Eqs. (1.1.38) and (1.1.40) are linear and the continuity equation has to hold, we can separate the field equations into longitudinal and transverse equations with $\mathcal{F} = \mathcal{F}_{\parallel} + \mathcal{F}_{\perp}$, $\mathcal{D} \cdot \mathcal{F}_{\parallel} = \mathcal{Q}$, and $\mathcal{D} \cdot \mathcal{F}_{\perp} = 0$

$$\mathcal{D} \cdot \mathcal{F}_{\parallel}(\vec{r}, t) = \mathcal{Q}(\vec{r}, t) = \mathcal{Q}(\vec{r}, t_0) - \int_{t_0}^t d\tau \mathcal{D} \cdot \mathcal{J}_{\parallel}(\vec{r}, \tau), \quad (3.3.24)$$

$$i\hbar \frac{\partial}{\partial t} \mathcal{F}_{\parallel}(\vec{r}, t) = \mathcal{H} \mathcal{F}_{\parallel}(\vec{r}, t) - i\hbar \mathcal{J}_{\parallel}(\vec{r}, t), \quad (3.3.25)$$

$$\mathcal{D} \cdot \mathcal{F}_{\perp}(\vec{r}, t) = 0, \quad (3.3.26)$$

$$i\hbar \frac{\partial}{\partial t} \mathcal{F}_{\perp}(\vec{r}, t) = \mathcal{H} \mathcal{F}_{\perp}(\vec{r}, t) - i\hbar \mathcal{J}_{\perp}(\vec{r}, t). \quad (3.3.27)$$

According to Eq. (3.3.9) we introduce the two auxiliary six-component Riemann-Silberstein vectors $\mathcal{F}_{\mathcal{J}_{\parallel}}(\vec{r}, t)$ and $\mathcal{F}_{\mathcal{J}_{\perp}}(\vec{r}, t)$

$$\mathcal{F}_{\mathcal{J}_{\parallel}}(\vec{r}, t) = \int_{t_0}^t d\tau \mathcal{J}_{\parallel}(\vec{r}, \tau), \quad (3.3.28)$$

$$\mathcal{F}_{\mathcal{J}_{\perp}}(\vec{r}, t) = \int_{t_0}^t d\tau \mathcal{J}_{\perp}(\vec{r}, \tau), \quad (3.3.29)$$

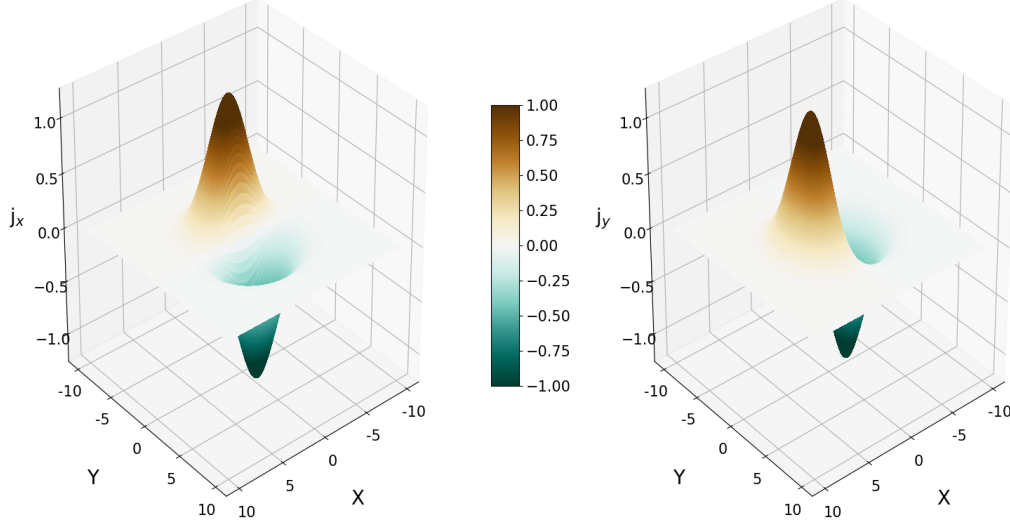


Figure 3.7: Spatial distribution of a transverse current density along the xy -plane. The figure on the right-hand side shows the x -component of the current density vector, whereas the figure on the left-hand side illustrates the y -component.

which are longitudinal respectively transverse. In terms of these Riemann-Silberstein vectors, Eqs. (3.3.25)-(3.3.27) become

$$i\hbar \frac{\partial}{\partial t} \left(\mathcal{F}_{\parallel}(\vec{r}, t) + \mathcal{F}_{\mathcal{J}_{\parallel}}(\vec{r}, t) \right) = \mathcal{H} \mathcal{F}_{\parallel}(\vec{r}, t) , \quad (3.3.30)$$

$$i\hbar \frac{\partial}{\partial t} \left(\mathcal{F}_{\perp}(\vec{r}, t) + \mathcal{F}_{\mathcal{J}_{\perp}}(\vec{r}, t) \right) = \mathcal{H} \mathcal{F}_{\perp}(\vec{r}, t) . \quad (3.3.31)$$

As a consequence, the charge density and the longitudinal part of the current density contribute to the longitudinal Riemann-Silberstein vector, whereas only the transverse current density causes a transverse electromagnetic field. Additionally, due to the continuity equation, a longitudinal current implies always a motion of charge, which can be obtained only by inspecting the underlying electromagnetic field. In turn, a transverse current density means that although the current density can change in time, there is no motion of charge and the charge density stays always constant.

Using our previous considerations for Figure 3.6 means that only the transverse part of the total current leads to the observed outgoing waves in all four cases. In contrast, the longitudinal part of the current density causes the localized electromagnetic field. This can only be seen in Figure 3.6 1-a) to 1-c) since the corresponding current density flows only into the positive z -direction. The remaining three current densities in 2-4 have a reverse current that moves the charge density almost back into its initial state at the end of the current pulse.

To investigate the relation of transverse and longitudinal contributions further, we show in the following two simulations with one longitudinal and one transverse current density.

As longitudinal $\vec{j}_{\text{long}}(\vec{r}, t)$ and transverse $\vec{j}_{\text{trans}}(\vec{r}, t)$ current densities we select

$$\vec{j}_{\text{long}}(\vec{r}, t) = \vec{j}_{\text{long},0}(\vec{r}) \exp\left(-\frac{(t-10.0)^2}{8}\right), \quad (3.3.32)$$

$$\vec{j}_{\text{trans}}(\vec{r}, t) = \vec{j}_{\text{trans},0}(\vec{r}) \exp\left(-\frac{(t-10.0)^2}{8}\right), \quad (3.3.33)$$

with

$$\vec{j}_{\text{long},0}(\vec{r}) = \begin{pmatrix} -x \\ -y \\ -z \end{pmatrix} \exp\left(\frac{-x^2 - y^2 - z^2}{2}\right), \quad (3.3.34)$$

$$\vec{j}_{\text{trans},0}(\vec{r}) = \begin{pmatrix} -y \\ x \\ 0 \end{pmatrix} \exp\left(\frac{-x^2 - y^2 - z^2}{2}\right). \quad (3.3.35)$$

To illustrate the spatial distribution of the current density we plot the x- and y-component of the transverse current $\vec{j}_{\text{trans},0}(\vec{r})$ in Figure 3.7. The z-component for the transverse current is zero and the shape of all components of the longitudinal current density are very similar to the transverse ones presented in Figure 3.7 and only differ in their orientation, so that we do not illustrate them. Using the same simulation parameters as in Sec. 3.3.1, we run the two longitudinal and transverse current simulations. The results in Figure 3.8 for the longitudinal case agree with our previous considerations, where the current density causes only a localized field without any radiation. The plot sequence for a) with $t = 7.0$, b) with $t = 10.0$, and c) with $t = 30.0$ shows that the electric field increases in time without any outgoing signal. In contrast, the transverse snapshot sequence in Figure 3.9 demonstrate a radial anti-symmetric wave form that propagates to the outside and leaves almost no localized field inside the simulation box. In panel a) at time $t = 16.0$ the wave is still inside the box, and almost outside the plot section at time $t = 25.0$ in panel b).

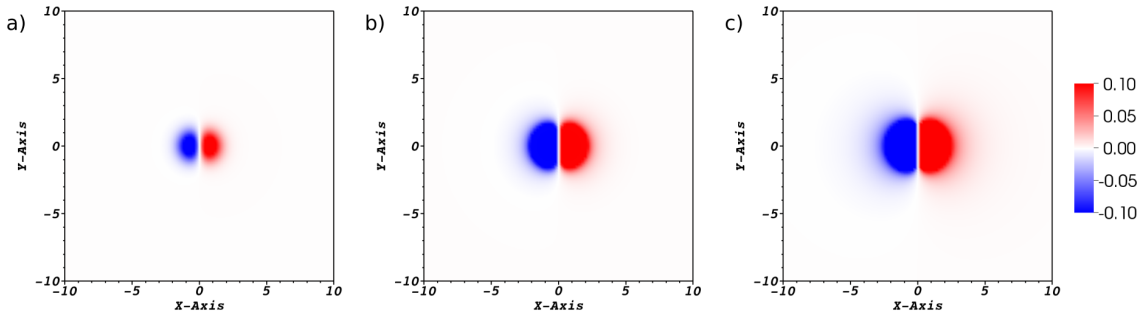


Figure 3.8: Snapshots of the electric field in z-direction for the longitudinal current density at times $t = 7.0$, $t = 10.0$ and $t = 30.0$.

Taking Eq. (3.3.19) for the longitudinal current density $\vec{j}_{\text{long}}(\vec{r}, t)$ gives the charge density with

$$\rho_{\text{long}}(\vec{r}, t) \approx \sqrt{2\pi} e^{-\frac{1}{2}(-x^2 - y^2 - z^2)} (-3 + x^2 + y^2 + z^2) \left[\text{Erf}\left(\frac{t-10.0}{2\sqrt{2}}\right) + 1 \right], \quad (3.3.36)$$

that corresponds to the electric field snapshots in Figure 3.8. In turn, the charge density for the transverse current density $\vec{j}_{\text{trans}}(\vec{r}, t)$ is constant for all three snapshots in Figure 3.9.

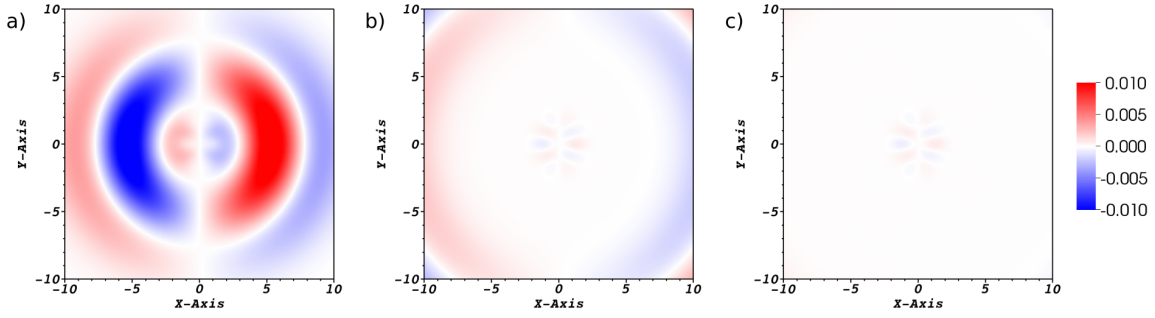


Figure 3.9: Snapshots of the electric field in z-direction for the transverse current density at times $t = 16.0$, $t = 25.0$ and $t = 30.0$.

In a last plot in Figure 3.10, we evaluate the electric field, the magnetic field for different relevant directions, as well as the absolute value of the fields for the grid point $(5.0,0,0)$. Panel a) shows only the time-dependent part of the current pulse which follows the intensity behavior of the external current. In panel b) both graphs give the electric field in z-direction, whereas panel c) shows the corresponding magnetic field in the y-direction. Comparing all four curves emphasizes the wave character of the transverse current propagation, where the electric field and the magnetic field are very similar in shape and magnitude for our selected unit system. The longitudinal current density causes only an electric field, which can be seen in panel e), where the absolute value of the magnetic field is plotted and returns zero for the longitudinal current run. In addition, panel d) illustrates the absolute value of the electric field, which confirms, that the main contribution of the electric field is polarized along the z-axis.

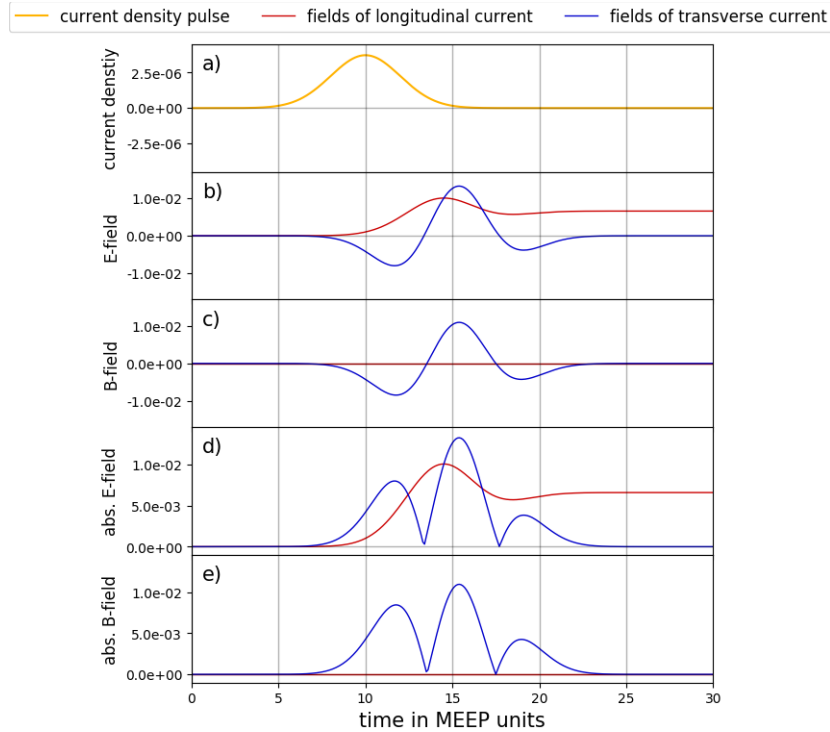


Figure 3.10: Electric and magnetic field reaction in z-direction for the longitudinal and transverse current density detected at point $(5.0,0,0)$.

The decomposition of the electromagnetic field into longitudinal and transverse fields with different radiative features becomes an important ingredient when we consider later the electromagnetic fields in quantum electrodynamics (QED). In QED using Coulomb gauge, the longitudinal matter current density operator couples only to the quantized longitudinal field, whereas the transverse matter current density operator couples to the quantized transverse field. We focus on this aspect in more detail by using the longitudinal-transverse field decomposition in chapter 4.

3.4 Maxwell boundaries

To properly define different boundary conditions, we already introduced in Sec. (3.1.1) and illustrated in Figure 3.1 different regions in the simulation box which we discuss here more in detail. The inner free Maxwell-propagation region obeys the physical Maxwell's equations whereas the outer boundary region obeys specified Maxwell's equations to fulfill the appropriate simulation condition. In the following sections we introduce two different schemes for absorbing boundaries to simulate open Maxwell systems, where outgoing Maxwell fields are damped with almost no reflections. For example in Sec. 3.3.1, we have shown an external current density in the box center that causes Maxwell fields which are moving to the box limits. In case of absorbing boundaries, we can use a much smaller simulation box to get the same results. As a third boundary option, we show incident wave boundaries to simulate incident plane waves, which arise at the boundaries and propagate as free plane waves through the box, if the whole box describes vacuum. In contrast, in presence of a linear medium inside the simulation box the electromagnetic waves couple and scatter. To avoid further scatter and reflection effects at the box boundaries, we have to combine the incident wave boundaries with the absorbing boundaries which we employ as another boundary option.

3.4.1 Absorbing boundaries by mask function

A simple method to implement and simulate absorbing boundaries is the mask absorption method, in which the Riemann-Silberstein vector is multiplied by a real mask function. The simulation box is split into two regions as shown in Figure 3.1, an inner free propagation region and an outer absorbing boundary region. Consequently the mask function is always equal to one inside the free propagation region. The shape of the weight function in the outer boundary region has to be chosen such that it simulates absorption in a proper way. It is clear that the mask function has to be continuous at the transition from the edge to the inner region. In addition to the simulation box limit, the mask function has to damp the Riemann-Silberstein vector to zero along the boundaries. To avoid almost all reflection and scatter effects in the free propagation region, the negative damping slope has to be smooth. A possible mask function $f_{\text{mask}}^{\text{1D}}(u)$ in one dimension that fulfills all that conditions is given by

$$f_{\text{mask}}^{\text{1D}}(u) = \begin{cases} 1 & \text{for } |u| \leq b_u \\ 1 - \sin\left(\frac{\pi|u-b_u|}{2|L_u-b_u|}\right)^2 & \text{for } |u| > b_u, \quad |u| \leq L_u, \end{cases} \quad (3.4.1)$$

where u represents one of the three possible dimensions x, y, z , and the length b_u denotes the limit of the inner free propagation box and L_u the outer simulation box limit. The total shape of the mask function $f_{\text{mask}}^{\text{1D}}(x)$ with box limits b_x and L_x is illustrated in figure (3.11).

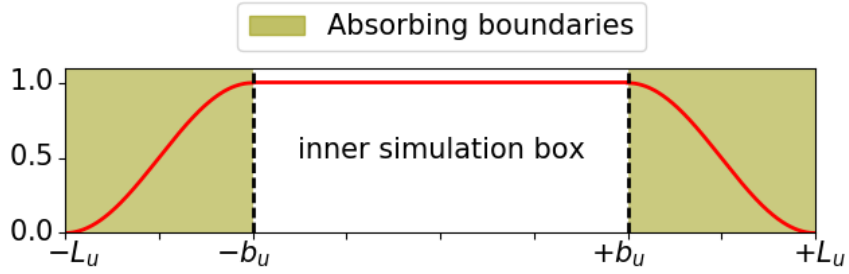


Figure 3.11: Mask function along a cartesian axis $u = x, y, z$ with its characteristic profile. Inside the inner simulation box limit $[-b_u, b_u]$ the mask function is equal to one, whereas the function decreases smoothly to zero in the mask boundary region $[-L_u, -b_u[$, and $] + b_u, +L_u]$. The decreasing function has a turning point and is point-symmetric to that point.

For numerical grids in more than one dimension, the total mask function is simply a product of all corresponding one-dimensional mask functions. Hence, the two-dimensional and three-dimensional mask functions $f_{\text{mask}}^{2\text{D}}(x, y)$ and $f_{\text{mask}}^{3\text{D}}(x, y, z)$ are given by

$$f_{\text{mask}}^{2\text{D}}(x, y) = f_{\text{mask}}^{1\text{D}}(x) \cdot f_{\text{mask}}^{1\text{D}}(y) \quad (3.4.2)$$

$$f_{\text{mask}}^{3\text{D}}(x, y, z) = f_{\text{mask}}^{1\text{D}}(x) \cdot f_{\text{mask}}^{1\text{D}}(y) \cdot f_{\text{mask}}^{1\text{D}}(z) \quad (3.4.3)$$

A three-dimensional contour plot of a two-dimensional mask function $f_{\text{mask}}^{2\text{D}}(x, y)$ or a cut through a three-dimensional mask function $f_{\text{mask}}^{3\text{D}}(x, y, z)$ with constant z is shown in figure (3.12). It can be seen in this figure that due to the factorization of the mask function with corresponding one-dimensional mask functions, the overlap regions are continuous and smooth. Furthermore, the damping in the vertex regions is stronger than at the edges of the box, which avoids scatter effects especially in those more sensitive parts of the simulation box.

In case of a mask function as defined in equation (3.4.1), it is clear that only the distance of $|L_x - b_x|$ determines the shape of the function and therefore the ability to absorb the outgoing electromagnetic fields. Consequently, for larger absorbing boundary regions, the decreasing slope of the mask function is weaker and the efficiency of the simulated absorbing boundaries increases.

3.4.2 Absorbing boundaries by perfectly matched layer

A more accurate method for open Maxwell systems is the perfectly matched layer (PML) absorbing boundary condition. We have implemented such a PML analogous to the Berènger layer for the Yee finite difference time domain algorithm [65, 87], but now modified for the Riemann-Silberstein Maxwell propagation. The basic idea of the Berènger layer is to complement Maxwell's equations with an artificial lossy layer, which is described by a non-physical electric conductivity σ_{el} and a non-physical magnetic conductivity σ_{mag} . These conductivities are defined such as to yield minimal reflections at the boundaries, but have no physical meaning otherwise. The loss due to the conductivity parameters is linear in the corresponding $\vec{E}(\vec{r}, t)$ and $\vec{B}(\vec{r}, t)$. Therefore, the modified k-vector component of Faraday's and Ampère's laws without current density takes with Eqs. (1.1.10) and

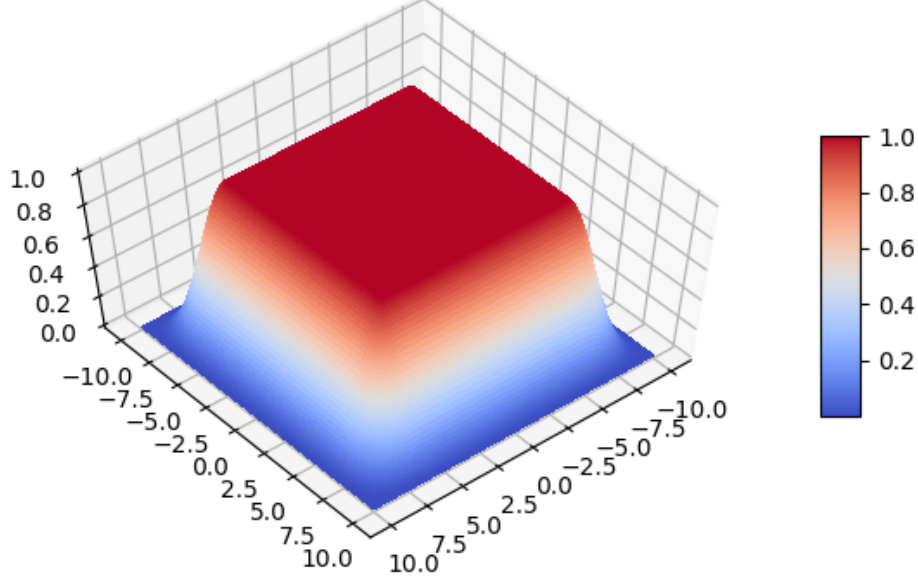


Figure 3.12: A three-dimensional contour plot of the mask function on the x-y plane. The inner plateau with the mask value equal to one marks the inner free Maxwell propagation region. The plot shows the smooth slope towards zero in the outer region and additionally the round corners at the overlapping x and y mask regions.

(1.1.11) the form

$$\partial_t B_k(\vec{r}, t) = - \sum_{l,m} \epsilon_{klm} \partial_l E_m(\vec{r}, t) - \sigma_{\text{mag}} B_k(\vec{r}, t), \quad (3.4.4)$$

$$\partial_t E_k(\vec{r}, t) = \frac{1}{\epsilon_0 \mu_0} \sum_{l,m} \epsilon_{klm} \partial_l B_m(\vec{r}, t) - \sigma_{\text{el}} E_k(\vec{r}, t), \quad (3.4.5)$$

where ϵ_{klm} denotes the Levi-Civita symbol. We note here, that the PML is in principle not restricted to vacuum conditions but also valid for other homogeneous dielectric conditions. In other words, the Riemann-Silberstein PML that we have implemented also works in a linear medium, but with the constraint that $\epsilon(\vec{r}, t)$ and $\mu(\vec{r}, t)$, and consequently $c(\vec{r}, t)$ are constant at the border and inside the boundaries for all time. According to Eq. (1.2.29) with

$$\epsilon(\vec{r}, t) = \epsilon, \quad \mu(\vec{r}, t) = \mu, \quad \Rightarrow \vec{F}_{\pm, \text{lm}}(\vec{r}, t) = \vec{F}_{\pm}(\vec{r}, t) = \sqrt{\frac{\epsilon}{2}} \vec{E}(\vec{r}, t) + i \sqrt{\frac{1}{2\mu}} \vec{B}(\vec{r}, t) \quad (3.4.6)$$

and

$$\vec{\nabla} \epsilon = \vec{\nabla} \mu = \dot{\epsilon} = \dot{\mu} = 0, \quad c = \frac{1}{\sqrt{\epsilon \mu}} \quad (3.4.7)$$

Eqs. (3.4.4) and (3.4.5) combined into the Riemann-Silberstein representation yields

$$i\hbar \frac{\partial}{\partial t} \vec{F}_{\pm}(\vec{r}, t) = \pm \hbar c \vec{\nabla} \times \vec{F}_{\pm}(\vec{r}, t) - i\hbar \sigma_e \frac{1}{2} \left(\vec{F}_+(\vec{r}, t) + \vec{F}_-(\vec{r}, t) \right) \mp i\hbar \sigma_m \frac{1}{2} \left(\vec{F}_+(\vec{r}, t) - \vec{F}_-(\vec{r}, t) \right). \quad (3.4.8)$$

Transforming Eq. (1.1.6)-(1.1.2) to frequency domain, and using the Riemann-Silberstein vector in frequency space $\vec{\tilde{F}}_{\pm}(\vec{r}, \omega)$ with

$$\vec{\tilde{F}}_{\pm}(\vec{r}, \omega) = \int dt e^{i\omega t} \vec{F}_{\pm}(\vec{r}, t) \quad (3.4.9)$$

leads to the underlying Riemann-Silberstein Maxwell's equation for the k^{th} component in time-harmonic form [96, 97] of Eqs. (3.4.5) and (3.4.4) for the absorbing layer

$$\begin{aligned} -\omega \hbar \vec{\tilde{F}}_{\pm, k}(\vec{r}, \omega) &= \mp \hbar c \sum_{l, m} \epsilon_{klm} \partial_l \vec{\tilde{F}}_{\pm, m}(\vec{r}, \omega) \\ &\quad - i \hbar \frac{1}{2} \sigma_e \left(\vec{\tilde{F}}_{+, k}(\vec{r}, \omega) + \vec{\tilde{F}}_{-, k}(\vec{r}, \omega) \right) \\ &\quad \mp i \hbar \frac{1}{2} \sigma_{\text{mag}} \left(\vec{\tilde{F}}_{+, k}(\vec{r}, \omega) - \vec{\tilde{F}}_{-, k}(\vec{r}, \omega) \right), \end{aligned} \quad (3.4.10)$$

where the first term on the right-hand side describes the curl operation. The principle of a PML is to propagate the respective field components in the absorbing boundary region which are necessary for a correct propagation inside the free Maxwell region, and to damp the remaining components without causing strong reflections back into the free Maxwell region. For this purpose, Berenger's method splits up Maxwell's equations for each direction in two equations which form the basis for the so-called split PML [98, 87, 65]. The field component in k -direction is split into one component for l and one for m with $k \neq l \neq m$, so that the vector k component $\vec{\tilde{F}}_{\pm}^k$ is given by

$$\vec{\tilde{F}}_{\pm, k}(\vec{r}, \omega) = \vec{\tilde{F}}_{\pm, k, (l)}(\vec{r}, \omega) + \vec{\tilde{F}}_{\pm, k, (m)}(\vec{r}, \omega). \quad (3.4.11)$$

The field component $\vec{\tilde{F}}_{\pm, k}$ is split such that the $\vec{\tilde{F}}_{\pm, k, (l)}$ part is responsible for the field propagation parallel to direction l and accordingly $\vec{\tilde{F}}_{\pm, k, (m)}$ parallel to direction m . In other words, there are two separate propagations which simulate only the free propagation along the corresponding direction. Thus, one propagation could be where the field enters the PML region while the other part is still in the free propagation box. The damping of the fields is applied by the electric and magnetic conductivities σ_{el} , σ_{mag} which are artificially modified and depend now on the splitted direction, i.e., l direction for $\vec{\tilde{F}}_{\pm, k, (l)}$, not the field direction. In addition, each equation only contains one part of the two curl terms. Applying all these considerations to the six components of the Maxwell's equations in Riemann-Silberstein form yields twelve relations for the PML. Explicitly, the two equations for the x component in equation (3.4.10) are

$$\begin{aligned} -\omega \hbar \vec{\tilde{F}}_{\pm, x, (y)}(\vec{r}, \omega) &= \pm \hbar c \partial_y \left(\vec{\tilde{F}}_{\pm, z, (x)}(\vec{r}, \omega) + \vec{\tilde{F}}_{\pm, z, (y)}(\vec{r}, \omega) \right) \\ &\quad - i \hbar \frac{1}{2} \sigma_{\text{el}, (y)} \left(\vec{\tilde{F}}_{+, x, (y)}(\vec{r}, \omega) + \vec{\tilde{F}}_{-, x, (y)}(\vec{r}, \omega) \right) \\ &\quad \mp i \hbar \frac{1}{2} \sigma_{\text{mag}, (y)} \left(\vec{\tilde{F}}_{+, x, (y)}(\vec{r}, \omega) - \vec{\tilde{F}}_{-, x, (y)}(\vec{r}, \omega) \right), \end{aligned} \quad (3.4.12)$$

$$\begin{aligned} -\omega \hbar \vec{\tilde{F}}_{\pm, x, (z)}(\vec{r}, \omega) &= \mp \hbar c \partial_z \left(\vec{\tilde{F}}_{\pm, y, (x)}(\vec{r}, \omega) + \vec{\tilde{F}}_{\pm, y, (z)}(\vec{r}, \omega) \right) \\ &\quad - i \hbar \frac{1}{2} \sigma_{\text{el}, (z)} \left(\vec{\tilde{F}}_{+, x, (z)}(\vec{r}, \omega) + \vec{\tilde{F}}_{-, x, (z)}(\vec{r}, \omega) \right) \\ &\quad \mp i \hbar \frac{1}{2} \sigma_{\text{mag}, (z)} \left(\vec{\tilde{F}}_{+, x, (z)}(\vec{r}, \omega) - \vec{\tilde{F}}_{-, x, (z)}(\vec{r}, \omega) \right), \end{aligned} \quad (3.4.13)$$

for the y component

$$\begin{aligned}
-\omega\hbar\tilde{F}_{\pm,y,(z)}(\vec{r},\omega) &= \pm\hbar c\partial_z\left(\tilde{F}_{\pm,x,(y)}(\vec{r},\omega)+\tilde{F}_{\pm,x,(z)}(\vec{r},\omega)\right) \\
&\quad -i\hbar\frac{1}{2}\sigma_{\text{el},(z)}\left(\tilde{F}_{+,y,(z)}(\vec{r},\omega)+\tilde{F}_{-,y,(z)}(\vec{r},\omega)\right) \\
&\quad \mp i\hbar\frac{1}{2}\sigma_{\text{mag},(z)}\left(\tilde{F}_{+,y,(z)}(\vec{r},\omega)-\tilde{F}_{-,y,(z)}(\vec{r},\omega)\right),
\end{aligned} \tag{3.4.14}$$

$$\begin{aligned}
-\omega\hbar\tilde{F}_{\pm,y,(x)}(\vec{r},\omega) &= \mp\hbar c\partial_x\left(\tilde{F}_{\pm,z,(x)}(\vec{r},\omega)+\tilde{F}_{\pm,z,(y)}(\vec{r},\omega)\right) \\
&\quad -i\hbar\frac{1}{2}\sigma_{\text{el},(x)}\left(\tilde{F}_{+,y,(x)}(\vec{r},\omega)+\tilde{F}_{-,y,(x)}(\vec{r},\omega)\right) \\
&\quad \mp\hbar i\frac{1}{2}\sigma_{\text{mag},(x)}\left(\tilde{F}_{+,y,(x)}(\vec{r},\omega)-\tilde{F}_{-,y,(x)}(\vec{r},\omega)\right),
\end{aligned} \tag{3.4.15}$$

and for the z component

$$\begin{aligned}
-\omega\hbar\tilde{F}_{\pm,z,(x)}(\vec{r},\omega) &= \pm\hbar c\partial_x\left(\tilde{F}_{\pm,y,(x)}(\vec{r},\omega)+\tilde{F}_{\pm,y,(z)}(\vec{r},\omega)\right) \\
&\quad -i\hbar\frac{1}{2}\sigma_{\text{el},(x)}\left(\tilde{F}_{+,z,(x)}(\vec{r},\omega)+\tilde{F}_{-,z,(x)}(\vec{r},\omega)\right) \\
&\quad \mp i\hbar\frac{1}{2}\sigma_{\text{mag},(x)}\left(\tilde{F}_{+,z,(x)}(\vec{r},\omega)-\tilde{F}_{-,z,(x)}(\vec{r},\omega)\right),
\end{aligned} \tag{3.4.16}$$

$$\begin{aligned}
-\omega\hbar\tilde{F}_{\pm,z,(y)}(\vec{r},\omega) &= \mp\hbar c\partial_y\left(\tilde{F}_{\pm,x,(y)}(\vec{r},\omega)+\tilde{F}_{\pm,x,(z)}(\vec{r},\omega)\right) \\
&\quad -i\hbar\frac{1}{2}\sigma_{\text{el},(y)}\left(\tilde{F}_{+,z,(y)}(\vec{r},\omega)+\tilde{F}_{-,z,(y)}(\vec{r},\omega)\right) \\
&\quad \mp i\hbar\frac{1}{2}\sigma_{\text{mag},(y)}\left(\tilde{F}_{+,z,(y)}(\vec{r},\omega)-\tilde{F}_{-,z,(y)}(\vec{r},\omega)\right).
\end{aligned} \tag{3.4.17}$$

Similar to Berènger's split field PML derivation for the Yee-Algorithm, we want to include also in our case the frequency ω and the electric and magnetic conductivity σ_{el} and σ_{mag} in a factor multiplied by the corresponding split field [98, 87, 65] before we recombine the two split field equations. Using the two factors

$$\tilde{\eta}_{(l)}(\omega) = -\frac{i\omega(\sigma_{\text{el},(l)} + \sigma_{\text{mag},(l)} - 2i\omega)}{2(\sigma_{\text{el},(l)} - i\omega)(\sigma_{\text{mag},(l)} - i\omega)}, \tag{3.4.18}$$

$$\tilde{\xi}_{(l)}(\omega) = \frac{i\omega(\sigma_{\text{mag},(l)} - \sigma_{\text{el},(l)})}{2(\sigma_{\text{el},(l)} - i\omega)(\sigma_{\text{mag},(l)} - i\omega)}, \tag{3.4.19}$$

the system of the split equations in Eqs. (3.4.12)-(3.4.17) can be rearranged equivalently to

$$\begin{aligned}
-\omega\hbar\tilde{F}_{\pm,x,(y)}(\vec{r},\omega) &= \pm\hbar c\tilde{\eta}_{(y)}(\omega)\partial_y\left(\tilde{F}_{\pm,z,(x)}(\vec{r},\omega)+\tilde{F}_{\pm,z,(y)}(\vec{r},\omega)\right) \\
&\quad \pm\hbar c\tilde{\xi}_{(y)}(\omega)\partial_y\left(\tilde{F}_{\mp,z,(x)}(\vec{r},\omega)+\tilde{F}_{\mp,z,(y)}(\vec{r},\omega)\right),
\end{aligned} \tag{3.4.20}$$

$$\begin{aligned}
-\omega\hbar\tilde{F}_{\pm,x,(z)}(\vec{r},\omega) &= \mp\hbar c\tilde{\eta}_{(z)}(\omega)\partial_z\left(\tilde{F}_{\pm,y,(x)}(\vec{r},\omega)+\tilde{F}_{\pm,y,(z)}(\vec{r},\omega)\right) \\
&\quad \mp\hbar c\tilde{\xi}_{(z)}(\omega)\partial_z\left(\tilde{F}_{\pm,y,(x)}(\vec{r},\omega)+\tilde{F}_{\pm,y,(z)}(\vec{r},\omega)\right)
\end{aligned} \tag{3.4.21}$$

for the x component, and

$$\begin{aligned}
-\omega\hbar\tilde{F}_{\pm,y,(z)}(\vec{r},\omega) &= \pm\hbar c\tilde{\eta}_{(z)}(\omega)\partial_z\left(\tilde{F}_{\pm,x,(y)}(\vec{r},\omega)+\tilde{F}_{\pm,x,(z)}(\vec{r},\omega)\right) \\
&\quad \pm\hbar c\tilde{\xi}_{(z)}(\omega)\partial_z\left(\tilde{F}_{\mp,x,(y)}(\vec{r},\omega)+\tilde{F}_{\mp,x,(z)}(\vec{r},\omega)\right),
\end{aligned} \tag{3.4.22}$$

$$\begin{aligned}
-\omega \hbar \tilde{F}_{\pm,y,(x)}(\vec{r}, \omega) &= \mp \hbar c \tilde{\eta}_{(x)}(\omega) \partial_x \left(\tilde{F}_{\pm,z,(x)}(\vec{r}, \omega) + \tilde{F}_{\pm,z,(y)}(\vec{r}, \omega) \right) \\
&\mp \hbar c \tilde{\xi}_{(x)}(\omega) \partial_x \left(\tilde{F}_{\pm,z,(x)}(\vec{r}, \omega) + \tilde{F}_{\pm,z,(y)}(\vec{r}, \omega) \right)
\end{aligned} \tag{3.4.23}$$

for the y component, and

$$\begin{aligned}
-\omega \hbar \tilde{F}_{\pm,z,(x)}(\vec{r}, \omega) &= \pm \hbar c \tilde{\eta}_{(x)}(\omega) \partial_x \left(\tilde{F}_{\pm,y,(x)}(\vec{r}, \omega) + \tilde{F}_{\pm,y,(z)}(\vec{r}, \omega) \right) \\
&\pm \hbar c \tilde{\xi}_{(x)}(\omega) \partial_x \left(\tilde{F}_{\mp,y,(x)}(\vec{r}, \omega) + \tilde{F}_{\mp,y,(z)}(\vec{r}, \omega) \right),
\end{aligned} \tag{3.4.24}$$

$$\begin{aligned}
-\omega \hbar \tilde{F}_{\pm,z,(y)}(\vec{r}, \omega) &= \mp \hbar c \tilde{\eta}_{(y)}(\omega) \partial_y \left(\tilde{F}_{\pm,x,(y)}(\vec{r}, \omega) + \tilde{F}_{\pm,x,(z)}(\vec{r}, \omega) \right) \\
&\mp \hbar c \tilde{\xi}_{(y)}(\omega) \partial_y \left(\tilde{F}_{\pm,x,(y)}(\vec{r}, \omega) + \tilde{F}_{\pm,x,(z)}(\vec{r}, \omega) \right)
\end{aligned} \tag{3.4.25}$$

for the z component. Finally, adding each of the two Eqs. (3.4.20)-(3.4.21), Eqs. (3.4.23)-(3.4.22), and Eqs. (3.4.24)-(3.4.25) using Eq. (3.4.11) yields the PML equations in frequency domain for the Riemann-Silberstein representation

$$\begin{aligned}
-\omega \hbar \begin{pmatrix} \tilde{F}_{+,k}(\vec{r}, \omega) \\ \tilde{F}_{-,k'}(\vec{r}, \omega) \end{pmatrix} &= \hbar \hbar c \begin{pmatrix} \sum_{l,m} \epsilon_{klm} \tilde{\eta}_{(l)}(\omega) \partial_l \tilde{F}_{+,m}(\vec{r}, \omega) \\ \sum_{l',m'} -\epsilon_{klm} \tilde{\eta}_{(l')}(\omega) \partial_{l'} \tilde{F}_{-,m'}(\vec{r}, \omega) \end{pmatrix} \\
&+ \hbar c \begin{pmatrix} \hbar \sum_{l,m} \epsilon_{klm} \tilde{\xi}_{(l)}(\omega) \partial_l \tilde{F}_{-,m}(\vec{r}, \omega) \\ \hbar \sum_{l',m'} -\epsilon_{k'l'm'} \tilde{\xi}_{(l')}(\omega) \partial_{l'} \tilde{F}_{+,m'}(\vec{r}, \omega) \end{pmatrix}.
\end{aligned} \tag{3.4.26}$$

In our PML implementation for simplicity, we do not introduce new correction terms in $\tilde{\eta}^{(l)}$ or $\tilde{\xi}^{(l)}$ to improve the PML and to reduce low-frequency reflections like it is commonly applied for the Yee algorithm [98, 87, 65]. While such extensions are possible in future refinements of our implementation, we found the simple form without correction terms already to provide good absorbance at the boundaries. By back transforming Eq. (3.4.26) from frequency domain into time domain, we arrive at

$$\begin{aligned}
\eta_{(l)}(t) &= \delta(t) - \frac{1}{2} \left(\sigma_{\text{el},(l)} e^{-\sigma_{\text{el},(l)} t} + \sigma_{\text{mag},(l)} e^{-\sigma_{\text{mag},(l)} t} \right) \Theta(t) \\
&= \delta(t) + \zeta(t) \Theta(t),
\end{aligned} \tag{3.4.27}$$

$$\begin{aligned}
\xi_{(l)}(t) &= -\frac{1}{2} \left(\sigma_{\text{el},(l)} e^{-\sigma_{\text{el},(l)} t} - \sigma_{\text{mag},(l)} e^{-\sigma_{\text{mag},(l)} t} \right) \Theta(t) \\
&= \xi(t) \Theta(t).
\end{aligned} \tag{3.4.28}$$

The electric conductivity σ_{el} and the magnetic conductivity σ_{mag} have to be chosen such that the reflection becomes minimal. As is well-known in FDTD [98, 87, 65], the relation between the electric conductivity σ_{el} and the magnetic conductivity σ_{mag} to minimize the reflection coefficient has to obey

$$\frac{\sigma_{\text{el}}}{\epsilon} = \frac{\sigma_{\text{mag}}}{\mu} \tag{3.4.29}$$

at the border between the free Maxwell simulation box and the absorbing boundaries. Using this relation between the two conductivities, it is convenient to use only one conductivity with $\sigma = \sigma_{\text{el}}$, and the updated forms of the expressions $\zeta_{(l)}(t)$, and $\xi_{(l)}(t)$ are

$$\zeta_{(l)}(t) = -\frac{1}{2} \sigma_{(l)} e^{-\sigma_{(l)} t} \left(1 + \frac{\mu}{\epsilon} e^{-(\mu/\epsilon - 1) \sigma_{(l)} t} \right), \tag{3.4.30}$$

$$\xi_{(l)}(t) = -\frac{1}{2}\sigma_{(l)}e^{-\sigma_{(l)}t} \left(1 - \frac{\mu}{\epsilon}e^{-(\mu/\epsilon-1)\sigma_{(l)}t}\right), \quad (3.4.31)$$

As a result, the back transformation of Eq. (3.4.26) becomes

$$\begin{aligned} i\hbar c\partial_0 \begin{pmatrix} F_{+,k}(\vec{r}, t) \\ F_{-,k'}(\vec{r}, t) \end{pmatrix} &= \hbar c \begin{pmatrix} \sum_{l,m} \epsilon_{klm} \left(\delta * \partial_l F_{+,m}(\vec{r}) \right) (t) \\ \sum_{l',m'} -\epsilon_{k'l'm'} \left(\delta * \partial_{l'} F_{-,m'}(\vec{r}) \right) (t) \end{pmatrix} \\ &+ \hbar c \begin{pmatrix} \sum_{l,m} \epsilon_{klm} \left(\zeta_{(l)} * \partial_l F_{+,m}(\vec{r}) \right) (t) \\ \sum_{l',m'} -\epsilon_{k'l'm'} \left(\zeta_{(l')} * \partial_{l'} F_{-,m'}(\vec{r}) \right) (t) \end{pmatrix} \\ &+ \hbar c \begin{pmatrix} \sum_{l,m} \epsilon_{klm} \left(\xi_{(l)} * \partial_l F_{-,m}(\vec{r}) \right) (t) \\ \sum_{l',m'} -\epsilon_{k'l'm'} \left(\xi_{(l')} * \partial_{l'} F_{+,m'}(\vec{r}) \right) (t) \end{pmatrix}. \end{aligned} \quad (3.4.32)$$

which contains several convolutions in time. Whereas the first convolution on the right-hand side in Eq. (3.4.32) is simply

$$\left(\delta * \partial_l F_{\pm,m}(\vec{r}) \right) (t) = \partial_l F_{\pm,m}(\vec{r}, t), \quad (3.4.33)$$

the remaining convolutions are explicitly given by

$$\left(\zeta_{(l)} * \partial_l F_{\pm,m}(\vec{r}) \right) (t) = \int_0^t \zeta_{(l)}(t-\tau) F_{\pm,m}(\vec{r}, \tau) d\tau, \quad (3.4.34)$$

$$\left(\xi_{(l)} * \partial_l F_{\pm,m}(\vec{r}) \right) (t) = \int_0^t \xi_{(l)}(t-\tau) F_{\pm,m}(\vec{r}, \tau) d\tau. \quad (3.4.35)$$

This completes the construction of the PML for our Riemann-Silberstein formulation when we use the curl operation in Eq. (1.1.25) with spin matrices to obtain

$$\begin{aligned} i\hbar c\partial_0 \begin{pmatrix} \vec{F}_+(\vec{r}, t) \\ \vec{F}_-(\vec{r}, t) \end{pmatrix} &= \hbar c \begin{pmatrix} (-i\vec{S} \cdot \vec{\nabla}) \vec{F}_+(\vec{r}, t) \\ (i\vec{S} \cdot \vec{\nabla}) \vec{F}_-(\vec{r}, t) \end{pmatrix} \\ &+ \hbar c \begin{pmatrix} \int_0^t d\tau \left[-i \sum_k \zeta_{(k)}(t-\tau) S_k \partial_k \right] \vec{F}_+(\vec{r}, \tau) \\ \int_0^t d\tau \left[i \sum_k \zeta_{(k)}(t-\tau) S_k \partial_k \right] \vec{F}_-(\vec{r}, \tau) \end{pmatrix} \\ &+ \hbar c \begin{pmatrix} \int_0^t d\tau \left[-i \sum_k \xi_{(k)}(t-\tau) S_k \partial_k \right] \vec{F}_-(\vec{r}, \tau) \\ \int_0^t d\tau \left[i \sum_k \xi_{(k)}(t-\tau) S_k \partial_k \right] \vec{F}_+(\vec{r}, \tau) \end{pmatrix}. \end{aligned} \quad (3.4.36)$$

Since we have already illustrated how to include a linear medium in the Riemann-Silberstein time-evolution in the previous sections, it becomes now straightforward to combine the PML with our existing implementation. Adding the PML expressions to the Riemann-Silberstein Hamiltonian \mathcal{H} in Eq. (1.1.41) and using

$$\mathcal{F}(\vec{r}, t) = \begin{pmatrix} \vec{F}_+(\vec{r}, t) \\ \vec{F}_-(\vec{r}, t) \end{pmatrix}, \quad (3.4.37)$$

we arrive at a propagation scheme with perfectly matched layer boundaries

$$\mathcal{H}_{\text{PML}}(\vec{r}, t) = \mathcal{H}(\vec{r}, t) + \mathcal{G}(\vec{r}, t)\mathcal{F}(\vec{r}, \tau), \quad (3.4.38)$$

where the 6x6 PML operation $\mathcal{G}(\vec{r}, t)\mathcal{F}(\vec{r}, \tau)$ is given by

$$\begin{aligned} \mathcal{G}(\vec{r}, t)\mathcal{F}(\vec{r}, \tau) = & \left[\begin{pmatrix} 1 & 0 \\ 0 & -1 \end{pmatrix}_{2 \times 2} \otimes \left(-i\hbar c \int_0^t d\tau \sum_k [\zeta_{(k)}(t-\tau) S_k \partial_k] \right)_{3 \times 3} \right] \mathcal{F}(\vec{r}, \tau) \\ & + \left[\begin{pmatrix} 0 & 1 \\ -1 & 0 \end{pmatrix}_{2 \times 2} \otimes \left(-i\hbar c \int_0^t d\tau \sum_k [\xi_{(k)}(t-\tau) S_k \partial_k] \right)_{3 \times 3} \right] \mathcal{F}(\vec{r}, \tau). \end{aligned} \quad (3.4.39)$$

The left factor of the second Kronecker product in Eq. (3.4.39) has entries in the off-diagonal, and therefore the two Riemann-Silberstein vectors \vec{F}_\pm always couple in the PML region.

In principle, the PML terms in Eq. (3.4.38) have to be calculated for each time step, which massively increases computational cost. However, taking a closer look at Eqs. (3.4.34) and (3.4.35), we notice that the two functions $\zeta_{(k)}(t-\tau)$ and $\xi_{(k)}(t-\tau)$ contain exponential factors. Therefore it is possible to obtain a rather accurate approximation of the terms by using a recursive-convolution method [99] with finite time steps Δt . The recursive-convolution method allows to express integrals of the form

$$g(t) = \int_0^t d\tau e^{-\alpha(t-\tau)} f_1(t-\tau) f_2(\tau) \quad (3.4.40)$$

in terms of

$$\begin{aligned} g(m\Delta t) &= \int_0^{m\Delta t} d\tau e^{-\alpha((m+1)\Delta t - \tau)} f_1((m+1)\Delta t - \tau) f_2(\tau) \\ &= e^{-\alpha\Delta t} \underbrace{\int_0^{(m-1)\Delta t} d\tau e^{-\alpha((m-1)\Delta t - \tau)} f_1((m-1)\Delta t - \tau) f_2(\tau)}_{g((m-1)\Delta t)} \\ &\quad + \int_{(m-1)\Delta t}^{m\Delta t} d\tau e^{-\alpha((m-1)\Delta t - \tau)} f_1((m-1)\Delta t - \tau) f_2(\tau) \\ &= e^{-\alpha\Delta t} g((m-1)\Delta t) + \int_{(m-1)\Delta t}^{m\Delta t} d\tau e^{-\alpha((m+1)\Delta t - \tau)} f_1((m+1)\Delta t - \tau) f_2(\tau), \end{aligned} \quad (3.4.41)$$

where we have taken $t = m\Delta t$. For finite yet sufficiently small time steps Δt , it can be assumed that the function $f_2(\tau)$ in the last integral term on the right-hand side of Eq. (3.4.41) is constant. This allows to take $f_2((m-1)\Delta t)$ outside of the integral. In the next step, we substitute $\alpha = \sigma$, and the functions $f_1(t)$ and $f_2(t)$ with the corresponding ones in Eq. (3.4.38)

$$f_{1,\pm,l}(t) = -\frac{1}{2}\sigma_{(l)} \left(1 \pm \frac{\mu}{\epsilon} e^{-(\mu/\epsilon-1)\sigma_{(l)}t} \right), \quad (3.4.42)$$

$$f_{2,\pm,l}(t) = \partial_l F_{\pm,l}(\vec{r}, t). \quad (3.4.43)$$

However, the above recursive convolution applied to Eqs. (3.4.38) and Eq. (3.4.39) does not allow to express the term \mathcal{GF} in Eq. (3.4.38) as a matrix vector multiplication with an approximated matrix \mathcal{G} and vector \mathcal{F} . Nevertheless, it is possible to replace the whole \mathcal{GF} term by a 6x6 dimensional matrix, denoted as $\tilde{\mathcal{G}}$

$$\tilde{\mathcal{G}}(m\Delta t) = i\hbar c_0 \begin{pmatrix} \tilde{g}_{k,l}(m\Delta t) & \tilde{g}_{k,l'}(m\Delta t) \\ \tilde{g}_{k',l}(m\Delta t) & \tilde{g}_{k',l'}(m\Delta t) \end{pmatrix}. \quad (3.4.44)$$

The matrix $\tilde{\mathcal{G}}$ contains four 3x3 dimensional matrices, which are defined recursively and depend on the current $t = j\Delta t$ and the previous time $t' = (j-1)\Delta t$. With using Eqs. (3.4.39)-(3.4.43), these recursive matrices are given by

$$\begin{aligned} \tilde{g}_{k,l}(m\Delta t) &= a_k \tilde{g}_{k,l}((m-1)\Delta t) \delta_{kl} - b_{+,k} \epsilon^{qlp} \partial_p F_+(\vec{r}, m\Delta t) \delta_{kq}, \\ \tilde{g}_{k,l'}(m\Delta t) &= a_k \tilde{g}_{k,l'}((m-1)\Delta t) \delta_{kl'} - b_{+,k} \epsilon^{qlp} \partial_p F_+(\vec{r}, m\Delta t) \delta_{kq}, \\ \tilde{g}_{k',l}(m\Delta t) &= -a_{k'} \tilde{g}_{k',l}((m+1)\Delta t) \delta_{k'l} - b_{-,k'} \epsilon^{qlp} \partial_p F_-(\vec{r}, m\Delta t) \delta_{k'q}, \\ \tilde{g}_{k',l'}(m\Delta t) &= -a_{k'} \tilde{g}_{k',l'}((m+1)\Delta t) \delta_{k'l'} - b_{-,k'} \epsilon^{qlp} \partial_p F_-(\vec{r}, m\Delta t) \delta_{k'q}. \end{aligned} \quad (3.4.45)$$

The auxiliary variables a_k and $b_{\pm,k}$ result from the last line of Eq. (3.4.41) after taking $f_{2,\pm,k}((m-1)\Delta t)$ outside the integral. Hence, the factor a_k is the exponential function

$$a_k = e^{-\sigma_{(k)}\Delta t}, \quad (3.4.46)$$

and $b_{\pm,k}$ is the result of the integral

$$\begin{aligned} b_{\pm,k} &= \int_{(m-1)\Delta t}^{m\Delta t} d\tau e^{-\sigma_{(k)}((m+1)\Delta t - \tau)} f_{1,\pm,k}((m+1)\Delta t - \tau) \\ &= \frac{1}{2} e^{-2\sigma_{(k)}\Delta t} (1 - e^{\sigma_{(k)}\Delta t}) \pm \frac{1}{2} e^{-2\frac{\mu}{\epsilon}\sigma_{(k)}\Delta t} \left(1 - e^{\frac{\mu}{\epsilon}\sigma_{(k)}\Delta t} \right). \end{aligned} \quad (3.4.47)$$

Collecting all steps, we can express the Maxwell Riemann-Silberstein Hamiltonian \mathcal{H}_{PML} from Eq. (3.4.38) in discretized form

$$\mathcal{H}_{\text{PML}}(\vec{r}, m\Delta t) = \mathcal{H} + \tilde{\mathcal{G}}(\vec{r}, m\Delta t). \quad (3.4.48)$$

With this definition it is then straightforward to insert the above PML expression \mathcal{H}_{PML} in the Maxwell propagator \mathcal{U} of the numerical propagation equations in Eq. (5.3.3) or Eq. (5.3.4) to enable the simulation of open Maxwell systems via PML absorption.

In the last step, we have to determine the conductivity $\sigma_{(u)}$ adequately to get an optimal PML. In FDTD, several useful profiles for the conductivity $\sigma_{(u)}$ were found and we have chosen for our Riemann-Silberstein PML the FDTD polynomial grading profile which has the form [65]

$$\sigma_{(u)}(u) = \left(\frac{|u| - b_u}{L_u - b_u} \right)^q \sigma_{(u),\max} \quad (3.4.49)$$

with direction coordinate $u \in (x, y, z)$ where b_u and L_u denote the corresponding boundary dimensions in Fig. 3.1. The last variable $\sigma_{(u),\max}$ for the grading profile is determined by

$$\sigma_{(u),\max} = -\frac{\epsilon(q+1)\ln(R(0))}{2\mu(L_u - b_u)}, \quad (3.4.50)$$

where the tolerated reflection error for normal angle incidence equal to zero can be set manually. The only parameter that we still have to determine is the exponent q in Eq. (3.4.49), which can only be done by a numerical screening. Therefore, we use the same simulation setup as described in Sec. (3.3.1) also in MEEP units ($\epsilon = \mu = c = 1$), but select a smaller cubic simulation box with perfectly matched layers and a finite difference order of eight. The total size of the box depends on the width of the absorbing boundaries since the inner simulation box is in all cases equally sized. Additionally, the grid spacing is always $\Delta x = \Delta y = \Delta z = 0.2$ and the simulation time $\Delta t = 0.1$. We employ a series of runs by using the external current density given in Eq. (3.4.51)

$$\vec{j}_{\text{ext},4}(\vec{r}, t) = \vec{j}_{\text{ext},0}(\vec{r}) \exp\left(-\frac{(t-10.0)^2}{8}\right) \cos(2.0(t-10.0)) . \quad (3.4.51)$$

to compare the impact of the absorbing boundaries. The parameters except q , but including the absorbing width w_{ab} , that we change for each run are shown in Table 3.2.

| variable | run 1 | run 2 | run 3 | run 4 | run 5 | reference run |
|--------------------------------|-------|-------|-------|-------|-------|---------------|
| w_{ab} | 0.5 | 1.0 | 1.5 | 2.0 | 2.5 | 4.0 |
| L_x | 10.5 | 11.0 | 11.5 | 12.0 | 12.5 | 54.0 |
| L_y | 10.5 | 11.0 | 11.5 | 12.0 | 12.5 | 54.0 |
| L_z | 10.5 | 11.0 | 11.5 | 12.0 | 12.5 | 54.0 |
| b_x | 10.0 | 10.0 | 10.0 | 10.0 | 10.0 | 50.0 |
| b_y | 10.0 | 10.0 | 10.0 | 10.0 | 10.0 | 50.0 |
| b_z | 10.0 | 10.0 | 10.0 | 10.0 | 10.0 | 50.0 |
| $\Delta x, \Delta y, \Delta z$ | 0.2 | 0.2 | 0.2 | 0.2 | 0.2 | 0.2 |
| finite difference order | 8 | 8 | 8 | 8 | 8 | 8 |
| exponential order | 4 | 4 | 4 | 4 | 4 | 4 |
| Δt | 0.1 | 0.1 | 0.1 | 0.1 | 0.1 | 0.1 |
| ϵ | 1 | 1 | 1 | 1 | 1 | 1 |
| μ | 1 | 1 | 1 | 1 | 1 | 1 |
| c | 1 | 1 | 1 | 1 | 1 | 1 |

Table 3.2: Physical and simulation parameters of external current simulation for screening the parameters of the PML absorbing boundaries

To evaluate the quality of the absorbing boundary, we apply a reference run with a box that is chosen so large ($L_x = L_y = L_z = 54.0$) that boundary effects do not arise. In the following the index i denotes the run number referring to Table (3.2), except the reference which denoted by an "ref" index. First, we take a look at the energy inside the

Relative reflection error of the perfectly matched layer

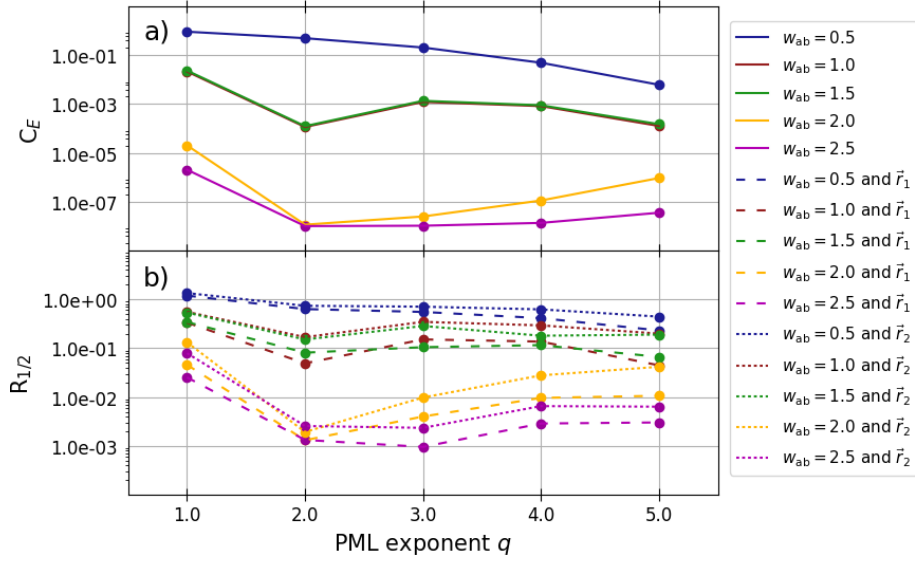


Figure 3.13: Relative variation of the energy and the electric field at two points for different parameters q . Panel a) shows the quotient of the Maxwell energy inside the box at time $t_2 = 40.0$, when the energy should be approximately zero, and time $t_1 = 14.7$, when the box energy reaches its maximum. Additionally, panel 2) gives the reflection coefficients at point \vec{r}_1 and \vec{r}_2 .

box. Since we know that the external current causes electromagnetic waves that leave the box, the electromagnetic energy should fall to zero when the wave reaches the boundaries. Therefore, we plot the quotient of the box energies $\langle E(t) \rangle$ at time $t_1 = 14.7$ and $t_2 = 40.0$ using Eq. (1.1.69) with the inner box limits

$$C_E = \frac{|\langle E_i(t_2) \rangle|}{|\langle E_i(t_1) \rangle|}. \quad (3.4.52)$$

According to Figure 3.5, time t_1 corresponds to the maximum box energy. Additionally, we evaluate the reflection coefficient based on the electric field at two grid points $\vec{r}_1 = (8, 0, 0)$ and $\vec{r}_2 = (8, 8, 0)$. In our case, we calculate the reflection coefficient via the energy density $u(t)$ using Eq. (1.1.67) at the corresponding point $\vec{r}_{1/2}$ and the reflection coefficient given by

$$R_{1/2} = \frac{\max |u_i(t) - u_{\text{ref}}(t)|}{\max |u_{\text{ref}}(t)|} \quad (3.4.53)$$

for the corresponding grid point and a maximum time of $t = 40.0$. Both variables, C_E and $R_{1/2}$, depending on the PML exponent parameter q is shown in Figure 3.4.2. The impact of the PML does not simply increase with the width of the absorbing boundaries. The exponential factor q is more relevant for the absorbing efficiency. According to our five runs, the optimal setting for q is between two and three, and the width of the PML region or equivalently the number of grid points along the axis ($w_{ab}/\Delta x$, $w_{ab}/\Delta y$, $w_{ab}/\Delta z$) should be larger than seven.

Relative reflection error of the PML

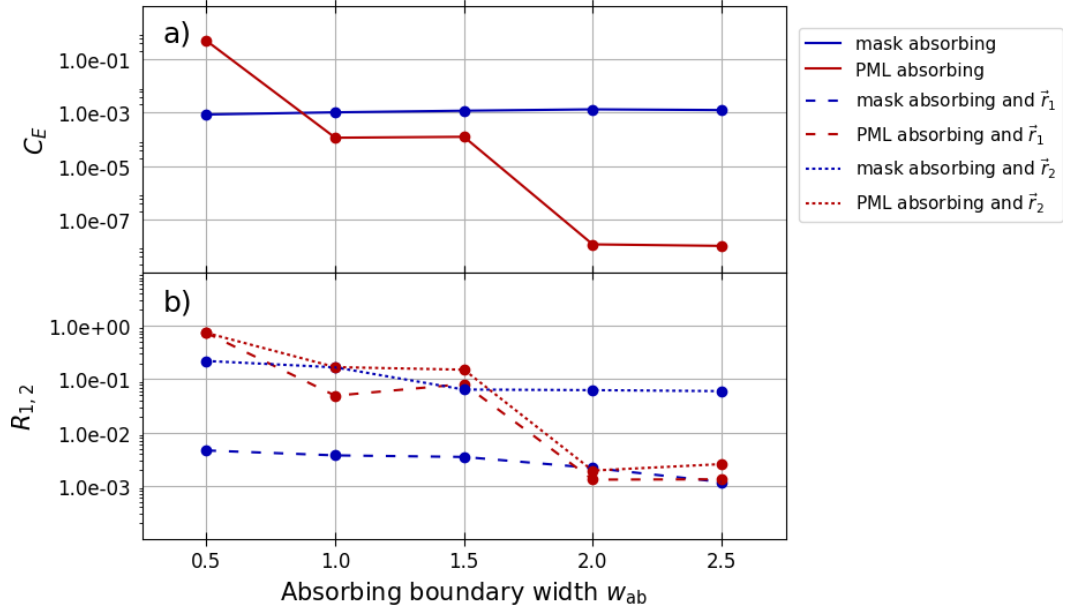


Figure 3.14: Comparison of absorbing mask and perfectly matched layer boundary conditions. Similar to Figure 3.4.2, the energy quotient of the box energy at $t_2 = 40.0$ divided by the box energy at time $t_1 = 14.7$ is plotted in panel a), and the reflection coefficients at \vec{r}_1 and \vec{r}_2 in panel b).

3.4.3 Comparison of absorbing mask and perfectly matched layer boundaries

In this section, we compare the two different absorbing boundary schemes, the absorbing mask boundary and the perfectly matched layer. For this reason, we use the same simulation setup as for finding the optimal parameters for the PML in Sec. 3.4.2. Again, we simulate five runs plus one reference run for each absorbing scheme using the parameters given in Table 3.2 and calculate the energy coefficient C_E of Eq.(3.4.52) and reflection coefficient $R_{1/2}$ of Eq. (3.4.52). Besides the width of the absorbing mask, there is no other characteristic parameter. For the PML we select for the comparison the parameter $q = 2$, which corresponds to the minimum reflection effects according to Figure 3.4.2. The comparison of C_E and $R_{1/2}$ for both absorbing methods as function of the absorbing boundary width w_{ab} is illustrated in Figure 3.14. It reveals that in case of the absorbing mask an increasing boundary width does not improve significantly the result. The C_E -Factor stays almost constant, and the reflection constant $R_{1/2}$ decreases slightly. In contrast, the PML absorbing improves all absorbing features for larger w_{ab} and becomes significantly better than the mask method. Only if the width w_{ab} is rather small, this behavior reverses.

3.4.4 Incident plane waves boundaries

Very common experimental setups to examine optical properties are based on disturbing a molecular system with various kinds of external electromagnetic pulses. In most cases, the used light pulse has a mathematically closed description and can be evolved in time analytically. For this situation, it is not necessary to chose such a large Maxwell simulation box so that the external light signal is completely inside the box. In addition, some analytical waves i.g. plane waves are in in principle only terminated parallel to their

wavevector \vec{k} , but conceptually constant in space and periodic in time in the direction perpendicular to \vec{k} . A convenient method to simulate such waves in the Maxwell simulation box can be obtained by using a boundary region as a frame where the grid point values are calculated via their analytical formula.

Figure FIG. 3.15 illustrates in a 2D cut the analytically calculated outer frame around the simulation box and a Gaussian shaped plane wave propagates parallel to the corresponding wavevector \vec{k} . All grid points which are inside the green frame boundary region are set by the analytical values of the plane wave function at the respective points. The number of necessary boundary grid points in each dimension is coupled to the given accuracy order of the spatial derivative operator. It is not sufficient to set only the points next to the box border, since we also have to take care of the discrete derivative operator and the corresponding stencil. The two-dimensional stencil in figure (3.2) shows that the spatial derivative of accuracy order n at the point $x_{i,j}$ is determined by the point values of $x_{i-n,j}, \dots, x_{i+n,j}$ and $x_{i,j-n}, \dots, x_{i,j+n}$. Therefore, the width of the plane wave region has to be chosen, such that it contains n points in each direction.

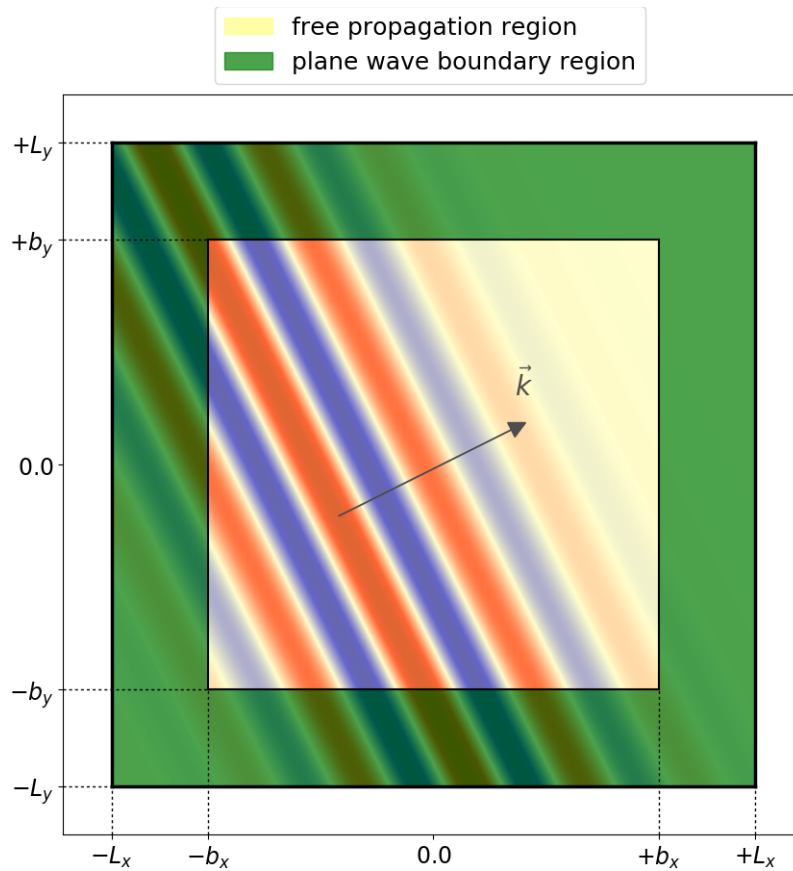


Figure 3.15: The green analytical wave region in this two-dimensional cut surrounds the free Maxwell propagation area to simulate incident waves and their propagation through the simulation box. The simulation box dimensions are denoted as L_x and L_y , and the inner free propagation box dimensions are b_x and b_y . The boundary width is determined by the size of the finite difference grid stencil. The figure shows schematically a Gaussian wave with wavevector \vec{k} propagating through the simulation box.

A single analytical wave with wave vector \vec{k} and corresponding frequency ω can be

expressed in terms of the six-component Riemann-Silberstein vector $\mathcal{F}(\vec{r}, t)$ that depends on the scalar propagation relation $(-\vec{k} \cdot \vec{r} - \omega t)$. In general, an arbitrary shaped analytical wave can be obtained by a superposition of different linear independent waves with

$$\mathcal{F}_{\text{pw}}(\vec{r}, t) = \sum_i \mathcal{F}_{\text{pw},(i)}(\vec{r}) \exp\left(i(\vec{k}_{(i)} \vec{r} - \omega_{(i)} t)\right), \quad (3.4.54)$$

where the i^{th} wave is represented by its wavevector $\vec{k}_{(i)}$ and frequency $\omega_{(i)}$ and by a Riemann-Silberstein vector $\mathcal{F}_{\text{pw},(i)}$ as initial vector.

In the following, we illustrate as example a simulation of two Gaussian light pulses, which enter the simulation box, interfere and leave the box. Specifically, we select the two electric field functions

$$\vec{E}_{\text{pw},(1)}(\vec{r}_1, t) = E_{0,1,z} \begin{pmatrix} 0 \\ 0 \\ 1 \end{pmatrix} \cos\left(\vec{k}_1 \cdot (\vec{r}_1 - \vec{r}_{1,0}) - c_0 |\vec{k}_1| t\right) \exp\left(-\frac{(\vec{r}_1 - \vec{r}_{1,0} - c_0 |\vec{k}_1| t)^2}{2w_1^2}\right), \quad (3.4.55)$$

$$\vec{E}_{\text{pw},(2)}(\vec{r}_2, t) = E_{0,2,z} \begin{pmatrix} 0 \\ 0 \\ 1 \end{pmatrix} \cos\left(\vec{k}_2 \cdot (\vec{r}_2 - \vec{r}_{2,0}) - c_0 |\vec{k}_2| t\right) \exp\left(-\frac{(\vec{r}_2 - \vec{r}_{2,0} - c_0 |\vec{k}_2| t)^2}{2w_2^2}\right), \quad (3.4.56)$$

Both electric fields have only a polarization along the z-direction and the corresponding wavevectors

$$\vec{k}_1 = \frac{\sqrt{2}}{2} \begin{pmatrix} 1 \\ -1 \\ 0 \end{pmatrix}, \quad \vec{k}_2 = \frac{1}{2\sqrt{5}} \begin{pmatrix} -2 \\ -1 \\ 0 \end{pmatrix}. \quad (3.4.57)$$

with corresponding frequencies $\omega_1 = c_0 |\vec{k}_1|$ and $\omega_2 = c_0 |\vec{k}_2|$. They are shifted by the vectors $\vec{r}_{1,0}$ and $\vec{r}_{2,0}$ with

$$\vec{r}_{1,0} = 25.0 \frac{\sqrt{2}}{2} \begin{pmatrix} -1 \\ 1 \\ 0 \end{pmatrix}, \quad \vec{r}_{2,0} = 25.0 \frac{1}{\sqrt{5}} \begin{pmatrix} -2 \\ 1 \\ 0 \end{pmatrix}. \quad (3.4.58)$$

The Gaussian width for the first one is $w_1 = 4.0$, the second one $w_2 = 6.0$, and the field amplitudes are given by $E_{0,1,z} = 0.5$ and $E_{0,2,z} = 0.5$. The laser pulses propagate perpendicular to their wavevectors and since the electric-field polarization is oriented along the z-axis the corresponding magnetic fields have the form

$$\vec{B}_{\text{pw},(1)}(\vec{r}_1, t) = \frac{E_{0,1,z}}{c_0 \sqrt{2}} \begin{pmatrix} -1 \\ -1 \\ 0 \end{pmatrix} \cos\left(\vec{k}_1 \cdot (\vec{r}_1 - \vec{r}_{1,0}) - c_0 |\vec{k}_1| t\right) \exp\left(-\frac{(\vec{r}_1 - \vec{r}_{1,0} - c_0 |\vec{k}_1| t)^2}{2w_1^2}\right), \quad (3.4.59)$$

$$\vec{B}_{\text{pw},(2)}(\vec{r}_2, t) = \frac{E_{0,2,z}}{c_0 \sqrt{5}} \begin{pmatrix} -1 \\ 2 \\ 0 \end{pmatrix} \cos\left(\vec{k}_2 \cdot (\vec{r}_2 - \vec{r}_{2,0}) - c_0 |\vec{k}_2| t\right) \exp\left(-\frac{(\vec{r}_2 - \vec{r}_{2,0} - c_0 |\vec{k}_2| t)^2}{2w_2^2}\right). \quad (3.4.60)$$

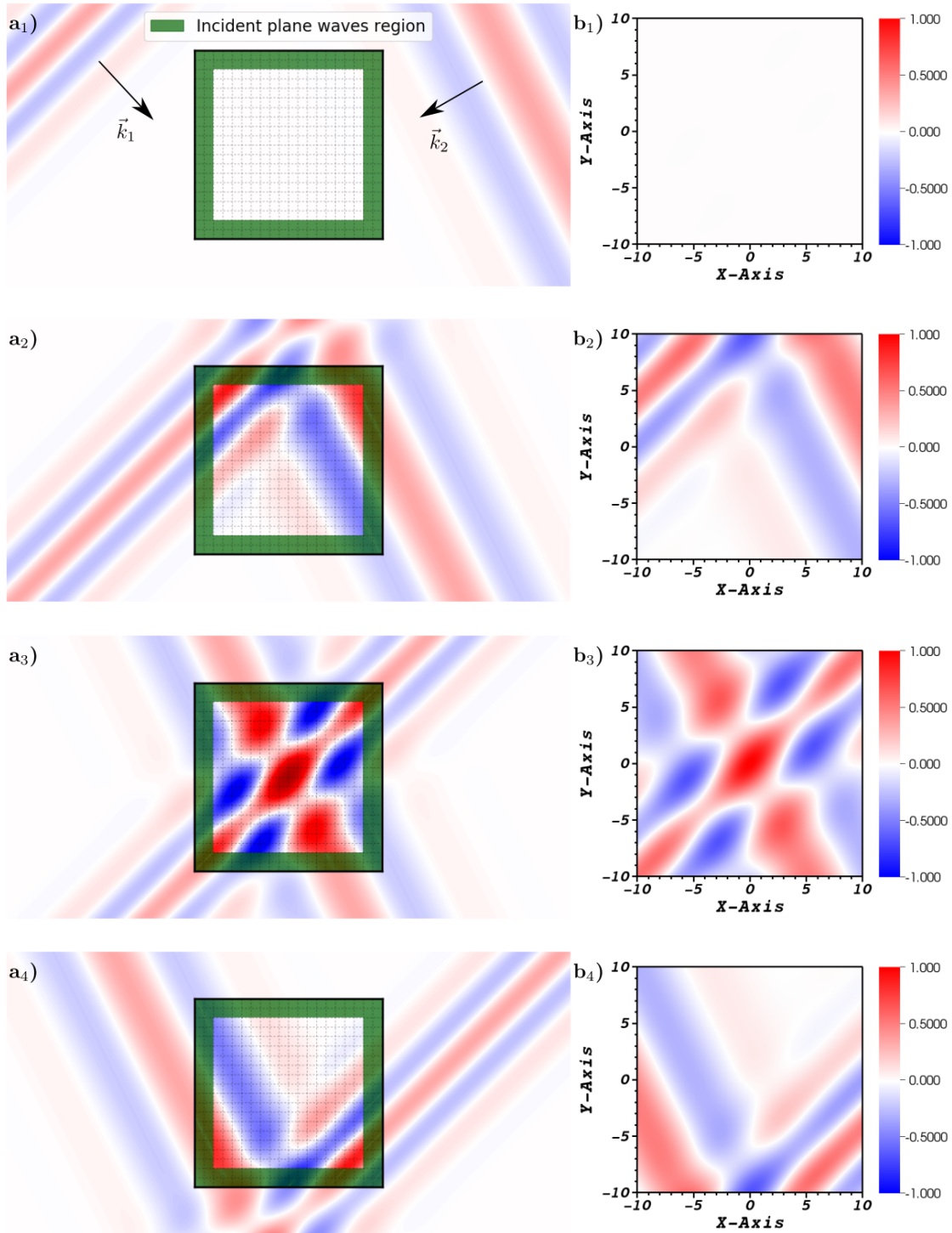


Figure 3.16: Incident plane wave simulation of two interfering plane waves. The panels $a_1 - a_4$ illustrate the box simulation scheme with the incident plane wave boundaries in green and the two Gaussian signals, which propagate into the direction of the box. On the right-hand side, denoted by $b_1 - b_4$, we show the two-dimensional cut of the simulation results. The four screenshots show relevant points in time, e.g., the two signals enter the box [a_2, b_2], their maximum interference in the middle of the box [a_3, b_3], and when they leave the box again [a_4, b_4].

Using the electric and magnetic fields in Eqs. (3.4.55)-(3.4.56) and (3.4.59)-(3.4.60), we can build the underlying Riemann-Silberstein vector $\mathcal{F}_{\text{pw}}(\vec{r}, t)$ for the superposition of the waves according to

$$\mathcal{F}_{\text{pw}}(\vec{r}, t) = \begin{pmatrix} \sqrt{\frac{\epsilon_0}{2}} \left(\vec{E}_{\text{pw},1}(\vec{r}, t) + \vec{E}_{\text{pw},2}(\vec{r}, t) \right) + i\sqrt{\frac{1}{2\mu_0}} \left(\vec{B}_{\text{pw},1}(\vec{r}, t) + \vec{B}_{\text{pw},2}(\vec{r}, t) \right) \\ \sqrt{\frac{\epsilon_0}{2}} \left(\vec{E}_{\text{pw},1}(\vec{r}, t) + \vec{E}_{\text{pw},2}(\vec{r}, t) \right) - i\sqrt{\frac{1}{2\mu_0}} \left(\vec{B}_{\text{pw},1}(\vec{r}, t) + \vec{B}_{\text{pw},2}(\vec{r}, t) \right) \end{pmatrix}. \quad (3.4.61)$$

This equation determines all Riemann-Silberstein values inside the plane wave boundary region. The remaining values inside the free propagation region are calculated by the homogeneous time-evolution Eq. (2.1.15), since we only consider a propagation in vacuum. As before, we use $\epsilon_0 = \mu_0 = c_0 = 1$ for the electromagnetic constants. The simulation box limits are $L_x = L_y = L_z = 10.0$ with spacing $\Delta x = \Delta y = \Delta z = 0.25$. We select a finite difference order of $n = 8$ and since the width w_{pw} of the plane wave boundaries are coupled to this order with $w_{\text{pw}} = n\Delta x = n\Delta y = n\Delta z$, the plane wave boundary limits are given by $b_x = b_y = b_z = 8$. All simulation parameters are given in Table (3.3). Two-dimensional

| variable | MEEP units | variable | MEEP units |
|--------------------------------|------------|-------------|------------|
| L_x | 10.0 | $k_{x,1}$ | 0.707 |
| L_y | 10.0 | $k_{y,1}$ | -0.707 |
| L_z | 10.0 | $k_{z,1}$ | 0.000 |
| $\Delta x, \Delta y, \Delta z$ | 0.25 | $E_{0,1,z}$ | 0.500 |
| finite difference order | 8 | w_1 | 4.000 |
| exponential order | 4 | $k_{x,2}$ | -0.447 |
| Δt | 0.144 | $k_{y,2}$ | -0.223 |
| ϵ_0 | 1 | $k_{z,2}$ | 0.000 |
| μ_0 | 1 | $E_{0,2,z}$ | 0.500 |
| c_0 | 1 | w_2 | 6.000 |

Table 3.3: Simulation parameters for the incident plane waves run with two interfering incident waves.

snapshots of the electric field in z-direction in the xy-plane are illustrated in Figure 3.16. All panels denoted by a_i) on the right-hand side of that figure, give the schematic setup of the simulation with a corresponding analytical calculation. The cut through the cubic simulation box is surrounded by the incident plane wave boundaries in green. In other words, the simulation box represents only a small section of the total environment and the boundaries ensure that the plane waves arise and propagate correctly through the box. The figures b₁) - b₄) on the right-hand side show a cut through the simulation box which corresponds to the section in a₁) - a₄). In contrast to the left-hand side, the given contour shows the simulation output calculated by Octopus. In a₁) and b₁), we display the initial Gaussian pulses at time $t_0 = 0$. Since the significant signal amplitudes are located outside the simulation box, the Riemann-Silberstein vector inside the box and on the plane wave frame is almost zero.

After several time steps at time $t_1 = 10.0$, in a₂) and b₂), the two Maxwell plane waves hit the simulation box. The plane wave region with the predetermined analytical values based on the given initial Maxwell plane waves ensure that the two electromagnetic signals arise at the border of the simulation box, when the significant signal amplitude reaches the box limits. The two plane waves propagate through the inner simulation region and start to interfere.

While one plane wave propagates from the upper left to the lower right side, and the other one in the opposite direction from the upper left to the lower right, the interference pattern moves from the upper to the lower box boundary. At the time $t_2 = 25.0$, shown in a₃) and b₃), the electric field reaches a maximum of the two interfered plane waves, which is in the middle of the simulation box. Due to the linearity of Maxwell's equations, the two plane waves continue their propagation independently.

Finally, in a₄) and b₄), at time $t_3 = 35.0$, both Maxwell plane waves passed the simulation box and are outside again, but contrary to the initial state in a₁) and b₁). The first Gaussian plane wave pulse with higher carrier frequency reached the lower right side and whereas the second Gaussian plane wave pulse with lower carrier frequency is in the lower left side. Without any Maxwell-matter coupling, the Maxwell fields return to zero inside the simulation box.

Comparing both cases, the analytical plotted figures a_i) and the numerically calculated ones of a_i) show, that both propagation results agree very well. In the next section, we compare more quantitatively the difference and error between the exact analytical and numerical propagation of plane waves.

3.4.5 Numerical dispersion for plane wave propagation

In this section we evaluate our Riemann-Silberstein Maxwell-propagation method by benchmarking the numerical propagation with analytical wave solutions. As a simulation setup, we chose a Maxwell simulation box with incident plane waves boundaries where a Gaussian shaped wave is shifted outside the box and propagates through the simulation box over time similar to Sec 3.4.4. It can be assumed that the error between the numerical and exact propagation depends on the wavelength of the plane wave. To get systematic results, we simulate a batch of different wavelengths λ for the Gaussian plane wave where we also couple the Gaussian width to the wavelength. The wavevector is set parallel to the x-axis and the polarization direction of the wave is chosen along the z-axis. The analytical formula for the Gaussian plane wave electric field $\vec{E}_{\text{pw}}(\vec{r}, t)$ takes the form

$$\vec{E}_{\text{pw}}(\vec{r}, \vec{r}_0, t) = \vec{e}_z \exp\left(\frac{(x - x_0)^2}{2\lambda^2}\right) \cos(2\pi/\lambda(x - x_0) - \omega t), \quad (3.4.62)$$

with corresponding magnetic field

$$\vec{B}_{\text{pw}}(\vec{r}, t) = -\vec{e}_y \frac{1}{c_0} \vec{E}_{\text{pw}}(\vec{r}, t), \quad (3.4.63)$$

which leads to the plane wave Riemann-Silberstein six-vector $\mathcal{F}_{\text{pw}}(\vec{r}, t)$

$$\mathcal{F}_{\text{pw}}(\vec{r}, t) = \begin{pmatrix} \sqrt{\frac{\epsilon_0}{2}} \vec{E}_{\text{pw}}(\vec{r}, t) + i\sqrt{\frac{1}{2\mu_0}} \vec{B}_{\text{pw}}(\vec{r}, t) \\ \sqrt{\frac{\epsilon_0}{2}} \vec{E}_{\text{pw}}(\vec{r}, t) - i\sqrt{\frac{1}{2\mu_0}} \vec{B}_{\text{pw}}(\vec{r}, t) \end{pmatrix}. \quad (3.4.64)$$

The shift parameter x_0 is set such that the Gaussian amplitude $\exp\left(\frac{(x-x_0)^2}{2\lambda^2}\right)$ is lower than $1e^{-6}$ inside the whole simulation box. Consequently, we get two distinguished times, the first one t_{start} represents the time, where the Gaussian amplitude at the origin is lower than $1e^{-6}$ before the light pulse passes the box and in turn t_{end} gives the time, when the whole Gaussian amplitude is again lower than $1e^{-6}$ inside the box after the light pulse propagation. The outer dimensions of the parallelepiped simulation box is 35.0 in x-direction and 10 in y- and z-direction.

| variable | MEEP units |
|-------------------|------------|
| L_x | 10.0 |
| L_y | 10.0 |
| L_z | 10.0 |
| exponential order | 4 |
| Δt | 0.144 |
| ϵ_0 | 1 |
| μ_0 | 1 |
| c_0 | 1 |

Table 3.4: Simulation box and time parameters for the numerical dispersion run with an incident wave pulse.

In addition to the wave length dependency for the numerical Riemann-Silberstein propagator, we examine the differences of our Maxwell simulation for two different grid spacings and four different finite difference orders for the spatial first derivative operation. Therefore, we perform a series of runs with different selected wavelengths. The wavelength with corresponding run number can be found in Table 3.5.

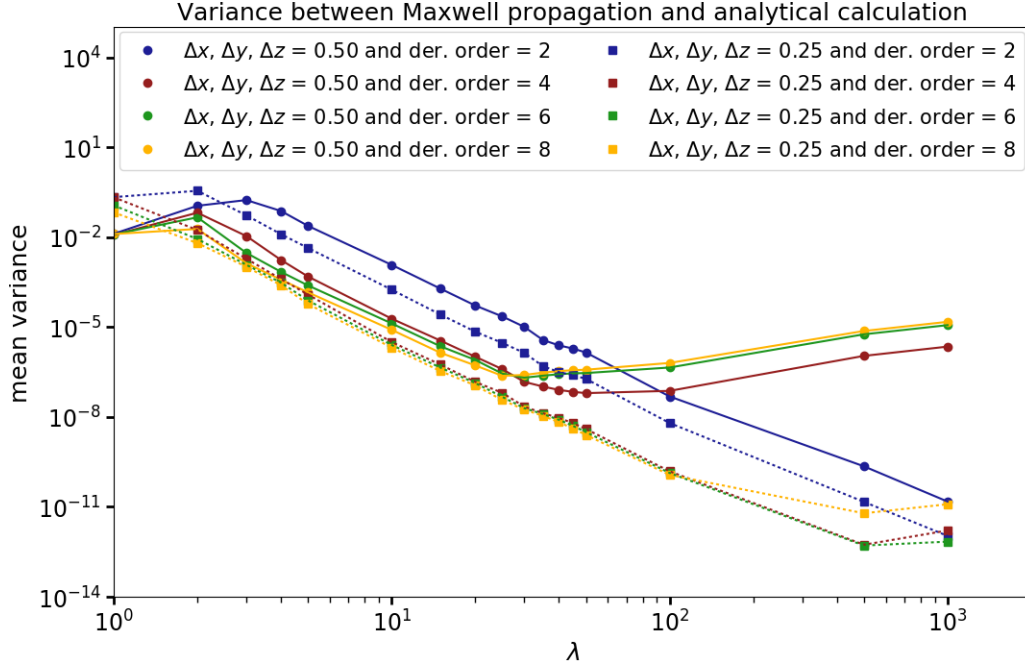


Figure 3.17: The graph of the numerical dispersion shows that the numerical accuracy depends on the wavelength of the propagated plane waves. Except the three graphs for grid spacing 0.5 and higher derivative accuracy order of $n = 2$, the accuracy of the free Maxwell plane wave propagation increases approximately linearly with the wavelength dispersion on a log-log scale. The excepted three graphs feature a knee around $\lambda = 25.0$ where the accuracy begins to decrease for higher wavelengths.

Since we evaluate the quality of the plane wave propagation we have to find a scalar variable that represent the variation between the exact analytical propagation and our numerical simulation. In a first step we have to take into account, that the wavelength dependency of Eq. (3.4.62) scales the length and time of the signal. Therefore, we map each

| | | | | | | | | | |
|----------------------|-----|-----|-----|-----|-----|------|------|------|------|
| run number | 1 | 2 | 3 | 4 | 5 | 6 | 7 | 8 | 9 |
| wavelength λ | 1.0 | 2.0 | 3.0 | 4.0 | 5.0 | 10.0 | 15.0 | 20.0 | 25.0 |

| | | | | | | | | |
|----------------------|------|------|------|------|------|-------|-------|--------|
| run number | 10 | 11 | 12 | 13 | 14 | 15 | 16 | 17 |
| wavelength λ | 30.0 | 35.0 | 40.0 | 45.0 | 50.0 | 100.0 | 500.0 | 1000.0 |

Table 3.5: Simulation box and time parameters for the numerical dispersion run with an incident wave pulse.

Gaussian plane wave pulse to normalized times with $t_{\text{start}} \rightarrow 0$ and $t_{\text{end}} \rightarrow 1$. Consequently, each Gaussian pulse has the same shape and temporal scale. After that, we take the calculated mapped Riemann-Silberstein vector $\mathcal{F}_{\text{map}}(\vec{r}, t, \lambda_i)$ and the analytical mapped Riemann-Silberstein vector $\mathcal{F}_{\text{pw, map}}(\vec{r}, t, \lambda_i)$ of run i and define the integral

$$\begin{aligned}
var_i &= \int_0^1 dt \sqrt{\left(\mathcal{F}_{\text{map}}(\vec{r}_0, t, \lambda_i) - \mathcal{F}_{\text{pw, map}}(\vec{r}_0, t, \lambda_i)\right)^2} \\
&= \begin{pmatrix} 1 \\ 1 \end{pmatrix} \int_0^1 dt \sqrt{\left(\vec{F}_{\text{map, +}}(\vec{r}_0, t, \lambda_i) - \vec{F}_{\text{pw, map, +}}(\vec{r}_0, t, \lambda_i)\right) \left(\vec{F}_{\text{map, -}}(\vec{r}_0, t, \lambda_i) - \vec{F}_{\text{pw, map, -}}(\vec{r}_0, t, \lambda_i)\right)},
\end{aligned} \tag{3.4.65}$$

where \vec{r}_0 denotes the origin of the simulation box. The variance var_i characterizes the numerical dispersion relation, which means it determines the error between the exact analytical and the calculated light pulse propagation since it depends on the wavelength λ . In Figure 3.17 we plot in log-log scale the variance var_i for all considered wavelengths from Table 3.5 and different finite difference orders and grid spacings. The plot reveals that the variance is rather significant for small wavelengths. This corresponds to the general feature of numerical grids that the resolution of waves are of low quality when the wavelength is near the same magnitude as the grid spacing. Therefore, the variance decreases for increasing wavelength and in most cases, a finer grid spacing leads to a smaller variance. Whereas the log-log graph of the 0.25 grid spacing shows a linear decrease, the variances for the 0.5 grid spacing increases for wavelengths larger than 50.0.

3.4.6 Incident waves boundaries plus absorbing boundaries

The incident waves boundaries simulate a signal that enters the simulation box. In contrast, the perfectly matched layer damps all outgoing electromagnetic fields. For our purpose, we want to combine both boundary condition. We know, due to the analytical behavior of the incident waves, the incoming fields for all times. In addition, the outgoing electromagnetic signals should not cause any reflection at the boundaries. In the previous section, we have seen how the PML looks like only for the absorbing boundary condition. Hence, since we know how an undisturbed wave passes the simulation box, we can subtract this wave in the entire simulation box from the total disturbed field and apply the PML. For proper incident waves with absorbing boundaries, we split the boundary region into two regions, one outer region for the incident waves frame, and an inner one for the PML as it is shown in figure FIG. (3.18). The limits of the inner boundary region are still represented by b_x, b_y, b_z , the outer boundaries are denoted by a_x, a_y, a_z and are located between the inner boundary region and the total box limits L_x, L_y, L_z .

Now, a combined wave plus PML step applies first a subtraction of the undisturbed wave. After that the PML acts on the remaining field. As a last step, the undisturbed wave

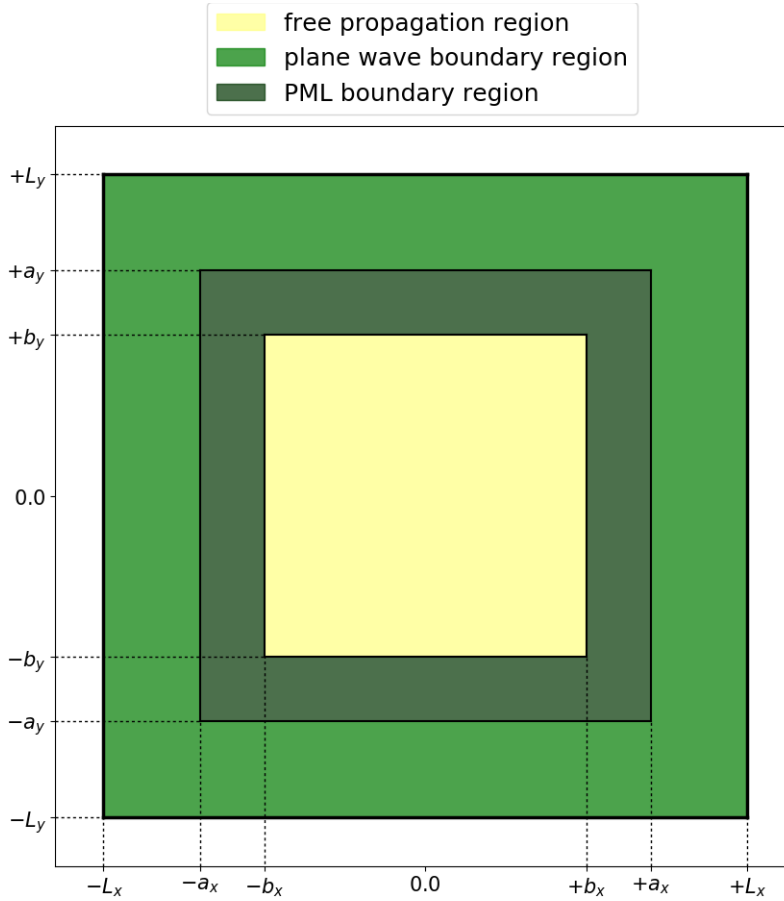


Figure 3.18: In the 2-dimensional cut of the simulation box with total dimensions L_x , and L_y , the boundary region is split into two subareas with analytical waves and PML boundary conditions. The outer boundaries with the limits L_x , b_x , and L_y , b_y are the analytical waves boundaries, whereas the inner boundaries determined by a_x , b_x , and a_y , b_y belong to the PML region.

is added again to the field. We note, that there are two options to get the values of the incident wave which have to be subtracted. First, one can use simply the analytical wave values for the current time step. The second option requires a second auxiliary propagation which has to be performed concurrently with the full system propagation. In this case, the unperturbed wave propagation is calculated by the discretized Maxwell time-evolution operator. This method avoids numerical reflection artefacts at the boundary due to the fact, that there is always a numerical error between the analytical wave and a numerically simulated one.

3.5 Riemann-Silberstein Maxwell propagation for linear media

After introducing in the previous sections electromagnetic simulations based on the microscopic Maxwell's equations, we demonstrate in this section our implementation for electromagnetic field propagations in the presence of a linear medium. As set up we consider a laser pulse in vacuum that hits a simulation box which contains a linear medium which

scatters the light pulse. To describe the incident laser pulse, we take a simulation box with incident plane waves boundaries to propagate the light pulse starting outside the box and entering at the boundaries. Since we simulate an open system, we have to absorb the scattered light by the combined incident plane waves boundaries plus perfectly matched layer, which we introduced in Sec. 3.4.6. A two-dimensional cut through the simulation box with corresponding relevant coordinates can be seen in Figure 3.19. The simulation box is similar to Figure 3.18, but in addition we include the perpendicular medium box centered at the origin. The corresponding box dimensions are determined by $l_{\text{lm},x}$, $l_{\text{lm},y}$, $l_{\text{lm},z}$, which is half of the box length in each direction. The medium box size parameters for the simulations that we present in the following are $l_{\text{lm},x} = l_{\text{lm},y} = l_{\text{lm},z} = 5.0$ and the total simulation box sizes are given by $L_x = L_y = L_z = 20.0$ with the grid spacing $\Delta x = \Delta y = \Delta z = 0.1$. To obtain a high quality of electromagnetic field absorption at the boundaries, we chose an absorbing boundary width $w_{\text{ab}} = 4.2$. Furthermore, taking a derivative order of eight for the finite difference operation leads with the selected grid spacing to a width $w_{\text{pw}} = 0.8$. Hence, the total boundary width becomes $w_{\text{b}} = w_{\text{ab}} + w_{\text{pw}} = 5.0$ and the inner free simulation box area dimensions are $b_x = b_y = b_z = 15.0$.

Inside the medium box, the electric permittivity ϵ_{lm} and the magnetic permeability μ_{lm} differ from the vacuum constants ϵ_0 , μ_0 . We keep the electromagnetic constants equal to one ($\epsilon_0 = \mu_0 = c_0 = 1$) as before in the previous sections and chose the corresponding medium values $\epsilon_{\text{lm}} = \mu_{\text{lm}} = 2.0$, and $c_{\text{lm}} = 0.5$. All necessary box and medium parameters are listed in Table 3.6 on the left-hand side.

The external laser pulse is given by the incident wave of Eq. (3.4.54) parallel to the x-axis. Instead of a Gaussian shaped pulse like in Sec. 3.4.6, we select a cosinusoidally shaped pulse, which is given in closed form by

$$\vec{E}_{\text{pw}}(\vec{r}, t) = \vec{e}_z E_{0,z} \cos\left(k_x(x-x_0) - \frac{2\pi}{\lambda}t\right) \cos\left(\frac{\pi(x-2\xi-x_0-c_0t)}{2\xi} + \pi\right) \cdot \theta\left(\xi - \frac{|k_x(x-x_0) - \frac{2\pi}{\lambda}t|}{|k_x|}\right), \quad (3.5.1)$$

and determines the electric field. The arising $\theta(x)$ denotes the usual Heaviside theta function. The wavevector \vec{k} has only a k_x component, the light pulse is shifted by x_0 , and the pulse shift is determined by its characteristic width parameter ξ . The orthogonal condition between electric field, magnetic field and electromagnetic wave yields for the magnetic field

$$\vec{B}_{\text{pw}}(\vec{r}, t) = -\vec{e}_y \frac{1}{c_0} \vec{E}_{\text{pw}}(\vec{r}, t). \quad (3.5.2)$$

Therefore the plane wave six-component Riemann-Silberstein vector $\mathcal{F}_{\text{pw}}(\vec{r}, t)$ takes the form

$$\mathcal{F}_{\text{pw}}(\vec{r}, t) = \begin{pmatrix} \sqrt{\frac{\epsilon_0}{2}} \vec{E}_{\text{pw}}(\vec{r}, t) + i\sqrt{\frac{1}{2\mu_0}} \vec{B}_{\text{pw}}(\vec{r}, t) \\ \sqrt{\frac{\epsilon_0}{2}} \vec{E}_{\text{pw}}(\vec{r}, t) - i\sqrt{\frac{1}{2\mu_0}} \vec{B}_{\text{pw}}(\vec{r}, t) \end{pmatrix}. \quad (3.5.3)$$

The corresponding laser parameters together with the medium parameters can be taken from the right-hand side of Table 3.6.

In case of an electromagnetic propagation with a linear medium, the underlying Maxwell's equations in Riemann-Silberstein representation are given by Eq (1.2.38). Since we have no external current density, they take here the simpler form

$$i\hbar \frac{\partial}{\partial t} \mathcal{F}(\vec{r}, t) = \mathcal{H}_{\text{lm}}(\vec{r}, t) \mathcal{F}(\vec{r}, t), \quad (3.5.4)$$

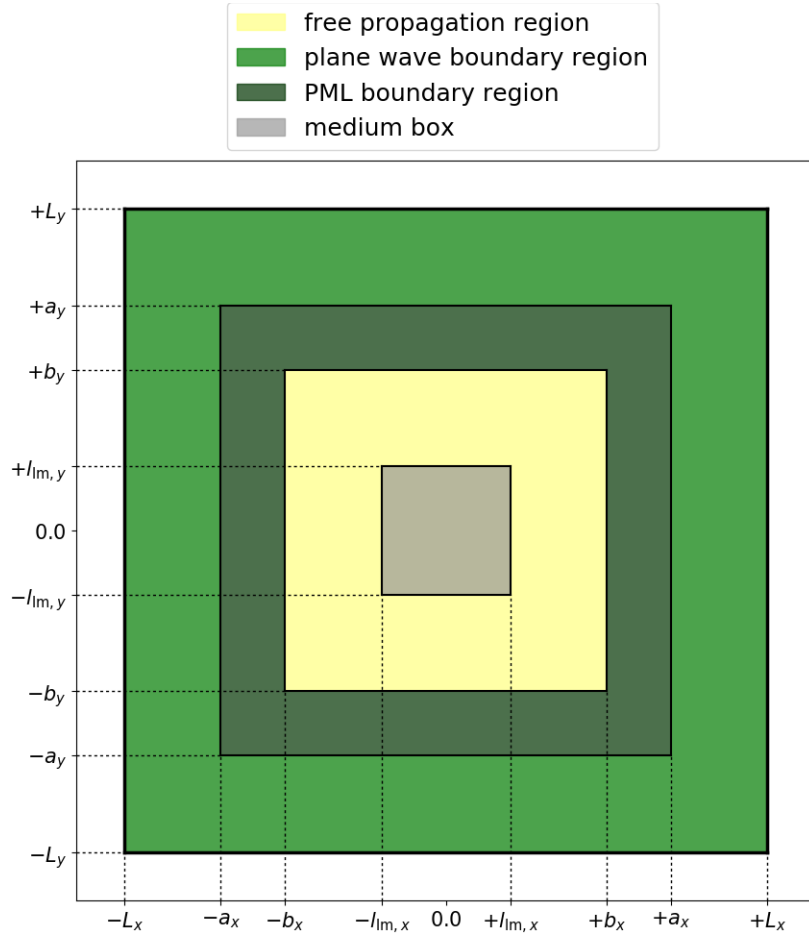


Figure 3.19: Simulation box illustration with an linear medium box in the center and combined incident waves and perfectly matched layer boundaries. The used parameters are equal to the ones of Figure 3.18. In addition we consider here the medium box limits l_x, l_y which correspond to half the length of the box.

where $\mathcal{H}_{\text{lm}}(\vec{r}, t)$ of Eq. (1.2.39) gives

$$\mathcal{H}_{\text{lm}}(\vec{r}, t) = \mathcal{H}_{\text{lm},(0)}(\vec{r}, t) + \mathcal{K}_{\text{lm}}(\vec{r}, t), \quad (3.5.5)$$

with

$$\mathcal{H}_{\text{lm},(0)}(\vec{r}, t) = \begin{pmatrix} 1 & 0 \\ 0 & 1 \end{pmatrix}_{2 \times 2} \otimes \begin{pmatrix} -i\hbar c(\vec{r}, t) \vec{\nabla} \cdot \vec{\mathbf{S}} \end{pmatrix}_{3 \times 3}. \quad (3.5.6)$$

For our medium we take a linear medium constant in time without any losses. Therefore, the time derivatives of ϵ_{lm} and μ_{lm} as well as the electric and magnetic conductivity σ_e and σ_m are equal to zero. Hence, the medium matrix function $\mathcal{K}_{\text{lm}}(\vec{r}, t)$ of the total $\mathcal{H}_{\text{lm}}(\vec{r}, t)$ simplifies with Eq. (1.2.41) to

$$\begin{aligned} \mathcal{K}_{\text{lm}}(\vec{r}, t) = & \begin{pmatrix} -1 & -1 \\ 1 & 1 \end{pmatrix}_{2 \times 2} \otimes \begin{pmatrix} -i\hbar \frac{c(\vec{r}, t)}{4\epsilon(\vec{r}, t)} [\vec{\mathbf{S}} \cdot (\vec{\nabla} \epsilon(\vec{r}, t))] \end{pmatrix}_{3 \times 3} \\ & + \begin{pmatrix} -1 & 1 \\ -1 & 1 \end{pmatrix}_{2 \times 2} \otimes \begin{pmatrix} -i\hbar \frac{c(\vec{r}, t)}{4\mu(\vec{r}, t)} [\vec{\mathbf{S}} \cdot (\vec{\nabla} \mu(\vec{r}, t))] \end{pmatrix}_{3 \times 3}. \end{aligned} \quad (3.5.7)$$

| variable | MEEP units | variable | MEEP units |
|--------------------------------|------------|-----------------|------------|
| L_x | 20.0 | k_x | 0.628 |
| L_y | 20.0 | $E_{0,z}$ | 0.001 |
| L_z | 20.0 | ξ | 10.0 |
| b_x | 15.0 | x_0 | - 40.0 |
| b_y | 15.0 | ϵ_0 | 1 |
| b_z | 15.0 | μ_0 | 1 |
| a_x | 19.2 | c_0 | 1 |
| a_y | 19.2 | $l_{lm,x}$ | 5.0 |
| a_z | 19.2 | $l_{lm,y}$ | 5.0 |
| $\Delta x, \Delta y, \Delta z$ | 0.25 | $l_{lm,z}$ | 5.0 |
| finite difference order | 8 | ϵ_{lm} | 2.0 |
| exponential order | 4 | μ_{lm} | 2.0 |
| Δt | 0.144 | c_{lm} | 0.5 |

Table 3.6: Simulation parameters for the laser pulse run that hits a cubic linear medium box.

The six-dimensional Hamiltonian-like matrix $\mathcal{H}_{lm}(\vec{r}, t)$ determines the time-evolution, which is given by the time-evolution operator Eq. (2.3.6) for a constant linear medium

$$\mathcal{U}_{lm}(t, t_0) = \exp \left[-\frac{i}{\hbar}(t - t_0)\mathcal{H}_{lm}(\vec{r}) \right]. \quad (3.5.8)$$

Finally, we take this time evolution operator and use the recursive time-evolution Eq. (3.2.2) and adapt it for the present simulation, which leads to

$$\mathcal{F}_{lm}(\vec{r}, (m + 1)\Delta t) = \mathcal{U}_{lm}((m + 1)\Delta t, m\Delta t)\mathcal{F}_{lm}(\vec{r}, m\Delta t). \quad (3.5.9)$$

Based on the previous considerations, we run our Riemann-Silberstein implementation in Octopus and present some snapshots of the electric field motion. All figures have the same color table limits between -0.300 and $+0.300$ to ease the comparison of the presented electric fields. Figure 3.20 shows a sequence of electric fields for a time interval of 6.0 starting at time $t = 20.0$. At that time, the incident plane wave enters the simulation box and is reaching the beginning of the medium as can be seen in Figure 3.20 a). Following the propagation further in panel b) at time $t = 26.0$, we can see the scattering effects of the medium. Due to the selected medium parameters, the speed of light is half compared to the speed of light in vacuum. Consequently, the wave front outside the medium box already passed the box, whereas the wave front inside passed one half of the box. Shortly later in panel c) at time $t = 32.0$, the center of the external laser pulse passed the medium box. The wave front is dented around the box area and the light diffracts. The figure clearly visualizes the different wave lengths of the laser pulse inside the box, which corresponds to the dispersion rule for a linear medium $\lambda_{lm} = \lambda/\sqrt{\epsilon_{lm}\mu_{lm}}$. The next snapshot in panel d) at time $t = 38.0$ demonstrates one consequence of the retarded light pulse propagation inside the medium box. When the light pulse passed through the box it interferes with the external diffracted light and here the maxima meet and cause a large electric field enhancement right outside the medium box. The electric field is more than three times larger compared to the incident pulse maximum. The same snapshot shows that the external laser left already half of the free Maxwell simulation area and hit the absorbing perfectly matched layer region. The last two panels e) and f) at times $t = 44.0$ respectively $t = 50.0$ visualize the electric field reaction when the external laser left the simulation box.

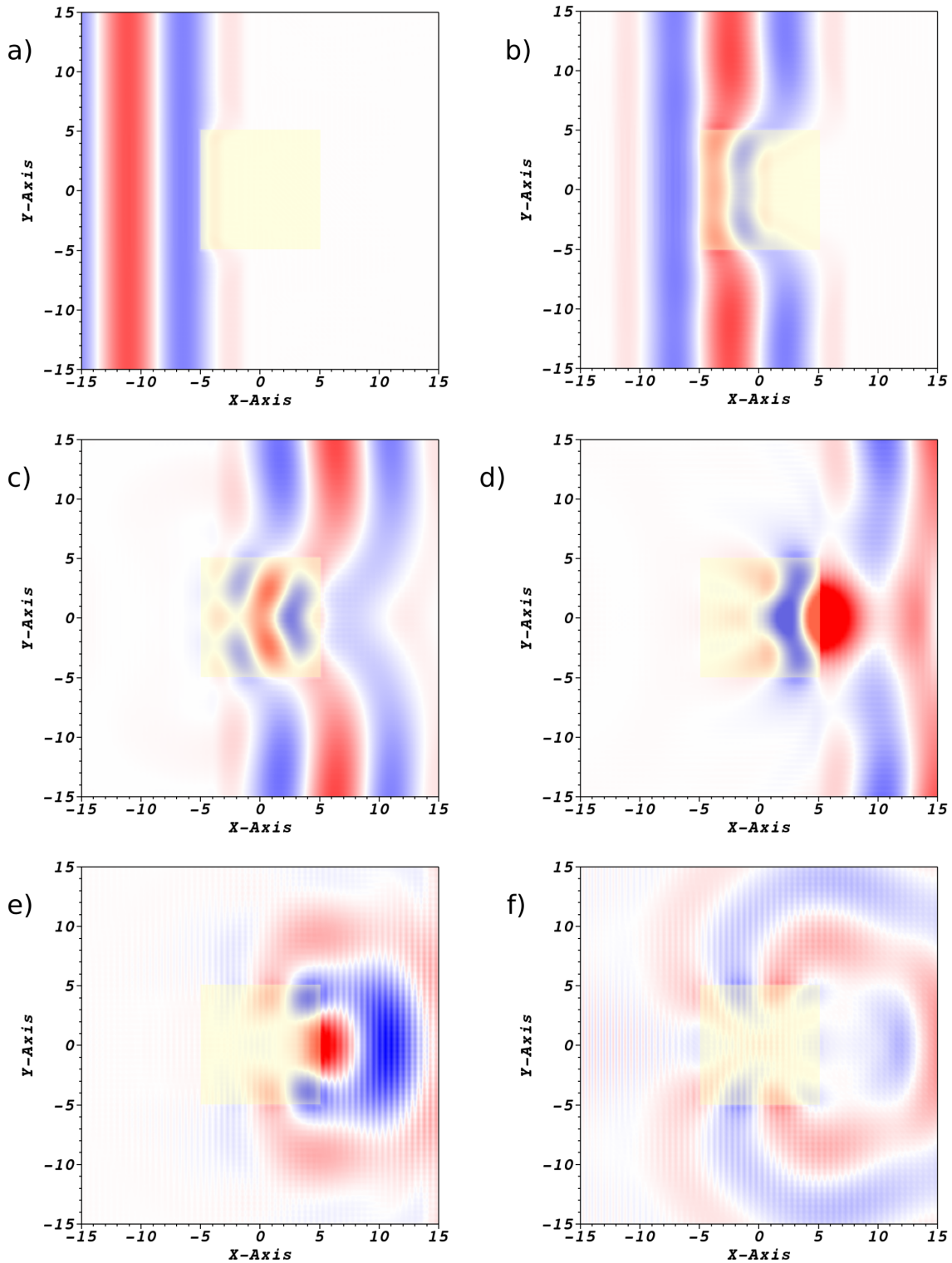


Figure 3.20: Sequence of the electric field simulated by a Riemann-Silberstein Maxwell propagation including a linear medium box. The snapshots were taken for a time interval of 6.0 starting at time $t = 20.0$. The light pulse has already entered the simulation box and hits the medium box in panel a). Following the propagation further in panel b) and c) shows the scattering effects of the medium. The incoming external signal plus the scattered and diffracted field causes a field enhancement, which is shown in panel d). The last two panels e) and f) show the emitted field radiation of the medium box.

Due to the interaction with the medium, there is still a significant electric field inside the box which radiates and slowly decrease in time since the PML absorbs the outgoing field.

The present example of a Maxwell propagation with a linear medium demonstrates that the implemented code can handle arbitrary simulation box designs with a linear medium geometry. In addition to the medium parameters ϵ_{lm} , μ_{lm} and c_{lm} that we used in the application, the implemented Riemann-Silberstein propagator also handles electric σ_e and magnetic conduction σ_m . These parameters are useful to setup mirrors, semi-transparent mirrors or perfect electric conductor mirrors, to simulate cavities or waveguides. Since we considered the Riemann-Silberstein propagation in a more general form, the geometry parameters can be time-dependent which leads us to the important aspect to consider the matter more in detail in the following chapter. Up to now, we only considered matter as a classical linear medium which leads to helicity coupling for the six-component Riemann-Silberstein vector according to Sec. 1.2.4. The question how to replace the classical linear medium as well as the external current density by adequate quantum mechanical variables and proper coupling is discussed in the following chapters 4-6.

Chapter 4

Theoretical fundamentals of light-matter coupling

Quantum electrodynamics (QED) extends the classical electrodynamics that we considered in the previous chapters to a quantum field theory for coupled light-matter systems. In a non-relativistic setting, we use in the present chapter the Pauli equation to build a general Pauli-Fierz Hamiltonian for different species of charged particles which couple to the quantized electromagnetic field. Based on this starting point, we discuss constructively the different levels of Hamiltonians, starting from a non-interacting many-particle Hamiltonian, then a Photon Hamiltonian coupled to a classical current, the longitudinal interaction Hamiltonian and the transverse interaction Hamiltonian. By combining these building blocks, we introduce a multi-species many-particle Hamiltonian for nuclei, electrons, and photons. For this Hamiltonian we establish a quantum electromagnetic density functional theory (QEDFT) for multi-species systems. In the mean-field limit this density functional approach reduces to coupled Maxwell-Pauli-Kohn-Sham equations. In these equations the classical electromagnetic field is determined by the Maxwell's equations in Riemann-Silberstein representation taking the Kohn-Sham current density as the inhomogeneous Maxwell current term. The novel Maxwell-Kohn-Sham equations with Pauli magnetization term are simplified in a last step by considering classical nuclei which obey Ehrenfest dynamics.

4.1 Relativistic covariant notation

In the previous chapters it was convenient to use standard vector notation to describe classical electrodynamics (ED) and non-relativistic quantum mechanics (QM). To extend our level of theory to quantum electrodynamics (QED), it is now beneficial to use additionally relativistic covariant notation.

In relativistic notation the position of the vector component indices matters. Upper and lower indices distinguish two vector types (co- and contravariant vectors) that are connected by the Minkowski metric with the signature $g \equiv (+, -, -, -)$, and matrix form

$$g = g^{\mu\nu} = g_{\nu\mu} = \begin{pmatrix} 1 & 0 & 0 & 0 \\ 0 & -1 & 0 & 0 \\ 0 & 0 & -1 & 0 \\ 0 & 0 & 0 & -1 \end{pmatrix}. \quad (4.1.1)$$

A vector in relativistic theories is a four-component vector denoted with upper Greek

indices. An arbitrary vector a^μ with $\mu = 0, 1, 2, 3$ is given by

$$a^\mu = \begin{pmatrix} a^0 \\ a^1 \\ a^2 \\ a^3 \end{pmatrix}, \quad (4.1.2)$$

whereas a vector with roman indices, i.e., a^k with $k = 1, 2, 3$, is used in the following to represent only the three spatial dimensions

$$\vec{a} = \begin{pmatrix} a^1 \\ a^2 \\ a^3 \end{pmatrix}. \quad (4.1.3)$$

The contravariant counterpart of a^μ is denoted with lower indices a_μ . It is a standard convention to use the Einstein summation convention to sum over repeated upper and lower indices. In general, the contravariant version a_μ of a four-component covariant vector a^μ can be obtained per definition by

$$a_\mu = g_{\mu\nu} a^\nu. \quad (4.1.4)$$

Additionally to the full Minkowski metric $g_{\mu\nu}$, we define the corresponding spatial submatrix g_{kl} with $k = \{1, 2, 3\}$, $l = \{1, 2, 3\}$, and ϵ^{klm} the anti-symmetric Levi-Civita tensor. The following table of equations summarizes the relations between the standard vector notation and the relativistic notation, where we use two four component vectors a^μ , b^μ and a 3x3 matrix M_l^k

$$\vec{a} \equiv a^k, \quad (4.1.5)$$

$$M\vec{a} \equiv M_l^k a^l \quad (4.1.6)$$

$$\vec{a} \cdot \vec{b} \equiv -a^k b_k = -a_k b^k = -a^k b^l g_{lk}, \quad (4.1.7)$$

$$\vec{\nabla} \cdot \vec{a} \equiv \partial_k a^k, \quad (4.1.8)$$

$$a_k = g_{kl} a^l \equiv -\vec{a}, \quad (4.1.9)$$

$$\vec{\nabla} \times \vec{a} \equiv -\epsilon^{klm} \partial_l a_m \quad (4.1.10)$$

$$\epsilon_{klm} = \epsilon^{abc} g_{ak} g_{bl} g_{cm} \quad (4.1.11)$$

In section Sec. (1.1.3), we introduced the curl operation in terms of spin-1 matrices, which appears on the right-hand side of Eq. (1.1.25). It is given by the scalar product $(\vec{\mathbf{S}} \cdot \vec{\nabla})$ of the spin matrices vector $\vec{\mathbf{S}}$ from Eq. (1.1.15) and the Nabla vector. This scalar product in relativistic notation takes the form

$$(\vec{\mathbf{S}} \cdot \vec{\nabla}) = \mathbf{S}^k \partial_k. \quad (4.1.12)$$

Hence, the k-component of the corresponding curl operation in terms of the spin-1 matrices in relativistic notation is with Eq. (4.1.10) expressed by

$$[\vec{\nabla} \times \vec{a}]^k = [-i (\mathbf{S} \cdot \vec{\nabla}) \vec{a}]^k = -i (\mathbf{S}^l \partial_l)_m^k a^m. \quad (4.1.13)$$

In the following, to distinguish the covariant indices from other used indices we put the non-covariant indices in parenthesis.

4.2 Relativistic decomposition of spin particles and derivation of Maxwell's equations

Relativistic particles obey the energy-momentum relation

$$E^2 = m^2 c_0^2 + c_0^2 p_k p^k \quad (4.2.1)$$

for particles with mass like electrons and nuclei, and

$$E^2 = p^k p_k c_0^2 \quad (4.2.2)$$

for massless particles like photons. Substituting $E = i\hbar \frac{\partial}{\partial t}$ and $p^k = -i\hbar \partial^k$ leads to the wave equations

$$\left(E^2 - c_0^2 p_k p^k - m^2 c_0^2 \right) \Psi(\vec{r}, t) = c_0^2 \left(-\frac{\hbar^2}{c_0^2} \partial_t^2 + \hbar^2 \partial^k \partial_k - m^2 c_0^2 \right) \Psi(\vec{r}, t) = 0, \quad (4.2.3)$$

and

$$\left(E^2 - c_0^2 p_k p^k \right) \Psi(\vec{r}, t) = c_0^2 \left(-\frac{\hbar^2}{c_0^2} \partial_t^2 + \hbar^2 \partial^k \partial_k \right) \Psi(\vec{r}, t) = 0. \quad (4.2.4)$$

Both equations are second order differential equations and in general their solutions are scalar plane wave functions and describe spinless particles. In Eq. (4.2.4) the particles are massless and the Klein-Gordon equation in Eq. (4.2.3) takes additionally particle masses into account. Due to the squared expressions in Eqs (4.2.4) and (4.2.3), both terms can be decomposed into

$$c_0^2 \left(-\frac{\hbar}{c_0} \partial_t + \hbar \partial^k - m \right) \left(-\frac{\hbar}{c_0} \partial_t - \hbar \partial_k + m \right) \Psi(\vec{r}, t) = 0. \quad (4.2.5)$$

and

$$c_0^2 \left(-\frac{\hbar}{c_0} \partial_t + \hbar \partial^k \right) \left(-\frac{\hbar}{c_0} \partial_t - \hbar \partial_k \right) \Psi(\vec{r}, t) = 0, \quad (4.2.6)$$

Considering different spin-types, the fundamental energy-momentum relation does not hold for scalar wavefunctions $\psi(\vec{r}, t)$, hence each type of spin requires a specific matrix algebra that transforms the corresponding second order differential equations into a first order differential equation. Dirac used such an ansatz to describe free spin-1/2 particles in space with respect to the relativistic energy-momentum relation and introduced the well known γ matrices with [100]

$$\gamma^0 = \begin{pmatrix} \mathbb{1}_2 & 0 \\ 0 & \mathbb{1}_2 \end{pmatrix}, \quad \gamma^k = \begin{pmatrix} 0 & \sigma^k \\ -\sigma^k & 0 \end{pmatrix}. \quad (4.2.7)$$

The $\mathbb{1}_2$ denotes the two-dimensional identity matrix and σ^k the three Pauli-matrices [100]

$$\sigma^0 = \begin{pmatrix} 1 & 0 \\ 0 & 1 \end{pmatrix}, \quad \sigma^1 = \begin{pmatrix} 0 & 1 \\ 1 & 0 \end{pmatrix}, \quad \sigma^2 = \begin{pmatrix} 0 & -i \\ i & 0 \end{pmatrix}, \quad \sigma^3 = \begin{pmatrix} 1 & 0 \\ 0 & -1 \end{pmatrix}. \quad (4.2.8)$$

The Pauli-matrices are related to each other by

$$\begin{aligned} \sigma^k \sigma^l &= \frac{1}{2} \left(\{ \sigma^k, \sigma^l \} + [\sigma^k, \sigma^l] \right) \\ &= \delta^{kl} \mathbb{1}_2 - i \epsilon^{klj} \sigma_j. \end{aligned} \quad (4.2.9)$$

Due to the four-dimensional Dirac-matrices, the corresponding wavefunctions $\Psi_4(\vec{r}, t)$ have four spinor components. The underlying relativistic energy-momentum relation is with help of Eq. (4.2.3) given by

$$\left(\mathbb{1}_4 E^2 - \mathbb{1}_4 c_0^2 p_k p^k - \mathbb{1}_4 m^2 c_0^2\right) \Psi_4(\vec{r}, t) = c_0^2 \left(-\mathbb{1}_4 \frac{\hbar}{c_0^2} \partial_t^2 + \mathbb{1}_4 \hbar \partial^k \partial_k - \mathbb{1}_4 m^2\right) \Psi_4(\vec{r}, t) = 0. \quad (4.2.10)$$

Using the Dirac-matrices leads to the corresponding decomposition of Eq. (4.2.10) [100]

$$c_0^2 \left(-\gamma_0 \frac{\hbar}{c_0} \partial_t + \hbar \gamma^k \partial_k - \mathbb{1}_4 m\right) \left(-\gamma_0 \frac{\hbar}{c_0} \partial_t - \hbar \gamma^k \partial_k + \mathbb{1}_4 m\right) \Psi_4(\vec{r}, t) = 0. \quad (4.2.11)$$

This decomposition of the basic relativistic wave function can also be applied to massless spin-1 particles, e.g. photons. Photon wave functions $\psi_3(\vec{r}, t)$ are three-dimensional and the energy-momentum relation takes with the three-dimensional identity operator $\mathbb{1}_3$ the form

$$\left(\mathbb{1}_3 E^2 - \mathbb{1}_3 c_0^2 p_k p^k\right) \Psi_3(\vec{r}, t) = \hbar^2 c_0^2 \left(\mathbb{1}_3 \partial^k \partial_k - \mathbb{1}_3 \frac{1}{c_0^2} \partial_t^2\right) \Psi_3(\vec{r}, t) = 0. \quad (4.2.12)$$

The corresponding decomposition requires spin-1 matrices. We introduced them in Eq. (1.1.3) to express an identity operation for the curl, here given by their covariant notation

$$S^1 = \begin{pmatrix} 0 & 0 & 0 \\ 0 & 0 & -i \\ 0 & i & 0 \end{pmatrix}, \quad S^2 = \begin{pmatrix} 0 & 0 & i \\ 0 & 0 & 0 \\ -i & 0 & 0 \end{pmatrix}, \quad S^3 = \begin{pmatrix} 0 & -i & 0 \\ i & 0 & 0 \\ 0 & 0 & 0 \end{pmatrix}. \quad (4.2.13)$$

Similar to the Pauli-matrices, the spin-1 matrices obey the following algebra

$$[S^k, S^l] = -i \epsilon^{klm} S_m, \quad \vec{S}^2 = \mathbb{1}_3. \quad (4.2.14)$$

Although, the spin-1 matrices and higher-order spin-matrices obey the same algebra as the spin-1/2 matrices, their decomposition cannot be written in a pure binomial form. We have to add an additional term as a side condition for the three-dimensional $\Psi_3(\vec{r}, t)$ wavefunctions. The spin-1 decomposition form has been considered in Ref. [69, 70], and is given by

$$\hbar^2 c_0^2 \left(-\mathbb{1}_3 \frac{1}{c_0} \partial_t + S^k \partial_k\right) \left(-\mathbb{1}_3 \frac{1}{c_0} \partial_t - S^k \partial_k\right) \Psi_3(\vec{r}, t) + \hbar^2 c_0^2 \begin{pmatrix} \partial_1^2 & \partial_1 \partial_2 & \partial_1 \partial_3 \\ \partial_2 \partial_1 & \partial_2^2 & \partial_2 \partial_3 \\ \partial_3 \partial_1 & \partial_3 \partial_2 & \partial_3^2 \end{pmatrix} \Psi_3(\vec{r}, t) = 0, \quad (4.2.15)$$

with S^k from Eq. (1.1.3) and the relativistic scalar product of Eq. (4.1.7). The corresponding complex conjugate of Eq. (4.2.15) is

$$\hbar^2 c_0^2 \left(-\mathbb{1}_3 \frac{1}{c_0} \partial_t - S^k \partial_k\right) \left(-\mathbb{1}_3 \frac{1}{c_0} \partial_t + S^k \partial_k\right) \Psi_3^*(\vec{r}, t) + \hbar^2 c_0^2 \begin{pmatrix} \partial_1^2 & \partial_1 \partial_2 & \partial_1 \partial_3 \\ \partial_2 \partial_1 & \partial_2^2 & \partial_2 \partial_3 \\ \partial_3 \partial_1 & \partial_3 \partial_2 & \partial_3^2 \end{pmatrix} \Psi_3^*(\vec{r}, t) = 0. \quad (4.2.16)$$

The two brackets inside the first terms of the left-hand side of Eq. (4.2.15) and Eq. (4.2.16) commute, so that both can be combined into one six-dimensional equation by

$$\begin{aligned} \hbar^2 c_0^2 \left[\begin{pmatrix} 1 & 0 \\ 0 & 1 \end{pmatrix}_{2 \times 2} \otimes \begin{pmatrix} \mathbb{1}_3 & -1 \\ & c_0 \end{pmatrix}_{3 \times 3} \partial_t + \begin{pmatrix} 1 & 0 \\ 0 & -1 \end{pmatrix}_{2 \times 2} \otimes \begin{pmatrix} S^k & \partial_k \end{pmatrix}_{3 \times 3} \right] \left[\begin{pmatrix} 1 & 0 \\ 0 & 1 \end{pmatrix}_{2 \times 2} \otimes \begin{pmatrix} \mathbb{1}_3 & -1 \\ & c_0 \end{pmatrix}_{3 \times 3} \partial_t - \begin{pmatrix} 1 & 0 \\ 0 & -1 \end{pmatrix}_{2 \times 2} \otimes \begin{pmatrix} S^k & \partial_k \end{pmatrix}_{3 \times 3} \right] \begin{pmatrix} \Psi_3(\vec{r}, t) \\ \Psi_3^*(\vec{r}, t) \end{pmatrix} \\ + \hbar^2 c_0^2 \left[\begin{pmatrix} 1 & 0 \\ 0 & 1 \end{pmatrix}_{2 \times 2} \otimes \begin{pmatrix} \partial_1^2 & \partial_1 \partial_2 & \partial_1 \partial_3 \\ \partial_2 \partial_1 & \partial_2^2 & \partial_2 \partial_3 \\ \partial_3 \partial_1 & \partial_3 \partial_2 & \partial_3^2 \end{pmatrix}_{3 \times 3} \right] \begin{pmatrix} \Psi_3(\vec{r}, t) \\ \Psi_3^*(\vec{r}, t) \end{pmatrix} = 0. \end{aligned} \quad (4.2.17)$$

This equation holds if both terms are equal to zero independently, but other combinations are also possible [70]. The first term on the left-hand side of Eq. (4.2.17) is equal to zero, if either

$$\left[\begin{pmatrix} 1 & 0 \\ 0 & 1 \end{pmatrix}_{2 \times 2} \otimes \begin{pmatrix} -\mathbb{1}_3 \hbar \partial_t \end{pmatrix}_{3 \times 3} - \begin{pmatrix} 1 & 0 \\ 0 & -1 \end{pmatrix}_{2 \times 2} \otimes \begin{pmatrix} c_0 \hbar S^k \partial_k \end{pmatrix}_{3 \times 3} \right] \begin{pmatrix} \Psi_3(\vec{r}, t) \\ \Psi_3^*(\vec{r}, t) \end{pmatrix} = 0. \quad (4.2.18)$$

or

$$\left[\begin{pmatrix} 1 & 0 \\ 0 & 1 \end{pmatrix}_{2 \times 2} \otimes \begin{pmatrix} -\mathbb{1}_3 i \hbar \partial_t \end{pmatrix}_{3 \times 3} + \begin{pmatrix} 1 & 0 \\ 0 & -1 \end{pmatrix}_{2 \times 2} \otimes \begin{pmatrix} -i c_0 \hbar S^k \partial_k \end{pmatrix}_{3 \times 3} \right] \begin{pmatrix} \Psi_3(\vec{r}, t) \\ \Psi_3^*(\vec{r}, t) \end{pmatrix} = 0. \quad (4.2.19)$$

In Eq. (4.2.11), the corresponding spin-1/2 4-spinor wavefunction obeys the one particle relativistic equation of motion for a fermion. As before, we consider Eq. (4.2.17) as the relativistic spin-1 equation of motion and $\Psi_3(\vec{r}, t)$ its one particle photon wavefunction. Comparing Eq. (4.2.18) with Eq. (1.1.43) shows that both are equivalent if the Riemann-Silberstein vectors $\vec{F}_+(\vec{r}, t)$, $\Psi_3^*(\vec{r}, t)$, and $\mathcal{F}(\vec{r}, t)$ correspond directly to the one photon wavefunction

$$\vec{F}_+(\vec{r}, t) = \Psi_3(\vec{r}, t), \quad \vec{F}_-(\vec{r}, t) = \Psi_3^*(\vec{r}, t), \quad \mathcal{F}(\vec{r}, t) = \begin{pmatrix} \Psi_3(\vec{r}, t) \\ \Psi_3^*(\vec{r}, t) \end{pmatrix}. \quad (4.2.20)$$

The term on the left-hand side of Eq. (4.2.18) multiplied by the imaginary unit leads to the combined Ampère's and Faraday's law in Riemann-Silberstein representation

$$\left[\begin{pmatrix} 1 & 0 \\ 0 & 1 \end{pmatrix}_{2 \times 2} \otimes \begin{pmatrix} -\mathbb{1}_3 i \hbar \partial_t \end{pmatrix}_{3 \times 3} + \begin{pmatrix} 1 & 0 \\ 0 & -1 \end{pmatrix}_{2 \times 2} \otimes \begin{pmatrix} -i c_0 \hbar S^k \partial_k \end{pmatrix}_{3 \times 3} \right] \mathcal{F}(\vec{r}, t) = [\mathcal{H} - \mathbb{1}_6 i \hbar \partial_t] \mathcal{F}(\vec{r}, t) = 0, \quad (4.2.21)$$

with \mathcal{H} given in Eq. (1.1.41). Considering the second terms on the left-hand side of Eq. (4.2.15) and Eq. (4.2.16), they describe a side condition for each equation. Both terms have to be equal to zero for all times and can be expressed in component notation by

$$\hbar^2 c_0^2 \begin{pmatrix} \partial_1^2 & \partial_1 \partial_2 & \partial_1 \partial_3 \\ \partial_2 \partial_1 & \partial_2^2 & \partial_2 \partial_3 \\ \partial_3 \partial_1 & \partial_3 \partial_2 & \partial_3^2 \end{pmatrix} \Psi_3(\vec{r}, t) = \partial_k \partial_l \Psi_3^l(\vec{r}, t), \quad (4.2.22)$$

$$\hbar^2 c_0^2 \begin{pmatrix} \partial_1^2 & \partial_1 \partial_2 & \partial_1 \partial_3 \\ \partial_2 \partial_1 & \partial_2^2 & \partial_2 \partial_3 \\ \partial_3 \partial_1 & \partial_3 \partial_2 & \partial_3^2 \end{pmatrix} \Psi_3^*(\vec{r}, t) = \partial_k \partial_l \Psi_3^{*l}(\vec{r}, t). \quad (4.2.23)$$

Using Eqs. (4.2.20) and defining the component vector notation for a six-component vector with

$$\mathcal{F}(\vec{r}, t) = \begin{pmatrix} \Psi_3^k(\vec{r}, t) \\ \Psi_3^{*k'}(\vec{r}, t) \end{pmatrix} = \begin{pmatrix} F_+^k \\ F_-^{*k'} \end{pmatrix}, \quad (4.2.24)$$

the two Eqs. (4.2.22) and (4.2.23) can be combined to a six-component vector by

$$\hbar^2 c_0^2 \begin{pmatrix} \partial_k \partial_l F_+^l(\vec{r}, t) \\ \partial_{k'} \partial_{l'} F_-^l(\vec{r}, t) \end{pmatrix} = 0. \quad (4.2.25)$$

This equation holds if

$$\begin{pmatrix} \partial_l F_+^l(\vec{r}, t) \\ \partial_{l'} F_-^l(\vec{r}, t) \end{pmatrix} = \mathcal{D} \cdot \mathcal{F}(\vec{r}, t) = 0 \quad (4.2.26)$$

where we use the six-component divergence operator \mathcal{D} in Eq. (1.1.37) and the dot product definition in Eq. (1.1.39).

We emphasize here, that we thus have derived the classical homogeneous Maxwell's equations starting with Dirac's decomposition Eq.(4.2.17) for the relativistic spin-1 energy-momentum relation and ending with the combination of the homogeneous Faraday's and Ampère's laws in Eq. (4.2.21) and the combination of the homogeneous Gauß laws in Eq.(4.2.26). In contrast to the spin-1/2 particle wavefunction, where its spinor components refer to spin states, the spinor components of the photon wavefunction \mathcal{F} refer to positive and negative helicity. The previous considerations can be repeated for arbitrary spins and particles with mass, but it is not always possible to find simple and physical side conditions.

4.3 Multi-species Hamiltonian

In this section, we use the different parts of the multi-species Hamiltonian which is discussed in Appendix A to build the corresponding total Pauli-Fierz Hamiltonian of the multi-species system. First, we use the matter Hamiltonian of Eq. (A.3.6) coupled to the vector potential $\hat{A}^k(\vec{r}, t)$ instead of $A_{\text{ext}}^k(\vec{r}, t)$. In contrast, we take only the external zero-component $A_{\text{ext}}^0(\vec{r}, t)$ for the second term, since the zero-component of the internal vector potential appears in the longitudinal interaction Hamiltonian term in Eq. (A.5.5). The external scalar potential interaction Hamiltonian $\hat{H}_{\text{mat,int,ext}}^{(n)}$ is given by

$$\hat{H}_{\text{mat,int,ext}}^{(n)}(t) = \int d^3r q A_{\text{ext}}^0(\vec{r}, t) \sum_s \hat{\Phi}_{(n)}^\dagger(\vec{r}, s) \hat{\Phi}_{(n)}(\vec{r}, s). \quad (4.3.1)$$

The free Photon-Hamiltonian $\hat{H}_{\text{Ph,free}}$ for the electromagnetic field does not depend on N and is equal to Eq. (A.4.17)

$$\hat{H}_{\text{Ph,free}} = \int d^3r : \hat{F}_{+,\perp,k}(\vec{r}) \hat{F}_{-,\perp}^k(\vec{r}) : . \quad (4.3.2)$$

The transverse interaction Hamiltonian $\hat{H}_{\text{int}}^\perp$ of Eq. (A.5.14) includes the total current $\hat{j}^k(\vec{r}, t)$ of the system given in Eq.(A.5.12) that arises from the N species plus the external current, and reads

$$\hat{H}_{\text{int}}^\perp(t) = \frac{1}{c_0} \int d^3r \hat{j}^k(\vec{r}, t) \hat{A}_k(\vec{r}, t). \quad (4.3.3)$$

Taking Eqs. (A.5.5) and (A.5.4) gives the longitudinal interaction Hamiltonian $\hat{H}_{\text{int}}^\parallel$ with

$$\begin{aligned} \hat{H}_{\text{int}}^\parallel(t) &= \frac{1}{2c_0} \int d^3r \sum_n : \hat{j}_{\text{mat},(n)}^0(\vec{r}) \hat{A}_{\text{int},(n)}^0(\vec{r}) : \\ &+ \frac{1}{2c_0^2} \int d^3r d^3r' w(\vec{r}, \vec{r}') \sum_n : \hat{j}_{\text{mat},(n)}^0(\vec{r}) \hat{j}_{\text{mat},(n)}^0(\vec{r}') : . \end{aligned} \quad (4.3.4)$$

Finally, adding all previous terms and summing over all different N species leads to the complete N-species Pauli-Fierz Hamiltonian

$$\hat{H} = \sum_{n=1}^N \left\{ \hat{H}_{\text{mat,kin}}^{(n)}(t) + \hat{H}_{\text{mat,int,ext}}^{(n)}(t) + \hat{H}_{\text{mat,Stern}}^{(n)}(t) \right\} + \hat{H}_{\text{Ph,free}} + \hat{H}_{\text{int}}^{\perp}(t) + \hat{H}_{\text{int}}^{\parallel}(t) . \quad (4.3.5)$$

The total vector potential $\hat{A}^{\mu}(\vec{r}, t)$

$$\hat{A}^{\mu}(\vec{r}, t) = \hat{A}_{\text{mat}}^{\mu}(\vec{r}, t) + \hat{A}_{\text{ext}}^{\mu}(\vec{r}, t) \quad (4.3.6)$$

and the total current density $\hat{j}^{\mu}(\vec{r}, t)$

$$\hat{j}^{\mu}(\vec{r}, t) = \hat{j}_{\text{mat}}^{\mu}(\vec{r}, t) + \hat{j}_{\text{ext}}^{\mu}(\vec{r}, t) \quad (4.3.7)$$

are coupled in Coulomb gauge by the inhomogeneous Maxwell's Eqs. (A.5.7) and (A.4.13). Hence, we obtain

$$\begin{aligned} \hat{A}^0(\vec{r}, t) &= \frac{1}{c_0} \int d^3r' w(\vec{r}, \vec{r}') \left(\hat{j}_{\text{mat}}^0(\vec{r}', t) + j_{\text{ext}}^0(\vec{r}', t) \right) + A_{\text{ext}}^0(\vec{r}, t) , \quad (4.3.8) \\ (\partial_0^2 + \partial_l \partial^l) \hat{A}^k(\vec{r}) &= \mu_0 c_0 \left(\hat{j}_{\text{mat}}^k(\vec{r}, t) + j_{\text{ext}}^k(\vec{r}, t) \right) - \partial^k \partial^0 \frac{1}{c_0} \int d^3r' w(\vec{r}, \vec{r}') \hat{j}_{\text{mat}}^0(\vec{r}', t) . \end{aligned} \quad (4.3.9)$$

Substituting the last term in Eq. (4.3.9) with the longitudinal current density Eq. (A.4.14), here in terms of the internal current density j_{mat}^k leads to

$$\begin{aligned} (\partial_0^2 + \partial_l \partial^l) \hat{A}^k(\vec{r}, t) &= \mu_0 c_0 \left(\hat{j}_{\text{mat}}^k(\vec{r}, t) + j_{\text{ext}}^k(\vec{r}, t) \right) - \mu_0 c_0 \hat{j}_{\text{mat},\parallel}^k(\vec{r}, t) \\ \Leftrightarrow (\partial_0^2 + \partial_l \partial^l) \hat{A}^k(\vec{r}, t) &= \mu_0 c_0 \left(\hat{j}_{\text{mat},\perp}^k(\vec{r}, t) + j_{\text{ext}}^k(\vec{r}, t) \right) . \end{aligned} \quad (4.3.10)$$

Referring Eq. (A.5.7), the zero-component of the external current modifies the external A_{ext}^0 , and therefore it does not appear in Maxwell's equations. According to Appendix A.4, we can equivalently express the inhomogeneous Maxwell's equations, Eq. (4.3.9), in terms of the Riemann-Silberstein vector. Adapting Eqs. (A.4.18)-(A.4.21) with the total field vectors $\vec{F}_{\pm}^{\mu}(\vec{r}, t)$ and current density $\hat{j}^{\mu}(\vec{r}, t)$ leads to the underlying quantized Maxwell's equations in Riemann-Silberstein representation

$$i\hbar \partial_t \hat{F}_{\pm}^k(\vec{r}, t) = \mp i\hbar c_0 \left(S^l \partial_l \right)_m^k \hat{F}_{\pm}^m(\vec{r}, t) - i \frac{\hbar}{\sqrt{2\epsilon_0}} \left(\hat{j}_{\text{mat}}^k(\vec{r}, t) + j_{\text{ext}}^k(\vec{r}, t) \right) , \quad (4.3.11)$$

$$\partial_k \hat{F}_{\pm}^k(\vec{r}, t) = \sqrt{\frac{1}{2\epsilon_0}} \hat{j}_{\text{mat}}^0(\vec{r}, t) . \quad (4.3.12)$$

In principle, the N-species Pauli-Fierz Hamiltonian in Eq. (4.3.5) determines the non-relativistic light-matter system that consists of N different species. Since the Hamiltonian is described in Fock-space, the corresponding wave function Ψ has no fixed particle number, for both particles with mass and for photons. Due to the arising infinite degrees of freedom, it is not possible to apply the common wavefunction-based Hamiltonian formalism to solve the problem. Even the constraint of a fixed particle number does not lead to a solution, since the photon degrees of freedom are still infinite.

However, to deal with such systems, one can also fix the photon particle number by describing few photon modes, e.g. in a photon cavity [48, 57]. Another possible way is to describe such a large number of photons with arbitrary modes, that their electromagnetic

field expectation value becomes classical [101]. In this case, the corresponding vector potential becomes also classical. The matter system is still quantized, but trying to solve the many-body problem is very restricted to only few particles since the degrees of freedom of all particles, which are coupled to each other, increase exponentially. One method to deal with such problems of large coupled many-particle systems is density functional theory (DFT) [66]. In recent work the standard density functional theory has been extended to quantum-electrodynamical density-functional theory (QEDFT). In the following section, we transform the N-species Pauli-Fierz Hamiltonian of Eq. (4.3.5) into a multi-species Hamiltonian of quantum-electrodynamical density-functional theory.

4.4 Quantum-electrodynamical density-functional theory for multi species

Many-body Schrödinger equations are not solvable for a large number of particles to obtain the corresponding wavefunctions due to their amount of degrees of freedom. To circumvent this situation, the common density functional formalism [66, 67] circumvents the actual degrees of freedom by calculating all measurable observables $\hat{O}_{(n)}$ in terms of the particle densities $n_{(n)}$ of species n instead of the many-body wave functions $\Psi_{(n)}$. The species wavefunction $\Psi_{(n)}$ depends on $3N_{(n)}$ coordinates

$$\Psi_{(n)} = \Psi_{(n)}(\vec{r}_1, \vec{r}_2, \dots, \vec{r}_{N_{(n)}}), \quad (4.4.1)$$

whereas the corresponding particle density

$$n_{(n)}(\vec{r}) = N_{(n)} \int d^3r_2 \dots d^3r_{N_{(n)}} |\Psi_{(n)}(\vec{r}, \vec{r}_2, \dots, \vec{r}_{N_{(n)}})|^2 \quad (4.4.2)$$

depends only on 3 coordinates. Using the Hohenberg-Kohn theorem [102], there is a one-to-one correspondence between the ground state wavefunction $\Psi_{(n,0)}(\vec{r}, \vec{r}_2, \dots, \vec{r}_{N_{(n)}})$ expressed by the coordinates and $\tilde{\Psi}_{(n,0)}[n_{(n)}(\vec{r})]$ given in terms of the particle density $n_{(n)}(\vec{r})$

$$\Psi_{(n,0)}(\vec{r}, \vec{r}_2, \dots, \vec{r}_{N_{(n)}}) \rightarrow \tilde{\Psi}_{(n,0)}[n_{(n)}(\vec{r})]. \quad (4.4.3)$$

This means that all ground state observables \hat{O} , which are usually expressed in terms of $\Psi_{(n,0)}(\vec{r}, \vec{r}_2, \dots, \vec{r}_{N_{(n)}})$ with

$$\langle \hat{O}_{(n)} \rangle = \langle \Psi_{(n,0)}(\vec{r}, \vec{r}_2, \dots, \vec{r}_{N_{(n)}}) | \hat{O}_{(n)} | \Psi_{(n,0)}(\vec{r}, \vec{r}_2, \dots, \vec{r}_{N_{(n)}}) \rangle \quad (4.4.4)$$

can be also expressed in terms of the particle density $n_{(n)}(\vec{r})$

$$\langle \hat{O}_{(n)} \rangle = \langle \tilde{\Psi}_{(n,0)}[n_{(n)}(\vec{r})] | \hat{O}_{(n)} | \tilde{\Psi}_{(n,0)}[n_{(n)}(\vec{r})] \rangle. \quad (4.4.5)$$

Consequently, the species current density $\vec{j}_{(n)}$ can be described in terms of $\tilde{\Psi}_{(n,0)}[n_{(n)}(\vec{r})]$. This gives us the opportunity to employ the Runge-Gross theorem [103, 67], here on the non-relativistic level of the Pauli-Fierz Hamiltonian. The one-to-one correspondence using the Pauli-Fierz Hamiltonian for one species was proofed in Ref. [104], in that case for electrons. Following those steps conceptually and expanding the proof by using properties of the total wavefunctions Ψ , which solve the Schrödinger equation using the multi-species Hamiltonian of Eq. (4.3.5), leads to the corresponding proof for N species [63]. We note,

the proof is based on the assumptions that the external vector potential $\vec{A}_{\text{ext}}(\vec{r}, t)$ is given in Coulomb gauge by

$$\partial_k \vec{A}_{\text{ext}}^k(\vec{r}, t) = 0, \quad (4.4.6)$$

and the external current density has also to be transverse

$$\partial_k \vec{j}_{\text{ext}}^k(\vec{r}, t) = 0. \quad (4.4.7)$$

This important one-to-one correspondence is the basis of constructing a Maxwell-Pauli-Kohn-Sham scheme in the next section.

4.5 Coupled Maxwell-Pauli-Kohn-Sham equations

Explicitly solving for the wavefunction of the generalized N -species Pauli-Fierz Hamiltonian in Eq. (4.3.5) is computationally not feasible. However, instead of solving the full problem, we can find an auxiliary effective non-interacting system that has the same densities. In the following the index \mathbf{s} represents the variables of this non-interacting system. This so called Kohn-Sham construction [105, 106, 104, 107] exploits the previously discussed one-to-one correspondence in Sec. 4.4, which leads to a bijection between external and internal matter pairs

$$\left(A_{\text{ext},(\mathbf{s})}^\mu, j_{\text{ext},(\mathbf{s})}^k \right) \leftrightarrow \left(j_{\text{mat}}^\mu, A_{\text{mat}}^k \right). \quad (4.5.1)$$

Since the one-to-one correspondence also holds for the non-interacting system, we can find two mappings with

$$\begin{aligned} \left(j_{\text{mat}}^\mu, A_{\text{mat}}^k \right) &\mapsto \left(A_{\text{mat}}^\mu, j_{\text{ext}}^k \right) \\ \left(j_{\text{mat}}^\mu, A_{\text{mat}}^k \right) &\mapsto \left(A_{\text{mat},(\mathbf{s})}^\mu, j_{\text{ext},(\mathbf{s})}^k \right), \end{aligned} \quad (4.5.2)$$

which maps the internal matter variables j_{mat}^μ and A_{mat}^k to external external ones based on first the interacting species wavefunction $\Psi_{(n)}$ and second on the non-interacting wavefunction $\Phi_{(\mathbf{s},n)}$. At this point, the extended Runge-Gross theorem for multi-species of Sec. 4.4 shows that the full coupled problem is equivalent to the non-interacting problem using effective currents and potentials. This non-interacting Kohn-Sham picture includes an uncoupled photon field. Instead of solving this photon field with infinitely many degrees of freedom, we equivalently use the classical inhomogeneous Maxwell's equations [104], since both descriptions, the classical field as well as the full quantized field lead per construction to the same internal matter vector potential A_{mat}^k . As a consequence, we select a non-interacting wavefunction $\Phi_{(\mathbf{s},n,0)}$, which obeys [63]

$$\left\langle \Psi_{(n,0)} \left| \hat{j}_{\text{mat}}^0 \Psi_{(n,0)} \right. \right\rangle = \left\langle \Phi_{(\mathbf{s},n,0)} \left| \hat{j}_{\text{mat}}^0 \Phi_{(\mathbf{s},n,0)} \right. \right\rangle. \quad (4.5.3)$$

Since this expectation value is equivalent to the initial matter charge density $j_{\text{mat}}^0 = \rho_{\text{mat}}$ [63], this condition determines the initial Maxwell field by using the Gauß law. Next, we consider the relations of the external current densities $j_{\text{ext}}^k, j_{\text{ext},(\mathbf{s})}^k$. Using the linearity of Maxwell's equations both mappings of the interacting external current density and the non-interacting current density are equal, and hence

$$j_{\text{ext}}^k \left[j_{\text{mat}}^\nu, A_{\text{mat}}^l \right] = j_{\text{ext},(\mathbf{s})}^k \left[j_{\text{mat}}^\nu, A_{\text{mat}}^l \right]. \quad (4.5.4)$$

Taking all previous considerations into account, we can follow the Kohn-Sham construction of Ref. [107], which requires the introduction of a mean-field exchange-correlation (mxc) potential A_{mxc}

$$A_{\text{mxc}} = A_{\text{ext},(\mathbf{s})}^{\mu} \left[j_{\text{mat}}^{\nu}, A_{\text{ext}}^l \right] - A_{\text{ext}}^{\mu} \left[j_{\text{mat}}^{\nu}, A_{\text{ext}}^l \right]. \quad (4.5.5)$$

The non-interacting potential $A_{\text{ext},(\mathbf{s})}^{\mu}$ is usually denoted as Kohn-Sham potential A_{KS}^{μ} and reads with Eq. (4.5.5)

$$A_{\text{KS}}^{\mu} = A_{\text{mxc}} + A_{\text{ext}}^{\mu}. \quad (4.5.6)$$

We emphasize, that in case of having an exact mean-field exchange-correlation potential A_{mxc} , the solution of the coupled MPKS problem leads to the exact internal matter pair $(j_{\text{mat}}^{\mu}, A_{\text{mat}}^k)$ for a given generalized Pauli-Fierz Hamiltonian $\hat{H} [A_{\text{ext}}^{\mu}, j_{\text{ext}}^k]$.

Finally, the initial wavefunctions Ψ , or $\Phi_{(\mathbf{s})}$ of the considered species have to be distinguished between anti-symmetric ones describing fermions and symmetric ones for bosons. Tensor products of Slater determinants and permanents obey the corresponding feature [108] Taking this and the Kohn-Shame scheme into account, we can find the auxiliary Maxwell-Pauli-Kohn-Sham (MPKS) equation

$$i\partial_t \phi_{(n,i)}(\vec{r}, s_{(n)}, t) = \left\{ \mathcal{P}_{(n),k} \mathcal{P}_{(n)}^k - qA_{\text{KS}}^0 + \frac{q\hbar}{2M_{(n)}c_0} S_k^{(n)} \epsilon^{klm} \partial_l A_{\text{KS}}^m \right\} \phi_{(n,i)}(\vec{r}, s_{(n)}, t). \quad (4.5.7)$$

with the canonical momentum

$$\mathcal{P}_{(n)}^k = -i\hbar\partial^k - \frac{q}{c_0} A_{\text{KS}}^k. \quad (4.5.8)$$

The MPKS equation describes the Schrödinger equation with Pauli term for non-interacting one-particle Kohn-Sham orbitals $\phi_{(n,i)}(\vec{r}, s_{(n)}, t)$. Depending on bosons or fermions, total wavefunction is symmetric or anti-symmetric. In case of bosons, the corresponding symmetric wavefunction of \mathcal{N} -particles of species n is a normalized permanent [108]

$$\Phi_{\text{sym},(n)}(\vec{r}_1, s_{(n,1)}; \dots; \vec{r}_{\mathcal{N}}, s_{(n,\mathcal{N})}) = \sqrt{\frac{1}{\mathcal{N}! \prod_k m_k!}} \sum_p \phi_{(n)}(\vec{r}_{p(1)}, s_{(n,1)}) \dots \phi_{(n)}(\vec{r}_{p(\mathcal{N})}, s_{(n,\mathcal{N})}) \quad (4.5.9)$$

with permutations p acting on \mathcal{N} -particles. The product symbol Π multiplies the factorial m_k , the quantity for the number of times each single particle states k appears in the state. The fermion wavefunction is antisymmetrized by the normalized Slater determinant with

$$\Phi_{\text{a-sym},(n)}(\vec{r}_1, s_{(n,1)}; \dots; \vec{r}_{\mathcal{N}}, s_{(n,\mathcal{N})}) = \sqrt{\frac{1}{\mathcal{N}!}} \sum_p \text{sgn}(p) \phi_{(n)}(\vec{r}_{p(1)}, s_{(n,1)}) \dots \phi_{(n)}(\vec{r}_{p(\mathcal{N})}, s_{(n,\mathcal{N})}) \quad (4.5.10)$$

where $\text{sgn}(p)$ denotes the sign of each permutation. The Kohn-Sham orbitals are spin-dependent according to their species spin and represented by the index $s_{(n)}$.

From Eqs. (4.4.4), (4.4.5) and the one-one-correspondence Eq. (4.5.1), we know that for the ground state we have

$$\left\langle \Psi_{(n,0)} \left| \hat{j}_{\text{mat}}^{\mu} \right| \Psi_{(n,0)} \right\rangle = \left\langle \Phi_{(\mathbf{s},n,0)} \left| \hat{j}_{\text{mat}}^{\mu} \right| \Phi_{(\mathbf{s},n,0)} \right\rangle, \quad (4.5.11)$$

which gives the initial classical current density. However, in general for arbitrary excited states the classical exact current density cannot be obtained by the non-interacting state $\Phi_{(s,n)}$. In principle, the current density has to be described by current density functionals [109], which is not included in our implementation. Nevertheless, we approximate the exact current density by taking the non-interacting wavefunctions $\Phi_{(s,n)}$ to get j_{mat}^μ also beyond the ground state. Taking the operator valued Maxwell's Eqs. (4.3.8) and (4.3.10) classically, turns to the classical Maxwell's equation in terms of the total vector potential A^μ of the system

$$A^0(\vec{r}, t) = \frac{1}{c_0} \int d^3r' w(\vec{r}, \vec{r}') (j_{\text{mat}}^0(\vec{r}', t) + j_{\text{ext}}^0(\vec{r}', t)) + A_{\text{ext}}^0(\vec{r}, t), \quad (4.5.12)$$

$$(\partial_0^2 + \partial_l \partial^l) A^k(\vec{r}, t) = \mu_0 c_0 \left(j_{\text{mat}, \perp}^k(\vec{r}, t) + j_{\text{ext}}^k(\vec{r}, t) \right). \quad (4.5.13)$$

Consequently, the operator valued Riemann-Silberstein Maxwell's Eqs (4.3.11)-(4.3.12) become classical equations with

$$i\hbar \partial_t F_{\pm}^k(\vec{r}, t) = \mp i\hbar c_0 \left(S^l \partial_l \right)_m^k F_{\pm}^m(\vec{r}, t) - i \frac{\hbar}{\sqrt{2\epsilon_0}} \left(j_{\text{mat}}^k(\vec{r}, t) + j_{\text{ext}}^k(\vec{r}, t) \right), \quad (4.5.14)$$

$$\partial_k F_{\pm}^k(\vec{r}, t) = \sqrt{\frac{1}{2\epsilon_0}} j_{\text{mat}}^0(\vec{r}, t), \quad (4.5.15)$$

which determines the classical electromagnetic field of the total system.

We emphasize here that only the two coupled systems together, i.e., the electron-nucleus system and the photon field, without external fields are invariant with respect to the total momentum and total angular momentum of the coupled matter-photon system [62]. Consequently, translating or rotating only the matter system breaks this symmetry.

Due to the Kohn-Sham potential A_{KS}^μ used in Eq. (4.5.7) and the physical total potential A^μ in Eq. (4.5.13), we have in principle to find a relation between those two potentials.

At this point we note that we have quite some freedom in establishing the mappings as well as the MPKS systems. For instance, we can look at each individual particle-species' internal current and find that also each species' internal current can be used to establish a mapping individually. We could then (unphysically) assume that each species sees a different external field and then establish purpose built $A_{\text{mxc},(n)}^\mu$. Building the complete mxc potentials step by step could lead to an easier established and more accurate approximation for the mxc potentials. We do not discuss this issue in this work, but try to find a first approximation to simplify the MPKS construction, because even solving the coupled generalized Pauli-Fierz problem in terms of single-particle equations. Furthermore, for the initial states, which can be determined from a ground-state reformulation of the generalized Pauli-Fierz problem following Ref. [50], it is often beneficial to make the Born-Oppenheimer approximation and treat the nuclei semi-classically.

Since finding $A_{\text{mxc},(n)}^\mu$ is a non-trivial problem, we use later in the applications the mean-field approximation

$$A_{\text{KS}}^0 = A_{\text{mat}}^0 + A_{\text{ext}}^0 + A_{\text{xc}}^0, \quad (4.5.16)$$

$$A_{\text{KS}}^k \approx A_{\text{mat}}^k + A_{\text{ext}}^k = A^k, \quad (4.5.17)$$

where A_{xc}^0 denotes the scalar exchange correlation functional [67].

4.6 Classical limit for Nuclei

In general, nuclei consists of protons and neutrons, which are have almost the same mass as protons. The fact that nuclei are much heavier than the electrons leads to very different

time scales of motion, which means that the electrons are significantly faster than the nuclei. This feature is usually exploited by treating the nuclei classical. Although there are more advanced alternatives, e.g., factorization of electron-nuclear wavefunctions [33, 34], we illustrate in the present section how to simplify our MPKS scheme by describing the nuclei classically.

As a first step, we neglect the Stern-Gerlach term, since this term is suppressed with respect to the other fields by $1/M_{(n)}$. In a next step, we express the spatial orbitals in polar representation

$$\phi_{(n,i)}(\vec{r}, t) = |\phi_{(n,i)}(\vec{r}, t)| e^{(i/\hbar)S_{(n,i)}(\vec{r}, t)}, \quad (4.6.1)$$

and substitute Eq. (4.6.1) into the MPKS Eq. (4.5.7). After dropping the last term (Stern-Gerlach term), we find a Hamilton-Jacobi-type equation for the phase $S_{(n,i)}(\vec{r}, t)$ [110]

$$\partial_t S_{(n,i)}(\vec{r}, t) = -\frac{\left(\vec{\nabla} S_{(n,i)}(\vec{r}, t) - \frac{q_{(n)}}{c_0} \vec{A}_{\text{KS}}(\vec{r}, t)\right)^2}{2M_{(n)}} - q_{(n)} A_{\text{KS}}^0(\vec{r}, t) + \frac{\hbar^2}{2M_{(n)}} \frac{\vec{\nabla}^2 |\phi_{(n,i)}(\vec{r}, t)|}{|\phi_{(n,i)}(\vec{r}, t)|}, \quad (4.6.2)$$

In a next step, we express the classical observables by their quantum variables. Starting with the matter current

$$\tilde{j}_{\text{mat}}^k(\vec{r}, t) = j_{\text{pmc}}^k(\vec{r}, t) + j_{\text{dmc}}^k(\vec{r}, t) \quad (4.6.3)$$

from Eq.(A.5.8) without the magnetization current j_{mc}^k , we find

$$\begin{aligned} \vec{j}_{(n,i)}(\vec{r}, t) &= \vec{j}_{\text{pmc}}^{(n,i)}(\vec{r}, t) + \vec{j}_{\text{dmc}}^{(n,i)}(\vec{r}, t) \\ &= \frac{q_{(n)}}{M_{(n)}} |\phi_{(n,i)}(\vec{r}, t)| \vec{\nabla} S_{(n,i)}(\vec{r}, t) - \frac{q_{(n)}^2}{M_{(n)} c_0} \vec{A}_{\text{KS}}(\vec{r}, t) |\phi_{(n,i)}(\vec{r}, t)|. \end{aligned} \quad (4.6.4)$$

Furthermore, the total velocity field becomes

$$\vec{v}_{(n,i)}(\vec{r}, t) = \frac{\vec{j}_{(n,i)}(\vec{r}, t)}{q_{(n)} |\phi_{(n,i)}(\vec{r}, t)|} = \frac{1}{M_{(n)}} \left(\vec{\nabla} S_{(n,i)}(\vec{r}, t) - \frac{q_{(n)}}{c_0} \vec{A}_{\text{KS}}(\vec{r}, t) \right), \quad (4.6.5)$$

and accordingly we can define the total momentum field $\vec{p}_{(n,i)} = \vec{v}_{(n,i)}/M_{(n)}$. Next, we take the classical limit $\hbar \rightarrow 0$ for the nuclei, and the quantum-potential contribution (last term) in Eq. (4.6.2) goes to zero. The remaining terms can be expressed by

$$\partial_t S_{(n,i)}(\vec{r}, t) = -\left(\vec{v}_{(n,i)}(\vec{r}, t) \cdot \vec{\nabla}\right) \vec{p}_{(n,i)}(\vec{r}, t) - q_{(n)} A_{\text{KS}}^0(\vec{r}, t) + \frac{q_{(n)}}{M_{(n)}} \vec{p}_{(n,i)}(\vec{r}, t) \times \vec{B}_{\text{KS}}(\vec{r}, t), \quad (4.6.6)$$

where $\vec{B}_{\text{KS}}(\vec{r}, t) = \frac{1}{c_0} \vec{\nabla} \times \vec{A}_{\text{KS}}(\vec{r}, t)$. Next, we add the partial time-derivative of the Kohn-Sham vector potential to both sides and define the total derivative for a co-moving reference frame that moves with the velocity field $\vec{v}_{(n,i)}$ with

$$\dot{\vec{p}}_{(n,i)}(\vec{r}, t) = \partial_t \vec{p}_{(n,i)}(\vec{r}, t) + \left(\vec{v}_{(n,i)}(\vec{r}, t) \cdot \vec{\nabla}\right) \vec{p}_{(n,i)}(\vec{r}, t). \quad (4.6.7)$$

Using both, turns Eq. (4.6.7) into the classical Lorentz equation

$$\dot{\vec{p}}_{(n,i)}(\vec{r}, t) = q_{(n)} \vec{v}_{(n,i)}(\vec{r}, t) \times \vec{B}_{\text{KS}}(\vec{r}, t) + q_{(n)} \vec{E}_{\text{KS}}(\vec{r}, t). \quad (4.6.8)$$

We exploit here, that $-\partial_0 \vec{A}_{\text{KS}} = E_{\text{KS},\perp}$ and $-\vec{\nabla} A_{\text{KS}}^0 = \vec{E}_{\text{KS},\parallel}$ gives the transverse and longitudinal Kohn-Sham electric field such that $E_{\text{KS}} = E_{\text{KS},\perp} + \vec{E}_{\text{KS},\parallel}$. It can be solved by

the method of characteristics, i.e., we can follow a specific classical trajectory that starts at $\vec{r}_{(n,i)}$ and $\vec{p}_{(n,i)}$. The initial wave function then gives us the initial distribution of these trajectories. This classical approximation determines the charge current of the nuclei that contributes to the total current and also to the Kohn-Sham vector potential A_{KS}^μ . We denote this limit of classical nuclei for our MPKS scheme the Ehrenfest-Maxwell-Pauli-Kohn-Sham (EMPKS) approach, analogous to matter-only quantum dynamics.

Chapter 5

Maxwell-Pauli-Kohn-Sham propagation on a three-dimensional grid

In chapter 4, we introduced a theory to describe molecular many-body systems in terms of a density-functional theory based on quantum electrodynamics (QED). Furthermore, we argued why a full QED calculation is not feasible for large systems. As a consequence, we first assume slowly moving particles (Pauli description) and a semiclassical description of the Maxwell fields. In this way, we have two coupled systems, the quantum mechanical Kohn-Sham system and the classical Maxwell system.

Usually the semiclassical picture is simplified further by considering only the electromagnetic field-to-matter coupling, but no back reaction, i.e., matter does not influence the transverse electric field. In this case, the Maxwell field has an external component and a purely longitudinal internal component. The external field interacts with the matter, i.e., induces electric currents and charge motion inside the matter, but the matter does not act back on the transverse degrees of the electric field. Thus, the external electromagnetic field propagates freely. In this approximation, the total electromagnetic field is a superposition of the external field and the internal field is purely longitudinal due to the Coulomb interaction. This approach is valid for many cases, especially small systems. But the influence of the external electric field can be large enough to induce a significant back-reaction of matter such that an effective screening or polarization appears. This happens when significant currents are present in the system. Hence, the backward coupling of matter to light becomes important. In the chapters 1-3, we introduced the Riemann-Silberstein formalism of Maxwell fields and developed a numerical propagation scheme to solve inhomogeneous Maxwell equations in a similar manner as is done in quantum mechanics for the time-dependent Schrödinger equation. We can use the same time-evolution method for the propagation of Kohn-Sham orbitals. We consider the electrons as the only quantum mechanical species, which we described in chapter 4. The nuclei are treated as classical particles, which obey the Ehrenfest equations [111].

In this chapter, we introduce our full coupled Ehrenfest-Maxwell-Pauli-Kohn-Sham system. Therefore, we use the Kohn-Sham charge and current density as the inhomogeneity. We use them to adapt the microscopic Riemann-Silberstein Maxwell's equation, such that these quantum-mechanical based variables couple to the classical electromagnetic field. In turn, we use the 'minimal coupling' for the electromagnetic field to matter coupling. Additionally, we transform the Kohn-Sham Hamiltonian with the Power-Zienau-Woolley transformation to get a gauge independent light-matter coupling in terms of the electro-

magnetic field variables instead of the gauge dependent vector potential. The electric multipole interaction terms in turn require only transverse components of the electromagnetic field, which we obtain by a Helmholtz decomposition by solving a Poisson equation for each field dimension. Our full propagation on two separated coupled grids leads to various combination possibilities for the different grids which we introduce. Furthermore, the different physical length and time scales for light and matter demand a multi-scale consideration in space and time. In order to solve the coupled Maxwell-Kohn-Sham propagation, we describe a efficient self-consistent propagation scheme. In the final part of this chapter, we consider the Maxwell-matter system as an open quantum system and introduce electromagnetic detectors to measure directly the outgoing electromagnetic field.

5.1 Riemann-Silberstein Maxwell's equations with Kohn-Sham current density

In section Sec. 1.1.5 we have introduced the microscopic Riemann-Silberstein Maxwell's equations and the six-component vector $\mathcal{F}(\vec{r}, t)$. They describe the Maxwell fields in vacuum in the presence of the charge density $\rho(\vec{r}, t)$ and the current density $\vec{j}(\vec{r}, t)$ which are represented by the $\mathcal{Q}(\vec{r}, t)$ in Eq. (1.1.36) and by the $\mathcal{J}(\vec{r}, t)$ in Eq. (1.1.42). Since we want to describe coupled Maxwell-Kohn-Sham systems, we apparently have to express the classical variables $\mathcal{Q}(\vec{r}, t)$ and $\mathcal{J}(\vec{r}, t)$ in Eq. (1.1.40) and Eq. (1.1.37) in terms of the corresponding quantum-mechanical Kohn-Sham expectation values. All Kohn-Sham variables for the selected species n depend on the Kohn-Sham density $n_{(n,i)}(\vec{r}, s_{(n)})$. According to Sec. 4.5 each species is described by auxiliary one-particle Kohn-Sham orbitals $\phi_{(n,i)}(\vec{r}, s_{(n)})$ and the particle density $n_{(n,i)}(\vec{r}, s_{(n)})$ is given by

$$n_{(n,i)}(\vec{r}, s_{(n)}) = |\phi_{(n,i)}(\vec{r}, s_{(n)})|^2. \quad (5.1.1)$$

Using Eqs. (A.5.1) with the Kohn-Sham wavefunctions leads to $j^0(\vec{r})$

$$j^0(\vec{r}, t) = \sum_{n=1}^N c_0 q_{(n)} \sum_i^{I_{(n)}} \sum_{s_{(n)}} n_{(n,i)}(\vec{r}, s_{(n)}, t). \quad (5.1.2)$$

With the Riemann-Silberstein charge density Eq. (1.1.36), $\mathcal{Q}(\vec{r}, t)$ reads

$$\mathcal{Q}(\vec{r}, t) = \begin{pmatrix} 1 \\ 1 \end{pmatrix}_{2 \times 1} \otimes \left(\frac{1}{c_0 \sqrt{2\epsilon_0}} j^0(\vec{r}, t) \right)_{1 \times 1}. \quad (5.1.3)$$

For the Riemann-Silberstein current density in terms of the k-component of the quantum-mechanical current density $j^\mu(\vec{r}, t)$ we have to follow some considerations, starting with Eq. (A.5.8) plus an external current $j_{\text{ext}}^\mu(\vec{r}, t)$

$$j^k(\vec{r}, t) = j_{\text{pmc}}^k(\vec{r}, t) + j_{\text{dmc}}^k(\vec{r}, t) + j_{\text{mc}}^k(\vec{r}, t) + j_{\text{ext}}^k(\vec{r}, t). \quad (5.1.4)$$

The paramagnetic current $j_{\text{pmc}}^k(\vec{r}, t)$, the diamagnetic current $j_{\text{dmc}}(\vec{r}, t)$, and the magnetization current $j_{\text{mc}}^k(\vec{r}, t)$ in terms of the Kohn-Sham orbitals are explicitly given by

$$j_{\text{pmc}}^k(\vec{r}, t) = \sum_{n=1}^N \frac{\hbar q_{(n)}}{i2M_{(n)}} \sum_i^{I_{(n)}} \sum_{s_{(n)}} \left[\left(\partial^k \phi_{(n,i)}^\dagger(\vec{r}, s_{(n)}, t) \right) \phi_{(n,i)}(\vec{r}, s_{(n)}, t) - \phi_{(n,i)}^\dagger(\vec{r}, s_{(n)}, t) \left(\partial^k \phi_{(n,i)}(\vec{r}, s_{(n)}, t) \right) \right], \quad (5.1.5)$$

$$j_{\text{dmc}}^k(\vec{r}, t) = - \sum_{n=1}^N \frac{q_{(n)}^2}{M_{(n)} c_0} \left[\sum_i^{I_{(n)}} \sum_{s_{(n)}} n_{(n,i)}(\vec{r}, s_{(n)}, t) \right] A^k(\vec{r}, t), \quad (5.1.6)$$

$$j_{\text{mc}}^k(\vec{r}, t) = - \sum_{n=1}^N \left[\sum_i^{I_{(n)}} \sum_{s_{(n)}} \epsilon^{klm} \partial_l \phi_{(n,i)}^\dagger(\vec{r}, s_{(n)}, t) \left(\frac{q_{(n)} \hbar}{2M_{(n)}} S_m^{(n)} \right) \phi_{(n,i)}(\vec{r}, s_{(n)}, t) \right]. \quad (5.1.7)$$

All three current contributions depend on the particle charge $q_{(n)}$, particle mass $M_{(n)}$, and the single-particle wavefunctions. While the paramagnetic current and magnetization current do not depend explicitly on the Maxwell field, the diamagnetic current does depend on the vector potential $A^k(\vec{r}, t)$. The vector potential is implicitly given by the Riemann-Silberstein vectors $F_{\pm}^k(\vec{r}, t)$. It can be expressed in two ways.

First, using the relation between the vector potential $A^k(\vec{r}, t)$ and the magnetic field in Eq. (A.1.3) leads, after solving for $A^k(\vec{r}, t)$, to [75, 80]

$$\begin{aligned} A^k(\vec{r}, t) &= -c_0 \int d^3r' \frac{\epsilon^{klm} \partial_l' B_m(\vec{r}', t)}{4\pi |\vec{r} - \vec{r}'|} \\ &= i \sqrt{\frac{c_0^2 \mu_0}{2}} \underbrace{\int d^3r' \frac{\epsilon^{klm} \partial_l'}{4\pi |\vec{r} - \vec{r}'|} (F_{+,m}(\vec{r}', t) - F_{-,m}(\vec{r}', t))}_{\text{Solution of poisson equation}}. \end{aligned} \quad (5.1.8)$$

The integral operation in Eq. (5.1.8) is a simple Poisson equation. Efficient methods exists to solve the Poisson equation which makes this equation easy to handle. In the second possibility is to use the electric field in terms of the vector and scalar potential in Eq. (5.1.8). In Coulomb gauge with $\partial_k \vec{A}^k = 0$, it can be reduced to

$$\begin{aligned} E^k(\vec{r}, t) &= -\partial^k \Phi(\vec{r}, t) + \frac{1}{c_0} \frac{\partial}{\partial t} A^k(\vec{r}, t) \\ \Leftrightarrow E_{\perp}^k(\vec{r}, t) + E_{\parallel}^k(\vec{r}, t) &= -\partial^k \Phi(\vec{r}, t) + \frac{1}{c_0} \frac{\partial}{\partial t} A^k(\vec{r}, t) \\ \Leftrightarrow E_{\perp}^k(\vec{r}, t) &= \frac{1}{c_0} \frac{\partial}{\partial t} A^k(\vec{r}, t). \end{aligned} \quad (5.1.9)$$

Hence, we have to split the electric field in its transverse $\vec{E}_{\perp}(\vec{r}, t)$ and longitudinal $\vec{E}_{\parallel}(\vec{r}, t)$ components. We use the general vector field properties [112] that the gradient of a scalar field is always a longitudinal vector and A^k is purely transverse due to the Coulomb gauge condition. The last expression in Eq. (5.1.9) after replacing $\vec{E}_{\perp}(\vec{r}, t)$ by the corresponding Riemann-Silberstein vector expression of Eq. (1.1.6) and integrating from time t_0 to time t leads to

$$A^k(\vec{r}, t) = -\sqrt{\frac{c_0^2}{2\epsilon_0}} \int_{t_0}^t dt' \left(F_{+}^k(\vec{r}, t') + F_{-}^k(\vec{r}, t') \right)_{\perp} + A^k(\vec{r}, t_0). \quad (5.1.10)$$

Here, the initial vector potential is $A^k(\vec{r}, 0)$. Thus, the diamagnetic current term can be obtained by the two different vector potential calculations, and therefore $j_{\text{dmc}}^k(\vec{r}, t)$ and its corresponding Riemann-Silberstein vector $\mathcal{J}_{\text{dmc}}(\vec{r}, t)$ is either non-local in space or time. Consequently, taking Eq. (1.1.40) leads to the Riemann-Silberstein equation

$$i\hbar \frac{\partial}{\partial t} \mathcal{F}(\vec{r}, t) = \mathcal{H}(\vec{r}, t) \mathcal{F}(\vec{r}, t) - i\hbar \mathcal{J}_{\text{loc}}(\vec{r}, t). \quad (5.1.11)$$

Since the diamagnetic current term $\mathcal{J}_{\text{loc}}(\vec{r}, t)$ depends on the Riemann-Silberstein vector $\mathcal{F}(\vec{r}, t)$, we can combine the right-hand side of Eq. (5.1.23), which in turn means the we cannot simply use the matrix-times-vector operation $\mathcal{H}\mathcal{F}(\vec{r}, t)$ which we introduced in Eq. (1.1.40). The diamagnetic current contributes as an integral operation. Therefore it is necessary to generalize $\mathcal{H}\mathcal{F}(\vec{r}, t)$ to

$$\bar{\mathcal{H}}(\vec{r}, t) \mathcal{F}(\vec{r}, t) := \int d^3 r' \int_{t_0}^t dt' \bar{\mathcal{H}}(\vec{r}, \vec{r}', t, t') \mathcal{F}(\vec{r}', t'). \quad (5.1.12)$$

Hence we denote this integration operation in short form with two bold calligraphic letters $\bar{\mathcal{H}}(\vec{r}, t) \mathcal{F}(\vec{r}, t)$. The first operator with "bar" represents the operator kernel and the second one the six-component Riemann-Silberstein vector. Note, that for an initial time t_0 , Eq. (5.1.12) becomes

$$\bar{\mathcal{H}}(\vec{r}, t_0) \mathcal{F}(\vec{r}, t_0) = \int d^3 r' \bar{\mathcal{H}}(\vec{r}, \vec{r}', t_0, t_0) \mathcal{F}(\vec{r}', t_0). \quad (5.1.13)$$

The operator $\bar{\mathcal{H}}(\vec{r}, t)$ is determined by its corresponding integral kernel $\bar{\mathcal{H}}(\vec{r}, \vec{r}', t, t')$ with four variables, the two position vectors \vec{r} , \vec{r}' , and the two times t , t' . We can express $\bar{\mathcal{H}}(\vec{r}, \vec{r}', t, t')$ as a sum of the two linear operators $\bar{\mathcal{H}}_{(0)}(\vec{r}, \vec{r}', t, t')$ and $\mathcal{K}(\vec{r}, \vec{r}', t, t')$

$$\bar{\mathcal{H}}(\vec{r}, \vec{r}', t, t') = \bar{\mathcal{H}}_{(0)}(\vec{r}, \vec{r}', t, t') + \mathcal{K}(\vec{r}, \vec{r}', t, t'). \quad (5.1.14)$$

The kernel $\bar{\mathcal{H}}_{(0)}$ includes the curl operation in Eq. (1.1.25) with the spin-1 matrices of Eq. (1.1.15), but without any diamagnetic current term, i.e.,

$$\bar{\mathcal{H}}_{(0)}(\vec{r}, \vec{r}', t, t') = \begin{pmatrix} 1 & 0 \\ 0 & -1 \end{pmatrix}_{2 \times 2} \otimes \left(i\hbar c_0 \delta(\vec{r} - \vec{r}') \delta(t - t') [S^m \partial'_m] \right)_{3 \times 3}, \quad (5.1.15)$$

and represents the corresponding integral kernel for the microscopic Maxwell Hamiltonian \mathcal{H} given in Eq. (1.1.41). Due to the delta functions, integrating Eq. (5.1.15) over \vec{r}' and t' results in

$$\bar{\mathcal{H}}_{(0)}(\vec{r}, t) \mathcal{F}(\vec{r}, t) = \mathcal{H} \mathcal{F}(\vec{r}, t). \quad (5.1.16)$$

The diamagnetic current operator kernel in equation (5.1.14) can be determined by the above two ways. The first is based on Eq. (5.1.8) which uses the magnetic field of the system. Hence, the integral kernel $\mathcal{K}(\vec{r}, t)$ for the diamagnetic current yields with Eq. (A.5.10)

$$\mathcal{K}(\vec{r}, \vec{r}', t, t') = \begin{pmatrix} 1 & -1 \\ 1 & -1 \end{pmatrix}_{2 \times 2} \otimes \left(\hbar \sqrt{2\mu_0} \delta(t - t') \kappa(\vec{r}, t) \frac{S^m \partial'_m}{4\pi |\vec{r} - \vec{r}'|} \right)_{3 \times 3}. \quad (5.1.17)$$

The second option is in principle also expressible as a integral kernel. But since we obtain non-locality in space and time, we do not consider this version in the present work. The factor $\kappa(\vec{r}, t)$ includes all common matter specific variables with

$$\kappa(\vec{r}, t) = \sum_{n=1}^N \frac{q_{(n)}^2}{M_{(n)}} \left[\sum_{i=1, s_{(n)}}^{I_{(n)}} n_{(n,i)}(\vec{r} s_{(n)}, t) \right]. \quad (5.1.18)$$

Now, the Riemann-Silberstein diamagnetic current Eq. (A.5.10) is with Eq. (5.1.12), Eq. (5.1.17), and Eq. (5.1.8) given by

$$\mathcal{J}_{\text{dmc}}(\vec{r}, t) = \int d^3r' \int_{t_0}^t dt' \bar{\mathcal{K}}(\vec{r}, \vec{r}', t, t') \mathcal{F}(\vec{r}', t'). \quad (5.1.19)$$

The remaining current densities J_{pmc}^k and J_{mc}^k in Eq. (A.5.9) and Eq. (5.1.7) together with an external current j_{ext}^k lead to $\mathcal{J}_{\text{loc}}(\vec{r}, t)$

$$\mathcal{J}_{\text{loc}}(\vec{r}, t) = \begin{pmatrix} 1 \\ 1 \end{pmatrix}_{2 \times 1} \otimes \left(\frac{i}{\sqrt{2\epsilon_0}} \left(j_{\text{pmc}}^k(\vec{r}, t) + j_{\text{sc}}^k(\vec{r}, t) + j_{\text{ext}}^k(\vec{r}, t) \right) \right)_{3 \times 1}. \quad (5.1.20)$$

Consequently, the six-component Riemann-Silberstein vector $\mathcal{J}(\vec{r}, t)$ for the total Kohn-Sham current is

$$\mathcal{J}(\vec{r}, t) = \mathcal{J}_{\text{loc}}(\vec{r}, t) + \mathcal{J}_{\text{dmc}}(\vec{r}, t) \quad (5.1.21)$$

Finally, the complete Ampère's and Faraday's Maxwell's equations in Riemann-Silberstein representation with microscopic quantum mechanical current densities can be expressed with Eq. (1.1.40), Eq. (5.1.14), and Eq. (5.1.20) in terms of the total current $\mathcal{J}(\vec{r}, t)$ by

$$i\hbar \frac{\partial}{\partial t} \mathcal{F}(\vec{r}, t) = \mathcal{H}(\vec{r}, t) \mathcal{F}(\vec{r}, t) - i\hbar \mathcal{J}(\vec{r}, t), \quad (5.1.22)$$

where the \mathcal{J} implicitly depend on the actual Riemann-Silberstein vector due to Eq. (5.1.19). Secondly, the diamagnetic current contribution \mathcal{J}_{dmc} can be separated from \mathcal{J} and combined with the Hamiltonian function which leads to Eq. (5.1.12). In this case, the corresponding Riemann-Silberstein Maxwell's equation reads

$$i\hbar \frac{\partial}{\partial t} \mathcal{F}(\vec{r}, t) = \bar{\mathcal{H}}(\vec{r}, t) \mathcal{F}(\vec{r}, t) - i\hbar \mathcal{J}_{\text{loc}}(\vec{r}, t), \quad (5.1.23)$$

which is equivalent with Eq. (5.1.22). The non-local Hamiltonian in this expression requires some adaptations for the real-time propagation, which is the subject of the next section.

In future publications, we will examine the relation between the coupling in a linear medium determined by $\mathcal{K}_{\text{lm}}(\vec{r}, t)$ in Eq. (1.2.41) and $\bar{\mathcal{K}}$ in Eq. (5.1.17), since both terms couple the two helicity Riemann-Silberstein vectors \vec{F}_+ and \vec{F}_- .

5.2 Riemann-Silberstein Maxwell propagation coupled to the Kohn-Sham current density

In the previous section, we expressed in Eq. (5.1.22) the Ampère's and Faraday's law as an inhomogeneous Schrödinger-like equation in the Riemann-Silberstein formalism. To get a general expression for the Riemann-Silberstein time-propagation with quantum-mechanical current density, we derive the corresponding equation in two steps. First, we start with only diamagnetic current contribution $\mathcal{J}_{\text{dmc}}(\vec{r}, t)$ and the corresponding Eq. (5.1.23). In this form, using the inhomogeneous time-evolution Eq. (2.2.14) leads directly to

$$\mathcal{F}(\vec{r}, t) = \mathcal{U}(t, t_0) \mathcal{F}(\vec{r}, t_0) - \int_{t_0}^t d\tau \mathcal{U}(t, \tau) \mathcal{J}_{\text{loc}}(\vec{r}, \tau) \quad (5.2.1)$$

On the other hand, in case of $\mathcal{J}_{\text{loc}}(\vec{r}, t)$ equal to zero and a non-zero $\mathcal{J}_{\text{dmc}}(\vec{r}, t)$ the Eq. (5.1.23) becomes homogeneous

$$i\hbar \frac{\partial}{\partial t} \mathcal{F}(\vec{r}, t) = \bar{\mathcal{H}}(\vec{r}, t) \mathcal{F}(\vec{r}, t), \quad (5.2.2)$$

Consequently, we can also provide an homogeneous expression for a time-evolution operator $\bar{\mathcal{U}}(t, t_0)$, that propagates the Maxwell's fields from a given time t_0 to t similar to chapter (2), but considering the non-local integral kernel $\bar{\mathcal{H}}(\vec{r}, \vec{r}', t, t')$ of Eq. (5.1.14). The time-evolution operator $\bar{\mathcal{U}}(t, t_0)$ has to obey the group composition laws known from quantum mechanics [113]

$$\begin{aligned} 1.) \quad \bar{\mathcal{U}}^\dagger \bar{\mathcal{U}} &= \mathbb{1}, \\ 2.) \quad \lim_{t \rightarrow t_0} \bar{\mathcal{U}}(t, t_0) &= \mathbb{1}, \\ 3.) \quad \bar{\mathcal{U}}(t_2, t_0) &= \bar{\mathcal{U}}(t_2, t_1) \bar{\mathcal{U}}(t_1, t_0). \end{aligned} \quad (5.2.3)$$

Let us first consider the homogeneous case. The operator $\bar{\mathcal{U}}(t, t_0)$ should then obey the evolution equation

$$\frac{\partial}{\partial t} \bar{\mathcal{U}}(t, t_0) \mathcal{F}(\vec{r}, t_0) = -\frac{i}{\hbar} \bar{\mathcal{H}}(\vec{r}, t) \bar{\mathcal{U}}(t, t_0) \mathcal{F}(\vec{r}, t_0). \quad (5.2.4)$$

This leads via integration to

$$\bar{\mathcal{U}}(t, t_0) \mathcal{F}(\vec{r}, t_0) = \mathcal{F}(\vec{r}, t_0) + \frac{i}{\hbar} \int_{t_0}^t dt' \bar{\mathcal{H}}(\vec{r}, t') \bar{\mathcal{U}}(t', t_0) \mathcal{F}(\vec{r}, t_0), \quad (5.2.5)$$

and satisfies the conditions in Eq. (5.2.3). Iterating Eq. (5.2.5) leads to a series expansion for the time evolution operation $\bar{\mathcal{U}}(t, t_0) \mathcal{F}(\vec{r}, t_0)$

$$\bar{\mathcal{U}}(t, t_0) \mathcal{F}(\vec{r}, t_0) = \mathcal{F}(\vec{r}, t_0) + \sum_{k=1}^{\infty} \frac{1}{k!} \left(\frac{i}{\hbar} \right)^k \mathcal{T} \prod_{p=1}^k \int_{t_0}^t d\tau_p \int d^3 r_p \int_{t_0}^{\tau_p} dt_p \bar{\mathcal{H}}(\vec{r}_{p-1}, \vec{r}_p, t_p, t_0) \mathcal{F}(\vec{r}_p, t_0), \quad (5.2.6)$$

where we used Eq. (5.1.12), $\vec{r}_0 = \vec{r}$, and \mathcal{T} is the time-ordering operator such that earlier times go to the right. For the simplest case, where also the diamagnetic current and \mathcal{J} are zero, the time evolution equation in (5.2.6) reduces and the underlying Riemann-Silberstein Maxwells time-evolution equation in (5.1.22) becomes

$$i\hbar \frac{\partial}{\partial t} \mathcal{F}(\vec{r}, t) = \mathcal{H} \mathcal{F}(\vec{r}, t), \quad (5.2.7)$$

which is equivalent to Eq. (2.1.2). The corresponding time-evolution equation is given in Eq. (2.1.15), i.e.,

$$\mathcal{F}(\vec{r}, t) = \mathcal{U}(t, t_0) \mathcal{F}(\vec{r}, t_0), \quad (5.2.8)$$

$$\mathcal{U}(t, t_0) = \exp \left[-\frac{i}{\hbar} \mathcal{H}(t - t_0) \right]. \quad (5.2.9)$$

Since the two underlying Eqs. (5.1.23) and Eq. (5.1.12) are equivalent, the corresponding two different time-evolution Eqs (5.1.12) and (5.2.6) are also equivalent.

In a second step, we consider a non-zero current densities $\mathcal{J}_{\text{dmc}}(\vec{r}, t)$ and $\mathcal{J}_{\text{loc}}(\vec{r}, t)$ and start without loss of generality with Eq.(5.1.22) In this case, the Riemann-Silberstein Maxwell's equation takes

$$\frac{\partial}{\partial t} \mathcal{F}(\vec{r}, t) = -\frac{i}{\hbar} \mathcal{H} \mathcal{F}(\vec{r}, t) - \mathcal{J}(\vec{r}, t). \quad (5.2.10)$$

Using Eq. (2.2.14) as before gives

$$\mathcal{F}(\vec{r}, t) = \mathcal{U}(t, t_0) \mathcal{F}(\vec{r}, t_0) - \int_{t_0}^t d\tau \mathcal{U}(t, \tau) \mathcal{J}(\vec{r}, \tau). \quad (5.2.11)$$

including all quantum-mechanical current densities of Eqs. (A.5.9)-(5.1.7). If we consider the separation of $\mathcal{J}(\vec{r}, t)$ from Eq. (5.1.21), we can rewrite Eq. (5.2.11) to

$$\mathcal{F}(\vec{r}, t) = \mathcal{U}(t, t_0) \mathcal{F}(\vec{r}, t_0) - \int_{t_0}^t d\tau \mathcal{U}(t, \tau) \mathcal{J}_{\text{dmc}}(\vec{r}, \tau) - \int_{t_0}^t d\tau \mathcal{U}(t, \tau) \mathcal{J}_{\text{loc}}(\vec{r}, \tau). \quad (5.2.12)$$

The first two terms of the right-hand side of this equation are equivalent to Eqs. (5.2.1), and Eq. (5.2.6). Hence, we can find for Eq. (5.2.13) the equivalent expression

$$\mathcal{F}(\vec{r}, t) = \bar{\mathcal{U}}(t, t_0) \mathcal{F}(\vec{r}, t_0) - \int_{t_0}^t d\tau \mathcal{U}(t, \tau) \mathcal{J}_{\text{loc}}(\vec{r}, \tau), \quad (5.2.13)$$

which is our requested general form of a time-evolution equation for quantum-mechanical current.

In Sec. (2.4) we show that the Maxwell Gauß laws as side conditions hold during the time-propagation. This property is also given for the microscopic time-evolution in Eq. (5.2.11). To show this we apply the \mathcal{D} operator from Eq. (1.1.37) on Eq. (5.2.11) to get $\mathcal{D} \cdot \mathcal{F}(\vec{r}, t)$ with

$$\mathcal{D} \cdot \mathcal{F}(\vec{r}, t) = \mathcal{D} \cdot \mathcal{U}(t, t_0) \mathcal{F}(\vec{r}, t_0) - \int_{t_0}^t d\tau \mathcal{D} \cdot \mathcal{U}(t, \tau) \mathcal{J}(\vec{r}, \tau), \quad (5.2.14)$$

Since the current density $\mathcal{J}(\vec{r}, \tau)$ is classical, and $\mathcal{U}(t, t_0)$ in its containing Hamiltonian \mathcal{H} is equivalent to the ones considered in Sec. 2.4, we can directly conclude that the Gauß side condition for the electromagnetic fields hold, if it holds for the initial Riemann-Silberstein vector.

5.3 Discretized time-evolution and Time-reversal symmetry of the Maxwell system

Our previously considered discretized time-evolution operator in Eq. (3.2.2) takes with the time-evolution Eq. (5.2.11) coupled to Kohn-Sham current densities the recursive form

$$\mathcal{F}(\vec{r}, (m+1)\Delta t) = \bar{\mathcal{U}}((m+1)\Delta t, m\Delta t) \mathcal{F}(\vec{r}, m\Delta t) - \int_{m\Delta t}^{(m+1)\Delta t} d\tau \bar{\mathcal{U}}(\tau, m\Delta t) \mathcal{J}_{\text{loc}}(\vec{r}, \tau). \quad (5.3.1)$$

Using this equation, the six-component Riemann-Silberstein vector $\mathcal{F}(\vec{r}, m\Delta t)$ at the discrete time $m\Delta$ with $m \in \mathbb{N}$, evolves the system for a small time step Δt . Unfortunately this direct propagation scheme breaks the fundamental time-symmetry of the system.

The Pauli-Fierz Hamiltonian in (4.3.5), describing the full coupling Maxwell-Matter system, and the corresponding Maxwell-Kohn-Sham equation are in principle symmetric under a time reversal transformation $t \rightarrow -t$. This constraint is only strictly given, if we consider the whole coupled Maxwell-matter system where both systems influence each other. Considering only forward coupling breaks the symmetry. Consequently, in the time-evolution step for full Maxwell-matter coupling, the time-evolution equation has to obey the property that a reverse time step from $\mathcal{F}(\vec{r}, m\Delta t)$ leads again to the previous result $\mathcal{F}(\vec{r}, (m-1)\Delta t)$. In general, this constraint is not fulfilled for simple time evolution steps. However, we can construct a numerical time-evolution equation based on the enforced time-reversal symmetry (ETRS) [114] for quantum mechanic systems. The underlying condition requires that a propagation forward starting from $\mathcal{F}(\vec{r}, m\Delta t)$ with $\Delta t/2$ and one backwards starting from $\mathcal{F}(\vec{r}, (m+1)\Delta t)$ with $\Delta t/2$ has to give the same value of $\mathcal{F}(\vec{r}, (m+1/2)\Delta t)$. A modified numerical recursive time-evolution equation for ETRS based on (3.2.2) takes the form

$$\begin{aligned} \mathcal{F}(\vec{r}, (m+1)\Delta t) &= \bar{\mathcal{U}}((m+1)\Delta t, m\Delta t) \mathcal{F}(\vec{r}, t) \\ &\quad - \int_{m\Delta t}^{(m+\frac{1}{2})\Delta t} d\tau \mathcal{U}(m\Delta t, \tau) \mathcal{J}_{\text{loc}}(\vec{r}, \tau) + \int_{m\Delta t}^{(m+\frac{1}{2})\Delta t} d\tau \mathcal{U}((m+1)\Delta t, \tau) \mathcal{J}_{\text{loc}}(\vec{r}, \tau). \end{aligned} \quad (5.3.2)$$

The included integrals in (3.2.2) and (5.3.2) can be approximated by trapezoidal rule so that the numerical time-evolution equations take the explicit forms

$$\begin{aligned} \mathcal{F}(\vec{r}, (m+1)\Delta t) &\approx \bar{\mathcal{U}}((m+1)\Delta t, m\Delta t) \mathcal{F}(\vec{r}', m\Delta t) \\ &\quad - \frac{\Delta t}{2} \mathcal{U}((m+1)\Delta t, m\Delta t) \mathcal{J}_{\text{loc}}(\vec{r}', (m+1)\Delta t) \\ &\quad - \frac{\Delta t}{2} \mathcal{J}_{\text{loc}}(\vec{r}, m\Delta t), \end{aligned} \quad (5.3.3)$$

for the simple direct propagation, and

$$\begin{aligned} \mathcal{F}(\vec{r}, (m+1)\Delta t) &\approx \bar{\mathcal{U}}((m+1)\Delta t, m\Delta t) \mathcal{F}(\vec{r}, m\Delta t) \\ &\quad - \frac{\Delta t}{4} \mathcal{U}((m+1)\Delta t, m\Delta t) \mathcal{J}_{\text{loc}}(\vec{r}', m\Delta t) \\ &\quad - \frac{\Delta t}{4} \mathcal{U}((m+1)\Delta t, (m+1/2)\Delta t) \mathcal{J}_{\text{loc}}(\vec{r}, (m+1/2)\Delta t) \\ &\quad - \frac{\Delta t}{4} \mathcal{J}_{\text{loc}}(\vec{r}, (m+1)\Delta t) \\ &\quad - \frac{\Delta t}{4} \mathcal{U}(m\Delta t, (m+1/2)\Delta t) \mathcal{J}_{\text{loc}}(\vec{r}, (m+1/2)\Delta t) \end{aligned} \quad (5.3.4)$$

for the ETRS propagation.

5.4 Discretized time-evolution and Time-reversal symmetry of the matter system

In contrast to our novel quantum mechanical like time-evolution equation for the six-component Maxwell-Riemann-Silberstein vector in chapter 2, various types of time-evolution

schemes for Kohn-Sham orbitals are considered in the literature [114, 115] and implemented in quantum mechanical computer programs like octopus. In the present work, we use consistently the ETRS time-evolution method for both, matter and Maxwell, propagations. According to Eq. (4.5.7) the one-particle MPKS Hamiltonian $\hat{h}_{\text{MPKS}}^{(n)}$ for species n is

$$\hat{h}_{\text{MPKS}}^{(n)} = -\frac{1}{2M_{(n)}}\tilde{\mathcal{P}}_{(n)}^k\tilde{\mathcal{P}}_{(n),k} + q_{(n)}A_{\text{KS}}^0 - \frac{q_{(n)}\hbar}{2M_{(n)}c_0}S_k^{(n)}\left[\epsilon^{klm}\partial_l A_{\text{KS},m}\right], \quad (5.4.1)$$

where the canonical momentum is given by

$$\tilde{\mathcal{P}}_{(n)}^k = -i\hbar\partial^k + \frac{q_{(n)}}{c_0}A_{\text{KS}}^k. \quad (5.4.2)$$

The total non-interacting many-body MPKS Hamiltonian is the sum over all one-particle Hamiltonian $\hat{h}_{\text{MPKS}}^{(n)}(\vec{r}_i)$ of species n

$$\hat{H}_{\text{MPKS}}^{(n)}(t) = \sum_i \hat{h}_{\text{MPKS}}^{(n)}(\vec{r}_i, t). \quad (5.4.3)$$

The time evolution equation of the Kohn-Sham orbitals $\phi_{(n,i)}$ from starting time t_0 to time t is given by

$$\phi_{(n,i)}(\vec{r}, t) = \hat{u}_{\text{MPKS}}^{(n)}(t, t_0)\phi_{(n,i)}(\vec{r}, t_0) \quad (5.4.4)$$

with the corresponding time-ordered MPKS time evolution operator $\hat{u}_{\text{MPKS}}^{(n)}(t, t_0)$

$$\hat{u}_{\text{MPKS}}^{(n)}(t, t_0) = \hat{\mathcal{T}} \exp \left[-i \int_{t_0}^t d\tau \hat{h}_{\text{MPKS}}^{(n)}(\tau) \right]. \quad (5.4.5)$$

The total Kohn-Sham wavefunction $\Phi^{(n)}$ of species n evolves in time by

$$\Phi^{(n)}(t) = \hat{U}^{(n)}(t, t_0)\Phi^{(n)}(t_0), \quad (5.4.6)$$

based on its time evolution operator

$$\hat{U}^{(n)}(t, t_0) = \otimes_{q=1}^{N^{(n)}} \hat{u}_{\text{MPKS}}^{(n)}(\vec{r}_q, t, t_0). \quad (5.4.7)$$

It is a Kronecker product of $N^{(n)}$ occupied Kohn-Sham orbitals for species (n) . The evolution operators do not need to be (anti-)symmetrized, since the symmetry of the initial state is preserved.

We use for both subsystems, light and matter, the same propagation scheme and construct also a numerical enforced-time-reversal-symmetry propagation for the Kohn-Sham orbitals. The numerical ETRS time-evolution equation for the $(m+1)\Delta t$ time step for the Kohn-Sham orbital $\phi_{n,i}(m\Delta t)$ is given by

$$\phi_{(n,i)}(\vec{r}, (m+1)\Delta t) = \hat{U}_{\text{MPKS}}^{\text{ETRS},(n)}((m+1)\Delta t, m\Delta t)\phi_i(\vec{r}, m\Delta t) \quad (5.4.8)$$

with the corresponding ETRS time-evolution operator [114]

$$\hat{U}_{\text{MPKS}}^{\text{ETRS},(n)}((m+1)\Delta t, m\Delta t) = \exp \left[-i \frac{\Delta t}{2} \hat{H}_{\text{MPKS}}^{(n)}((m+1)\Delta t) \right] \exp \left[-i \frac{\Delta t}{2} \hat{H}_{\text{MPKS}}^{(n)}(m\Delta t) \right]. \quad (5.4.9)$$

Similar to the Maxwell time-evolution, the time step parameter Δt has to yield to a stable and quite accurate propagation. In contrast to the Maxwell system, there is no CFL criterion for the Kohn-Sham evolution since in our non-relativistic approximation the speed of matter waves is not capped by a fixed velocity. However, for our applications we have a non-relativistic low energy region for the electrons in mind for which the Kohn-Sham orbitals motion is much slower than the speed of light. Hence, the maximum Δt is in most cases much larger than the one for the Maxwell fields. We focus on this issue later in Sec. 5.6 when we discuss different propagation levels.

5.5 Kohn-Sham interaction Hamiltonian

The electromagnetic field interaction with matter is in principle described by extending the Dirac equation with the full minimal coupling term. The full minimal coupling takes both, the Lorentz- and gauge-invariance into account. The non-relativistic MPKS approach of Sec. 4.3 breaks this symmetry. However, it is still an accurate approximation for particles in a low energy limit. Higher order extension of the Pauli-Fierz Hamiltonian exists that consider relativistic corrections. But for most applications, the MPKS approach leads to sufficiently accurate results.

In this section, we derive the multipole expansion as one possible approximation, which gives in first order the most commonly used Maxwell-to-matter interaction term, the dipole approximation. We introduce additionally electric quadrupole and magnetic dipole coupling to investigate later effects beyond the dipole coupling to show the influence of this approximation.

5.5.1 Full minimal coupling

The full minimal coupling was applied by substituting the canonical momentum transformation Eq. (A.2.1) into the Dirac Eq. (4.2.10). Based on the Pauli and QEDFT approaches, we get the full minimal coupling Kohn-Sham Hamiltonian from Eq. (5.4.1). Next, we separate the Hamiltonian into a kinetic Hamiltonian \hat{H}_{kin} and an interaction Hamiltonian \hat{H}_{int} which includes Maxwell and matter variables

$$\hat{H}_{\text{MPKS}}^{(n)} = \hat{H}_{\text{MPKS}}^{\text{kin},(n)} + \hat{H}_{\text{MPKS}}^{\text{int},(n)} = \sum_i \hat{h}_{\text{MPKS}}^{\text{kin},(n)} + \sum_i \hat{h}_{\text{MPKS}}^{\text{int},(n)}, \quad (5.5.1)$$

where the kinetic piece is given by

$$\hat{h}_{\text{MPKS}}^{\text{kin},(n)} = \frac{\hbar^2}{2M_{(n)}} \partial^k \partial_k, \quad (5.5.2)$$

and the light-matter coupling is contained in

$$\hat{h}_{\text{MPKS}}^{\text{int},(n)} = \frac{-i\hbar q_{(n)}}{M_{(n)}} A_{\text{KS}}^k \partial_k + \frac{q_{(n)}^2}{2M_{(n)}} A_{\text{KS}}^k A_{\text{KS},k} + q_{(n)} A_{\text{KS}}^0 - \frac{q_{(n)} \hbar}{2M_{(n)} c_0} \sigma_k \epsilon^{klm} \partial_l A_{\text{KS},m}. \quad (5.5.3)$$

From Sec. 4.5 we know that we get the physical total vector potential A^k with the Riemann-Silberstein propagation. Finding accurate approximations for the corresponding Kohn-Sham potential A_{KS}^k is one aspect for future work. As a first approximation for A_{KS}^k , we use here Eq. (4.5.17). The mean field vector potential A^k is determined by the Riemann-Silberstein vector via Eq. (5.1.8). We note here, that the total vector potential especially the scalar potential component A_{KS}^0 , given in Eq. (4.5.16), in principle includes all electronic and nuclear potentials.

5.5.2 Multipole expansion

In many applications, the correct full minimal coupling is expensive to calculate or not needed since the length scales of matter and radiation differ vastly. Therefore, the minimal coupling is often approximated by a multipole expansion using the electric and magnetic fields variables. As is well-known, the ubiquitous electric dipole approximation is equivalent to the lowest order term of the multipole expansion. In the following, we briefly summarize the derivation of the multipole expansion based on the Power-Zienau-Woolley transformation (cf. chapter 5.2 of Ref. [116]) and adapt it to the present Maxwell-Pauli-Kohn-Sham case. As first step, we introduce the polarization $\vec{P}^{(n)}(\vec{r})$

$$\vec{P}^{(n)}(\vec{r}) = \frac{q^{(n)}}{c_0} \sum_i \vec{r}_i \int_0^1 \delta(\vec{r} - \alpha \vec{r}_i) d\alpha. \quad (5.5.4)$$

In Coulomb gauge with $\vec{\nabla} \cdot \vec{A}_{\text{KS}} = 0$, the vector potential is always transverse and hence the unitary Power-Zienau-Woolley transformation $\hat{U}_{\text{PZW}}^{(n)}$ is defined by

$$\begin{aligned} \hat{U}_{\text{PZW}}^{(n)} &= \exp \left[\frac{i}{\hbar} \int d^3r \vec{P}_{\perp}^{(n)}(\vec{r}) \cdot \vec{A}_{\text{KS}}(\vec{r}) \right] \\ &= \exp \left[\frac{iq^{(n)}}{\hbar} \sum_i \int_0^1 \vec{r}_i \cdot \vec{A}_{\text{KS}}(\alpha \vec{r}_i) d\alpha \right]. \end{aligned} \quad (5.5.5)$$

Next, we transform the MPKS Hamiltonian $\hat{H}_{\text{MPKS}}^{(n)}$ from Eq. (5.5.1) using $\hat{U}_{\text{PZW}}^{(n)}$ into

$$\hat{H}'_{\text{MPKS}} = \hat{U}_{\text{PZW}}^{(n),-1} \hat{H}_{\text{MPKS}}^{(n)} \hat{U}_{\text{PZW}}^{(n)} \quad (5.5.6)$$

In this case, the nabla operator of particle i transforms to

$$\hat{U}_{\text{PZW}}^{-1} \vec{\nabla}_i \hat{U}_{\text{PZW}} = \vec{\nabla}_i + \frac{iq^{(n)}}{\hbar c_0} \int_0^1 \left(\vec{\nabla}_i \vec{r}_i \cdot \vec{A}_{\text{KS}}(\alpha \vec{r}_i, t) d\alpha \right). \quad (5.5.7)$$

According to the Power-Zienau-Woolley transformation, the corresponding wavefunctions are given by $\Phi^{(n)} = \hat{U}_{\text{PZW}}^{-1} \Phi^{(n)}$, and the transformed Kohn-Sham equation reads

$$\begin{aligned} i\hbar \partial_t \phi'_{(n,i)}(\vec{r}, s_{(n)}, t) &= \left\{ \frac{1}{2M_{(n)}} \left(-i\hbar \vec{\nabla} + \frac{q^{(n)}}{c_0} \int_0^1 \alpha \vec{r} \times \vec{B}_{\text{KS}}(\alpha \vec{r}, t) d\alpha \right)^2 + q_{(n)} A_{\text{KS}}^0(\vec{r}, t) \right\} \phi'_{(n,i)}(\vec{r}, s_{(n)}, t) \\ &+ \left\{ q_{(n)} \int_0^1 \vec{r} \cdot \vec{E}_{\text{KS},\perp}(\alpha \vec{r}, t) d\alpha - \frac{q_{(n)} \hbar}{2M_{(n)}} \vec{S}^{(n)} \cdot \vec{B}_{\text{KS}}(\vec{r}, s_{(n)}, t) \right\} \phi'_{(n,i)}(\vec{r}, t) \end{aligned} \quad (5.5.8)$$

Rewriting the transformed Hamiltonian of the previous equation leads to the multipole expansion of the Kohn-Sham Hamiltonian with

$$\hat{H}'_{\text{MPKS}} = \hat{H}_{\text{MPKS}}^{\text{kin},(n)} + \underbrace{\hat{H}_{\text{MPKS}}^{\text{ED},(n)} + \hat{H}_{\text{MPKS}}^{\text{MD},(n)} + \hat{H}_{\text{MPKS}}^{\text{EQ},(n)} + \dots}_{\hat{H}_{\text{MPKS}}^{\text{int},(n)}}, \quad (5.5.9)$$

where the kinetic Hamiltonian $\hat{H}_{\text{MPKS}}^{\text{kin},(n)}$ is given in Eq. (5.5.2). The remaining multipole terms until second order are the electric dipole term $\hat{H}_{\text{MPKS}}^{\text{ED},(n)}$

$$\hat{h}_{\text{MPKS}}^{\text{ED},(n)}(\vec{r}, \vec{r}_0) = e\vec{r} \cdot \vec{E}_\perp(\vec{r}_0) \quad (5.5.10)$$

$$\hat{H}_{\text{MPKS}}^{\text{ED},(n)} = \sum_i \hat{h}_{\text{MPKS}}^{\text{ED},(n)}(\vec{r}_i, \vec{r}_0), \quad (5.5.11)$$

the magnetic dipole term $\hat{H}_{\text{MPKS}}^{\text{MD},(n)}$

$$\hat{h}_{\text{MPKS}}^{\text{MD},(n)}(\vec{r}, \vec{r}_0) = \left(-i \frac{e\hbar}{2m} \vec{B}(\vec{r}_0) \cdot (\vec{r}_i \times \vec{\nabla}) \right) \quad (5.5.12)$$

$$\hat{H}_{\text{MPKS}}^{\text{MD},(n)} = \sum_i \hat{h}_{\text{MPKS}}^{\text{MD},(n)}(\vec{r}_i, \vec{r}_0), \quad (5.5.13)$$

and the electric quadrupole term $\hat{H}_{\text{MPKS}}^{\text{EQ},(n)}$

$$\hat{h}_{\text{MPKS}}^{\text{EQ},(n)}(\vec{r}, \vec{r}_0) = \frac{1}{2} e (\vec{r} \cdot \vec{\nabla}) \vec{r} \cdot (\vec{E}_\perp(\vec{r})) \Big|_{\vec{r}=\vec{r}_0} \quad (5.5.14)$$

$$\hat{H}_{\text{MPKS}}^{\text{EQ},(n)} = \sum_i \hat{h}_{\text{MPKS}}^{\text{EQ},(n)}(\vec{r}_i, \vec{r}_0). \quad (5.5.15)$$

They are all expanded around the expansion point \vec{r}_0 , which can be chosen in good approximation either as center of mass or center of charge of the matter system. We note here, that we employed the Power-Zienau-Woolley transformation on classical Kohn-Sham fields. For quantized fields, the result differ and a usual Taylor expansion is not applicable [5, 117, 62].

5.5.3 Transverse Riemann-Silberstein vector calculation

The Power-Zienau-Woolley transformed Hamiltonian results in Maxwell-matter coupling in terms of the electric and magnetic field. Whereas the magnetic dipole term depends on the total magnetic field, the electric dipole and quadrupole terms depend only on the transverse component of the electric field. Consequently, we have to decompose the Riemann-Silberstein vector into its transverse and longitudinal components. In general, the Helmholtz-decomposition [112] formula for the Riemann-Silberstein vector is given by

$$\vec{F}_\pm^\perp(\vec{r}, t) = \underbrace{\vec{\nabla} \times \int_V d^3r' \frac{\vec{\nabla}_{\vec{r}'} \times \vec{F}_\pm(\vec{r}', t)}{4\pi|\vec{r} - \vec{r}'|}}_{\text{Solution of poisson equation}} - \frac{1}{4\pi} \oint_S dS' \vec{n} \times \frac{\vec{F}_\pm(\vec{r}', t)}{4\pi|\vec{r} - \vec{r}'|}. \quad (5.5.16)$$

The first term on the right-hand side of Eq. (5.5.16) can be computed efficiently by a Poisson solver since it is the solution of the Poisson equation. Octopus provides several effective Poisson solvers [93, 118] to obtain Kohn-Sham potentials for matter systems, which we adapt here for the Riemann-Silberstein decomposition. The second integral in Eq. (5.5.16) is a surface integral which is necessary, if the Riemann-Silberstein vector does not vanish at the simulation box boundaries. Since the Riemann-Silberstein vector in the multipole expansion Hamiltonian in Eq. (5.5.9) does only depend on the expansion point \vec{r}_0 of the multipole expansion and its corresponding Riemann-Silberstein vector inside the box, it is sufficient to calculate the values of the surface integral only for the stencil points that correspond to the expansion center \vec{r}_0 of the multipole expansion. This reduces the computational cost for the boundary term significantly.

Note, that in principle the field decomposition of coupled Maxwell-matter systems can be achieved by calculating the longitudinal electric field caused by the Kohn-Sham orbitals of all species. But some of the simulations for large matter systems that we have performed have shown instabilities after a long time of propagation. Therefore, we decompose the field for each time step when it couples to the matter to avoid small errors, which possibly result in an incorrect simulation run.

5.6 Maxwell-Kohn-Sham multi-scale implementation

Up to now, we have seen in the previous sections that both physical systems, matter and Maxwell, can be expressed mathematically very similar. Both can be propagated in time by a Schrödinger-like equation. Nevertheless some fundamental differences require different physical parameters to simulate each system properly, especially for length and time scale. Some examples are molecular systems interacting with infrared, optical or ultraviolet laser pulses. In all cases, the matter wavefunctions are localized in a small volume compared to the laser field. Additionally, the wavefunctions fluctuate rather strongly, whereas typical experiments show that the Maxwell fields reaction is often smoother. The length scale difference of Maxwell radiation and matter motion can differ by about some orders of magnitude. Although our implementation is not restricted to such simulations, we introduce some grid types which are especially designed for laser-molecule interactions.

5.6.1 Multi-grid types

In Figure 5.1, we illustrate different kinds of combined matter and Maxwell grids, and consider without loss of generality only matter grid spacings smaller or equal to the Maxwell grid spacing. In principle, our implementation can also reverse this grid relation to simulate high frequency Maxwell signals, e.g. x-rays.

The grids in Figure 5.1 a) and b) represent equal sized grid for both systems. In general, the Maxwell grid points do not necessarily have to lie on the top of a matter grid point, illustrated in a). For both grid types a) or b), it is not possible to use the grid point values directly in the respective coupling terms of the propagation equations. For example, the finer matter grid points have to be sorted in clusters which map to the next nearest Maxwell grid point and different methods to get the weighted mean value yield the coupling value for that Maxwell point. Vice versa, a Taylor series extrapolation of the Maxwell values can be used to obtain the coupling values for the matter points. These grid types of equally sized dimensions are well suited to simulate periodic systems.

The two schemes in Figure FIG. 5.1 c) and d) show matter grid types, in first case without common grid points, and in second case with common grid points, but compared to the previous grids with smaller dimensions for the matter grid than for the Maxwell one. As before, the values for the corresponding coupling terms have to be calculated by weighted mean and interpolation. Those grid types can describe efficiently bound molecules and nanoparticles, especially when focussing on electromagnetic far-fields.

In case of near field effects, where the electromagnetic field fluctuation correlate strongly with the matter wavefunctions, it is consequently a good choice to select the same grid spacings for both grids and to place matter and Maxwell grid points on top of each other as shown in Figure 5.1 e) and f). In this case, the values for both respective coupling terms can be obtained directly from the field point at the respective grid point. Besides the near-field simulation, the grid type f) with larger Maxwell grid dimensions is suited to study the onset of the electromagnetic far-field and allows to define electromagnetic detectors at the box boundaries.

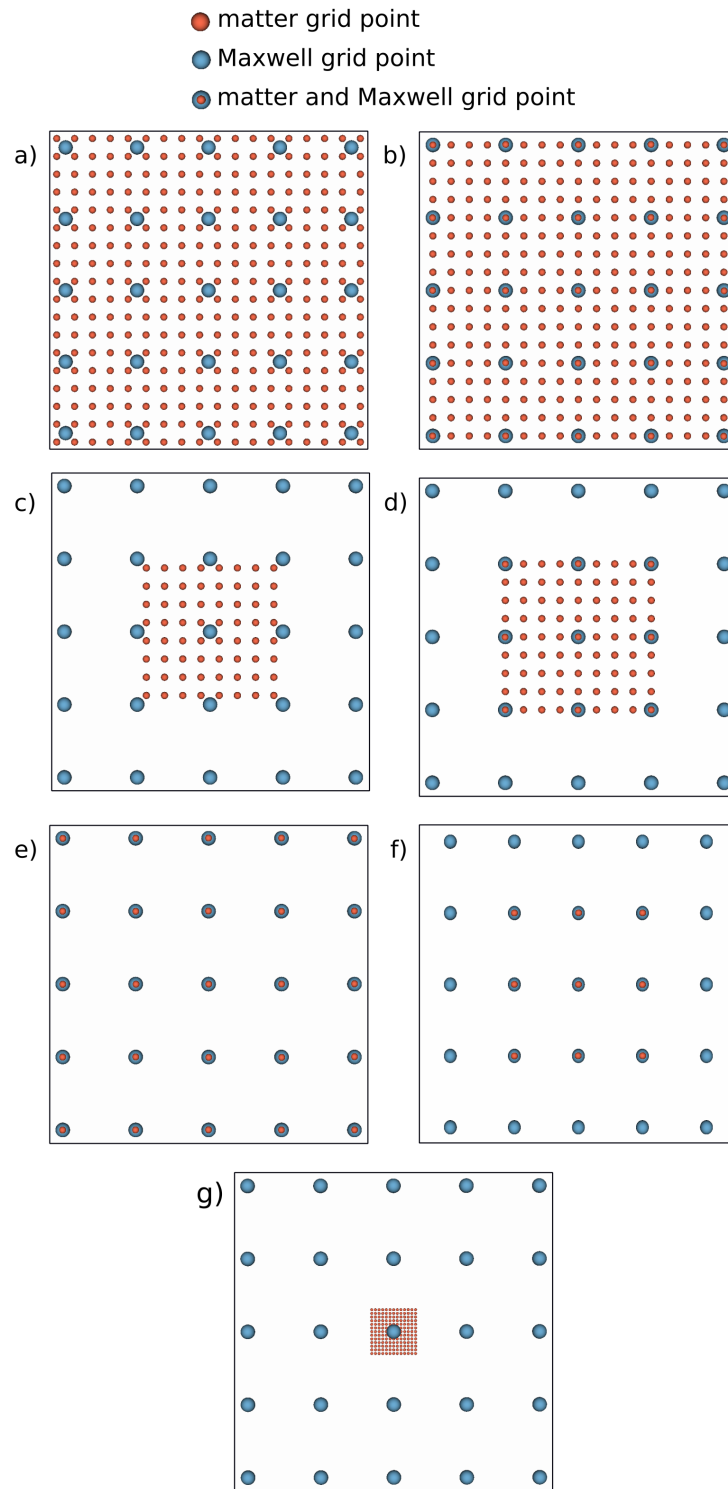


Figure 5.1: An overview over some multiscale grid types. The red dots represent grid points for the Kohn-Sham wavefunctions and the blue dots show the grid point for the Maxwell field variables. In most relevant applications, the Kohn-Sham grid is finer than the Maxwell grid, like in a), b), c), d), and g). The grid types e) and f) represent special cases, where both grids lie on top of each other, but they are not necessarily of same size which is given in f). Only the equal sized grids in a), b), and e) are suitable for periodic systems, whereas the remaining types describe proper bound non-periodic systems.

The last grid type in Figure 5.1 g) illustrates the case, where the matter grid is chosen much finer than the Maxwell grid. Only one Maxwell grid point lies in the middle of the matter grid. Here, it is assumed that the Maxwell field is approximately constant for all matter grid points. Vice versa, the coupling value for the Maxwell grid is obtained by the mean value of all matter points.

5.6.2 Multi-scales in time

After setting up the two spatial system grids and their different length scales, we focus in this section on the different time scales. The different scales for matter and radiation in time require a more detailed consideration about the propagation time steps of each subsystem.

In principle, it is possible to chose identical parameters with the condition that both propagators have to run stable in time, but this is for most physical cases not the most efficient choice. According to the underlying Maxwell Hamiltonian-like operator in H_{Mx} Eq. (1.1.30), which forms the 6x6 \mathcal{H} operator in Eq. (1.1.41) for the Maxwell propagation, the gradient operation is multiplied by the speed of light c_0 (roughly 137 in atomic units). This factor imposes the speed for the electromagnetic waves on the grid.

On the other hand, the matter Hamiltonian in our non-relativistic Pauli limit is lacking the factor of c_0 and yields a much smaller spectral range of the maximum and minimum eigenvalue of the Hamiltonian. Consequently, the underlying time step variables have to propagate "fast" photon motion and "slow" motion of matter. This results in a much smaller maximum time step $\Delta t_{\text{KS,max}}$ for the Maxwell propagation compared to the maximum time step of the matter $\Delta t_{\text{KS,max}}$.

A similar situation of different physical time scales is already known in electron-nuclear dynamics, where the large nuclear mass leads to a rather slow motion of the nuclei compared to the faster motion of the lighter electrons. Now, the propagation of the Maxwell fields also with electron-nuclear dynamics adds a third timescale. In our numerical time-stepping scheme, we exploit the different time scales explicitly to increase the computational efficiency.

Several test simulations that we have performed have shown, that the coupled propagation of nuclei, electrons and Maxwell fields keeps relatively accurate, stable and converged, if we perform several Maxwell propagation steps Δt_{Mx} as intermediate steps between the Kohn-Sham propagation steps Δt_{KS} and Ehrenfest steps for the nuclei. We select the Kohn-Sham time steps $\Delta t_{\text{KS}} < \Delta t_{\text{KS,max}}$ as the basic time step parameter for the entire MPKS system. The number $N_{\text{Mx-steps}}$ of intermediate Maxwell steps is automatically chosen such that

$$\Delta t_{\text{KS}} \leq N_{\text{Mx-steps}} \Delta t_{\text{Mx,CFL}} , \quad (5.6.1)$$

where $\Delta t_{\text{Mx,CFL}}$ denotes the Courant time step given in equation (3.2.4).

Performing these intermediate Maxwell time steps, assumes that the intermediate Maxwell propagation between the $m\Delta t_{\text{KS}}$ time step and the following $(m+1)\Delta t_{\text{KS}}$ time step does not affect the matter propagation significantly. Therefore, the current density for the corresponding i^{th} is we approximated by the linear expansion

$$\mathcal{J}_{\text{loc}}(\vec{r}, m\Delta t_{\text{KS}} + i\Delta t_{\text{Mx}}) = \mathcal{J}_{\text{loc}}(\vec{r}, m\Delta t_{\text{KS}}) + \left[\frac{\mathcal{J}_{\text{loc}}(\vec{r}, (m+1)\Delta t_{\text{KS}}) - \mathcal{J}_{\text{loc}}(\vec{r}, m\Delta t_{\text{KS}})}{N_{\text{Mx-steps}}} \right] i . \quad (5.6.2)$$

The recursive ETRS time-evolution equation for the i^{th} step then takes with Eq. (5.3.4) the form

$$\begin{aligned}
\mathcal{F}(\vec{r}, t_{m,i+1}) &\approx \bar{\mathcal{U}}(t_{m,i+1}, t_{m,i}) \mathcal{F}(\vec{r}, t_{m,i}) \\
&- \frac{\Delta t_{\text{Mx}}}{4} \mathcal{U}(t_{m,i+1}, t_{m,i}) \mathcal{J}_{\text{loc}}(\vec{r}, t_{m,i}) \\
&- \frac{\Delta t_{\text{Mx}}}{4} \mathcal{U}(t_{m,i+1}, t_{m,i+1/2}) \mathcal{J}_{\text{loc}}(\vec{r}, t_{m,i+1/2}) \\
&- \frac{\Delta t_{\text{Mx}}}{4} \mathcal{U}(t_{m,i}, t_{m,i+1/2}) \mathcal{J}_{\text{loc}}(\vec{r}, t_{m,i+1/2}) \\
&- \frac{\Delta t_{\text{Mx}}}{4} \mathcal{J}_{\text{loc}}(\vec{r}, t_{m,i})
\end{aligned} \tag{5.6.3}$$

with

$$\begin{aligned}
t_{m,i} &= m\Delta t_{\text{KS}} + i\Delta t_{\text{Mx}} , \\
t_{m,i+1} &= m\Delta t_{\text{KS}} + (i+1)\Delta t_{\text{Mx}} , \\
t_{m,i+1/2} &= m\Delta t_{\text{KS}} + (i+1/2)\Delta t_{\text{Mx}} .
\end{aligned} \tag{5.6.4}$$

To reduce computational cost even further, we can assume in most cases that the last for inhomogeneity terms in Eq. (5.6.3) are approximately constant for all intermediate time steps during the time interval Δt_{KS} . Thus, we use in this case for all occurring $\mathcal{J}_{\text{loc}}(\vec{r}, t)$ in equation (5.6.3) the arithmetic mean of $\mathcal{J}_{\text{loc}}(\vec{r}, m\Delta t)$, and $\mathcal{J}_{\text{loc}}(\vec{r}, (m+1)\Delta t)$ which reduces the amount of necessary computational expensive $\bar{\mathcal{U}}$ operations. These considered approximations to the full time-evolution requires always a check of convergence for a given application.

5.6.3 Finite difference operators and parallelization strategy

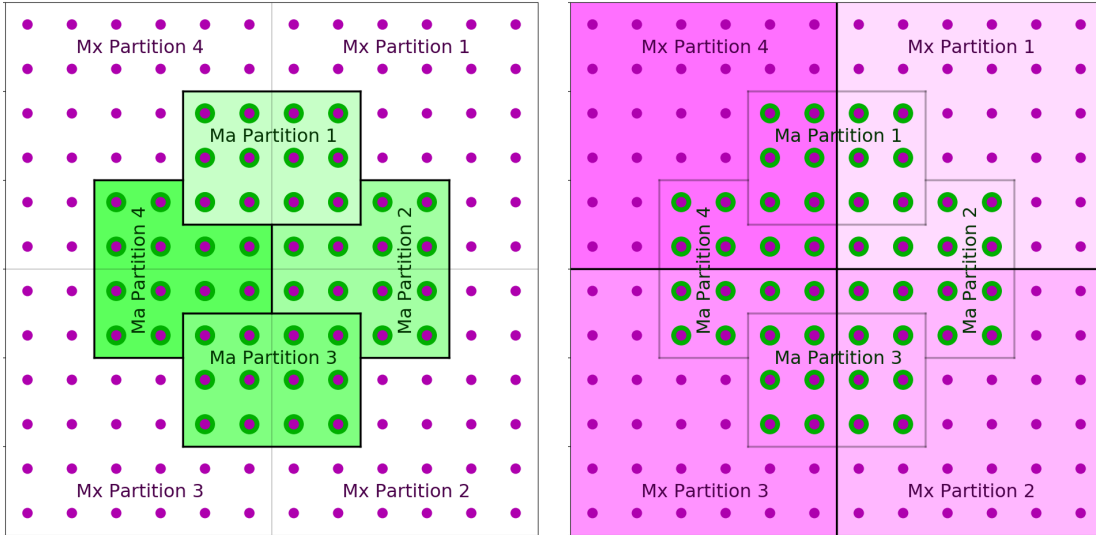


Figure 5.2: Domain parallelization of matter and Maxwell grid. Both schematic drawings show the same two matter and Maxwell grids, and represent grid type f) in Figure (5.1). The matter grid points are bold green dots, and the Maxwell grid points are the smaller purple dots. The left one emphasize partition of the matter grid, and the right one the partition of the Maxwell grid. Both grid partitions have common points with more than one other partition, since each division is independent from each other.

The previously introduced grids provide the basis to express approximately the matter wavefunctions and the Maxwell field variables. In addition, the grid point values deter-

mine the spatial derivatives of both systems. In Sec. 5.3 and Sec. 5.4, we show both time-evolution equations, which we use to propagate the corresponding system. Their underlying time-evolution operations depend on first-order spatial derivatives in case of the Maxwell fields and second-order spatial derivatives in case of the matter wavefunctions. We obtain both operations with the finite-difference method [89, 90, 91]. Since we introduce and consider mainly the Maxwell field propagation the present work, which have a Schrödinger-like form, but with first-order derivatives, we introduce the first derivative finite-difference stencil in Sec. 3.1. The second derivatives, which we need for the kinetic operator of the Pauli-Fierz Hamiltonian, are established and discussed in literature [93, 118]. Finite difference routines for first and second derivatives for selectable accuracy order are implemented in octopus [118].

We also considered in Sec. 3.1 the parallelization scheme for the Maxwell propagation. In case of coupled Maxwell-matter simulations, we speed up the time-evolution by using additionally a parallel propagation scheme for the matter. Octopus provides an optimized parallelization in domains and in "states" or "orbitals/k-points" [93]. Since the Riemann-Silberstein vector is always a six-dimensional vector whose components are considered as six states in the routines of the code, parallelization in states is not so effective in this case. As already described in Sec. 3.1, Octopus has to share the values from some grid points of the grid partition and share them with other partitions to get the correct derivative operations. This technique is illustrated in Figure 3.3 for the Maxwell grid. Furthermore, this communication of shared data has to be expanded now. Both system grids could vary in size, grid points and they are partitioned independently from each other. As a consequence, the point mapping between the grids leads in general to a mapping between different partitions.

Figure 5.6.3 illustrates an example for such a partitioning of a Maxwell-matter system. The matter grid points are marked with large dots and divided into four domains also highlighted in green on the left in Figure 5.6.3. The Maxwell grid partitions with their grid points are plotted and highlighted in purple on the right in Figure 5.6.3. It can be seen in both figures, that the matter grid points of partition 1 maps on Maxwell partitions 1 and 4. On the other hand, the Maxwell partition 1 has common grid points with the matter partitions 1 and 2. We have implemented a mapping, that considers the parallelization in domains of each grid and arranges the necessary data shares to get the right coupling values from the respective other subsystem.

5.6.4 Predictor-corrector method

Previously, in Sec. 5.3 and Sec. 5.4 we described the two propagation schemes for matter and electromagnetic fields separately. In the following, we show a predictor-corrector method that enforces a self-consistent propagation of the system.

5.6.5 Forward coupling

In most studies in the literature, light-matter coupling is restricted to forward Maxwell-matter coupling. The electromagnetic fields influence the matter, but the induced back-reaction due to charge motion does not influence the propagation of the electromagnetic fields. In only forward coupling simulations, the external electromagnetic field propagates without any perturbation by the matter and is calculated separately either analytically or numerically. Such a propagation scheme for one time step is illustrated on the left-hand side in FIG. 5.6.4.

According to the time-evolution operator in Eq. (5.4.9), the operator $\hat{U}_{\text{MPKS}}^{\text{ETRS},(n)}((m +$

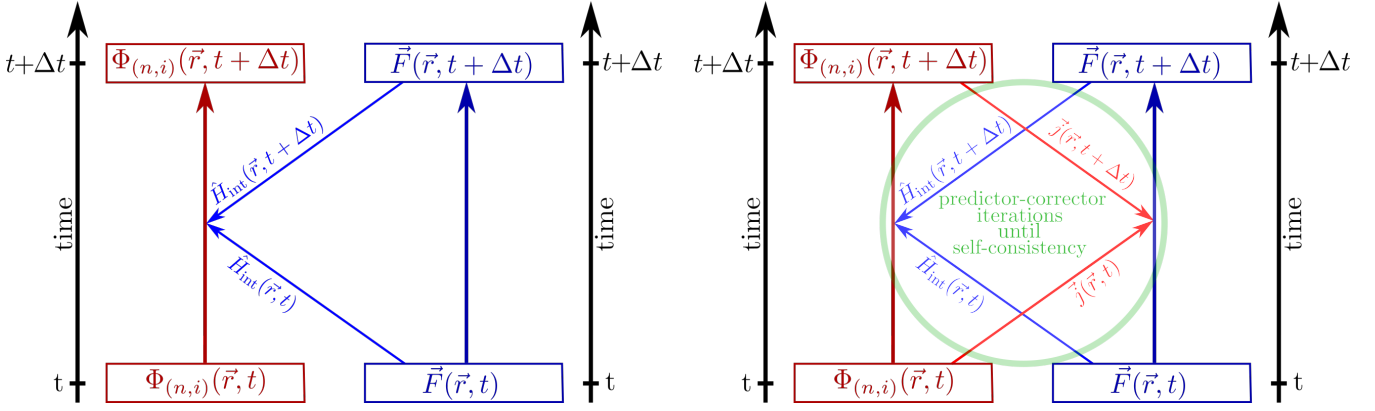


Figure 5.3: The figure on the left-hand side illustrates the most common coupling situation for light-matter coupling in quantum mechanical many-body simulations. The electromagnetic fields (in blue) propagate freely and only influence the propagation of the matter (in red). The back reaction of the matter currents on the electromagnetic fields is neglected. As a consequence, the Maxwell propagation is not calculated numerically, since in most cases, the time-evolution is taken from analytical solutions of Maxwell’s equations or the paraxial wave equation. In case of taking the back reaction into account, the Maxwell propagation is in general not solvable analytically and requires a numerical propagation as for the matter evolution. In the figure on the right-hand side, we show a fully self-consistent predictor-corrector scheme for a coupled Maxwell-Pauli-Kohn-Sham time step. As before, the electromagnetic field influence the propagation of the matter (forward coupling), and additionally the arising currents influence the electromagnetic fields and their time-evolution (backward coupling). Both propagations have to be self-consistent, and therefore, a given coupled time-step is repeated with successively corrected variables until self-consistency is found. Only then the simulation continues to perform the next time step.

1) $\Delta t_{\text{KS}}, m\Delta t_{\text{KS}}$) depends on the Hamiltonian operator $\hat{H}_{\text{MPKS}}^{(n)}((m+1)\Delta t_{\text{KS}})$ at the future time $t = (m+1)\Delta t_{\text{KS}}$. This future Hamiltonian is not only determined by the external Maxwell fields but also by the motions of the ions and electrons and their interactions. Therefore, it is necessary to apply a predictor corrector cycle for the matter propagation. In a first step, the future Hamiltonian is estimated by an extrapolation [119] and the calculated time propagation returns an estimated Kohn-Sham potential which is again used for an updated extrapolation of the Hamiltonian. These steps are repeated until the absolute value of the variance of two subsequently Kohn-Sham potentials falls below a small threshold value. For our calculations, we set a threshold value of $1e^{-6}$ in atomic units for the potential variance and adjust the time step Δt_{KS} for the propagation so that the matter system is converged in at least two iterations if the system is only disturbed very weakly by the external field. During the full run and stronger perturbations, we notice that the number of iterations is barely larger than five.

5.6.6 Forward and backward coupling

The back-reaction of matter on the Maxwell field appears in the MPKS formulation due to the current density in Eq. (5.1.21) which is caused by the motion of matter. The three current types, paramagnetic, diamagnetic and magnetization current, influence the Maxwell propagation Eq. (5.2.11). The influence of the paramagnetic current, the magnetization

current and optional external currents result directly summed up in the inhomogeneity $\mathcal{J}_{\text{loc}}(\vec{r}, t)$ term in Eq. (5.1.20). The diamagnetic current implicitly effects the time-evolution due to the modified Maxwell time-evolution operator $\tilde{\mathcal{U}}$ for this case given in (5.2.6). The full forward and backward coupling scheme is shown on the right-hand side in figure FIG. 5.6.4.

In a fully self-consistent scheme, both systems and accordingly their time-evolution propagation equations in (5.2.11) and (5.4.4) couple to each other. First we apply the extrapolation of the future matter Hamiltonian to get a prediction for the Kohn-Sham orbitals. These orbitals and the initial ones give us the necessary current density, which couple to the Maxwell fields. Using the first predicted updated current density at time $(m+1)\Delta t_{\text{KS}}$ leads to an updated Riemann-Silberstein vector. At this point, the predictor-corrector loop restarts by updating the Kohn-Sham orbitals, but now with a corrected matter Hamiltonian, which includes the updated Riemann-Silberstein vector. As a consequence, the previously predicted variables get a correction closer to the values which make the coupled system self-consistent. We additionally check the consistency of the Maxwell fields by comparing the Maxwell energy inside the simulation box for two successive updated Riemann-Silberstein vectors. Therefore, we use the same threshold value $1e^{-6}$ like for the matter convergence. Additionally, we chose the system propagation time Δt that the predictor-corrector step iterates at least two times until the self-consistency thresholds are fulfilled for weak perturbations. Again, the number of iterations for strong perturbation periods should not be larger than five steps.

5.7 Simulation of open quantum systems with the Maxwell-Kohn-Sham propagation

In Sec. 3.4 we introduced absorbing boundaries for the electromagnetic field to simulate outgoing fields. While this is a standard procedure in FDTD simulations, we emphasize here that such absorbing boundaries effectively allow to turn our coupled light-matter system into an open quantum system from first principles. Therefore, the forward-backward coupled light-matter simulation damps the quantum-mechanical system, due to the fact that the matter transfers energy to the electromagnetic field, which in turn transfers the energy via radiation to the absorbing boundaries. Consequently, no artificial bath degrees of freedom have to be introduced in our simulation scheme as commonly done in the description of open quantum systems.

5.8 Electromagnetic detectors

Due to the self-consistent forward-backward coupling, we have established a methodology to investigate the local field distribution of the electromagnetic fields inside the simulation box. Hence, we can measure the optical properties of the matter directly from the electromagnetic observables. Since we can evaluate the field values at each grid point, we can examine in this way near field effects of the field. Furthermore, if the matter system is surrounded by vacuum, the outgoing waves propagate analytically. In other words, whatever arrives in the boundary region would propagate to the far field and contributes to what can be measured in the far field by a detector. For this purpose, we define right before the boundary region a small closed area as a far field detector. This detector region can consist of only a closed surface to get field values, e.g., the energy flow through the surface, or the region builds a three-dimensional frame box. We illustrate such a detector frame region in Figure 5.4, where we use the incident plane wave plus PML boundaries simula-

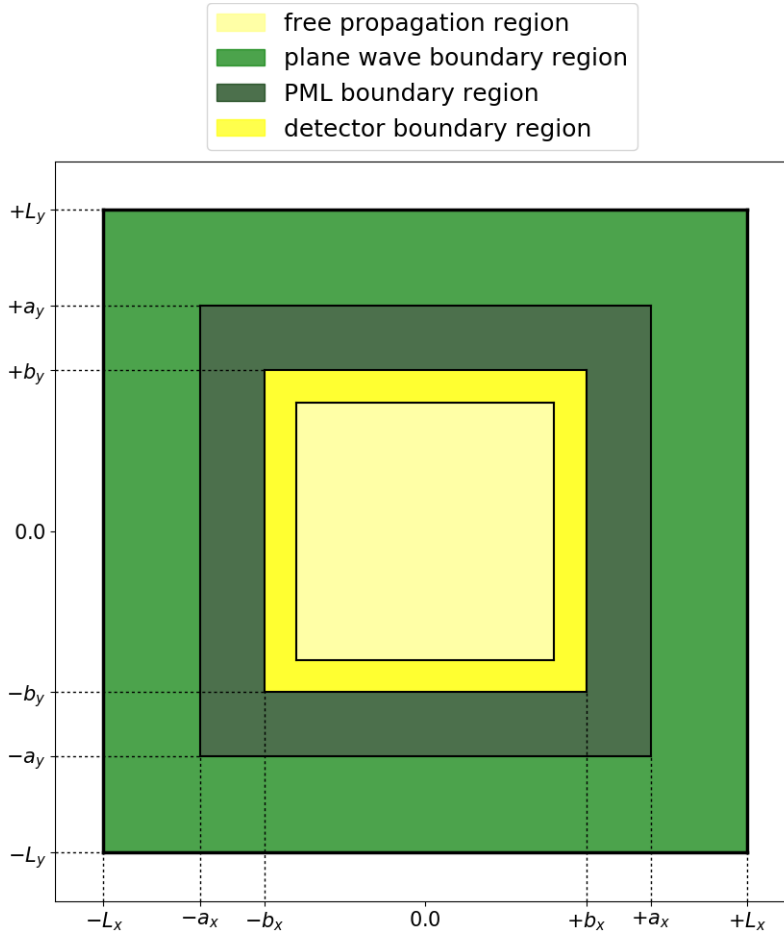


Figure 5.4: A small blue closed area at boundaries of the inner free Maxwell propagation area illustrates the detector region, where the included grid point values are used to analyze the Maxwell far-field.

tion box from Sec. 3.4.6. Hence, the electromagnetic field inside the detector box can be used to extrapolate the far field beyond the simulation box. Detecting the electromagnetic field directly and not indirectly by matter variables, as it is done in common methods of spectroscopy, is a paradigm shift to measure optical spectra, to avoid possible errors and to reveal new effects.

5.9 Broken time reversal symmetry

In Secs. 5.3 and 5.4 we discuss the time-reversal symmetry of the total Pauli-Fierz Hamiltonian of our system given in Eq. (4.3.5). This property only holds if we consider the total Maxwell-matter system as a closed system. For instance, the incident plane wave boundaries simulate an open system since energy enters the system through the analytical calculated boundaries. The time-reversal symmetry does not hold for open systems, especially in presence of magnetic fields [67], and consequently the ETRS propagator in equation (5.3.4) does not hold. However, we assume in the present work that the full coupled Hamiltonian stays time-reversal since the main breaking of the symmetry arises if we consider the magnetic field propagation without any back-reaction of the matter.

Chapter 6

Applications

In this section, we demonstrate the significance of simulating the fully self-consistent coupling of the time-dependent Kohn-Sham equations for the electrons, Ehrenfest dynamics for the nuclei, and Maxwell’s equations for the electromagnetic fields. We use our EMPKS implementation in the Octopus code, which we introduced in the previous sections to simulate different scenarios and coupling levels. They range from conventional forward light-matter coupling in dipole approximation with fixed nuclei to a theory level with forward-backward self-consistent light-matter coupling including electric quadrupole and magnetic dipole terms. In addition, we can include the motion of the ions and classical Lorentz forces on the ions. An overview of the various EMPKS theory levels, that we use in the present work, is shown in Table 6.1. The advantage of switching on and off different degrees of freedom and coupling levels lies in the direct study of the impact and significance of physical mechanisms.

| Acronym | Description |
|----------------------|--|
| <u>F@ED</u> | Forward coupling with E lectric D ipole term |
| <u>FB@ED</u> | Forward and B ackward coupling with E lectric D ipole term |
| <u>F@(ED+MD+EQ)</u> | Forward coupling with E lectric D ipole, M agnetic D ipole and E lectric Q uadrupole term |
| <u>FB@(ED+MD+EQ)</u> | Forward and B ackward coupling with E lectric D ipole, M agnetic D ipole and E lectric Q uadrupole term |

Table 6.1: Table of acronyms that are used in the present work to indicate the level of EMPKS theory.

6.1 Laser pulse simulation scheme for a plasmonic nanoparticle system and simulation parameters

In a typical experimental setup, a molecule gets excited by an incoming laser pulse. The molecule gets excited, absorbs and emits light. The absorbed and emitted light is detected by the outgoing electromagnetic fields. Analyzing the incident and outgoing light draws conclusions about the optical properties of the studied molecule. In the following, we apply our novel ab-initio EMPKS propagation to simulate such laser pulse experiments.

In principle, the simulation setup is very similar to the one in Sec. 3.6, where we hit a linear medium box with a laser pulse. Instead of the medium box, we can place any matter system inside the simulation. Hence, according to the medium box simulation, we

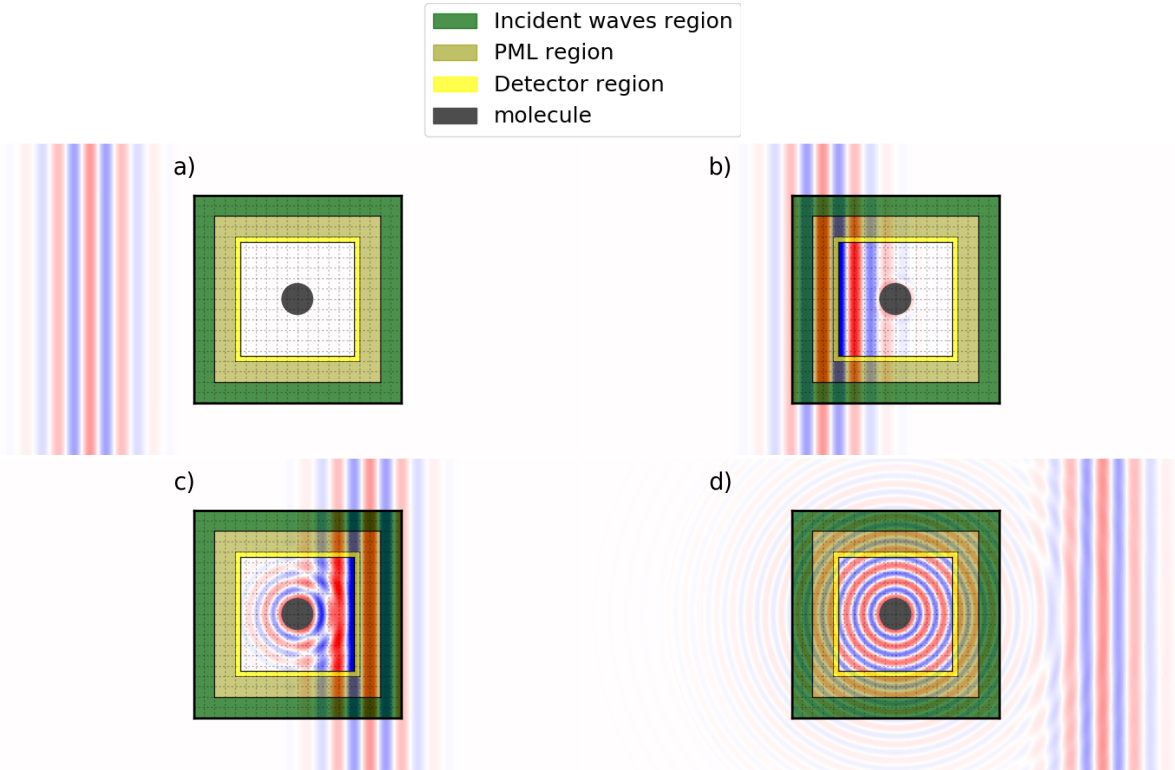


Figure 6.1: Simulation scheme of a laser pulse excitation of a quantum-mechanical system. a) Inside the simulation Box, the quantum mechanical system is grounded in its initial state. Outside the box we place a laser pulse that propagates into the direction of the matter system. Due to the incident waves. b) The incident wave boundaries simulate the incoming wave and the matter system gets excited. c) Due to this excitation, the induced charge motion and current cause an electromagnetic reaction. d) The induced motion of charges leads still to a radiation although the laser pulse left the box.

use a simulation box with combined incident plane waves and perfectly matched layer boundaries, which we introduced in Sec. 3.4.6. In addition to the boundaries, we define a small detector region as it is described in Sec. 5.8. A schematic overview of the entire simulation is presented in Figure 6.1. The first illustration a) shows the initial setup. The matter system in its ground state is placed in the center of the simulation box. In the beginning, the external laser pulse is outside the box, here represented by its electric field polarized perpendicular to the drawing plane. The wave vector is perpendicular to the laser wave front and heads into the direction of the matter. After several time steps shown in b), the laser pulse enters the simulation box and excites the matter system. Due to the electric field oscillation, the electrons and hence the corresponding charge density starts to oscillate, which induce an electric current density. This arising current density influences the total Maxwell field. The external laser field and the induced inner Maxwell field, both interfere which is illustrated in c). Since our implementation solves the forward-backward Maxwell-matter coupling, we can directly analyze the localized electromagnetic field inside the simulation box to examine near-field effects. If we drive the molecule by its resonance frequency, the charge oscillation of the electrons will continue even when the laser passed the simulation box. As shown in d) the corresponding electromagnetic radiation can be measured at the detector region to get information about far-field effects. Although the driven laser left the simulation box, the matter system still radiate a electromagnetic

field. Due to this radiation, energy from the excited matter system transfers via the electromagnetic field to the boundaries of the box. The Maxwell PML simulates the outgoing waves and as a consequence, the matter loses energy, in principle until it returns into the ground state.

6.1.1 Na_{297} -dimer geometry and optical spectra

Recent experiments and theoretical considerations have revealed that large nanoparticles, excited by a laser pulse, create large induced currents. Hence, to test and demonstrate our EMPKS implementation, we select a nanoplasmonic particle, which was already examined in previous work by Alejandro Varas et. al. [120].

The system consists of two almost spherical nanoparticles with 297 sodium atoms each, which are arranged in a dimer configuration. A corresponding illustration of the dimer geometry with two different distances between the dimer is shown in Figure 6.2. Both nanoclusters have together 594 sodium atoms with 594 valence electrons [121, 122]. All inner electrons of the inner electron shell and the valence electron are approximated by Troullier-Martins pseudo-potentials in Octopus [93, 118, 123].

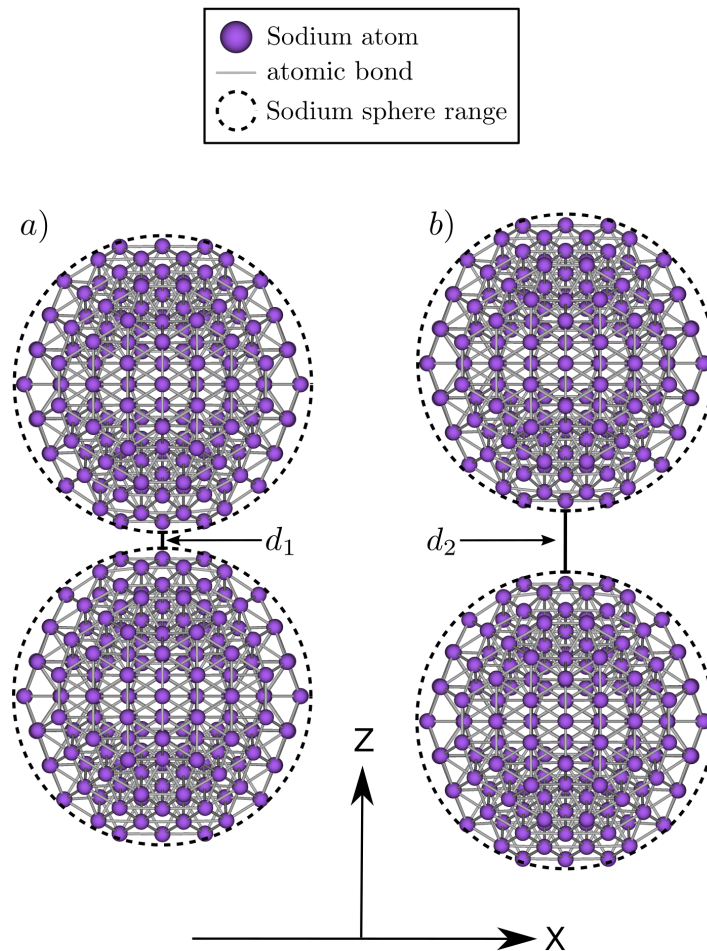


Figure 6.2: Geometry of the Na_{297} dimer in E2E configuration with different distances $d_1 = 0.1\text{nm}$ and $d_2 = 0.5\text{nm}$ between the two effective spheres of the clusters which are illustrated by the black dashed circle.

The icosahedral polyhydron is the most stable geometry for one sodium dimer. After performing standard geometry optimization with octopus, we obtain some characteristic parameters of the dimer geometry. The quite large polyhydron is approximately a sphere with an effective diameter of $2R$, with an effective radius $R \approx 2.61nm$, given by the optimization calculation. Further geometry parameters describe the distance between the two nanoparticles. First, the parameter b gives the distance between the two centered sodium atoms of each icosahedron so that d is defined as $d = b - 2R$, and does not depend on the relative orientation of the two clusters to each other. The two icosahedrons can be orientated in several constellations. We use a relative orientation such that the 3-atoms edge of the hexagons are lying face to face. This so called E2E configuration is illustrated in figure FIG. 6.2. The dimer axis is oriented parallel to the z-axis, therefore the dimer is symmetric in x- and y-axis.

To investigate the effect of internal dipole and quadrupole of the system on the coupled time-evolution, we consider two different distances $d_1 = 0.1nm$ and $d_2 = 0.5nm$. The maximum absorbing frequency of the corresponding optical absorption cross sections in Ref. [120] shows a quadrupole (Q mode) localized surface plasmon resonance (LSPR) for the d_1 dimer, and a dipole (D mode) resonance for the d_2 dimer.

6.1.2 Simulation boxes and grid alignment

According to Sec. 6.1, we place the Na_{297} -dimer in the middle of the Maxwell-Kohn-Sham simulation box which corresponds to grid type f) in figure Figure. 5.1. The matter Kohn-Sham grid is smaller than the Maxwell grid, but both grids have the same grid spacing in each direction and all Kohn-Sham grid points lie on top of a Maxwell grid point. The Kohn-Sham grid geometry is based on the so called minimum box construction [93]. The minimum box of a molecule consists of the union all of Cartesian grid points which lie inside a fixed radius around each ion of the system. For all simulations, we select a radius of $R_{\min} = 0.794$ nm (15 a.u.). Taking the corresponding geometries for d_1 and d_2 into account, we obtain maximal extensions $L_{KS,x}$, $L_{KS,y}$, $L_{KS,z}$ in each direction given in the tables Table 6.2. The matter grid is surrounded by a significant larger parallelepiped shaped box for the Maxwell grid points with the extensions $L_{Mx,x}$, $L_{Mx,y}$, $L_{Mx,z}$ in negative and positive direction which is illustrated in figure Figure. (5.4). As grid spacing for both grids we select 0.053 nm (1.0 a.u.).

For the Kohn-Sham grid we use a zero Dirichlet boundary condition, whereas for the Maxwell grid we employ the combined incident plane wave plus absorbing boundaries via PML as introduced in section 3.4.6. Hence, the Maxwell simulation grid is separated into two areas, one outer for the incident plane wave boundaries and one inner for the PML. The incident plane wave boundary width depends on the derivative order for the operation stencil times the grid spacing. In the present case, we use a finite difference order of four, which corresponds to the width of the plane wave boundary region of 0.212 nm (4.0 a.u.). Additionally, we use 0.265 nm (5.0 a.u.) as PML region. The total inner simulation box for the free Maxwell propagation is therefore limited by $b_{Mx,x}$, $b_{Mx,y}$, and $b_{Mx,z}$ also given in table 6.2.

6.1.3 Measurement and detector regions

As mentioned before in Sec. 6.1 for the simulation scheme description, we can measure the electromagnetic field at all points inside the free Maxwell simulation region. However, in principle to show the main properties of the near-field and far-field effects it is sufficient to evaluate the variables only at distinguished points, which give characteristic information about the effects. Instead of taking just one point, we can integrate over several points,

| variable | distance d_1 | | distance d_2 | |
|------------------------|---------------------------------------|-----------------------|---------------------------------------|-----------------------|
| | conv. units | [a.u.] | conv. units | [a.u.] |
| ω | 3.05 eV | 0.112 | 2.83 eV | 0.104 |
| k_x | $1.55 \text{ e}^{-11} \text{ m}^{-1}$ | 8.17 e^{-4} | $1.43 \text{ e}^{-11} \text{ m}^{-1}$ | 7.59 e^{-4} |
| λ | 406.5 nm | 7681.84 | 438.1 nm | 8279.02 |
| $E_{0,z}$ | $5.142 \text{ e}^7 \text{ V/m}$ | 1.0 e^{-4} | $5.142 \text{ e}^7 \text{ V/m}$ | 1.0 e^{-4} |
| Intensity | $3.51 \text{ e}^{12} \text{ W/m}^2$ | 5.45 e^{-4} | $3.51 \text{ e}^{12} \text{ W/m}^2$ | 5.45 e^{-4} |
| ξ | 2034.08 nm | 38438.5 | 2034.08 nm | 41395.1 |
| x_0 | 4068.16 nm | 76877.0 | 4381.07 nm | 82790.2 |
| $L_{\text{KS},x}$ | 1.993 nm | 37.658 | 1.993 nm | 37.658 |
| $L_{\text{KS},y}$ | 1.993 nm | 37.658 | 1.993 nm | 37.658 |
| $L_{\text{KS},z}$ | 3.347 nm | 63.258 | 3.547 nm | 67.037 |
| $L_{\text{Mx},x}$ | 2.646 nm | 50.000 | 2.646 nm | 50.000 |
| $L_{\text{Mx},y}$ | 2.646 nm | 50.000 | 2.646 nm | 50.000 |
| $L_{\text{Mx},z}$ | 4.498 nm | 85.000 | 4.498 nm | 85.000 |
| $a_{\text{Mx},x}$ | 2.170 nm | 41.000 | 2.170 nm | 41.000 |
| $a_{\text{Mx},y}$ | 2.170 nm | 41.000 | 2.170 nm | 41.000 |
| $a_{\text{Mx},z}$ | 4.022 nm | 76.000 | 4.022 nm | 76.000 |
| Δx_{KS} | 0.053 nm | 1.000 | 0.053 nm | 1.000 |
| Δx_{Mx} | 0.053 nm | 1.000 | 0.053 nm | 1.000 |
| Δt_{KS} | $5.096 \text{ e}^{-3} \text{ fs}$ | 0.211 | $5.096 \text{ e}^{-3} \text{ fs}$ | 0.211 |
| Δt_{Mx} | $1.019 \text{ e}^{-4} \text{ fs}$ | 4.21 e^{-3} | $1.019 \text{ e}^{-4} \text{ fs}$ | 4.21 e^{-3} |

Table 6.2: Simulation parameters for the sodium dimer for distances $d_1 = 0.1 \text{ nm}$ and $d_2 = 0.5 \text{ nm}$.

surfaces or volumes of interest to get a mean value for evaluating the field.

For this application, we define three distinguished points, the mid point \vec{r}_{mp} at the origin of the box

$$\vec{r}_{\text{mp}} = (0, 0, 0), \quad (6.1.1)$$

which is the junction between the two dimer spheres to analyze the near-field. To measure the far-field, we select two far-field points, one along the x-axis with

$$\vec{r}_{\text{ffpx}} = (1.957 \text{ nm}, 0, 0) = (37.0 \text{ a.u.}, 0, 0), \quad (6.1.2)$$

and one along the y-axis with

$$\vec{r}_{\text{ffpy}} = (0, 1.957 \text{ nm}, 0) = (0, 37.0 \text{ a.u.}, 0). \quad (6.1.3)$$

Furthermore, we define a detector surface given by the parametrization

$$\vec{r}_{\text{sfx}}(\alpha, \beta) = \vec{r}_{\text{ffpx}} + \alpha \vec{e}_y + \beta \vec{e}_z, \quad \begin{cases} -37.0 \leq \alpha \leq 37.0 \\ 81.0 \leq \beta \leq 71.0 \end{cases}. \quad (6.1.4)$$

The detector surface for calculating a mean value of a measurable variable includes the far-field point \vec{r}_{ffpx} and the extension is determined by the box limits. We choose the limits such that all points have sufficient distance to the absorbing PML region.

6.1.4 Laser pulse shape

The external laser pulse propagates with a wavevector $\vec{k} = (k_x, 0, 0)$ along the x-axis. The electric field polarization is oriented along the z-axis and consequently the magnetic field

oscillates parallel to the y-axis. The spatial and time-dependent analytical expression for the external laser electric field $\vec{E}_{\text{pw}}(\vec{r}, t)$ has a cosinoidal envelope and is given by

$$\vec{E}_{\text{pw}}(\vec{r}, t) = \vec{e}_z E_{0,z} \cos(k_x(x-x_0) - \frac{2\pi}{\lambda}t) \cos\left(\frac{\pi(x-2\xi-x_0-c_0t)}{2\xi} + \pi\right) \cdot \theta\left(\xi - \frac{|k_x(x-x_0) - \frac{2\pi}{\lambda}t|}{|k_x|}\right). \quad (6.1.5)$$

We used the Heaviside-theta function $\theta(x)$. Since the wavevector $\vec{k} = (k_x, 0, 0)$ contributes only along the x-axis and the direction of the electric field \vec{E}_{pw} polarization is along the z-direction, the corresponding magnetic field \vec{B}_{pw} reads

$$\vec{B}_{\text{pw}}(\vec{r}, t) = -\vec{e}_y \frac{1}{c_0} \vec{E}_{\text{pw}}(\vec{r}, t). \quad (6.1.6)$$

Using $\vec{E}_{\text{pw}}(\vec{r}, t)$ and $\vec{B}_{\text{pw}}(\vec{r}, t)$, we can build the Riemann-Silberstein six-vector $\mathcal{F}_{\text{pw}}(\vec{r}, t)$

$$\mathcal{F}_{\text{pw}}(\vec{r}, t) = \begin{pmatrix} \sqrt{\frac{\epsilon_0}{2}} \vec{E}_{\text{pw}}(\vec{r}, t) + i\sqrt{\frac{1}{2\mu_0}} \vec{B}_{\text{pw}}(\vec{r}, t) \\ \sqrt{\frac{\epsilon_0}{2}} \vec{E}_{\text{pw}}(\vec{r}, t) - i\sqrt{\frac{1}{2\mu_0}} \vec{B}_{\text{pw}}(\vec{r}, t) \end{pmatrix}, \quad (6.1.7)$$

which is used to update the incident plane wave boundaries for each propagation time step. The laser pulse parameter differ for the two runs, since we drive both systems with their corresponding resonance frequency of maximum absorption. In case of the $d_1 = 0.1nm$ dimer, the Q-mode plasmon frequency reads $\omega_1 = 3.05eV$, and $\omega_2 = 2.83eV$ for D-mode frequency of the $d_2 = 0.5nm$ dimer [120]. The cosinoidal envelope width ξ of the laser pulse is coupled to the frequency respectively the corresponding wavelength. Both pulses are placed by x_0 outside the simulation box. All laser pulse parameters can be taken from Table 6.2

6.1.5 Propagators

Inside the Maxwell propagation region with $(-l_{\text{Mx},x} \leq x \leq l_{\text{Mx},x})$, $(-l_{\text{Mx},y} \leq y \leq l_{\text{Mx},y})$, $(-l_{\text{Mx},z} \leq z \leq l_{\text{Mx},z})$, we propagate the Kohn-Sham system with the matter ETRS propagator from Eq. (5.4.9) using the Power-Zienau-Woolley transformed MPKS Hamiltonian from Eq. (5.5.9) with multipole expansion. The Maxwell system is evolved in time by the Maxwell ETRS propagator from Eq. (5.3.4) with corresponding Hamiltonian kernel $\bar{\mathcal{H}}$ from Eq. (5.1.14), where we use only $\bar{\mathcal{H}}$ and switch off the internal diamagnetic current kernel $\bar{\mathcal{K}}$. The current density term \mathcal{J}_{loc} given in Eq. (5.1.20) only contains the paramagnetic current contribution. For all exponential operators inside the Maxwell and matter propagators a series expansion of the exponential of order of four is used, and we chose a finite difference stencil order of four for the derivative operations.

We propagate the Riemann-Silberstein vector corresponding to the total vector potential $A^k = A_{\text{mat}}^k + A_{\text{ext}}^k$ of external and internal fields. The nuclei are treated classically and are propagated with Ehrenfest equations of motion [111]. Since we have the electromagnetic fields available in the simulation box, we also include the classical Lorentz force that acts on the ions. For the transversal Kohn-Sham field we use the mean-field approximation $A_{\text{KS}}^k \approx A_{\text{mat}}^k + A_{\text{ext}}^k$ as well as the physical mass of the particles to take into account the bare vacuum fluctuations of the photon field. For the longitudinal Kohn-Sham field we use $A_{\text{KS}}^0 \approx A_{\text{mat}}^0 + A_{\text{ext}}^0 + A_{\text{xc,LDA}}$, where $A_{\text{xc,LDA}}$ is the adiabatic local density approximation (LDA) exchange-correlation approximation [124, 118].

In addition to the fully coupled EMPKS simulation, we propagate in addition the unperturbed Maxwell system inside the inner simulation box to get the required values for the

incident plane wave plus PML boundaries according to section 3.4.6. Hence, the Maxwell Hamiltonian has to be updated inside the PML boundaries by the additional PML matrix $\tilde{\mathcal{G}}$ according to Eq. (3.4.48).

6.2 Results from Ehrenfest-Maxwell-Pauli-Kohn-Sham simulations

After introducing the simulation scheme with external laser and the nanoplasmonic sodium dimer in the previous section, we provide in the following the most relevant results of the actual EMPKS simulations of the dimer for different theory levels according to Table 6.1. We compare the results of self consistently coupled light-matter propagation with conventional forward-coupling once with dipole approximation and beyond.

First, we produced a movie of four representative variables to visualize vividly the arising dynamics of the dimer interacting with the laser pulse. The full movies for the two different cluster distances d are provided in Ref. [125] for $d_1 = 0.1nm$ and Ref. [126] for $d_2 = 0.5nm$. Two representative snapshots of the first movie are presented in Figures 6.3 - 6.4. The first one was taken at time $6.89fs$ when the external laser maximum reached the center of the dimer, and the second one at time $8.33fs$, when the internal induced electric field enhancement becomes maximal. Both snapshots are divided into five figure panels. On the top we find schematically the location of the laser pulse and a two-dimensional enlarged picture of the ion geometry. The four remaining plots are 2D contour plots along the x-y plane of the 3D simulation box. The upper left one shows the induced paramagnetic current density. The other three plotted variables illustrate the differences of the current time step values and the ground state values since the differences are distinctly smaller than their ground state values. Therefore, we present the differences of the electron localization function (ELF) on the upper right, of the electric field on the lower left, and of the Maxwell density. The different opposed amplified ELF contour regions which are located outside the clusters shows clearly the induced surface plasmons. Since we see four extrema, two minima and two maxima, regions, the ELF contour plots emphasizes that the laser excites the dimer with Q-mode plasmons.

6.2.1 Electric field enhancement

The work of Varas et. al. reveals a large field enhancement right at the mid point \vec{r}_{mp} between the two nanoplasmonic clusters. This field enhancement is purely caused by the only longitudinal electric field of the matter plus the transverse external laser. In such conventional time-dependent Kohn-Sham calculations, the longitudinal component of the electric field can be obtained from the scalar Kohn-Sham potential. Solving Eq. (4.5.16) for the external potential plus the matter potential (Hartree potential), i.e., $A_{mat}(\vec{r}, t) + A_{ext}(\vec{r}, t) = A_{KS}(\vec{r}, t) - A_{xc}(\vec{r}, t)$, gives

$$\vec{E}_{||}(\vec{r}, t) = -\vec{\nabla} (A_{mat}(\vec{r}, t) + A_{ext}(\vec{r}, t)) . \quad (6.2.1)$$

The total electric field \vec{E}_{fw} for conventional forward-coupling simulations is the superposition of the longitudinal field from the matter plus the external transverse field, i.e., the laser

$$\vec{E}_{fw}(\vec{r}, t) = \vec{E}_{||}(\vec{r}, t) + \vec{E}_{pw}(\vec{r}, t) . \quad (6.2.2)$$

In case of a forward-backward simulation, we assume that also the transverse component of the total field influences the field enhancement. To investigate this, we use our

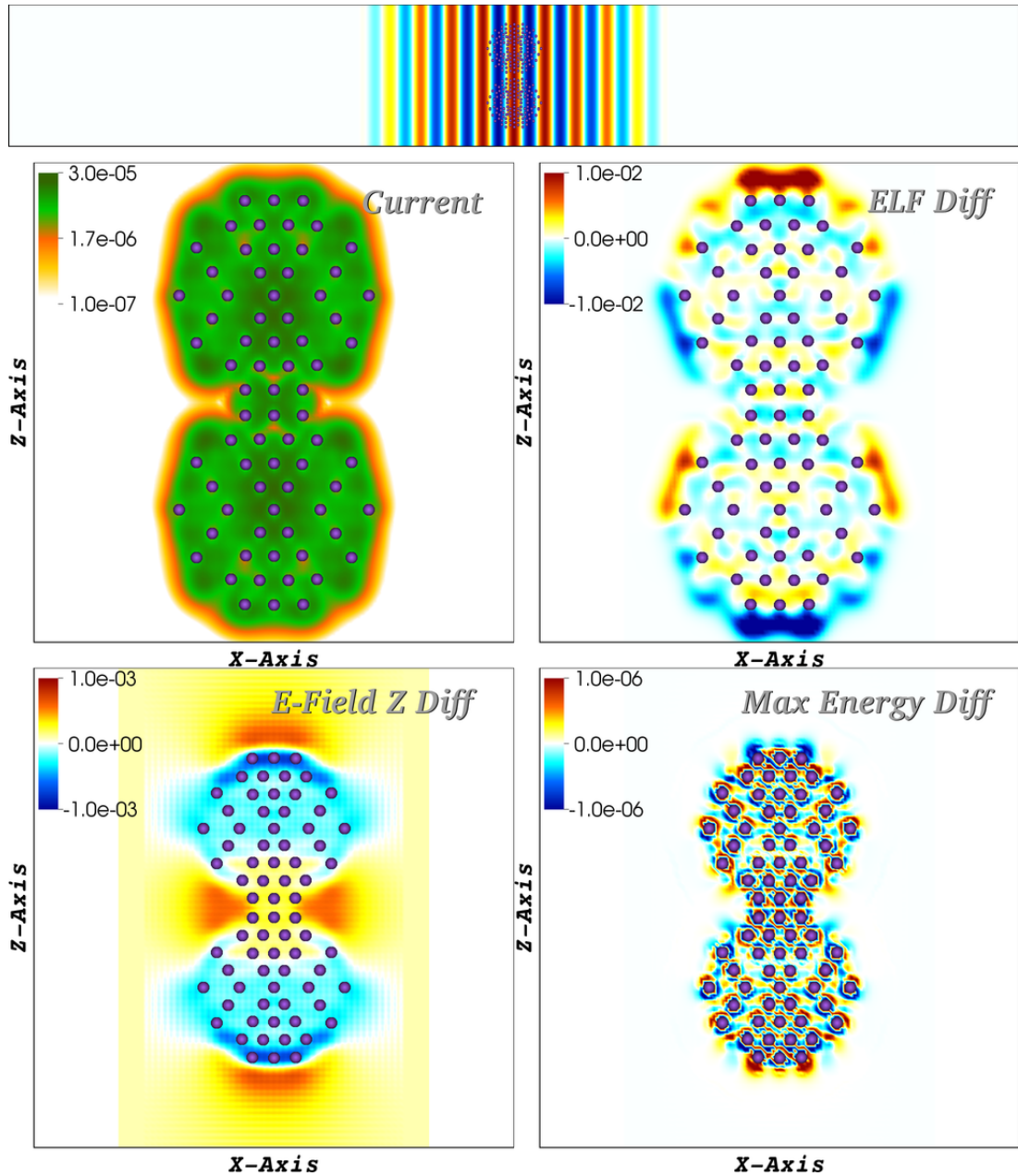


Figure 6.3: In the supplemental material we provide a movie that shows the real-time dynamics of the nanoplasmonic dimer with distance $d_1 = 0.1$ nm. In the figure, we show a frame of the movie at time 6.89 fs. The upper two panels show contour plots of matter variables, the absolute value of the current density and the electron localized function (ELF). The most relevant Maxwell field variables, the electric field along the laser polarization direction z and the total Maxwell energy are presented in the lower panels. In the top of the figure, we show the incident laser pulse and at the center the geometry of the nanoplasmonic dimer.

EMPKS approach to study the fully coupled electromagnetic field. An overview of the significant electric field behavior for the dimer $d_1 = 0.1\text{nm}$ is presented in Figure 6.5. The system is driven by its resonance frequency that induces quadrupole surface plasmons on the dimer. The initial external laser amplitude is plotted in panel a), and the induced current in panel b). The following three panels c) - e) show the electric field enhancement,

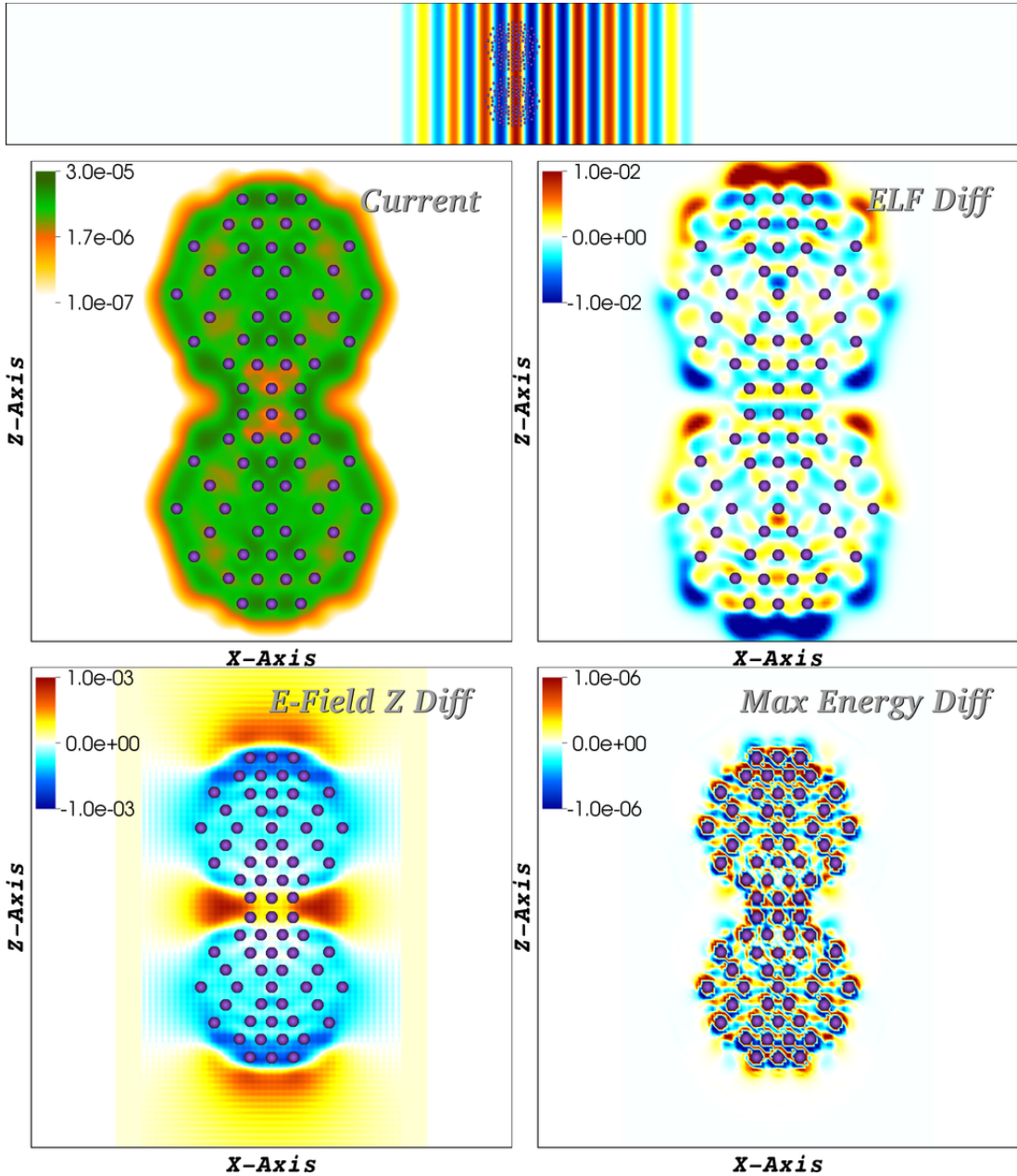


Figure 6.4: Similar movie frame as Fig. 6.3, but with the frame at time 8.33 fs.

first for the mid point \vec{r}_{mp} , the far field at point \vec{r}_{ffpx} and last the average electric field over the detector surface (\vec{r}_{sfx}), respectively. All blue curves in that figure refer to the forward coupling theory level with dipole approximation (F@ED) and are identical with the previous results of Varas et. al, but calculated with our EMPKS implementation by switching off the matter to Maxwell back-reaction. The overlap with the data of Varas et. al. provides a consistency-check of our implementation.

The black curve in panel a) and the light gray curve in panel b) display the same initial cosinoidal shaped free laser that passes through the box without any matter interaction. We include the pulse from panel a) again in panel c) to facilitate the comparison of the incident field amplitude (gray) with the actual field values when light-matter coupling is taking place (blue and green). The blue curve in panel c), our forward coupling simulation F@ED, confirms a field enhancement of Varas. et. al. at the mid point of about a factor

Induced current and electric field enhancement in z-direction between the dimer for $d_1=0.1\text{nm}$

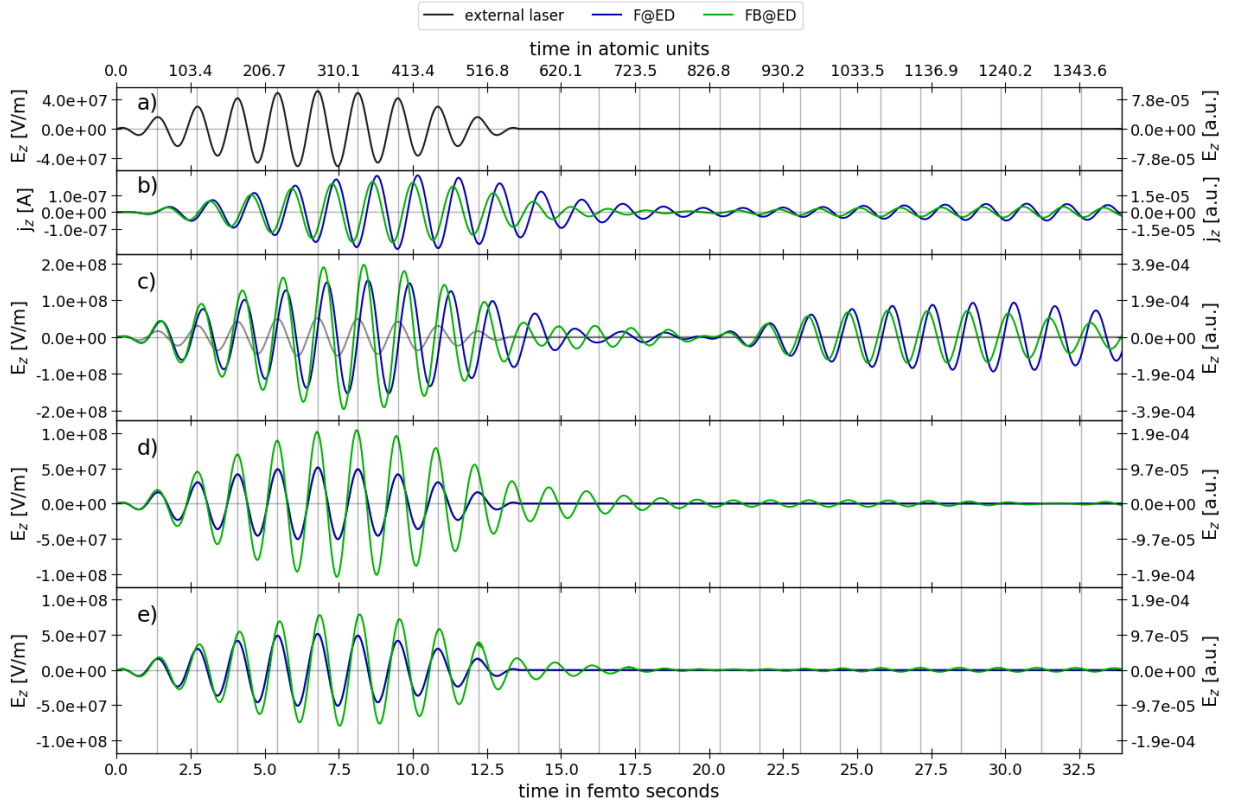


Figure 6.5: Electric field values and current density in z-direction in the center between the two Sodium clusters for $d_1 = 0.1\text{nm}$. The first panel *a*) illustrates the incident cosinusoidal laser pulse with frequency $\omega_1 = 3.05 \text{ eV}$ (0.112 a.u.) $\lambda_1 = 406.5 \text{ nm}$ (7681.84 a.u.) and amplitude of $E_z^0 = 5.142 * 10^7 \text{ V/m}$ (10^{-4} a.u.) which drives the system. The second panel *b*) displays the electric field enhancement in dipole approximation and only in forward coupling, while the red curve includes electric dipole, magnetic dipole and electric quadrupole terms and takes light-matter forward and backward coupling into account. The curve in bright gray illustrates the initial unperturbed laser. The last plots in panel *c*) show the corresponding current densities at the center point between the dimer and in panel *d*) the current density differences. The period $T_1 = 1.36 \text{ fs}$ corresponding to the laser frequency is ω_1 is indicated with grey vertical lines.

of three compared to the incident laser amplitude. Additionally, we see the same delay of the total induced electric field maximum compared to the maximum field amplitude of the driving laser. This shift of maxima can also be seen in panel *c*) by comparing the maxima of the gray and blue curves. For longer times, the mid point field in *c*) shows a significant beating signal, whereas the far field panels *d*) and *e*) present only a weak reaction.

The green curves in Figure 6.5 represent the run including the back-reaction of the matter on the electromagnetic fields in dipole approximation (FB@ED). The full forward-backward coupled system reveals in panel *c*) a similar enhancement for very short time, a slightly increased enhancement for intermediate times and a smaller beating for longer times. While the laser drives the dimer, the back-reaction is increasing the field at the mid point. The increasing effect still holds with a small delay when the external laser already decrease. Taking a look at the far field panels *d*) and *e*), the differences between the two runs are more significantly. The forward-backward coupled simulation in *e*) returns a field

Induced current and electric field enhancement in z-direction between the dimer for $d_2=0.5\text{nm}$

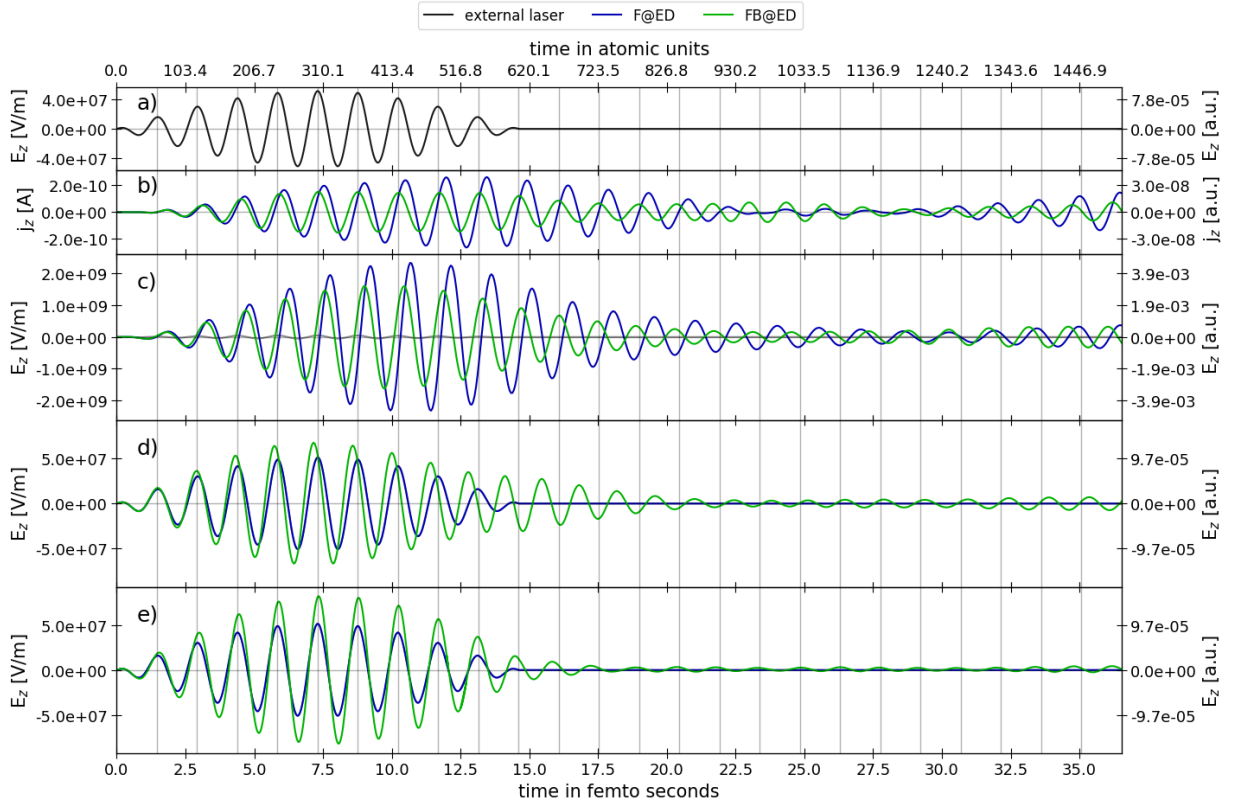


Figure 6.6: Similar to figure Fig. 6.5, we show here the electric field enhancements and current densities for the Sodium dimer with $d_2 = 0.5\text{nm}$.

at the far-field point \vec{r}_{ffpx} twice as large as the one of the forward coupling run. This effect is a bit weaker when we take the average field over the surface in f). Comparing the phases and frequencies of all evaluated fields, we notice that the far-fields are almost in phase with the incident laser whereas the near-field shows a small phase and frequency shift, for both the forward and forward-backward simulations.

The result of electric field for the second dimer configuration with delimiter $d_2 = 0.5\text{nm}$ is illustrated in Figure. 6.6. The laser pulse a resonance frequency that induces D-mode surface plasmons. We present the same characteristic variables and use the same ordering as before in Figure. 6.5. Due to the larger distance between the two Sodium clusters, the absolute value of the current density is significantly smaller than the one in $d_1 = 0.1\text{nm}$ run. The induced current densities in Figure 6.6 panel b) of the forward coupling F@ED case are larger than for the forward and backward coupled FB@ED case. The electric near-field enhancement in panel c) shows a opposite behavior than in Figure 6.5, where the forward-backward coupled field enhancement induces larger fields for short times. In case of the $d_2 = 0.5\text{nm}$ run with D-mode plasmons, we find a significantly smaller field enhancement for the forward-backward coupled run compared to the only forward coupling simulation. In turn, the far field behaviors shown in panel d) and e) show a similar picture as for the first dimer configuration. The full coupled system returns a stronger fields at our far field boundary. As before in the case of the d_1 separation, we find here that the average of the electric field over the detector surface in the far field as shown in panel e) is mostly locked to the phase of the incident laser. In contrast, the near field at the mid point between the two nanoparticles shows phase and frequency shifts. They are larger for the F@ED coupling at short times and the phase turns even to the opposite sign compared to

FB@ED coupling for intermediate times.

Due to the electric field construction in Eq. (6.2.2) for the forward coupling runs we know, that all related field enhancements are only longitudinal. To analyze further the nature of the field enhancement for the forward-backward coupling simulations, we performed a Helmholtz-decomposition of the electric field in the fully-coupled FB@ED case. The corresponding decomposed fields can be seen in Figures 6.7 and 6.7, for the $d_1 = 0.1nm$ dimer and $d_2 = 0.5nm$ dimer, respectively. In both figures, panels a) and c) illustrate the total field as a reference and their corresponding longitudinal fields. Since the transverse component is in all cases a magnitude smaller than the total or longitudinal fields, we plot them separately in b) and d). The plots in panel a) and c) respectively b) and d) differ in their evaluation point. The first two upper plots show the field decomposition at the mid point \vec{r}_{mp} , whereas the lower ones evaluate the fields at the far-point \vec{r}_{fpx} . In general, we find that the main contribution of the forward-backward coupled field enhancement arises also from the longitudinal field as in the forward coupled case. Besides the fact that the longitudinal enhancement is about one order of magnitude larger for the d_1 distance and even two orders of magnitude larger for the d_2 distance, we see some phase and frequency

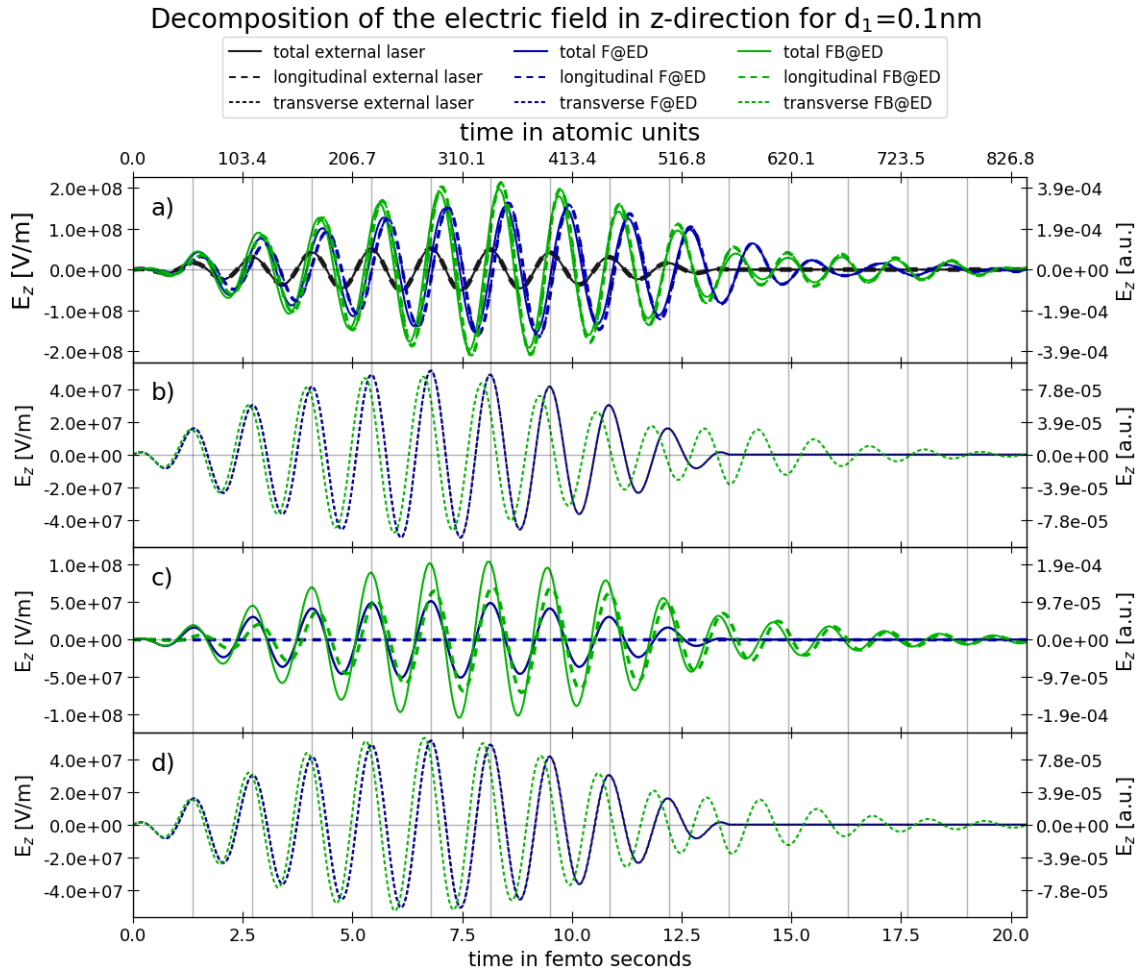


Figure 6.7: Decomposition of the total electric field into transverse and longitudinal components. Panel a) shows the total (solid lines) and the longitudinal (dashed lines) electric field in z-direction at \vec{r}_{mp} . The corresponding transverse field (dotted lines) is plotted in b). The same field decomposition at the surface point \vec{r}_{fpx} is plotted in c) and d).

shifts between the different fields. The phase shift between the longitudinal and the total field in Figure 6.7 a) and Figure 6.7 b) is very small for both distances. Although the phase shift to the transverse field is rather large, its small amplitude leads to a minor contribution for the total field. This behavior differs at the detector surface point \vec{r}_{ffpx} illustrated in Figure 6.7 c) and Figure 6.8 c). Here, both the longitudinal and the transverse field have almost the same magnitude and show a clear phase shift. The behaviour in the far field in Figure 6.7 d) and Figure 6.8 d) exhibits besides a phase shift also a slight frequency shift. Consequently, the incident laser pulse interferes with the induced transverse field which results in a frequency modification of the outgoing laser. Since the transverse field, which reaches the far-field detector region, propagates freely, our detector point measures this frequency shift. Figure 6.13 panel d) we shows the Fourier transform of the transverse field at point \vec{r}_{ffpx} which is plotted in the decomposition Figure 6.8. It directly visualizes the frequency shift of the emitted respectively passed electromagnetic field due to the dimer caused electromagnetic fields. The effect is similar to a classical medium.

Up to now, we have looked at the electric field enhancement as function of time. In Fig. 6.9, we show contour plots of the transversal electric field enhancement as function of space in the x-z plane of the nanoplasmonic dimer. The two plots in the top row correspond to the point in time where the incoming laser pulse reaches its maximum, whereas the two plots in the bottom row correspond to the point in time where the electric field enhancement

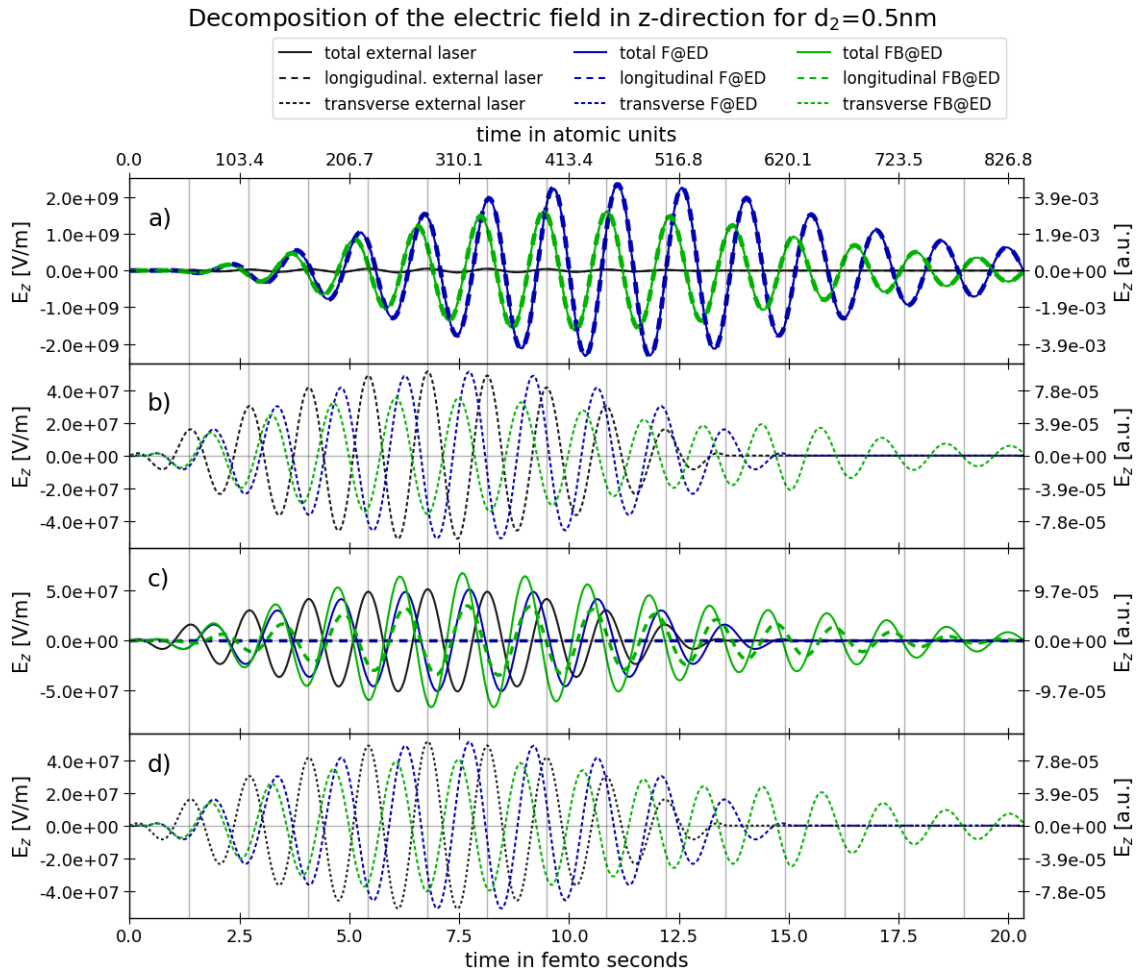


Figure 6.8: Decomposition of the electric field as in figure Fig. 6.7 for the sodium dimer with $d_2 = 0.5 \text{ nm}$.

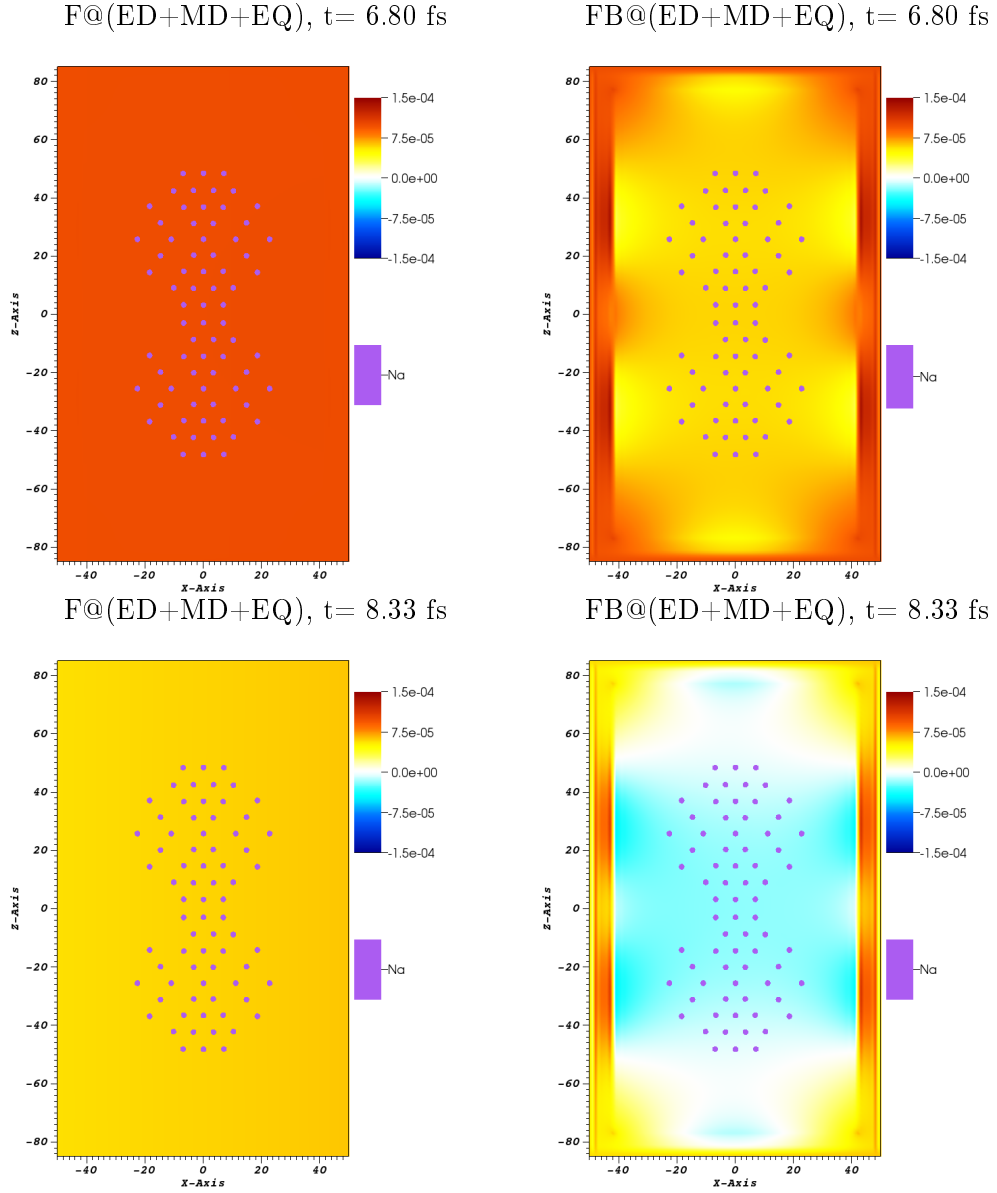


Figure 6.9: Contour plots for the electric field enhancement in the x-z plane of the nanoplasmonic dimer with $d_1 = 0.1nm$. The upper two panels show the field enhancement when the external laser reaches its maximum and in the lower two panels show the electric field when the field enhancement itself reaches its maximum. The two panels on the left (top and bottom) correspond to the $F@(ED+MD+EQ)$ theory level, whereas the two panels on the right (top and bottom) correspond to $FB@(ED+MD+EQ)$ coupling.

reaches its maximum. The two plots in the left column have been computed with light-matter forward coupling only and in the two plots in the right column we have used self-consistent forward-backward coupling. As can be seen, the forward coupled cases show a rather uniform electric field in the plane which is due to the dipole approximation and the fact that the incident wavelength is rather large on the scale of the dimer. On the other hand for the fully coupled case on the right hand side local field effects are clearly visible. In particular in the plot on the bottom right it can be seen that at the maximum of the field enhancement the transversal field contribution in fact counter acts the longitudinal

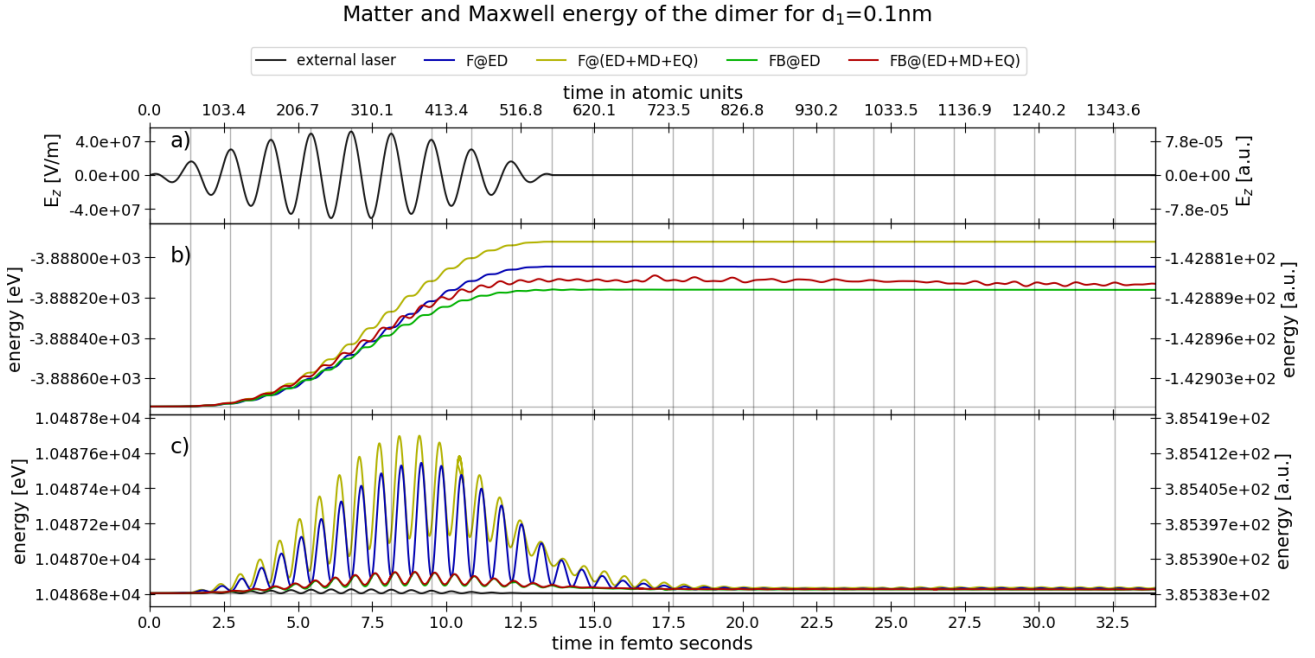


Figure 6.10: Matter and electromagnetic energies for the sodium dimer with $d_1 = 0.1\text{nm}$ separation. Panel a) illustrates the external laser amplitude, panel b) displays the electronic energy and in c) we show the corresponding Maxwell energy inside the simulation box.

contribution since it has turned to a negative sign in most regions of space.

6.2.2 Next order in multipole coupling and energies

In the previous section, we only focused on the electric dipole Maxwell to matter coupling, since higher order coupling terms do not change the results in Sec. 6.2.2 significantly. This turns when we consider for instance the corresponding matter and Maxwell energies. In that case, higher ordered coupling terms of the Kohn-Sham Hamiltonian, i.e., magnetic dipole (MD) and electric quadrupole (EQ), lead to different energy spectra, which we present in Figures 6.10 and 6.11. As before, we compare only forward coupling (F@ED) and the self-consistent forward-backward coupling (FB@(ED+MD+EQ)), but add here also the theory levels F@(ED+MD+EQ) and FB@(ED+MD+EQ) of higher multipole Hamiltonian terms.

First, we consider the corresponding simulations of the d_1 configuration in Figure 6.10. For referencing the amplitude of the actual external laser field on the system, we plot as before the laser pulse curve in panel a). The next panel b) shows the energy of the Kohn-Sham system, which splits significantly in time and stay constant when the laser has passed the simulation box. Similar to the enhanced fields, which exhibit a clear delay of reaction to the initial laser, the energy gain for the matter is very immediate to the external laser intensity. The blue curve shows the conventional F@ED in dipole approximation without back reaction of the matter to the field. If we add the second order multipole coupling terms, the corresponding F@(ED+MD+EQ) run gains more energy than in dipole approximation. This effect can readily be understood, since we drive the system with a Q mode resonance frequency, such that the quadrupole nature of the plasmons results in a larger transfer of energy to the electrons.

Switching on backward coupling reduces the energy absorption of the matter. Both en-

ergies of the forward-backward runs remain below the reference F@ED run. Again, the additional multipole terms in the FB@(ED+MD+EQ) run increase the energy curve compared to the FB@ED run, which confirms the higher influence of the magnetic dipole and the electric quadrupole term on the system. If we focus the behavior all increasing curves in detail they are in most cases shaped like cascades with small plateaus between one laser period. This feature indicates that we excite the system with a proper resonance frequency, otherwise the cascades would show some dips due to emitting energy, before the system absorbs energy of the next laser oscillation. Such small dips between the laser periods can only be seen in the red curve of the FB@(ED+MD+EQ) which leads to the assumption that the forward and backward coupling system with second order multipole expansion is not exactly resonant to the driven frequency $\omega_1 = 3.05eV$.

In panel c) we show the total electromagnetic energy inside the simulation box, which corresponds to an integration of the Maxwell energy inside the free Maxwell region (b_x, b_y, b_z) of the simulation box (b_x, b_y, b_z , cf. Figure 5.4). First, we note that all Maxwell energies oscillate with twice the frequency of the initial laser due to the squared electric and magnetic field expression of the energy density. The peak positions depend on the phase shift between electric and magnetic fields. Our coupled self consistent forward-backward coupling propagation shows, that the main magnetic field contribution bases on the external plane wave magnetic field. Only very small field amplifications in z and y direction are measured, but negligible. Hence, the magnetic field propagates almost like a plane wave through the simulation box. Further detailed observations have shown that the magnetic field increases the total energy peaks only a little. As we already noticed for the electric field enhancement, the dominant part of the total electric field is given by the longitudinal component. This means, that the largest contribution of the Maxwell energies also originates from the longitudinal electric field. This can be seen by comparing the scale of the black curve, which corresponds to the energy of the purely transversal incoming laser pulse, with the blue curve which shows the Maxwell energy for the forward coupled case in dipole approximation. Adding the higher order multipole terms to the Hamiltonian exceeds the Maxwell energy, which corresponds again to the Q mode excitation.

In turn, we focus at the second dimer configuration with $d_2 = 0.5$ nm, which is driven in D mode, which has dipole character. This fact can directly be seen in the corresponding Figure 6.11. While overall a similar situation emerges as for the smaller d_1 distance, the differences between higher order Maxwell to matter coupling and dipole coupling is less significant as before. The small added energies of the MD and EQ terms has only small effects on the electron energies and the electromagnetic fields. The F@Ed and F@(ED+MD+EQ) energies as well as the FB@ED and FB@(ED+MD+EQ) energies are almost on top of each other. Therefore, if we couple to a dipole mode of the system, the MD and EQ terms have almost no effect. This corresponds to a perturbative analysis of the system and considering the selection rules of the MD and EQ coupling Hamiltonians. This two exemplary runs show, that the underlying symmetry of the excited modes if higher order multipole terms become important.

The common fact, that for both distances d_1 and d_2 the forward- and backward coupling matter energies remain always below the forward coupling runs demonstrates that the matter absorbs less energy if the back-reaction is taken into account. In addition to the larger absorption of energy, the forward coupling causes larger Maxwell energy amplitudes inside the simulation box. This is remarkable since we observed in Fig. 6.5 and Fig. 6.6 that the self-consistent forward-backward coupling yields a larger enhancement of the field. As consequence, in some regions of the dimer large field enhancements occur, but the mean amplification is clearly weaker than for the only forward coupled cases. Furthermore, the forward coupling runs break energy conservation, since the laser pumps the matter system

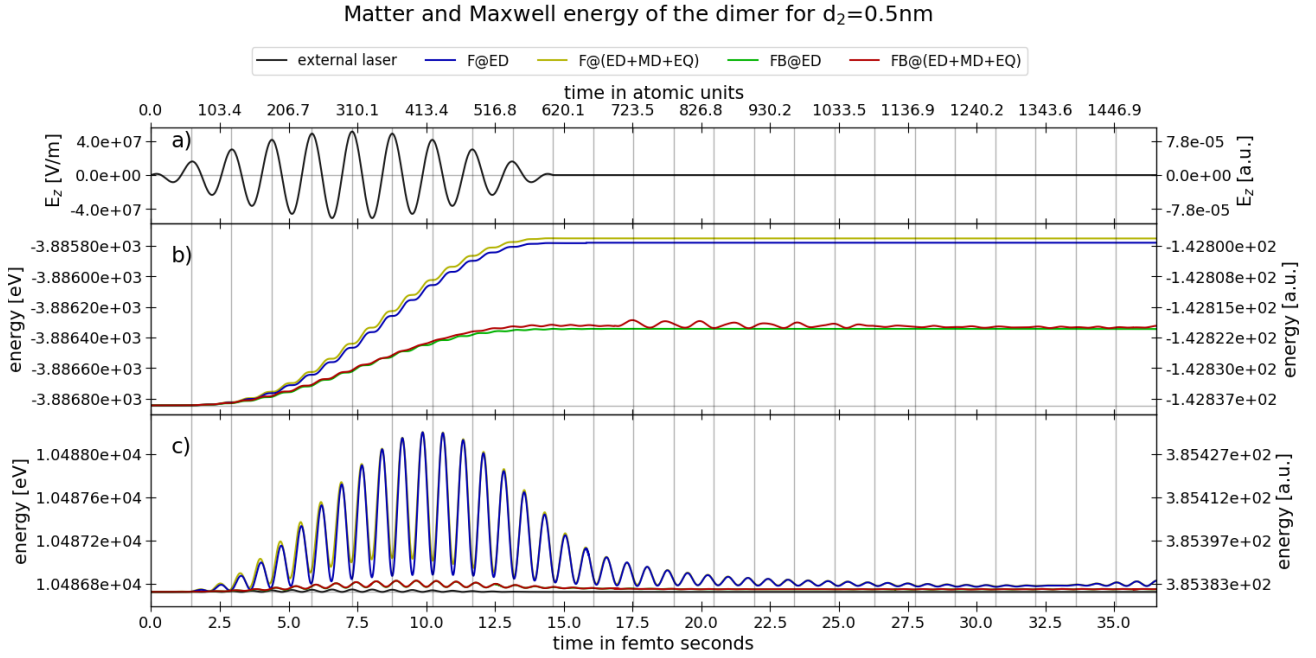


Figure 6.11: Similar to Figure 6.10, we present the matter and electromagnetic energies for the sodium dimer with $d_2 = 0.5\text{nm}$ separation.

without any loss. In the forward-backward coupled simulations this is not as severe anymore, and explains that the energy absorption and the mean Maxwell field enhancement is always smaller compared to the forward coupling runs. The situation would be entirely different if we could enclose the laser pulse completely in the Maxwell box. Then the pulse would not be external anymore and in the forward-backward case full energy conservation holds. For optical wavelengths this requires enormous Maxwell simulation boxes if atomic scale grid spacings are used. But it becomes feasible for hard x-rays, where much smaller Maxwell grids are needed due to the shorter wavelength.

6.2.3 Electromagnetic detectors and harmonic generation

It is a common practice in most quantum simulations to use matter expectation values to approximate optical spectra. For instance, the Fourier transform of the dipole expectation value is often used to compute absorption spectra in the linear case of high-harmonic spectra in the non-linear case. Since we propagate besides the matter system the coupled electromagnetic system, it becomes feasible to directly analyze the emitted radiation. In that sense it is not necessary take the matter observables and the assumption that their properties give approximately the emitted Maxwell field. According to Sec. 5.8, we define electromagnetic detector regions in the far-field close to the box boundaries, which provides a paradigm shift to perform numerical simulations that very closely resemble the experimental situation. To demonstrate this, we analyzed once the dipole expectation values of the dimer $d_2 = 0.5\text{ nm}$ separation in Figure 6.12 b) - e) and the x-component of the electric field far field. Panel a) visualizes the external laser field and we notice that the same frequency appears in the corresponding dipole expectation values as well as in the electric field component. According to common optical theoretical methodology, this means the matter oscillates resonantly with its excitation signal, and in turn since we hit the resonance frequency, it is assumed that it emits electromagnetic light with the same frequency perpendicular to the oscillation axis. For further concrete frequency analysis, we performed

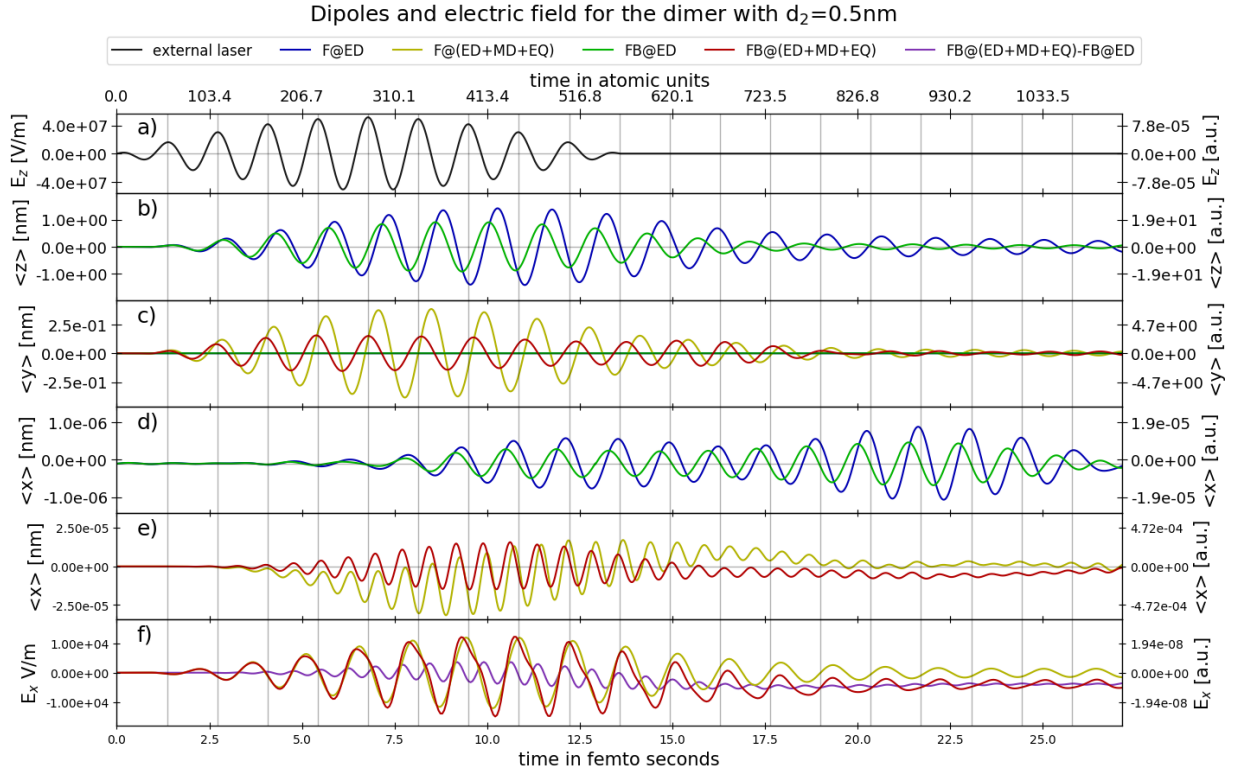


Figure 6.12: Position expectation values $\langle x \rangle$, $\langle y \rangle$, and $\langle z \rangle$ of the nanoplasmonic dimer with $d_1 = 0.1$ nm. In panel a) we show the initial laser pulse as reference signal and in b) - e) the dipoles of the dimer along different axis. Only beyond dipole approximation coupling reveals higher-order harmonics, which is directly detected by the E_x field component at the far-field point \vec{r}_{ffpy} along the y-axis.

a Fourier transform of panels e) and f), which are shown in Figure 6.13 in panel a) respectively b). Comparing the forward coupling cases, F@ED and FB@(ED+MD+EQ), with the fully coupled ones, FB@ED and FB@(ED+MD+EQ), show the same frequencies, but slightly phase shifted and with different strength. The oscillation amplitudes correspond with our previous considerations about the electric field enhancements and the energies. Adding the additional multipole Hamiltonians reveals new optical features of the system, which can directly be seen in panel e) in Figure 6.12. The two dipole expectation values along the x-axis shows in both cases, the forward and fully coupled runs, oscillate with twice the frequency of the incoming laser. Therefore, second harmonic generation is only found in beyond dipole Maxwell to matter couplings. We emphasize here, that both frequencies, the can directly measured in the electric field x-component at the far-field point \vec{r}_{ffpy} , which we present in panel f). Both runs, F@(ED+MD+EQ) and FB@(ED+MD+EQ), reproduce clearly the incoming frequency of the external laser. However, if we look at the FB@(ED+MD+EQ) curve, the field oscillation shows a small distortion compared to the F@(ED+MD+EQ) run, which looks more correctly cosinoidal. Subtracting both fields visualizes directly the reason for the deformed FB@(ED+MD+EQ) signal. It is superposed by the second harmonic frequency, which we do not see in the F@(ED+MD+EQ) curve, since we neglect the full coupled back-reaction of the matter to the electromagnetic field. We note here, that F@(ED+MD+EQ) includes indeed some back-reaction of the matter, namely the longitudinal field of the matter charge distribution. Otherwise, we would not see any oscillation in the yellow curve, since the x-component of the external laser field is

Fourier transform of the electric far field and electric dipole

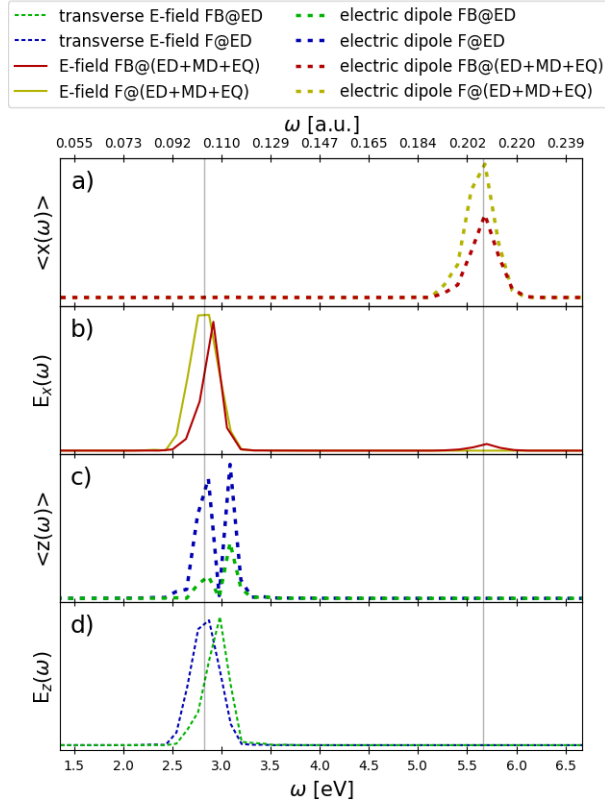


Figure 6.13: Fourier transform of the dipole expectation values and the electric field at the far-field detectors. Panel a) and b) show the Fourier transform of the dipole and the electric field at the far-field point \vec{r}_{ffpy} from panels e) and f) in Figure 6.12 respectively. While in the matter observable in a) only the second harmonic peak is visible, the Fourier spectrum of the electric field in b) contains the fundamental laser frequency and the second harmonic. In panel d) we show the Fourier transform of the electric field at the far-field point \vec{r}_{ffpx} along the laser propagation axis in dipole approximation. The field is shifted in frequency when self-consistent forward-backward coupling is used. The matter dipoles for this case are shown in panel e). The Fourier transform of panel d) correspond to the transverse fields shown in Figure 6.8. In the forward coupled case a spurious peak appears at the energy of the incoming laser (2.83 eV). This peak is suppressed in the forward-backward coupled case and the dipole spectrum also matches better the actual emitted radiation field in panel d).

zero. Consequently, we can deduce, that the second harmonic signal is a transverse radiation oscillating along the x-axis but propagating in y-direction, whereas the first harmonic oscillation in that direction(!) seems to be only longitudinal and hence localized to the matter.

6.2.4 Ion motion

In all the simulations that we have considered so far, we have used the Born-Oppenheimer approximation and clamped the classical nuclei at the optimized ground state. In this

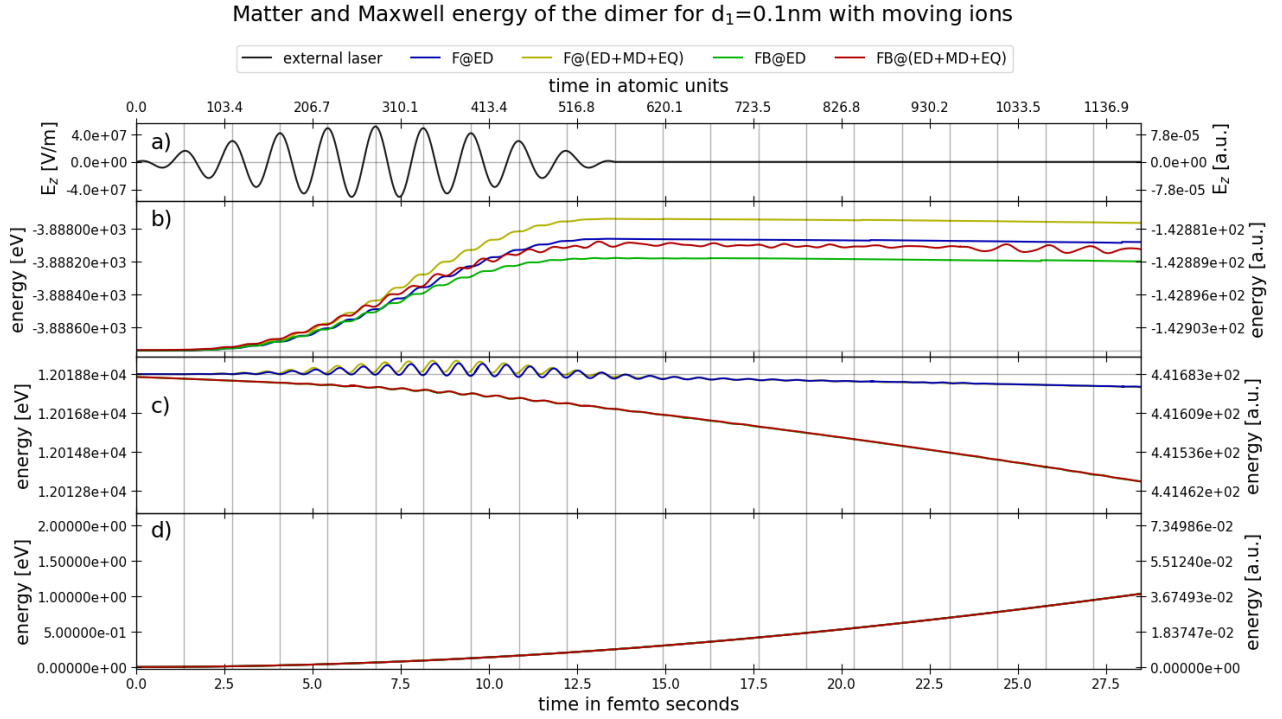


Figure 6.14: Same as Fig. 6.10 but now including the motion of the ions in classical Ehrenfest approximation.

section, we release this constraint. According to Sec. 4.6, we can propagate the classical motion of the nuclei using Ehrenfest equations of motion [111] and the Lorentz force, which we introduced in Eq. (4.6.8). In our case, we get the Lorentz forces in terms of the Riemann-Silberstein electric and magnetic field that we propagate in time. This allows to capture nuclear forces due to local field effects. For all the following cases, we take as initial condition for the Ehrenfest equations the atomic positions of the optimized ground state and set the initial velocities to zero. This effectively corresponds to a rather “cold” nuclear subsystem. More sophisticated velocity distributions could be used, e.g. thermalized velocity distributions from molecular dynamics runs coupled to a thermostat, but we leave such temperature studies for the future.

The ionic motion does not significantly change the behavior of the electromagnetic field within the first 50 fs, which is not quite remarkable, since typically ionic effects take place on a pico-second time scale. Nevertheless, taking a look at the corresponding energies reveals a strong difference that we present in Figure 6.14 for the nanoparticle distance d_1 and which corresponds to the clamped ions run in Figure 6.10. As before, panel a) shows the incoming laser, panel b) the matter energies and panel c) the Maxwell energies. In addition we add panel d) which illustrates the sum of kinetic energy of all nuclei as function of time. The additional ionic motion causes some additional fluctuations to the matter energy evolution, but the main behavior is very similar to the fixed ions simulation. Looking at the Maxwell energies in c) reveals a strong decrease of the Maxwell energy in the forward coupling and a rather strong decrease in the self-consistent forward-backward case. Since the electronic energy remains almost identical to the case of clamped ions, the losses in the Maxwell energy are directly transferred to the nuclei. As a consequence, the kinetic energy of the nuclei grows. This rather strong increasing of the ionic kinetic energy is remarkable, since it implies an untypical fast motion of the nuclei.

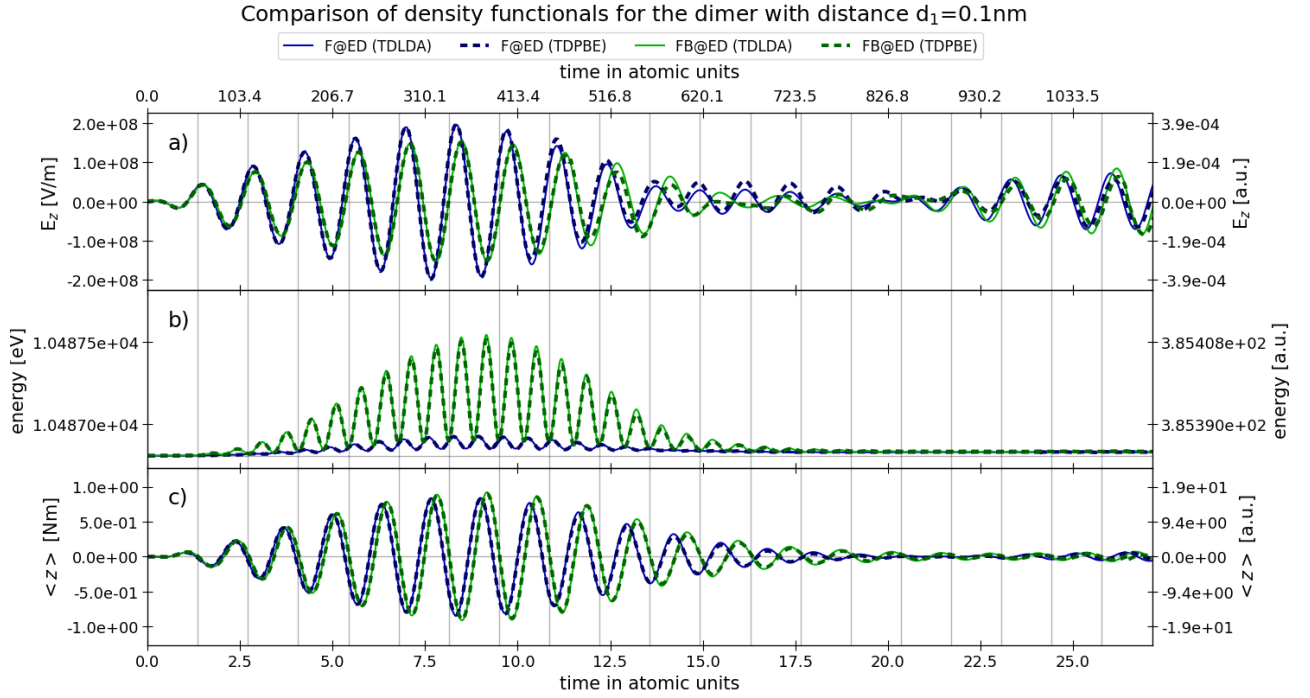


Figure 6.15: In the figure we show in panel a) the electric field at the origin, in panel b) the integrated Maxwell energy in the simulation box, and in panel c) the dipole expectation value in z-direction. We compare TDPBE results (dashed lines) with the TDLDA results (solid lines). The difference between TDPBE and TDLDA (dashed vs. solid lines) is much smaller than the difference between only forward coupling and self-consistent forward-backward coupling (blue vs. green lines). In particular, for forward-backward coupling a clear frequency shift is visible already after a short time.

6.2.5 Comparison of different density functionals

So far, all previous presented results have been computed with TDLDA functionals [124, 118] as choice for the approximate exchange-correlation functional that build the scalar potential for the longitudinal part of the light-matter interaction. In this section we asses the relative importance of exchange-correlation effects versus self-consistent light-matter interaction. For this purpose, we repeat the previous simulations, but using this time the PBE functional [127, 118]. To demonstrate the difference between the two different exchange-correlation runs, we plot in Figure 6.15 some characteristic variables like the electric field at the origin in panel a), the Maxwell energy inside the free-Maxwell region in panel b), and one dipole expectation value in panel c). In all panels, we compare the TDPBE results (dashed lines) with the TDLDA results (solid lines). In all cases the difference between the two different functionals (dashed vs. solid lines) is significantly smaller than the difference between the forward coupled and fully coupled simulation (blue vs. green lines). In case of Maxwell energy and dipole expectation value, the difference between the TDLDA and TDPBE run is rather small, whereas the electric field behaviors are only very similar in the beginning, but differ more and more when the electric field envelope decreases. However, our presented nanoplasmonic example reveals that it is more important in case of large induced currents and electromagnetic fields to use the self-consistent forward-backward light-matter interactions than to include further exchange-correlation contributions to the effective Kohn-Sham potentials. This supports the need

for a self-consistent coupling to Maxwell's equations to achieve a comprehensive description of light-matter interactions.

Summary, conclusion and outlook

In this thesis, we have faced the challenge of finding a feasible methodology and a first implementation of three-dimensional fully forward and backward coupled light-matter interactions. As a first key step, we have transformed the common Maxwell's equation into a Riemann-Silberstein representation, which provides the underlying equation of motion for the electromagnetic field in a inhomogeneous Schrödinger-like equation. This crucial step, gives us the opportunity to use quantum-mechanical time-evolution operators to propagate the electromagnetic field similar to matter wavefunctions. We use this advantage to implement a fundamental real-time real-space classical electromagnetic equation propagation into the existing quantum-mechanical simulation code Octopus. First, we implemented a stand-alone electromagnetic field simulation, which handles external current densities and linear media. We validate our novel propagation scheme and implementation with the established electromagnetic simulation program MEEP, which uses a standard finite-difference time-domain method for the Maxwell field propagation. The considered test simulations agree very well with the results of MEEP, also with regard to stability and efficiency of the runs.

To extend the possibilities for applications, we have considered adequate electromagnetic boundary conditions. As a first important boundary condition, we considered absorbing boundaries to simulate open Maxwell systems. We employ two different methods, first a mask absorption function which is easy to implement, and secondly a perfectly matched layer propagation. Our comparison of both different techniques has shown, that the PML provides a significantly better absorbing boundary and qualitatively better wave propagations in the simulation box. To simulate incoming signals which enter the simulation box, we have introduced incident plane wave boundaries, which we also combined with the perfectly matched layer boundaries to simulate incoming waves and scattered outgoing fields. This feature is useful to simulate pump-probe experiments or a particle excitation from several laser pulses and different incident angles. One possible way to get scattered fields from plane waves, for instance, is based on the interaction of the plane wave in vacuum and a linear medium, as we have shown in a first propagation example coupled to a linear medium. Our implemented propagator considers besides space- and time-dependent electric permittivity and magnetic permeability electric and magnetic conductivities. With this feature at hand, one can design a large set of purpose tailored simulation boxes, e.g., perfect and semi-transparent mirrors, wave guides, lossy layers, just to list a view options. Overall, the purely Maxwell propagation based on quantum-mechanical time-evolution operations is an equivalently alternative scheme to common electromagnetic time propagation via finite difference time domain, and it builds the first pillar for simulating fully coupled three-dimensional light-matter systems.

The second pillar is based on the many-body considerations for large matter systems. Starting on the theory level of quantum electrodynamics, we have deduced a multi-species auxiliary system, the Kohn-Sham system on a Pauli level to describe a non-relativistic low energy regime and based on density-functional theory (DFT). Using DFT instead of the

full many-body particle problem leads to a feasible but still very computational expensive problem. Hence, the underlying Maxwell-Pauli-Kohn-Sham equations determine the corresponding matter current density, which is used as the classical current inhomogeneity term of our Maxwell propagation equation. In that way, we coupled the matter reaction to the surrounded electromagnetic field.

Furthermore, we have considered the influence of the electromagnetic field on the Kohn-Sham Hamiltonian. Starting with the non-relativistic Pauli equation, we end up at the full minimal coupled Hamiltonian for the quantum mechanical system. We have solved the issue that the full minimal coupling term depends on the gauge dependent vector potential by transforming the Kohn-Sham Hamiltonian with a Power-Zienau-Woolley transformation to get multipole coupling terms, which depend now only on the electromagnetic fields. Since in this picture, only the transverse components of the fields couple to the matter, we use a Poisson solver and solve the Poisson equation which is part of a Helmholtz-decomposition to obtain the correct transverse fields. In a last step, we have handled the problem of a self-consistent time-step of the fully coupled light-matter system by introducing a predictor-corrector scheme. Taking into account, that the dynamics of our considered triad, nuclei, electron, and photon, differ fundamentally, we exploit these properties to get an efficient and accurate approach of the full coupled multi-scale problem. We employ our corresponding implementation to demonstrate fully coupled light-matter effects compared to only conventional forward coupling simulations.

Since nanoplasmonic systems reveal often a remarkable optical activity, we select a sodium dimer cluster as a first test system for our novel approach. Our first simulation uses only a simple subset of the presented full Ehrenfest-Pauli-Kohn-Sham scheme. Using only the paramagnetic current density, no spin matter states, static pseudopotentials and only mean-field vector potentials as a first approximation for the Kohn-Sham vector potential, the corresponding results show clearly the importance of simulating the light-matter system in a fully self-consistent description. All measurable variables, where we only selected the most relevant ones, i.e., energy, dipole, and electric field, reveal a significant different behavior compared to the conventional forward coupling runs. In addition, the direct performed measurements of the electromagnetic fields at our defined electromagnetic detectors to analyze the far field attributes has shown, that the usual approximation to deduce optical properties only indirectly by using matter variables in general does not hold. Furthermore, we observed that the difference of computed observables between local density approximation and gradient-corrected functional was minor compared to the difference of calculating only forward coupling and the self-consistent forward-backward coupling. Hence, our results contradict the often argued position in common literature, that the discrepancies between theory and experiment are based on missing exchange-correlation effects.

To sum up, based on our results, we come to the conclusion that self-consistent forward-backward couplings should always be included. Their effects can easily reach the magnitude of longitudinal exchange-correlation contributions or even exceed them.

The Ehrenfest-Maxwell-Pauli-Kohn-Sham scheme that we have introduced in this thesis as a mean-field limit of the exact density-functional formulation of the Pauli-Fierz field theory is only a first step. Future investigations have to focus on better approximations closer to the full field theory to go beyond the mean-field limit and to simulate and reveal more quantum effects. However, even in the EMPKS limit ensuing steps are the implementation of remaining mean-field features that we already discussed in this work. For instance, providing a propagation with total system current which includes the diamagnetic current and magnetization current. Taking the magnetization current into account,

the electromagnetic field back-reaction becomes spin-dependent, and we can investigate magnetic effects from a fully resolved magnetization of the system. To complete the total current density and get the full back-coupling, we have to add the ionic current of the nuclei.

We already found a relatively strong dispersion with shifted phase and frequency of the transverse electromagnetic field while it passes the dimer. The diamagnetic current should increase this effect since the corresponding current term couples directly the two Riemann-Silberstein helicity states similar to the coupling terms in the Riemann-Silberstein description of a linear medium. In general, since our implemented Maxwell propagation couples to quantum mechanical matter as well as linear media, the interesting question arises, to find a relation between these two different description of matter. In other words, a quantum mechanical simulation leads to classical space- and time-dependent electric permittivity and magnetic permeability, which approximately reproduce the electromagnetic field propagation replacing the quantum system by an artificially designed linear medium. In this case, we can exploit that our propagation can combine both, microscopic and macroscopic systems, in one simulation.

According to our observations for the sodium dimer, the fully coupled system induces effects on every system variable. Therefore, conventional used variables have to be modified to reach accurate approximated simulations. One important task is the construction of adapted exchange-correlation scalar and vector potentials to go beyond the classical mean-field approximation for photons to consider their quantum nature, for instance, vacuum fluctuations. In turn, the quantum nature of the matter can be shown by correcting the physical-mass approximation. Besides the scalar and vector exchange-correlation potentials, the pseudo-potentials require a dependency on the electromagnetic fields, starting from an all-electron consideration, since they have to take the full coupled electromagnetic field into account. Further, our nanoplasmonic simulations including ion motion and their remarkable raise in kinetic energy show that the electromagnetic fields very close to the ions is not correct. It seems that the calculated Lorentz-forces acting on the ions are too strong, which could be a consequence of the incorrect pseudo-potential behavior at that level.

Additionally, referring to the vector potential, which we already calculate in a first mean-field approximation using the Poisson solver, we can employ in principle the full minimal coupling interaction instead of the multipole expansion terms. However, having both interaction levels gives us the opportunity to find the order of the multipole expansion that shows the main responsibility of an observed effect. In our presented nanoplasmonic example we already show, that only the beyond dipole coupling terms cause the detected radiation of the second harmonic generation.

In this work, we found the nanoparticle groundstate by a conventional diagonalization of the Hamiltonian, since we focused on the electromagnetic time-propagation. However, fully coupled light-matter interactions should also already be considered to find the correct groundstate. This requires to solve stationary Maxwell equations self-consistently coupled to the stationary Kohn-Sham equations. The groundstate can also be modified by starting from a thermal initial state for the ions to catch temperature effects.

Expanding our so far used simulation box for finite quantum systems to infinite periodic systems in one, two or three dimensions also opens a whole new class of possibilities. For instance, the investigation of the influence of the self-consistent forward-backward reaction for large crystal structures, e.g., to improve the efficiency of solar cells.

As a final conclusion, we note that our fully coupled Ehrenfest-Maxwell-Pauli-Kohn-Sham implementation provides a rather practicable, flexible, and comprehensive simu-

lation approach to push research forward in optical material science (nano-optics, nano-plasmonics, (photo) electrocatalysis), in condensed matter or even in understanding chemical reactions, since they are mainly determined by the electromagnetic interactions between ions and electrons.

Appendices

Appendix A

Non-relativistic Pauli Hamiltonian in Coulomb gauge

In this appendix, we introduce step-by-step the full QED Hamiltonian. First, we briefly summarize the basic relativistic wave equations and their properties, which lead to the free matter Hamiltonians for different matter species and the free photon Hamiltonian. The full Hamiltonian includes an additional interaction Hamiltonian that is due to the minimal-coupling prescription.

A.1 Vector potential and Coulomb gauge

Instead of the common Maxwell's Eqs. (1.1.8)-(1.1.11) or the Riemann-Silberstein complex vector expression in Eq. (1.1.38) and Eq. (1.1.43), the Maxwell's equations can also be described by the more common four-vector potential $A^\mu(\vec{r}, t)$. The general inhomogeneous form with non-zero charge density $\rho(\vec{r}, t) = c_0 j^0(\vec{r}, t)$ and current density $j^k(\vec{r}, t)$ is [75]

$$\partial^\mu \partial_\mu A^k(\vec{r}, t) = -\mu_0 j^k(\vec{r}, t) + \frac{1}{c_0} \partial_k \partial_0 A^0(\vec{r}, t). \quad (\text{A.1.1})$$

This equation determines the Maxwell variables $E^k(\vec{r}, t)$ and $B^k(\vec{r}, t)$. In contrast to the physical measurable electromagnetic fields, the vector potential $A^\mu(\vec{r}, t)$ has a gauge freedom since the field variables and the vector potential are connected by

$$E^k(\vec{r}, t) = -\partial_k A^0(\vec{r}, t) - \partial_0 A^k(\vec{r}, t), \quad (\text{A.1.2})$$

$$B^k(\vec{r}, t) = -\frac{1}{c_0} \epsilon^{klm} \partial_l A_m(\vec{r}, t). \quad (\text{A.1.3})$$

Therefore, $E^k(\vec{r}, t)$ and $B^k(\vec{r}, t)$ are invariant under the vector potential transformation [75]

$$A^0(\vec{r}, t) \rightarrow A'^0(\vec{r}, t) = A^0(\vec{r}, t) - \frac{\partial \chi(\vec{r}, t)}{\partial t}, \quad (\text{A.1.4})$$

$$A^k(\vec{r}, t) \rightarrow A'^k(\vec{r}, t) = A^k(\vec{r}, t) + \partial_k \chi(\vec{r}, t), \quad (\text{A.1.5})$$

where $\chi(\vec{r}, t)$ is a scalar differentiable function. If $\rho(\vec{r}, t)$ and $j^k(\vec{r}, t)$ are equal to zero, Eq. (A.1.1) becomes homogeneous, i.e.,

$$\partial^\mu \partial_\mu A^k(\vec{r}, t) = 0. \quad (\text{A.1.6})$$

and Eq. (A.1.1) is equivalent to the Riemann-Silberstein Maxwell's Eqs. (4.2.21) and (4.2.26).

The Maxwell-matter coupling that we discuss in the following sections is determined in most cases by the gauge-dependent vector potential. Taking into account, that our Riemann-Silberstein description for the homogeneous case allows only two independent polarizations, we remain using the vector potential in Coulomb gauge, when we couple to matter. In coulomb gauge A^μ obeys [101]

$$\partial_k A^k(\vec{r}, t) = 0. \quad (\text{A.1.7})$$

In Coulomb gauge, Eq. (A.1.1) can be simplified to [75]

$$\left(\partial_0^2 + \partial_i \partial^i\right) A^k(\vec{r}, t) = -\mu_0 j_\perp^k(\vec{r}, t), \quad (\text{A.1.8})$$

where $j_\perp^k(\vec{r}, t)$ represents the transverse field of the total current density $j^k(\vec{r}, t)$.

A.2 Pauli-equation as non-relativistic limit of coupled light-matter systems

In Sec. (4.2), we introduced the relativistic equations of motion for different spin particles with and without mass. We mentioned that the same considerations can be repeated for other spins, but they are restricted due to not finding simple and physical side conditions similar to the one for spin-1 particles. Another feature of the Dirac-like description leads to an unfeasible method for numerical calculations. The energy spectrum of the full relativistic description of the system is in general unbound from below [128]. Therefore, we continue in the following by using the non-relativistic Pauli-equation for all different spins and particles with mass. For the Pauli-equation, we can find stable ground states and have a well-defined non-perturbative theory [62]. The Pauli-equation describes a particle with mass including an external Maxwell field, which is determined by its vector potential A_{ext}^μ . Replacing the Dirac operator by the corresponding one coupled to A_{ext}^μ with the minimal coupling prescription

$$\partial_\mu \rightarrow \partial_\mu + i \frac{q}{\hbar c_0} A_{\text{ext}, \mu}(\vec{r}, t) \quad (\text{A.2.1})$$

leads in first order of $\frac{1}{Mc_0^2}$ to the Pauli equation [129]

$$\hat{h}(\vec{r}, t) = \frac{1}{2M} \left(-i\hbar \vec{\nabla} - \frac{q}{c_0} \vec{A}_{\text{ext}}(\vec{r}, t) \right)^2 + qA_{\text{ext}}^0(\vec{r}, t) - \frac{q\hbar}{2M} \vec{S} \cdot \vec{B}_{\text{ext}}(\vec{r}, t). \quad (\text{A.2.2})$$

Here, q denotes the charge of the particle species with corresponding mass M and the general spin-matrices S^k , which also depend on the species. We use this generalized Pauli equation for particles with mass, i.e., electrons and nuclei, together with the homogeneous Maxwell's equations for photons to build our basic theory, a generalized form of the Pauli-Fierz Hamiltonian [62]. Although, there are some further developments beyond the Pauli-Fierz limit to deal with semi-relativistic problems [130, 131, 132], our considerations in the present work stay in the non-relativistic limit for matter.

We continue by considering first the non-interacting Hamiltonians with external Maxwell fields for particles with mass and the free Maxwell Hamiltonian before we discuss the interacting Hamiltonians between the different species including the interacting Maxwell fields.

A.3 Free matter Hamiltonians

In general, many-body Hamiltonians without forcing a fixed particle number for the total system are described in Fock-space, where particles can be created and annihilated by corresponding operators for the matter and photon fields [101]. To find a fundamental form for our many-body system coupled to Maxwell fields, we consider first non-interacting particles in Fock-space, but note here, that the description in Fock space is mathematically problematic [133]. However, since it eases formal derivations, we work in Fock space here. Later, we use particle conserved Hamiltonians of particle number N , so that we can switch back to the N -particles Hilbert space, where every object is well-defined. The Fock space field operators for particle creation, $\hat{\Phi}^\dagger(\vec{r}, s)$, and annihilation, $\hat{\Phi}(\vec{r}, s)$, obey the the common QED commutation and anti-commutation rules [101]

$$\left[\hat{\Phi}(\vec{r}, s), \hat{\Phi}^\dagger(\vec{r}', s') \right]_{\pm} = \delta_{(ss')} \delta^3(\vec{r} - \vec{r}'), \quad (\text{A.3.1})$$

where s denotes the possible spin states, and $+$ represents the anti-commutation relation for fermions, and $-$ the commutation relation for bosons. Using these field operators, we can construct the non-interacting many-particle Hamiltonian according to

$$\begin{aligned} \hat{H}_{\text{mat,ext}}^{(n)}(t) &= \int d^3r \sum_s \hat{\Phi}_{(n)}^\dagger(\vec{r}, s) \hat{h}(\vec{r}, t) \hat{\Phi}_{(n)}(\vec{r}, s) \\ &= -\int d^3r \frac{1}{2M_{(n)}} \sum_s \hat{\Phi}_{(n)}^\dagger(\vec{r}, s) \left(-i\hbar\partial_k + \frac{q_{(n)}}{c_0} A_{\text{ext},k}(\vec{r}, t) \right) \left(-i\hbar\partial^k + \frac{q_{(n)}}{c_0} A_{\text{ext}}^k(\vec{r}, t) \right) \hat{\Phi}_{(n)}(\vec{r}, s) \\ &\quad + \int d^3r q_{(n)} A_{\text{ext}}^0(\vec{r}, t) \sum_s \hat{\Phi}_{(n)}^\dagger(\vec{r}, s) \hat{\Phi}_{(n)}(\vec{r}, s) \\ &\quad - \int d^3r \frac{q_{(n)}\hbar}{2M_{(n)}} \sum_{s,s'} \hat{\Phi}_{(n)}^\dagger(\vec{r}, s) [S_k^{(n)}]_{s,s'} \hat{\Phi}_{(n)}(\vec{r}, s') \left(\frac{1}{c_0} \epsilon^{klm} \partial_l A_{\text{ext},m}(\vec{r}, t) \right), \end{aligned} \quad (\text{A.3.2})$$

where $[S_k]_{s,s'}$ denotes the s, s' components of the spin matrix S_k and the index n enumerates different particle species (electrons and effective nuclei here). The single-particle Hamiltonian $\hat{h}(\vec{r}, t)$ corresponds to the Pauli Hamiltonian in Eq. (A.2.2) and we allow for a coupling to an external Maxwell field $A_{\text{ext}}(\vec{r}, t)$. The first term in Eq. (A.3.2) represents the non-interacting kinetic Hamiltonian $\hat{H}_{\text{mat,kin,ext}}^{(n)}$

$$\begin{aligned} \hat{H}_{\text{mat,kin,ext}}^{(n)}(t) &= \\ &= -\int d^3r \frac{1}{2M_{(n)}} \sum_s \hat{\Phi}_{(n)}^\dagger(\vec{r}, s) \left(-i\hbar\partial_k + \frac{q_{(n)}}{c_0} A_{\text{ext},k}(\vec{r}, t) \right) \left(-i\hbar\partial^k + \frac{q_{(n)}}{c_0} A_{\text{ext}}^k(\vec{r}, t) \right) \hat{\Phi}_{(n)}(\vec{r}, s). \end{aligned} \quad (\text{A.3.3})$$

The second term in Eq. (A.3.2), denoted by $\hat{H}_{\text{mat,int,ext}}^{(0)}$, gives the interaction with an external electromagnetic field, and the last term represents the Stern-Gerlach Hamiltonian $\hat{H}_{\text{mat,Stern,ext}}^{(0)}$. Both are given by

$$\hat{H}_{\text{mat,int,ext}}^{(n)}(t) = \int d^3r q A_{\text{ext}}^0(\vec{r}, t) \sum_s \hat{\Phi}_{(n)}^\dagger(\vec{r}, s) \hat{\Phi}_{(n)}(\vec{r}, s), \quad (\text{A.3.4})$$

and

$$\hat{H}_{\text{mat,Stern,ext}}^{(n)}(t) = -\int d^3r \frac{q\hbar}{2M} \int d^3r \sum_{s,s'} \hat{\Phi}_{(n)}^\dagger(\vec{r}, s) [S_k^{(n)}]_{s,s'} \hat{\Phi}_{(n)}(\vec{r}, s') \left(\frac{1}{c_0} \epsilon^{klm} \partial_l A_{\text{ext},m}(\vec{r}, t) \right). \quad (\text{A.3.5})$$

Since we consider all particles here as non-interacting, we can use Eq. (A.3.2) for each species of particles. Therefore, for N different particle species, i.e., electrons and different effective nuclei species, the total non-interacting Hamiltonian $\hat{H}_{\text{mat,ext}}$ is defined in a sum of Fock spaces and given by

$$\begin{aligned}
\hat{H}_{\text{mat,ext}}(t) &= \sum_n^N \hat{H}_{\text{mat,ext}}^{(n)}(t) = \sum_n^N \hat{H}_{\text{mat,kin,ext}}^{(n)} + \sum_n^N \hat{H}_{\text{mat,int,ext}}^{(n)} + \sum_n^N \hat{H}_{\text{mat,Stern,ext}}^{(n)} \\
&= \sum_n^N -\int d^3r \frac{1}{2M} \sum_s \hat{\Phi}_{(n)}^\dagger(\vec{r}, s) \left(-i\hbar\partial_k + \frac{q}{c_0} A_{\text{ext},k}(\vec{r}, t) \right) \left(-i\hbar\partial^k + \frac{q}{c_0} A_{\text{ext}}^k(\vec{r}, t) \right) \hat{\Phi}_{(n)}(\vec{r}, s) \\
&\quad + \sum_n^N \int d^3r q A_{\text{ext}}^0(\vec{r}, t) \sum_s \hat{\Phi}_{(n)}^\dagger(\vec{r}, s) \hat{\Phi}_{(n)}(\vec{r}, s) \\
&\quad + \sum_n^N -\int d^3r \frac{q\hbar}{2M} \sum_{s,s'} \hat{\Phi}_{(n)}^\dagger(\vec{r}, s) \left[S_k^{(n)} \right]_{s,s'} \hat{\Phi}_{(n)}(\vec{r}, s') \left(\frac{1}{c_0} \epsilon^{klm} \partial_l A_{\text{ext},m}(\vec{r}, t) \right),
\end{aligned} \tag{A.3.6}$$

which uses the corresponding set of field operators, masses, charges and spin matrices

$$\left\{ \hat{\Phi}_{(n)} ; \hat{\Phi}_{(n)}^\dagger ; M_{(n)} ; q_{(n)} ; S_{(n)} \right\} . \tag{A.3.7}$$

We note, that the different particles do not interact, but they are all influenced by the same classical field A^μ in Coulomb gauge. Later in this chapter, we change the classical field to a quantum field and consider the particles interacting via the gauge bosons, i.e., the photons.

A.4 Free photon Hamiltonian

In chapters 1-3 we have treated the electromagnetic field only classically. To build the coupled Photon-matter Hamiltonian that we use in the next chapter, we start here from the fundamental QED Hamiltonian for photons [101]. Additionally, we show the connection to the Riemann-Silberstein formulation of QED which is discussed in more details in Ref. [78]. Quantizing the Maxwell field vector potential $\vec{A}(\vec{r})$ in Coulomb gauge shows that only the transverse fields, i.e., $\hat{E}_\perp^k(\vec{r})$ are affected [101], since in Coulomb gauge $\partial_0 A^k = -\hat{E}_\perp^k(\vec{r})$. The resulting canonical commutation relations read

$$\left[\hat{A}_k(\vec{r}); \epsilon_0 \hat{E}_{\perp,l}(\vec{r}') \right] = -i\hbar c_0 \delta_{\perp,kl}(\vec{r} - \vec{r}'),$$

where we employed the transversal delta distribution

$$\delta_{\perp,kl}(\vec{r} - \vec{r}') = \left(\delta_{kl} \partial_k \frac{1}{\nabla^2} \partial_l \right) \delta^3(\vec{r} - \vec{r}'). \tag{A.4.1}$$

The longitudinal part of the electromagnetic field stays classical and does not influence the quantized degrees of freedom. The vector-potential operator $\hat{A}^k(\vec{r})$ in terms of creation and annihilation field operators $\hat{a}^\dagger(\vec{k}, s), \hat{a}(\vec{k}, s)$ in momentum space reads [101]

$$\hat{A}^k(\vec{r}) = \sqrt{\frac{\hbar c_0^2}{\epsilon_0 (2\pi)^3}} \int \frac{d^3k}{\sqrt{2\omega_k}} \sum_{s=1}^2 \vec{\epsilon}(\vec{k}, s) \left[\hat{a}(\vec{k}, s) e^{i\vec{k}\cdot\vec{r}} + \hat{a}^\dagger(\vec{k}, s) e^{-i\vec{k}\cdot\vec{r}} \right]. \tag{A.4.2}$$

In Eq. (A.4.2) we use $\omega_k = c_0 |\vec{k}|$, $k = |\vec{k}|$, and $\vec{\epsilon}(\vec{k}, s)$ is the transversal polarization vector with $\vec{k} \cdot \vec{\epsilon}(\vec{k}, s) = \vec{\epsilon}(\vec{k}, 1) \cdot \vec{\epsilon}(\vec{k}, 2) = 0$ [101]. The momentum-space annihilation and creation

field operators obey the usual commutation relations. The transversal electric field is in accordance to the classical case given by $\partial_0 \hat{A}^k = -\hat{E}_\perp^k$, i.e., as [101]

$$\hat{E}_\perp^k(\vec{r}) = \sqrt{\frac{\hbar c_0^2}{\epsilon_0 (2\pi)^3}} \int \frac{d^3 k i \omega_k}{\sqrt{2\omega_k}} \sum_{s=1}^2 \vec{\epsilon}(\vec{k}, s) \left[\hat{a}(\vec{k}, s) e^{i\vec{k}\cdot\vec{r}} - \hat{a}^\dagger(\vec{k}, s) e^{-i\vec{k}\cdot\vec{r}} \right], \quad (\text{A.4.3})$$

and the magnetic field is $\hat{B}^k = -\frac{1}{c_0} \epsilon^{klm} \partial_l \hat{A}_m$, i.e., [101]

$$\hat{B}^k(\vec{r}) = \sqrt{\frac{\hbar c_0^2}{\epsilon_0 (2\pi)^3}} \int \frac{d^3 k}{\sqrt{2\omega_k}} \sum_{s=1}^2 i\vec{k} \times \vec{\epsilon}(\vec{k}, s) \left[\hat{a}(\vec{k}, s) e^{i\vec{k}\cdot\vec{r}} - \hat{a}^\dagger(\vec{k}, s) e^{-i\vec{k}\cdot\vec{r}} \right]. \quad (\text{A.4.4})$$

Following the classical definition of the energy of the electromagnetic field including an external current density j_{ext}^μ , we find

$$\begin{aligned} \hat{H}_{\text{Ph}}(t) &= \frac{\epsilon_0}{2} \int d^3 r : \left(\hat{E}_\perp^2(\vec{r}) + c_0^2 \hat{B}^2(\vec{r}) \right) : - \frac{\epsilon_0}{2} \int d^3 r \vec{E}_\parallel^2(\vec{r}, t) \\ &\quad + \frac{1}{c_0} \int d^3 r j_{\text{ext}}^k(\vec{r}, t) \hat{A}_k(\vec{r}) + \frac{1}{c_0} \int d^3 r j_{\text{ext}}^0(\vec{r}, t) A_0(\vec{r}, t) \\ &= \sum_{s=1}^2 \int d^3 k \hbar \omega_k \hat{a}^\dagger(\vec{k}, s) \hat{a}(\vec{k}, s) - \frac{\epsilon_0}{2} \int d^3 r \vec{E}_\parallel^2(\vec{r}, t) \\ &\quad + \frac{1}{c_0} \int d^3 r j_{\text{ext}}^k(\vec{r}, t) \hat{A}_k(\vec{r}) + \frac{1}{c_0} \int d^3 r j_{\text{ext}}^0(\vec{r}, t) A_0(\vec{r}, t). \end{aligned} \quad (\text{A.4.5})$$

Here we use normal ordering, denoted as $::$, to discard the constant energy shift [101]. The zero-component of the vector potential $A_0(\vec{r}, t)$ depends only on the zero component of the external current density $j_{\text{ext}}^\mu(\vec{r}, t)$, which can be seen by using the Green's function of the Laplacian in real-space representation

$$G(\vec{r}, \vec{r}') = \langle \vec{r} | (\vec{\nabla}^{-2}) \vec{r}' \rangle, \quad (\text{A.4.6})$$

and

$$w(\vec{r}, \vec{r}') = -\frac{1}{\epsilon_0} G(\vec{r}, \vec{r}') = \frac{1}{4\pi\epsilon_0 |\vec{r} - \vec{r}'|}. \quad (\text{A.4.7})$$

Therefore, A_0 is given by [101]

$$A^0(\vec{r}, t) = \frac{1}{\epsilon_0 c_0} \int_{\Omega} d^3 r' (-G(\vec{r}, \vec{r}')) j_{\text{ext}}^0(\vec{r}', t) = \frac{1}{c_0} \int_{\mathbb{R}^3} d^3 r' \frac{j_{\text{ext}}^0(\vec{r}', t)}{4\pi\epsilon_0 |\vec{r} - \vec{r}'|}. \quad (\text{A.4.8})$$

Hence, with $E_\parallel^k(\vec{r}, t) = -\partial_k A^0(\vec{r}, t)$ and partial integration, the free electromagnetic Hamiltonian \hat{H}_{Ph} can be written as [101]

$$\begin{aligned} \hat{H}_{\text{Ph}}(t) &= \sum_s \int d^3 k \hbar \omega_k \hat{a}^\dagger(\vec{k}, s) \hat{a}(\vec{k}, s) + \frac{1}{c_0} \int d^3 r j_{\text{ext}}^k(\vec{r}, t) \hat{A}_k(\vec{r}) \\ &\quad + \frac{1}{2c_0^2} \int \int d^3 r d^3 r' w(\vec{r}, \vec{r}') j_{\text{ext}}^0(\vec{r}', t) j_{\text{ext}}^0(\vec{r}, t). \end{aligned} \quad (\text{A.4.9})$$

The first term on the right-hand side of Eq. (A.4.9) represents free photons and does not couple to the external current. This operator term $\hat{H}_{\text{Ph,free}}$ creates or annihilates only transverse photons, which propagate through the vacuum, and reads

$$\hat{H}_{\text{Ph,free}} = \frac{\epsilon_0}{2} \int d^3 r : \left(\hat{E}_\perp^2(\vec{r}) + c_0^2 \hat{B}^2(\vec{r}) \right) : = \sum_s \int d^3 k \hbar \omega_k \hat{a}^\dagger(\vec{k}, s) \hat{a}(\vec{k}, s). \quad (\text{A.4.10})$$

The second term in Eq. (A.4.9) couples the photon field with transverse degrees of freedom of the external vector potential which we therefore denote by $\hat{H}_{\text{Ph,int,ext}}^\perp$

$$\hat{H}_{\text{Ph,int,ext}}^\perp(t) = \frac{1}{c_0} \int d^3r j_{\text{ext}}^k(\vec{r}, t) \hat{A}_k(\vec{r}) \quad (\text{A.4.11})$$

The last term in Eq. (A.4.9) corresponds to the longitudinal degrees of freedom of the field and gives rise to the longitudinal interaction to an external vector potential, which we discuss in Appendix A.5.1. The longitudinal $\hat{H}_{\text{Ph,int,ext}}^\parallel$ reads

$$\hat{H}_{\text{Ph,int,ext}}^\parallel(t) = \frac{1}{2c_0^2} \int \int d^3r d^3r' w(\vec{r}, \vec{r}') j_{\text{ext}}^0(\vec{r}', t) j_{\text{ext}}^0(\vec{r}, t). \quad (\text{A.4.12})$$

Since $j_{\text{ext}}^0(\vec{r}, t)$ is a classical field, the operator $\hat{H}_{\text{Ph,int,ext}}^\parallel$ commutes with all observables.

Using the Hamiltonian of Eq. (A.4.9), which describes a photon field coupled to a classical external current, the operator form of the inhomogeneous Maxwell equation in Coulomb gauge can be derived by applying the Heisenberg equation of motion twice, i.e.,

$$(\partial_0^2 + \partial_l \partial^l) \hat{A}^k(\vec{r}) = \mu_0 c_0 j_{\text{ext}}^k(\vec{r}, t) - \partial^k \partial^0 \frac{1}{c_0} \int d^3r' w(\vec{r}, \vec{r}') j_{\text{ext}}^0(\vec{r}', t). \quad (\text{A.4.13})$$

We assume that the external current density j_{ext}^μ obeys the continuity equation $\partial_\mu j_{\text{ext}}^\mu(\vec{r}, t) = 0$ and the external current density splits by $j_{\text{ext}}^k(\vec{r}, t) = j_{\text{ext},\parallel}^k(\vec{r}, t) + j_{\text{ext},\perp}^k(\vec{r}, t)$ into a longitudinal current density $j_{\text{ext},\parallel}^k(\vec{r}, t)$ and transverse one $j_{\text{ext},\perp}^k(\vec{r}, t)$. Therefore the last term of Eq. (A.4.13) becomes [75]

$$\partial^k \partial^0 \frac{1}{c_0} \int d^3r' w(\vec{r}, \vec{r}') j_{\text{ext}}^0(\vec{r}', t) = \mu_0 c_0 j_{\text{ext},\parallel}^k(\vec{r}, t), \quad (\text{A.4.14})$$

and the inhomogeneous Maxwell equation in terms of the vector potential in Coulomb gauge is

$$(\partial_0^2 + \partial_l \partial^l) \hat{A}^k(\vec{r}) = \mu_0 c_0 j_{\text{ext},\perp}^k(\vec{r}, t). \quad (\text{A.4.15})$$

As a consequence of Eq. (A.4.13), only the transverse current density $j_{\text{ext},\perp}^i$ couples to the transverse photon field. Additionally, the operator valued Eq. (A.4.13) is equivalent to the classical one in Eq. (A.1.8).

To build a bridge from the QED photon Hamiltonian to the Riemann-Silberstein formulation, we can define the Riemann-Silberstein transverse field operator by [78]

$$\hat{F}_{\pm,\perp}^k(\vec{r}) = \sqrt{\frac{\epsilon_0}{2}} \left(\hat{E}_\perp^k(\vec{r}) \pm i c_0 \hat{B}^k(\vec{r}) \right). \quad (\text{A.4.16})$$

Using this definition, we can express Eq. (A.4.10) by

$$\hat{H}_{\text{Ph,free}} = \frac{\epsilon_0}{2} \int d^3r : \left(\hat{E}_\perp^2(\vec{r}) + c_0^2 \hat{B}^2(\vec{r}) \right) : = \int d^3r : \hat{F}_{+,\perp,k}(\vec{r}) \hat{F}_{-,\perp}^k(\vec{r}) : . \quad (\text{A.4.17})$$

Similar to Eq. (A.4.13), which represents the inhomogeneous Maxwell's equation in terms of the scalar and vector potential $\hat{A}^\mu(\vec{r})$, we can apply the Heisenberg equation of motion to the Riemann-Silberstein vector $\hat{F}_{\pm,\perp}^k(\vec{r})$ and obtain the Maxwell's equation with first-order derivatives

$$i\hbar \partial_t \hat{F}_{\pm,\perp}^k(\vec{r}) = \mp i\hbar c_0 \left(S^l \partial_l \right)_m^k \hat{F}_{\pm,\perp}^m(\vec{r}) - i \frac{\hbar}{\sqrt{2\epsilon_0}} j_{\text{ext},\perp}^k(\vec{r}, t) \quad (\text{A.4.18})$$

for the transverse electromagnetic field. It obeys the divergence side condition

$$\partial_k \hat{F}_{\pm,\perp}^k(\vec{r}, t) = 0. \quad (\text{A.4.19})$$

Therefore, only the transverse component of the classical current density $j^\mu(\vec{r}, t)$ couples to the transverse quantized electromagnetic field. Since the longitudinal electromagnetic field stays classical in Coulomb gauge, it is determined classically by the longitudinal part of the classical current density with

$$i\hbar \partial_t F_{\pm,\parallel}^k(\vec{r}, t) = \mp i\hbar c_0 \left(S^l \partial_l \right)_m^k F_{\pm,\parallel}^m(\vec{r}, t) - i \frac{\hbar}{\sqrt{2\epsilon_0}} j_{\text{ext},\parallel}^k(\vec{r}, t) \quad (\text{A.4.20})$$

The divergence side condition leads now to the inhomogeneous Gauß law

$$\partial_k F_{\pm,\parallel}^k(\vec{r}, t) = \frac{1}{\sqrt{2\epsilon_0}} j_{\text{ext},\parallel}^0(\vec{r}, t), \quad (\text{A.4.21})$$

which gives the zero-component of the external current density. Consequently, similar to Sec. (3.3.2), we split up the electromagnetic field into a longitudinal with corresponding classical Eqs. (A.4.20)-(A.4.21) and transverse Eqs. (A.4.18)-(A.4.19), so that the total electromagnetic field is the sum of both.

The Riemann-Silberstein operator $\hat{F}_{\pm,\perp}^k(\vec{r})$ expressed by creation and annihilation field operators is given with Eqs. (A.4.3) and (A.4.4) by

$$\hat{F}_{\pm,\perp}^k(\vec{r}) = \sqrt{\frac{\hbar c_0^2}{2(2\pi)^3}} \int \frac{d^3k}{\sqrt{2\omega_k}} \sum_{s=1}^2 \left[\mp c_0 \vec{k} \times \vec{\epsilon}(\vec{k}, s) + i\omega_k \vec{\epsilon}(\vec{k}, s) \right] \left[\hat{a}(\vec{k}, s) e^{i\vec{k}\cdot\vec{r}} - \hat{a}^\dagger(\vec{k}, s) e^{-i\vec{k}\cdot\vec{r}} \right] \quad (\text{A.4.22})$$

In Sec. 1.1.6, we discussed that the classical Riemann-Silberstein vectors can be decomposed in positive and negative frequency parts. This can also be applied to Eq. (A.4.22) (cf. [78]). First, the transversal polarization vector times the creation and annihilation operator expressed in spin states, can be equivalently expressed in helicity states. Using the helicity unit vectors $\vec{\epsilon}(\vec{k}, +)$ and $\vec{\epsilon}(\vec{k}, -)$, we get the identity for the spin sum in Eq. (A.4.22) [78]

$$\hat{a}(\vec{k}, 1) \vec{\epsilon}(\vec{k}, 1) + \hat{a}(\vec{k}, 2) \vec{\epsilon}(\vec{k}, 2) = \hat{a}(\vec{k}, +) \vec{\epsilon}(\vec{k}, +) + \hat{a}(\vec{k}, -) \vec{\epsilon}(\vec{k}, -), \quad (\text{A.4.23})$$

$$\hat{a}^\dagger(\vec{k}, 1) \vec{\epsilon}(\vec{k}, 1) + \hat{a}^\dagger(\vec{k}, 2) \vec{\epsilon}(\vec{k}, 2) = \hat{a}^\dagger(\vec{k}, +) \vec{\epsilon}(\vec{k}, +) + \hat{a}^\dagger(\vec{k}, -) \vec{\epsilon}(\vec{k}, -). \quad (\text{A.4.24})$$

The creation and annihilation operators $\hat{a}^\dagger(\vec{k}, s), \hat{a}(\vec{k}, s)$ transform to $\hat{a}^\dagger(\vec{k}, s), \hat{a}(\vec{k}, s)$ with [78]

$$\hat{a}(\vec{k}, +) = \frac{1}{\sqrt{2}} \left(\hat{a}(\vec{k}, 1) - i\hat{a}(\vec{k}, 2) \right), \quad \hat{a}(\vec{k}, -) = \frac{1}{\sqrt{2}} e^{-i\delta} \left(-i\hat{a}(\vec{k}, 1) + \hat{a}(\vec{k}, 2) \right), \quad (\text{A.4.25})$$

$$\hat{a}^\dagger(\vec{k}, +) = \frac{1}{\sqrt{2}} \left(\hat{a}^\dagger(\vec{k}, 1) + i\hat{a}^\dagger(\vec{k}, 2) \right), \quad \hat{a}^\dagger(\vec{k}, -) = \frac{1}{\sqrt{2}} e^{i\delta} \left(i\hat{a}^\dagger(\vec{k}, 1) + \hat{a}^\dagger(\vec{k}, 2) \right), \quad (\text{A.4.26})$$

where δ denotes a free parameter. Hence, using the identities of Eqs (A.4.23), (A.4.24) and the relation $\vec{k}/|\vec{k}| \times \vec{\epsilon}_\pm = \mp i\vec{\epsilon}_\pm$ for Eq.(A.4.22) leads to the positive and negative frequency decomposition of the Riemann-Silberstein operator [78]

$$\hat{F}_{\pm,\perp}^k(\vec{r}) = \hat{F}_{\pm,\perp}^{(+),k}(\vec{r}) + \hat{F}_{\pm,\perp}^{(-),k}(\vec{r}) \quad (\text{A.4.27})$$

with

$$\hat{F}_{\pm,\pm}^{(+),k}(\vec{r}) = i\sqrt{\frac{\hbar c_0^2}{4(2\pi)^3}} \int d^3k \sqrt{\omega_k} \vec{\epsilon}(\vec{k}, \pm) \hat{a}(\vec{k}, \pm) e^{i\vec{k}\cdot\vec{r}}, \quad (\text{A.4.28})$$

$$\hat{F}_{\pm,\pm}^{(-),k}(\vec{r}) = i\sqrt{\frac{\hbar c_0^2}{4(2\pi)^3}} \int d^3k \sqrt{\omega_k} \vec{\epsilon}(\vec{k}, \pm) \hat{a}^\dagger(\vec{k}, \pm) e^{-i\vec{k}\cdot\vec{r}}. \quad (\text{A.4.29})$$

The positive frequency Riemann-Silberstein operator $\hat{F}_{\pm,\pm}^{(+),k}(\vec{r})$ annihilates a photon in case of $\hat{F}_{+,\pm}^{(+),k}(\vec{r})$ with positive helicity or in turn $\hat{F}_{-,\pm}^{(+),k}(\vec{r})$ with negative helicity. In contrast, $\hat{F}_{\pm,\pm}^{(-),k}(\vec{r})$ creates a photon with corresponding helicity.

A.5 Interaction Hamiltonians

After introducing the non-interacting Hamiltonians for different species in Eq. (A.3.6) and uncoupled Photons in Eq. (A.4.9), we consider in this section the corresponding interaction Hamiltonians. According to QED with minimal coupling interaction [101], the conserved total current j^μ of all species couples to the total vector potential operator \hat{A}^μ [104]. Being in Coulomb gauge allows us to separate the total interaction into a longitudinal and transverse one.

A.5.1 Longitudinal (Coulomb) interactions

The last term on the right-hand side of Eq. (A.4.9) represents the longitudinal interaction of the matter in Coulomb gauge. Replacing the classical zero component of j_{mat}^0 leads to an operator-valued contribution to the Photon Hamiltonian. The zero component of the internal matter four-current density operator \hat{j}_{mat}^0 , caused by n different species, is given by

$$\hat{j}_{\text{mat}}^0(\vec{r}) = \sum_{n=1}^N c_0 q_{(n)} \sum_s \hat{\Phi}_{(n)}^\dagger(\vec{r}, s) \hat{\Phi}_{(n)}(\vec{r}, s) = \sum_{n=1}^N \hat{j}_{\text{mat},(n)}^0(\vec{r}). \quad (\text{A.5.1})$$

It is based on the internal matter charge density

$$\hat{\rho}_{\text{mat},(n)}(\vec{r}) = \sum_{n=1}^N q_{(n)} \sum_s \hat{\Phi}_{(n)}^\dagger(\vec{r}, s) \hat{\Phi}_{(n)}(\vec{r}, s) \quad (\text{A.5.2})$$

multiplied by the speed of light c_0 due to unit consistency. We note here, that we use the zero-component of the matter current density $\hat{j}_{\text{mat}}^0(\vec{r})$ as the one of the total field and do not add a classical $j_{\text{ext}}(\vec{r}, t)$ at this point. We consider an external current density including its zero-component when discussing transverse interaction in the following. Adding an external zero-component current density in both cases would lead to double counting effects which we want to avoid. Thus, by replacing the matter charge density operator \hat{j}_{mat}^0 with the classical external current density j_{ext}^0 in Eq. (A.4.12), we arrive at the total longitudinal

interaction Hamiltonian of the system

$$\begin{aligned}
\hat{H}_{\text{int}}^{\parallel} &= \frac{1}{2c_0^2} \int d^3r d^3r' w(\vec{r}, \vec{r}') : \hat{j}_{\text{mat}}^0(\vec{r}) \hat{j}_{\text{mat}}^0(\vec{r}') : \\
&= \frac{1}{2c_0^2} \int d^3r d^3r' w(\vec{r}, \vec{r}') \sum_{n, n'} : \hat{j}_{\text{mat},(n)}^0(\vec{r}) \hat{j}_{\text{mat},(n')}^0(\vec{r}') : \\
&= \frac{1}{c_0^2} \int d^3r d^3r' w(\vec{r}, \vec{r}') \sum_{n > n'} \hat{j}_{\text{mat},(n)}^0(\vec{r}) \hat{j}_{\text{mat},(n')}^0(\vec{r}') \\
&\quad + \frac{1}{2c_0^2} \int d^3r d^3r' w(\vec{r}, \vec{r}') \sum_n : \hat{j}_{\text{mat},(n)}^0(\vec{r}) \hat{j}_{\text{mat},(n)}^0(\vec{r}') : ,
\end{aligned} \tag{A.5.3}$$

with normal ordering for the usual Coulomb form. The final expression in the last line of Eq. (A.5.3) consists of two terms. The first one describes the interaction of different effective nuclei and electrons with longitudinal photons, which we call the inter-species Coulomb interaction. Since their operators commute, the normal ordering does not affect this term. In contrast, the operators in the second term of the last line do not commute and require a time ordering. This intra-species Coulomb interaction describes the longitudinal interaction of particles within each species with each other. Since $w(\vec{r}, \vec{r}')$ denotes the Green's function of the Poisson equation, given in Eq. (A.4.7), we can define an internal scalar potential operator $\hat{A}_{\text{mat},(n)}^0$ with

$$\hat{A}_{\text{mat},(n)}^0(\vec{r}) = \sum_{\substack{n' \\ n' \neq n}} \frac{1}{c_0} \int d^3r' w(\vec{r}, \vec{r}') \hat{j}_{\text{mat},(n')}^0(\vec{r}') . \tag{A.5.4}$$

It describes the scalar potential that acts on species n , caused by all remaining species, and it commutes with all the electromagnetic field variables, and Eq. (A.5.3) can be expressed as

$$\begin{aligned}
\hat{H}_{\text{int}}^{\parallel} &= \frac{1}{2c_0} \int d^3r \sum_n : \hat{j}_{\text{mat},(n)}^0(\vec{r}) \hat{A}_{\text{mat},(n)}^0(\vec{r}) : \\
&\quad + \frac{1}{2c_0^2} \int d^3r d^3r' w(\vec{r}, \vec{r}') \sum_n : \hat{j}_{\text{mat},(n)}^0(\vec{r}) \hat{j}_{\text{mat},(n)}^0(\vec{r}') : .
\end{aligned} \tag{A.5.5}$$

A.5.2 Transverse interactions

For considering the transverse contribution of light-matter interaction, we use the corresponding Hamiltonian term given in Eq. (A.4.11). The arising total vector potential $A^k(\vec{r}, t)$ of the coupled system is the sum of the internal vector potential operator $\hat{A}_{\text{mat}}^k(\vec{r})$ from the matter and an external one $A_{\text{ext}}^k(\vec{r}, t)$

$$\hat{A}^k(\vec{r}, t) = \hat{A}_{\text{mat}}^k(\vec{r}) + A_{\text{ext}}^k(\vec{r}, t) . \tag{A.5.6}$$

In the same way, the zero-component of $\hat{A}^0(\vec{r}, t)$ is a sum of an external scalar potential $A_{\text{ext}}^0(\vec{r}, t)$ plus an external charge density $j_{\text{ext}}^0(\vec{r}, t)$

$$\hat{A}_{\text{ext}}^0(\vec{r}, t) = \frac{1}{c_0} \int d^3r' w(\vec{r}, \vec{r}') j_{\text{ext}}^0(\vec{r}', t) + A_{\text{ext}}^0(\vec{r}, t) . \tag{A.5.7}$$

We note here that with Eq. (A.5.7), the external charge density $j_{\text{ext}}^0(\vec{r}, t)$ becomes part of the total scalar potential. We use the total vector potential in Eq. (A.5.6) and replace the

external current density in Eq. (A.4.11) by the total conserved current density $j_{\text{mat}}^\mu(\vec{r}, t)$ of the matter system. After using the continuity equation $\partial_\mu j_{\text{mat}}^\mu(\vec{r}, t) = 0$ and the Pauli Hamiltonian in Eq.(A.3.6), the total matter current density consists of three different terms [134, 135]

$$\hat{j}_{\text{mat}}^k(\vec{r}, t) = \hat{j}_{\text{pmc}}^k(\vec{r}) + \hat{j}_{\text{dmc}}^k(\vec{r}, t) + \hat{j}_{\text{mc}}^k(\vec{r}). \quad (\text{A.5.8})$$

The first term is the paramagnetic current density operator $\hat{j}_{\text{pmc}}^k(\vec{r})$, which depends only on matter variables and reads

$$\hat{j}_{\text{pmc}}^k(\vec{r}) = \sum_{n=1}^N \sum_s \frac{\hbar q(n)}{2M(n)\text{i}} \left[\left(\partial^k \hat{\Phi}_{(n)}^\dagger(\vec{r}, s) \right) \hat{\Phi}_{(n)}(\vec{r}, s) + \hat{\Phi}_{(n)}^\dagger(\vec{r}, s) \left(\partial^k \hat{\Phi}_{(n)}(\vec{r}, s) \right) \right]. \quad (\text{A.5.9})$$

In contrast, the second term, the diamagnetic current density operator $\hat{j}_{\text{dmc}}^k(\vec{r}, t)$, depends additionally on the vector potential operator $\hat{A}^k(\vec{r}, t)$ of the total electromagnetic field and is given by

$$\hat{j}_{\text{dmc}}^k(\vec{r}, t) = \sum_{n=1}^N -\frac{q(n)}{M(n)c_0^2} \hat{j}_{(n)}^0(\vec{r}) \hat{A}^k(\vec{r}, t). \quad (\text{A.5.10})$$

The fact that the Maxwell field is part of the diamagnetic current density is based on the quadratic expression of the Pauli-Hamiltonian, which arises due to the anti-particle (positronic) contribution in the non-relativistic Pauli approximation [104]. The last current density term $\hat{j}_{\text{mc}}^k(\vec{r})$ is the magnetization current

$$\hat{j}_{\text{mc}}^k(\vec{r}) = \sum_{n=1}^N \sum_{s,s'} -\epsilon^{klm} \partial_l \hat{\Phi}_{(n)}^\dagger(\vec{r}, s) \left(\frac{q(n)\hbar}{2M(n)} \left[S_m^{(n)} \right]_{s,s'} \right) \hat{\Phi}_{(n)}(\vec{r}, s'), \quad (\text{A.5.11})$$

which comes from the Stern-Gerlach term of the Pauli-equation.

The total current density $\hat{j}_{\text{tot}}^k(\vec{r}, t)$ of the system includes $\hat{j}_{\text{mat}}^k(\vec{r}, t)$ plus an classical external current density $j_{\text{ext}}^k(\vec{r}, t)$

$$\hat{j}^k(\vec{r}, t) = \hat{j}_{\text{mat}}^k(\vec{r}, t) + j_{\text{ext}}^k(\vec{r}, t). \quad (\text{A.5.12})$$

Therefore, the external current interaction Hamiltonian $\hat{H}_{\text{ext,int}}^\perp(t)$ reads

$$\hat{H}_{\text{ext,int}}^\perp(t) = \frac{1}{c_0} \int d^3r \hat{j}_{\text{ext}}^k(\vec{r}, t) \hat{A}_k(\vec{r}, t). \quad (\text{A.5.13})$$

Replacing the external current density in Eq. (A.5.13) by the system current density $\hat{j}_{\text{mat}}^k(\vec{r}, t)$ leads to the transverse interaction Hamiltonian $\hat{H}_{\text{mat,int}}^\perp(t)$

$$\hat{H}_{\text{mat,int}}^\perp(t) = \frac{1}{c_0} \int d^3r \hat{j}_{\text{mat}}^k(\vec{r}, t) \hat{A}_k(\vec{r}, t). \quad (\text{A.5.14})$$

Substituting $\hat{j}_{\text{mat}}^k(\vec{r}, t)$ with all current terms from Eq. (A.5.8) and integrating by parts

yields

$$\begin{aligned}
\hat{H}_{\text{mat,int}}^\perp(t) = & - \sum_{n=1}^N \int d^3r \frac{i\hbar q(n)}{2M(n)c_0} \sum_{s,s'} \hat{\Phi}_{(n)}^\dagger(\vec{r},s) \partial_k \hat{A}^k(\vec{r},t) \hat{\Phi}_{(n)}(\vec{r},s) \\
& - \sum_{n=1}^N \int d^3r \frac{i\hbar q(n)}{2M(n)c_0} \sum_{s,s'} \hat{\Phi}_{(n)}^\dagger(\vec{r},s) \hat{A}_k(\vec{r},t) \partial^k \hat{\Phi}_{(n)}(\vec{r},s) \\
& + \sum_{n=1}^N \int d^3r \frac{q(n)^2}{2M(n)c_0^2} \sum_{s,s'} \hat{\Phi}_{(n)}^\dagger(\vec{r},s) \hat{A}_k(\vec{r},t) \hat{A}^k(\vec{r},t) \hat{\Phi}_{(n)}(\vec{r},s) \\
& + \sum_{n=1}^N \int d^3r \frac{q\hbar}{2M(n)} \sum_{s,s'} \hat{\Phi}_{(n)}^\dagger(\vec{r},s) [S_k^{(n)}]_{s,s'} \hat{\Phi}_{(n)}(\vec{r},s') \left(\frac{1}{c_0} \epsilon^{klm} \partial_l \hat{A}_m(\vec{r},t) \right)
\end{aligned} \tag{A.5.15}$$

Comparing Eq. (A.5.15) with Eq. (A.3.6) reveals that adding the zero-field Maxwell kinetic Hamiltonian $\hat{H}_{\text{mat,kin},0}^{(n)}$

$$\hat{H}_{\text{mat,kin},0}^{(n)} = \int d^3r \frac{\hbar^2}{2M(n)} \sum_{s,s'} \hat{\Phi}_{(n)}^\dagger(\vec{r},s) \partial_k \partial^k \hat{\Phi}_{(n)}(\vec{r},s) \tag{A.5.16}$$

allows to combine both into the kinetic energy Hamiltonian $\hat{H}_{\text{mat,kin}}^{(n)}$ with Maxwell field plus the Stern-Gerlach term. Hence,

$$\hat{H}_{\text{mat,kin}} = \sum_{n=1}^N \hat{H}_{\text{mat,kin},0}^{(n)}(t) + \hat{H}_{\text{mat,int}}^\perp(t), \tag{A.5.17}$$

$$= \sum_{n=1}^N \hat{H}_{\text{mat,kin}}^{(n)}(t) + \sum_{n=1}^N \hat{H}_{\text{mat,Stern}}^{(n)}(t), \tag{A.5.18}$$

with the specific species kinetic Hamiltonian $\hat{H}_{\text{mat,kin}}^{(n)}$ and Stern-Gerlach Hamiltonian $\hat{H}_{\text{mat,Stern}}^{(n)}$

$$\begin{aligned}
& \hat{H}_{\text{mat,kin}}^{(n)}(t) \\
& = - \int d^3r \frac{1}{2M(n)} \sum_s \hat{\Phi}_{(n)}^\dagger(\vec{r},s) \left(-i\hbar \partial_k + \frac{q}{c_0} \hat{A}_k(\vec{r},t) \right) \left(-i\hbar \partial^k + \frac{q}{c_0} \hat{A}^k(\vec{r},t) \right) \hat{\Phi}_{(n)}(\vec{r},s),
\end{aligned} \tag{A.5.19}$$

$$\hat{H}_{\text{mat,Stern}}^{(n)}(t) = \int d^3r \frac{q\hbar}{2M(n)} \sum_{s,s'} \hat{\Phi}_{(n)}^\dagger(\vec{r},s) [S_k^{(n)}]_{s,s'} \hat{\Phi}_{(n)}(\vec{r},s') \left(\frac{1}{c_0} \epsilon^{klm} \partial_l \hat{A}_m(\vec{r},t) \right) \tag{A.5.20}$$

That means that the transverse interaction of the considered matter with the photon field is implied in terms of the canonical kinetic energy Hamiltonian, only complemented by the Stern-Gerlach term.

In quantum electrodynamics to get physically correct results, $M(n)$ has to be renormalized by the electromagnetic mass $\delta_{M(n)}$, so that $M(n) = M_{\text{bare},(n)} + \delta_{M(n)}$. The electromagnetic mass depends on the photon energy, which means that the matter couples implicitly to the transverse photon field and vice versa via the electromagnetic mass $\delta_{M(n)}$. In many cases, if the electromagnetic mass contribution is rather small compared to the bare mass of the species, we can approximate $M(n) \approx M_{\text{bare},(n)}$. We use this approximation in our applications later in this work.

List of Figures

| | | |
|------|---|-----|
| 3.1 | Two-dimensional slice of a three-dimensional simulation box with different simulation regions | 35 |
| 3.2 | Two-dimensional stencil | 39 |
| 3.3 | Parallelization scheme for dividing the Maxwell grid into four partitions . . . | 40 |
| 3.4 | Spatial external current density distribution | 43 |
| 3.5 | Electromagnetic variables for external current signals, calculated by Octopus and MEEP | 45 |
| 3.6 | Contour snapshots along the xy-plane of the electric field in z-direction for the electromagnetic field propagation with four different external currents . . | 47 |
| 3.7 | Spatial distribution of a transverse current density along the xy-plane. . . . | 49 |
| 3.8 | Snapshots of the electric field in z-direction for the longitudinal current density | 50 |
| 3.9 | Snapshots of the electric field in z-direction for the transverse current density | 51 |
| 3.10 | Electric and magnetic field reaction in z-direction for the longitudinal and transverse current density | 51 |
| 3.11 | Mask function along a cartesian axis | 53 |
| 3.12 | A three-dimensional contour plot of the mask function in the x-y plane | 54 |
| 3.13 | Relative variation of the energy and the electric field at two points for different parameters q | 62 |
| 3.14 | Comparison of absorbing mask and perfectly matched layer boundary conditions | 63 |
| 3.15 | Two-dimensional scheme of incident waves boundaries | 64 |
| 3.16 | Incident plane wave simulation of two interfering plane waves | 66 |
| 3.17 | Numerical dispersion of the free Riemann-Silberstein Maxwell propagation . . | 69 |
| 3.18 | Two-dimensional scheme of incident waves boundaries combined with PML | 71 |
| 3.19 | Simulation box illustration for a laser pulse hitting a linear medium box . . . | 73 |
| 3.20 | Sequence of the electric field simulated by a Riemann-Silberstein Maxwell propagation including a linear medium box | 75 |
| 5.1 | Multiscale grid types for the Kohn-Sham and Maxwell grid | 103 |
| 5.2 | Domain parallelization of matter and Maxwell grid | 105 |
| 5.3 | Predictor-corrector scheme of a Maxwell-Kohn-Sham propagation step | 107 |
| 5.4 | Electromagnetic detectors at the simulation boundaries | 109 |
| 6.1 | Simulation scheme of a laser pulse excitation of a quantum-mechanical system. | 111 |
| 6.2 | Geometry of the Na ₂₉₇ dimer in E2E configuration with different distances $d_1 = 0.1\text{nm}$ and $d_2 = 0.5\text{nm}$ between the two effective spheres of the clusters which are illustrated by the black dashed circle. | 112 |
| 6.3 | Contour plots in the x-y plane for the current density, the electron localization function, electric field difference, and Maxwell energy difference | 117 |
| 6.4 | Similar movie frame as Fig. 6.3, but with the frame at time 8.33 fs. | 118 |

| | | |
|------|--|-----|
| 6.5 | Electric field values and current density in z-direction in the center between the two Sodium clusters for $d_1 = 0.1\text{nm}$ | 119 |
| 6.6 | Electric field values and current density in z-direction in the center between the two Sodium clusters for $d_2 = 0.5\text{nm}$ | 120 |
| 6.7 | Decomposition of the total electric field into transverse and longitudinal components for the dimer with $d_1 = 0.1\text{nm}$ | 121 |
| 6.8 | Decomposition of the electric field as in figure Fig. 6.7 for the sodium dimer with $d_2 = 0.5\text{ nm}$. | 122 |
| 6.9 | Contour plots for the electric field enhancement in the x-z plane of the nanoplasmonic dimer with $d_1 = 0.1\text{nm}$ | 123 |
| 6.10 | Matter and electromagnetic energies for the sodium dimer with $d_1 = 0.1\text{nm}$ separation | 124 |
| 6.11 | Matter and electromagnetic energies for the sodium dimer with $d_2 = 0.5\text{nm}$ separation | 126 |
| 6.12 | Position expectation value of the nanoplasmonic dimer with $d_1 = 0.1\text{ nm}$ separation | 127 |
| 6.13 | Fourier transform of the dipole expectationvalues and the electric field at the far-field detectors | 128 |
| 6.14 | Same as Fig. 6.10 but now including the motion of the ions in classical Ehrenfest approximation. | 129 |
| 6.15 | Electric field, Maxwell energy and dipole expectation value for the comparison between TDLDA, TDPBE, and fully coupled Maxwell to matter simulations | 130 |

List of Tables

| | | |
|-----|--|-----|
| 3.1 | Simulation parameters for the Octopus and MEEP comparison run. | 44 |
| 3.2 | Physical and simulation parameters of external current simulation for screening the parameters of the PML absorbing boundaries | 61 |
| 3.3 | Simulation parameters for the incident plane waves run with two interfering incident waves. | 67 |
| 3.4 | Simulation box and time parameters for the numerical dispersion run with an incident wave pulse | 69 |
| 3.5 | Simulation box and time parameters for the numerical dispersion run with an incident wave pulse | 70 |
| 3.6 | Simulation parameters for the laser pulse run that hits a cubic linear medium box | 74 |
| 6.1 | Table of acronyms that are used in the present work to indicate the level of EMPKS theory. | 110 |
| 6.2 | Simulation parameters for the sodium dimer for distances $d_1 = 0.1$ nm and $d_2 = 0.5$ nm. | 114 |

Bibliography

- [1] A. Szabo and N. Ostlund, Modern Quantum Chemistry: Introduction to Advanced Electronic Structure. Dover Books on Chemistry, Dover Publications, 2012.
- [2] R. Martin, L. Reining, and D. Ceperley, Interacting Electrons: Theory and Computational Approaches. Cambridge University Press, 2016.
- [3] U. Schollwöck, “The density-matrix renormalization group in the age of matrix product states,” Annals of Physics, vol. 326, no. 1, pp. 96 – 192, 2011.
- [4] E. Engel and R. M. Dreizler, Density functional theory: an advanced course. Springer Science & Business Media, 2011.
- [5] R. Loudon, The quantum theory of light. Oxford Science Publications, 1988.
- [6] G. Grynberg, A. Aspect, and C. Fabre, Introduction to quantum optics: from the semi-classical approach to quantized light. Cambridge University Press, 2010.
- [7] M. Born and E. Wolf, Principles of optics: electromagnetic theory of propagation, interference and diffraction of light. Elsevier, 2013.
- [8] R. Chikkaraddy, B. de Nijs, F. Benz, S. J. Barrow, O. A. Scherman, E. Rosta, A. Demetriadou, P. Fox, O. Hess, and J. J. Baumberg, “Single-molecule strong coupling at room temperature in plasmonic nanocavities,” Nature, vol. 535, no. 7610, pp. 127–130, 2016.
- [9] D. Wang, H. Kelkar, D. Martin-Cano, T. Utikal, S. Götzinger, and V. Sandoghdar, “Coherent coupling of a single molecule to a scanning fabry-perot microcavity,” Physical Review X, vol. 7, no. 2, p. 021014, 2017.
- [10] M. Sukharev and A. Nitzan, “Optics of exciton-plasmon nanomaterials,” Journal of Physics: Condensed Matter, vol. 29, no. 44, p. 443003, 2017.
- [11] T. W. Ebbesen, “Hybrid light–matter states in a molecular and material science perspective,” Accounts of Chemical Research, vol. 49, no. 11, pp. 2403–2412, 2016.
- [12] J. A. Hutchison, T. Schwartz, C. Genet, E. Devaux, and T. W. Ebbesen, “Modifying chemical landscapes by coupling to vacuum fields,” Angewandte Chemie International Edition, vol. 51, no. 7, pp. 1592–1596, 2012.
- [13] Y. S. Yamamoto, Y. Ozaki, and T. Itoh, “Recent progress and frontiers in the electromagnetic mechanism of surface-enhanced raman scattering,” Journal of Photochemistry and Photobiology C: Photochemistry Reviews, vol. 21, pp. 81–104, 2014.

- [14] X. Zhong, T. Chervy, L. Zhang, A. Thomas, J. George, C. Genet, J. A. Hutchison, and T. W. Ebbesen, “Energy transfer between spatially separated entangled molecules,” Angewandte Chemie International Edition, vol. 56, no. 31, pp. 9034–9038.
- [15] A. Shalabney, J. George, H. Hiura, J. A. Hutchison, C. Genet, P. Hellwig, and T. W. Ebbesen, “Enhanced raman scattering from vibro-polariton hybrid states,” Angewandte Chemie International Edition, vol. 54, no. 27, pp. 7971–7975, 2015.
- [16] T. Byrnes, N. Y. Kim, and Y. Yamamoto, “Exciton-polariton condensates,” Nature Physics, vol. 10, no. 11, pp. 803–813, 2014.
- [17] A. Sommer, E. Bothschafter, S. Sato, C. Jakubeit, T. Latka, O. Razskazovskaya, H. Fattahi, M. Jobst, W. Schweinberger, V. Shirvanyan, et al., “Attosecond nonlinear polarization and light–matter energy transfer in solids,” Nature, vol. 534, no. 7605, p. 86, 2016.
- [18] J. J. Maki, M. S. Malcuit, J. Sipe, and R. W. Boyd, “Linear and nonlinear optical measurements of the Lorentz local field,” Physical Review Letters, vol. 67, no. 8, p. 972, 1991.
- [19] T. H. Taminiau, S. Karaveli, N. F. Van Hulst, and R. Zia, “Quantifying the magnetic nature of light emission,” Nature communications, vol. 3, p. 979, 2012.
- [20] C. T. Schmiegelow, J. Schulz, H. Kaufmann, T. Ruster, U. G. Poschinger, and F. Schmidt-Kaler, “Transfer of optical orbital angular momentum to a bound electron,” Nature communications, vol. 7, p. 12998, 2016.
- [21] I. Bialynicki-Birula and Z. Bialynicka-Birula, “Quantum numbers and spectra of structured light,” Physica Scripta, vol. 93, no. 10, p. 104005, 2018.
- [22] Z. Yue, H. Ren, S. Wei, J. Lin, and M. Gu, “Angular-momentum nanometrology in an ultrathin plasmonic topological insulator film,” Nature Communications, vol. 9, no. 1, p. 4413, 2018.
- [23] H. R. Zengji Yue and M. Gu, “Angular-momentum nanometrology in an ultrathin plasmonic topological insulator film,” Nature Communications, vol. 9, 2018.
- [24] D. M. Coles, Y. Yang, Y. Wang, R. T. Grant, R. A. Taylor, S. K. Saikin, A. Aspuru-Guzik, D. G. Lidzey, J. K.-H. Tang, and J. M. Smith, “Strong coupling between chlorosomes of photosynthetic bacteria and a confined optical cavity mode,” Nature communications, vol. 5, 2014.
- [25] M. Ruggenthaler, N. Tancogne-Dejean, J. Flick, H. Appel, and A. Rubio, “From a quantum-electrodynamical light–matter description to novel spectroscopies,” Nature Reviews Chemistry, vol. 2, no. 3, p. 0118, 2018.
- [26] G. H. Booth, A. J. W. Thom, and A. Alavi, “Fermion monte carlo without fixed nodes: A game of life, death, and annihilation in slater determinant space,” The Journal of Chemical Physics, vol. 131, no. 5, p. 054106, 2009.
- [27] R. Orus, “A practical introduction to tensor networks: Matrix product states and projected entangled pair states,” Annals of Physics, vol. 349, pp. 117 – 158, 2014.
- [28] U. Schollwöck, “The density-matrix renormalization group,” Rev. Mod. Phys., vol. 77, pp. 259–315, Apr 2005.

- [29] G. Kotliar, S. Y. Savrasov, K. Haule, V. S. Oudovenko, O. Parcollet, and C. A. Marianetti, “Electronic structure calculations with dynamical mean-field theory,” Rev. Mod. Phys., vol. 78, pp. 865–951, Aug 2006.
- [30] E. Gull, A. J. Millis, A. I. Lichtenstein, A. N. Rubtsov, M. Troyer, and P. Werner, “Continuous-time Monte Carlo methods for quantum impurity models,” Rev. Mod. Phys., vol. 83, pp. 349–404, May 2011.
- [31] W. Metzner, M. Salmhofer, C. Honerkamp, V. Meden, and K. Schönhammer, “Functional renormalization group approach to correlated fermion systems,” Rev. Mod. Phys., vol. 84, pp. 299–352, Mar 2012.
- [32] H. Aoki, N. Tsuji, M. Eckstein, M. Kollar, T. Oka, and P. Werner, “Nonequilibrium dynamical mean-field theory and its applications,” Rev. Mod. Phys., vol. 86, pp. 779–837, Jun 2014.
- [33] A. Abedi, N. T. Maitra, and E. K. Gross, “Exact factorization of the time-dependent electron-nuclear wave function,” Physical Review Letters, vol. 105, no. 12, p. 123002, 2010.
- [34] A. Abedi, N. T. Maitra, and E. Gross, “Correlated electron-nuclear dynamics: Exact factorization of the molecular wavefunction,” The Journal of Chemical Physics, vol. 137, no. 22, p. 22A530, 2012.
- [35] R. Kapral, “Quantum dynamics in open quantum-classical systems,” Journal of Physics: Condensed Matter, vol. 27, no. 7, p. 073201, 2015.
- [36] J. C. Tully, “Perspective: Nonadiabatic dynamics theory,” The Journal of Chemical Physics, vol. 137, no. 22, p. 22A301, 2012.
- [37] W. H. Miller, “Perspective: Quantum or classical coherence?,” The Journal of Chemical Physics, vol. 136, no. 21, p. 210901, 2012.
- [38] E. Lorin, S. Chelkowski, and A. Bandrauk, “A numerical Maxwell–Schrödinger model for intense laser–matter interaction and propagation,” Computer Physics Communications, vol. 177, no. 12, pp. 908–932, 2007.
- [39] K. Lopata and D. Neuhauser, “Multiscale Maxwell–Schrödinger modeling: A split field finite-difference time-domain approach to molecular nanopolaritonics,” The Journal of chemical physics, vol. 130, no. 10, p. 104707, 2009.
- [40] K. Yabana, T. Sugiyama, Y. Shinohara, T. Otobe, and G. F. Bertsch, “Time-dependent density functional theory for strong electromagnetic fields in crystalline solids,” Phys. Rev. B, vol. 85, p. 045134, Jan 2012.
- [41] M. Lucchini, S. A. Sato, A. Ludwig, J. Herrmann, M. Volkov, L. Kasmi, Y. Shinohara, K. Yabana, L. Gallmann, and U. Keller, “Attosecond dynamical Franz-Keldysh effect in polycrystalline diamond,” Science, vol. 353, no. 6302, pp. 916–919, 2016.
- [42] Y. Li, S. He, A. Russakoff, and K. Varga, “Accurate time propagation method for the coupled maxwell and kohn-sham equations,” Phys. Rev. E, vol. 94, p. 023314, Aug 2016.
- [43] A. Yamada and K. Yabana, “Energy transfer from intense laser pulse to dielectrics in time-dependent density functional theory,” ArXiv e-prints, July 2018.

- [44] A. Yamada and K. Yabana, “Time-dependent density functional theory for a unified description of ultrafast dynamics: pulsed light, electrons, and atoms in crystalline solids,” ArXiv e-prints, Oct. 2018.
- [45] M. Uemoto, Y. Kuwabara, S. A. Sato, and K. Yabana, “Nonlinear polarization evolution using time-dependent density functional theory,” ArXiv e-prints, Oct. 2018.
- [46] S. Yamada, M. Noda, K. Nobusada, and K. Yabana, “Time-dependent density functional theory for interaction of ultrashort light pulse with thin materials,” ArXiv e-prints, Oct. 2018.
- [47] M. Ruggenthaler, F. Mackenroth, and D. Bauer, “Time-dependent Kohn-Sham approach to quantum electrodynamics,” Physical Review A, vol. 84, no. 4, p. 042107, 2011.
- [48] I. Tokatly, “Time-dependent density functional theory for many-electron systems interacting with cavity photons,” Physical Review Letters, vol. 110, no. 23, p. 233001, 2013.
- [49] M. Ruggenthaler, J. Flick, C. Pellegrini, H. Appel, I. V. Tokatly, and A. Rubio, “Quantum-electrodynamical density-functional theory: Bridging quantum optics and electronic-structure theory,” Physical Review A, vol. 90, no. 1, p. 012508, 2014.
- [50] M. Ruggenthaler, “Ground-state quantum-electrodynamical density-functional theory,” arXiv preprint arXiv:1509.01417, 2015.
- [51] J. Galego, F. J. Garcia-Vidal, and J. Feist, “Cavity-induced modifications of molecular structure in the strong-coupling regime,” Physical Review X, vol. 5, no. 4, p. 041022, 2015.
- [52] J. Flick, N. Rivera, and P. Narang, “Strong light-matter coupling in quantum chemistry and quantum photonics,” Nanophotonics, vol. 7, no. 9, pp. 1479–1501, 2018.
- [53] J. Feist, J. Galego, and F. J. Garcia-Vidal, “Polaritonic chemistry with organic molecules,” ACS Photonics, 2017.
- [54] R. F. Ribeiro, L. A. Martínez-Martínez, M. Du, J. Campos-Gonzalez-Angulo, and J. Y. Zhou, “Polariton chemistry: controlling molecular dynamics with optical cavities,” Chemical Science, 2018.
- [55] P. M. M. C. de Melo and A. Marini, “Unified theory of quantized electrons, phonons, and photons out of equilibrium: A simplified ab initio approach based on the generalized Baym-Kadanoff ansatz,” Phys. Rev. B, vol. 93, p. 155102, Apr 2016.
- [56] J. Flick, H. Appel, M. Ruggenthaler, and A. Rubio, “Cavity Born–Oppenheimer approximation for correlated electron–nuclear-photon systems,” Journal of chemical theory and computation, vol. 13, no. 4, pp. 1616–1625, 2017.
- [57] J. Flick and P. Narang, “Cavity correlated electron-nuclear dynamics from first principles,” ArXiv e-prints, 2018.
- [58] C. Schäfer, M. Ruggenthaler, and A. Rubio, “Ab initio nonrelativistic quantum electrodynamics: Bridging quantum chemistry and quantum optics from weak to strong coupling,” Physical Review A, vol. 98, no. 4, p. 043801, 2018.

- [59] J. Flick, D. M. Welakuh, M. Ruggenthaler, H. Appel, and A. Rubio, “Light-matter response functions in quantum-electrodynamical density-functional theory: Modifications of spectra and of the maxwell equations,” arXiv preprint arXiv:1803.02519, 2018.
- [60] J. Flick, M. Ruggenthaler, H. Appel, and A. Rubio, “Atoms and molecules in cavities, from weak to strong coupling in quantum-electrodynamics (QED) chemistry,” Proceedings of the National Academy of Sciences, p. 201615509, 2017.
- [61] J. Flick, C. Schäfer, M. Ruggenthaler, H. Appel, and A. Rubio, “Ab Initio Optimized Effective Potentials for Real Molecules in Optical Cavities: Photon Contributions to the Molecular Ground State,” ACS photonics, vol. 5, no. 3, pp. 992–1005, 2018.
- [62] H. Spohn, Dynamics of charged particles and their radiation field. Cambridge university press, 2004.
- [63] R. Jestädt, M. Ruggenthaler, M. J. Oliveira, A. Rubio, and H. Appel, “Real-time solutions of coupled Ehrenfest-Maxwell-Pauli-Kohn-Sham equations: fundamentals, implementation, and nano-optical applications,” ArXiv e-prints, 2018.
- [64] K. Yee, “Numerical solution of initial boundary value problems involving Maxwell’s equations in isotropic media,” Antennas and Propagation, IEEE Transactions on, vol. 14, pp. 302–307, May 1966.
- [65] A. Taflov and S. Hagness, Computational Electrodynamics: The Finite-difference Time-domain Method. Artech House antennas and propagation library, Artech House, 2005.
- [66] R. Dreizler and E. Gross, Density Functional Theory. Berlin: Springer Verlag, 1990.
- [67] M. A. Marques, Time-Dependent Density Functional Theory, vol. 706 of Lecture Notes in Physics. Springer, berlin, heidelberg ed., 2006.
- [68] L. Silberstein, “Elektromagnetische Grundgleichungen in bivectorieller Behandlung,” Annalen der Physik, vol. 327, pp. 579–586, 1907.
- [69] M. H. L. Pryce, “The mass-centre in the restricted theory of relativity and its connexion with the quantum theory of elementary particles,” Proceedings of the Royal Society of London A: Mathematical, Physical and Engineering Sciences, vol. 195, no. 1040, pp. 62–81, 1948.
- [70] A. Gersten, “Maxwell’s Equations as the One-Photon Quantum Equation,” Foundations of Physics Letters, vol. 12, no. 3, pp. 291–298, 1999.
- [71] P. J. Mohr, “Solutions of the maxwell equations and photon wave functions,” Annals of Physics, vol. 325, no. 3, pp. 607 – 663, 2010.
- [72] I. Bialynicki-Birula, “On the wave function of the photon,” Acta Physica Polonica A, vol. 86, pp. 97–116, 1994.
- [73] I. Bialynicki-Birula, “V photon wave function,” vol. 36 of Progress in Optics, pp. 245–294, Elsevier, 1996.
- [74] S. A. Khan, “An Exact Matrix Representation of Maxwell’s Equations,” Physica Scripta, vol. 71, no. 5, p. 440, 2005.
- [75] J. Jackson, Classical Electrodynamics. Wiley, 1998.

- [76] E. Wigner and J. Griffin, Group Theory and Its Application to the Quantum Mechanics of Atomic Spectra. Pure and applied Physics, Academic Press, 1959.
- [77] O. Keller, “Space-time description of photon emission from an atom,” Phys. Rev. A, vol. 62, p. 022111, Jul 2000.
- [78] O. Keller, Quantum Theory of Near-Field Electrodynamics. Springer, 2011.
- [79] M. Fox, Quantum optics: an introduction. Oxford Master Series in Atomic, Optical and Laser Physics, Oxford: Oxford Univ. Press, 2006.
- [80] D. J. Griffiths, Introduction to electrodynamics; 4th ed. Boston, MA: Pearson, 2013. Re-published by Cambridge University Press in 2017.
- [81] E. Schrödinger, “An undulatory theory of the mechanics of atoms and molecules,” Phys. Rev., vol. 28, pp. 1049–1070, Dec 1926.
- [82] D. Griffiths, Introduction to Quantum Mechanics. Always learning, Pearson, 2014.
- [83] V. Moretti, Spectral Theory and Quantum Mechanics. Springer-Verlag Mailand, 2013.
- [84] I. Serban, J. Werschnik, and E. K. U. Gross, “Optimal control of time-dependent targets,” Phys. Rev. A, vol. 71, p. 053810, May 2005.
- [85] M. Ndong, H. Tal-Ezer, R. Kosloff, and C. P. Koch, “A Chebychev propagator for inhomogeneous Schrödinger equations,” The Journal of Chemical Physics, vol. 130, no. 12, 2009.
- [86] R. Parr and Y. Weitao, Density-Functional Theory of Atoms and Molecules. International Series of Monographs on Chemistry, Oxford University Press, 1994.
- [87] J. Bérenger, Perfectly Matched Layer (PML) for Computational Electromagnetics. Synthesis lectures on computational electromagnetics, Morgan & Claypool Publishers, 2007.
- [88] A. F. Oskooi, D. Roundy, M. Ibanescu, P. Bermel, J. Joannopoulos, and S. G. Johnson, “Meep: A flexible free-software package for electromagnetic simulations by the FDTD method,” Computer Physics Communications, vol. 181, no. 3, pp. 687 – 702, 2010.
- [89] A. Itkin, Pricing Derivates Under Lévy Models. Pseudo-Differential Operators, Birkhäuser Basel, 2017.
- [90] J. Strikwerda, Finite Difference Schemes and Partial Differential Equations. Other Titles in Applied Mathematics, Society for Industrial and Applied Mathematics (SIAM, 3600 Market Street, Floor 6, Philadelphia, PA 19104), 2004.
- [91] H. Levy and F. Lessman, Finite Difference Equations. Macmillan, 1961.
- [92] G. Smith, Numerical Solution of Partial Differential Equations: Finite Difference Methods. Oxford Applied Mathematics and, Clarendon Press, 1985.
- [93] A. Castro, H. Appel, M. Oliveira, C. A. Rozzi, X. Andrade, F. Lorenzen, M. A. L. Marques, E. K. U. Gross, and A. Rubio, “octopus: a tool for the application of time-dependent density functional theory,” physica status solidi (b), vol. 243, no. 11, pp. 2465–2488.

- [94] R. Courant, K. Friedrichs, and H. Lewy, “Über die partiellen Differenzgleichungen der mathematischen Physik,” Mathematische Annalen, vol. 100, pp. 32–74, 1928.
- [95] R. Courant, K. Friedrichs, and H. Lewy, “On the Partial Difference Equations of Mathematical Physics,” IBM Journal of Research and Development, vol. 11, pp. 215–234, Mar. 1967.
- [96] J.-M. Jin, M. Zunoubi, K. C. Donepudi, and W. C. Chew, “Frequency-domain and time-domain finite-element solution of maxwell’s equations using spectral lanczos decomposition method,” Computer Methods in Applied Mechanics and Engineering, vol. 169, no. 3, pp. 279 – 296, 1999.
- [97] V. Dolean, H. Fol, S. Lanteri, and R. Perrussel, “Solution of the time-harmonic maxwell equations using discontinuous galerkin methods,” Journal of Computational and Applied Mathematics, vol. 218, no. 2, pp. 435 – 445, 2008. The Proceedings of the Twelfth International Congress on Computational and Applied Mathematics.
- [98] J.-P. Berenger, “Three-dimensional perfectly matched layer for the absorption of electromagnetic waves,” Journal of Computational Physics, vol. 127, no. 2, pp. 363 – 379, 1996.
- [99] R. J. Luebbers and F. Hunsberger, “FDTD for nth-order dispersive media,” IEEE Transactions on Antennas and Propagation, vol. 40, pp. 1297–1301, Nov 1992.
- [100] S. Weinberg, The Quantum Theory of Fields. No. Bd. 2 in The Quantum Theory of Fields 3 Volume Hardback Set, Cambridge University Press, 1995.
- [101] W. Greiner and J. Reinhardt, Field quantization. Springer, 2013.
- [102] P. Hohenberg and W. Kohn, “Inhomogeneous electron gas,” Phys. Rev., vol. 136, pp. B864–71, 1964.
- [103] E. Runge and E. K. U. Gross, “Density-functional theory for time-dependent systems,” Phys. Rev. Lett., vol. 52, pp. 997–1000, Mar 1984.
- [104] M. Ruggenthaler, J. Flick, C. Pellegrini, H. Appel, I. V. Tokatly, and A. Rubio, “Quantum-electrodynamical density-functional theory: Bridging quantum optics and electronic-structure theory,” Phys. Rev. A, vol. 90, Jul 2014.
- [105] W. Kohn and L. J. Sham, “Self-consistent equations including exchange and correlation effects,” Phys. Rev., vol. 140, p. A1133, 1965.
- [106] I. Tokatly, “Quantum many-body dynamics in a Lagrangian frame: II. Geometric formulation of time-dependent density functional theory,” Physical Review B, vol. 71, no. 16, p. 165105, 2005.
- [107] M. Ruggenthaler, M. Penz, and R. Van Leeuwen, “Existence, uniqueness, and construction of the density-potential mapping in time-dependent density-functional theory,” Journal of Physics: Condensed Matter, vol. 27, no. 20, p. 203202, 2015.
- [108] H. O. John W. Negele, Quantum many-particle systems. Advanced books classics, Westview Press, 1998.
- [109] J. W. Furness, J. Verbeke, E. I. Tellgren, S. Stopkowicz, U. Ekström, T. Helgaker, and A. M. Teale, “Current density functional theory using meta-generalized gradient exchange-correlation functionals,” Journal of Chemical Theory and Computation, vol. 11, no. 9, pp. 4169–4181, 2015. PMID: 26575912.

- [110] S. K. Min, F. Agostini, I. Tavernelli, and E. K. Gross, “Ab initio nonadiabatic dynamics with coupled trajectories: A rigorous approach to quantum (de) coherence,” The journal of physical chemistry letters, vol. 8, no. 13, pp. 3048–3055, 2017.
- [111] X. A. et al., “Modified ehrenfest formalism for efficient large-scale ab initio molecular dynamic,” Journal of Chemical Theory and Computation, vol. 5, pp. 728–741, Apr 2009.
- [112] G. Arfken and H. Weber, Mathematical Methods For Physicists International Student Edition. Elsevier Science, 2005.
- [113] J. J. Sakurai, Modern Quantum Mechanics (Revised Edition). Addison Wesley, 1 ed., Sept. 1993.
- [114] A. Castro, M. A. L. Marques, and A. Rubio, “Propagators for the time-dependent Kohn–Sham equations,” The Journal of Chemical Physics, vol. 121, no. 8, pp. 3425–3433, 2004.
- [115] A. G̃aszmez Pueyo, M. A. L. Marques, A. Rubio, and A. Castro, “Propagators for the time-dependent kohn–Sham equations: Multistep, runge–Kutta, exponential runge–Kutta, and commutator free magnus methods,” Journal of Chemical Theory and Computation, vol. 14, no. 6, pp. 3040–3052, 2018. PMID: 29672048.
- [116] R. Loudon, The Quantum Theory of Light. Oxford: Clarendon Press, second ed., 1983.
- [117] V. Rokaĵ, D. M. Welakuh, M. Ruggenthaler, and A. Rubio, “Light–matter interaction in the long-wavelength limit: no ground-state without dipole self-energy,” Journal of Physics B: Atomic, Molecular and Optical Physics, vol. 51, no. 3, p. 034005, 2018.
- [118] X. Andrade, D. Strubbe, U. De Giovannini, A. H. Larsen, M. J. T. Oliveira, J. Alberdi-Rodríguez, A. Varas, I. Theophilou, N. Helbig, M. J. Verstraete, L. Stella, F. Nogueira, A. Aspuru-Guzik, A. Castro, M. A. L. Marques, and A. Rubio, “Real-space grids and the octopus code as tools for the development of new simulation approaches for electronic systems,” Phys. Chem. Chem. Phys., vol. 17, pp. 31371–31396, 2015.
- [119] M. A. Marques, A. Castro, G. F. Bertsch, and A. Rubio, “octopus: a first-principles tool for excited electron–ion dynamics” E-mail: octopus@tddft.org.,” Computer Physics Communications, vol. 151, no. 1, pp. 60 – 78, 2003.
- [120] A. Varas, P. Garc̃a-Gonz̃alez, F. J. Garc̃a-Vidal, and A. Rubio, “Anisotropy effects on the plasmonic response of nanoparticle dimers,” The Journal of Physical Chemistry Letters, vol. 6, no. 10, pp. 1891–1898, 2015. PMID: 26263265.
- [121] E. G. Noya, J. P. Doye, D. J. Wales, and Aguado, “Geometric magic numbers of sodium clusters: Interpretation of the melting behaviour,” The European Physical Journal D, vol. 43, pp. 57–60, Jul 2007.
- [122] D. J. W. et. al. <http://www-wales.ch.cam.ac.uk/CCD.html>, 2018. The relaxed atomic structure of the dimer is taken from the Cambridge Cluster Database.
- [123] X. G. et. al., “Abinit: First-principles approach to material and nanosystem properties,” Computer Physics Communications, vol. 180, no. 12, pp. 2582–2615, 2009.

- [124] W. Kohn and L. Sham, “Self-consistent equations including exchange and correlation effects,” Phys. Rev., vol. 140 (4A), pp. 1133–1138, 1965.
- [125] R. Jestädt, M. Ruggenthaler, M. J. Oliveira, A. Rubio, and H. Appel, “Real-time dynamics of nanoplasmonic dimer, distance $d = 0.1$ nm,” nov 2018.
- [126] R. Jestädt, M. Ruggenthaler, M. J. Oliveira, A. Rubio, and H. Appel, “Real-time dynamics of nanoplasmonic dimer, distance $d = 0.5$ nm,” nov 2018.
- [127] J. P. Perdew, K. Burke, and M. Ernzerhof, “Generalized gradient approximation made simple,” Phys. Rev. Lett., vol. 77, pp. 3865–3868, Oct 1996.
- [128] B. Thaller, The dirac equation. Springer Science & Business Media, 2013.
- [129] A. Komech, Quantum Mechanics Genesis and Achievements. Dordrecht: Springer, 2013.
- [130] T. Miyao and H. Spohn, “Spectral analysis of the semi-relativistic Pauli–Fierz hamiltonian,” Journal of Functional Analysis, vol. 256, pp. 2123–2156, 2009.
- [131] M. Könenberg, O. Matte, and E. Stockmeyer, “Existence of ground states of hydrogen-like atoms in relativistic QED I: the semi-relativistic Pauli–Fierz operator,” Reviews in Mathematical Physics, vol. 23, no. 04, pp. 375–407, 2011.
- [132] F. Hiroshima, “Functional integral approach to semi-relativistic Pauli–Fierz models,” Advances in Mathematics, vol. 259, pp. 784 – 840, 2014.
- [133] W. Thirring, Quantum mathematical physics: atoms, molecules and large systems. Springer Science & Business Media, 2013.
- [134] P. W. Atkins and R. S. Friedman, Molecular quantum mechanics. 4th ed ed., 2005.
- [135] M. Nowakowski, “The quantum mechanical current of the pauli equation,” American Journal of Physics, vol. 67, no. 10, pp. 916–919, 1999.

Publication

- Title:** Real-time solutions of coupled Ehrenfest-Maxwell-Pauli-Kohn-Sham equations:
fundamentals, implementation, and nano-optical applications
- Authors:** René Jestädt¹, Michael Ruggenthaler¹, Micael J. T. Oliveira¹,
Angel Rubio^{1,2}, and Heiko Appel¹
- Affiliations:** ¹ Max Planck Institute for the Structure and Dynamics of Matter,
Center for Free Electron Laser Science, 22761 Hamburg, Germany
² Center for Computational Quantum Physics (CCQ),
Flatiron Institute, 162 Fifth Avenue,
New York NY 10010, USA
- Journal:** The Archive (ArXiv.org)
- Article number:** 1812.05049
- URL:** <https://arxiv.org/abs/1812.05049>
- Pages:** 54
- Remarks:** The publication describes the main part of my thesis
and shows the most relevant steps of my whole implementation.

Acronyms

| Acronym | Description |
|----------------|--|
| DFT | Density-functional theory |
| ED | Electric dipole |
| EQ | Electric quadrupole |
| F | Forward coupling |
| F@ED | Forward coupling in ED approximation |
| F@(ED+MD+EQ) | Forward coupling in ED, MD and EQ approximation |
| FB | Forward-backward coupling |
| FB@ED | Forward-backward coupling in ED approximation |
| FB@(ED+MD+EQ) | Forward-backward coupling in ED, MD and EQ approximation |
| FDTD | Finite difference time domain |
| KS | Kohn-Sham |
| lm | Linear medium |
| MD | Magnetic dipole |
| MEEP | MIT Electromagnetic Equation Propagation |
| MIT | Massachusetts Institute of Technology |
| MPKS | Maxwell-Pauli-Kohn-Sham equations |
| Mx | Maxwell |
| PML | Perfectly matched layer |
| QED | Quantum electrodynamics |
| QEDFT | Quantum-electrodynamical density-functional theory |
| RS | Riemann-Silberstein |

Acknowledgements

Successful work nowadays is never done alone and this thesis would never be possible without the help and support of many people

First of all, I want to thank my supervisor Heiko Appel for his amazing support, advices, group leading. I appreciate all the discussions and help for my thesis, also for the advices in using efficiently the computer.

I want to thank Angel Rubio for admitting me into his theory group at the MPSD, the advices, discussions, and providing a nice atmosphere for the scientific work.

I also want to thank Matthias Scheffler for his support at the beginning of my thesis, where I started to work for the FHI. It was very kind that I still could use my office some month longer although the group moved to Hamburg.

I am very thankful to all of my proofreaders, Michael Ruggenthaler, Christian Schäfer, Norah Hoffmann and again especially Heiko for correcting and improving my text, and to Michael Ruggenthaler for supporting me in the deeper theory background with our skype sessions.

I appreciate the whole affable working group first at the FHI and now at the MPSD, namely Christian, Florian, Guillem, Heiko, Henning, Johannes, Micael, Michael, Norah, Uliana, Tanja, Theresa.

I want to thank all my friends for supporting me, "spending power" and thinking of me during the harder time of the work, especially Agnes, Andres, Aquiles, Deniz, Didi, Joe, Julia, Katja, Mareen, Matthias, Nasti, Natalia, Peter.

Finally, I want to thank my family for all the support in the last few years to go my way.

Colophon

The presented work was written with L^AT_EX with "Computer Modern" font. Graphical plots that show curves have been created using Python-Matplotlib. Technical and schematic drawings have been illustrated by using Python-Matplotlib and Inkscape. The contour plots and the movies of the three-dimensional simulation have been created by Visit 2.12.